2013

Effects of Realistic Heat Straightening Repair on the Properties and Serviceability of Damaged Steel Beam Bridges

Amit H. Varma
Purdue University, ahvarma@gmail.com

Youngmoo Sohn
Purdue University, sohny@purdue.edu

JOINT TRANSPORTATION
RESEARCH PROGRAM
INDIANA DEPARTMENT OF TRANSPORTATION
AND PURDUE UNIVERSITY

Effects of Realistic Heat Straightening Repair on the Properties and Serviceability of Damaged Steel Beam Bridges

Amit H. Varma

Youngmoo Sohn

SPR-3105 • Report Number: FHWA/IN/JTRP-2013/03 • DOI: 10.5703/1288284315184

RECOMMENDED CITATION

Varma, A. H., and Y. Sohn. *Effects of Realistic Heat Straightening Repair on the Properties and Serviceability of Damaged Steel Beam Bridges*. Publication FHWA/IN/JTRP-2013/03. Joint Transportation Research Program, Indiana Department of Transportation and Purdue University, West Lafayette, Indiana, 2013. doi: 10.5703/1288284315184.

AUTHORS

Amit H. Varma, PhD
Associate Professor of Civil Engineering
School of Civil Engineering
Purdue University
(765) 496-3419
ahvarma@purdue.edu
Corresponding Author

Youngmoo Sohn
Graduate Research Assistant
School of Civil Engineering
Purdue University

JOINT TRANSPORTATION RESEARCH PROGRAM

The Joint Transportation Research Program serves as a vehicle for INDOT collaboration with higher education institutions and industry in Indiana to facilitate innovation that results in continuous improvement in the planning, design, construction, operation, management and economic efficiency of the Indiana transportation infrastructure. https://engineering.purdue.edu/JTRP/index_html

Published reports of the Joint Transportation Research Program are available at: http://docs.lib.purdue.edu/jtrp/

NOTICE

TECHNICAL REPORT STANDARD TITLE PAGE

1. Report No.	2. Government Accession No.	3. Recipient's Catalog No.
FHWA/IN/JTRP-2013/03		

4. Title and Subtitle	5. Report Date
Effects of Realistic Heat Straightening Repair on the Properties and Serviceability of Damaged Steel Beam Bridges	February 2012
	6. Performing Organization Code

7. Author(s)	8. Performing Organization Report No.
Amit H. Varma, Youngmoo Sohn	FHWA/IN/JTRP-2013/03

9. Performing Organization Name and Address	10. Work Unit No.
Joint Transportation Research Program Purdue University 550 Stadium Mall Drive West Lafayette, IN 47907-2051	
	11. Contract or Grant No. SPR-3105

12. Sponsoring Agency Name and Address	13. Type of Report and Period Covered
Indiana Department of Transportation State Office Building 100 North Senate Avenue Indianapolis, IN 46204	Final Report
	14. Sponsoring Agency Code

15. Supplementary Notes

Prepared in cooperation with the Indiana Department of Transportation and Federal Highway Administration.

16. Abstract

The permanent deformations in steel beam bridges caused by collision with high profile vehicles can be repaired by heat straightening, which is a structurally efficient and cost-effective repair process developed by many engineers over the years. Guidelines for conducting heat straightening repair have been developed by FHWA and many DOTS. The guidelines establish limits for: (a) the maximum damage that can be repaired, (b) the maximum restraining force, and (c) the maximum heating temperature to prevent the side effects of heat straightening repair process. However the heat straightening guidelines are violated in the field due to time and economic issues. These violations include, but are not limited to: (a) under heating below 1200°F, (b) overheating above 1200°F, (c) overstraining above restraining force limit (0.5 M_p) and (d) multiple heat straightening of the same beam more than two times.

Currently, there is a lack of knowledge of the effects of these imperfections in the heat straightening repair process on the condition and serviceability of the damaged-repaired beams. This knowledge is needed to develop more realistic guidelines for evaluating and replacing bridge members subjected to damage followed by imperfect heat straightening repair. The overall goal of this research is to develop recommendations and guidelines for evaluating steel beam bridges in Indiana subjected to damage followed by heat straightening repair with imperfections (overstraining, overheating, or multiple heat straightening).

17. Key Words	18. Distribution Statement
heat straightening repair, damaged steel beam bridge, overstraining, overheating, multiple heat straightening, SPR-3105	No restrictions. This document is available to the public through the National Technical Information Service, Springfield, VA 22161

19. Security Classif. (of this report)	20. Security Classif. (of this page)	21. No. of Pages	22. Price
Unclassified	Unclassified	136	

Form DOT F 1700.7 (8-69)

EXECUTIVE SUMMARY

EFFECTS OF REALISTIC HEAT STRAIGHTENING REPAIR ON THE PROPERTIES AND SERVICEABILITY OF DAMAGED STEEL BEAM BRIDGES

Introduction

Over-height trucks occasionally collide (impact) with steel highway bridges, causing structural damage to the steel beams. This permanent deformation can be repaired by heat straightening, which is a structurally efficient and cost-effective repair process. However, in the real field implementation of heat straightening, the repair process violated the limits and guidelines presented by various state highway agencies and the FHWA. These violations included, but were not limited to (a) underheating below 1200 °F and over restraining; (b) overheating above 1200 °F; and (c) multiple heat straightening of the same beam more than two times. Currently, there is a lack of knowledge of the effects of these imperfections in the heat straightening repair process on the condition and serviceability of the damaged-repaired beams.

The objectives of this research are to (a) determine and evaluate the realistic implementation of heat straightening repair (with imperfections) in Indiana using database analysis and in situ field measurements; (b) experimentally investigate the effects of realistic heat straightening (with imperfections such as overheating, overstraining, or multiple heat straightening) on the structural properties, fracture toughness, and serviceability performance of steel beam bridges; and (c) develop research-based guidelines and recommendations for damaged steel beam bridges subjected to realistic heat straightening with imperfections.

Findings

- Overheating (1400 °F) significantly reduced the required number of heating cycles to repair the damaged specimen when compared with normal heating (1200 °F).
- The overall fracture toughness of the small scale test specimens was lower than the overall fracture toughness of the undamaged steel.
- Compared with the undamaged specimen, the Charpy impact toughness values of all specimens were decreased by heat straightening.
- A maximum heating temperature of 1400 °F may be an acceptable imperfection. In this research, overheating specimens (heated up to 1400 °F) and normal-heating specimens (heated up to 1200 °F) showed similar test results. However, additional studies are required to support this recommendation.
- Three damage-repair cycles might be acceptable. The test results of this research indicated that the difference between three damage-repair specimens and single damage-repair specimens was not that significant. However, additional research will also be needed to validate this recommendation.
- An excessive restraining force over 0.5 Mp should not be combined with underheating (lower than 1000 °F).
- Service load deflections increased significantly after each damage process. However, the increased deflections reduced to undamaged deflections by the heat straightening repair.
- To avoid serviceability issues, unless the bridge traffic is closed, damaged girders should be repaired immediately.

Implementation

The research objectives were achieved by conducting the following tasks.

Task I—Evaluation of Heat Straightening in Indiana

Task I was focused on evaluating the realistic implementation of heat straightening in Indiana. The Indiana heat straightening repair site was visited to observe the realistic implementation of heat straightening in the field. Field measurements were performed to determine the damage location and magnitude, the restraining forces used in the repair process, and the maximum heating temperatures achieved using the oxy-fuel torches. Heat straightening database analysis was performed to finalize the test matrix based on the Indiana Department of Transportation's real bridge repair data.

Task II—Small Scale Experimental Investigations

In Task II, experimental investigations were conducted to evaluate the effects of realistic heat straightening with imperfections on the small scale test. Prior to the real scale test (large scale test), small pieces of steel girders were fabricated and tested to explore the effects of various damage and repair parameters on realistic heat straightening repair.

The small scale test setup focused on the damage and repair of the bottom flange of steel beam girders. In total, six built-up section specimens were prepared and tested. A hydraulic actuator placed at the midpoint applied damaging and restraining force to the test specimen. After the damage, Vee heat was applied on a plastically deformed region to repair the damage with restraining force. This damage and repair behavior was simulated by taking beam specimens with comparable flanges and subjecting them to weak axis bending.

The material properties, including the structural properties, fracture toughness, and microstructure of the damaged-repaired specimens, were determined and evaluated experimentally.

Task III—Large Scale Experimental Investigations

The large scale experimental investigations focus on evaluating the effects of heat straightening on damaged and heat straightened steel beam bridges. Similarly to the small scale test, the test variables of the large scale test were also identified using the database analysis. Prior to the experimental investigations, finite element analysis of the large scale test was conducted to estimate the bridge behavior during the damage and repair process.

The test bridge is composed of two steel rolled beams and concrete slab deck. Two main girders were placed over six abutment blocks. All four beam spans in the test setup were subjected to damage and realistic heat straightening repair simulating field activities and conditions. The specimens were damaged at each midspan. After the damage, Vee heats were applied at the bottom flange of the girders to repair the damage. After the specimens were subjected to damage and heat straightening repair, the serviceability performance of the repaired bridge was determined by subjecting static loads simulating the AASHTO (2007) live loading. The material properties, including the structural properties, fracture toughness, and microstructure of the damaged and repaired steel beam specimens, were also determined and evaluated experimentally.

Task IV—Guidelines and Recommendations for Realistic Heat Straightening

Based on the findings and experimental results from previous tasks, heat straightening guidelines and recommendations were developed for steel beam bridges in Indiana.

CONTENTS

LIST OF TABLES

LIST OF FIGURES

1. INTRODUCTION

1.1 Introduction

Over-height trucks occasionally collide with steel bridges causing structural damage to the steel beams. To repair the damaged portion of the bridge, total or partial replacement may be the best solution. But, in reality, the time and cost of the replacement is too high. Therefore, repair of the damaged part can be an appropriate option for the damage treatment.

Typical types of the structural damage induced by over-height truck collision include dents, gouges, nicks and cracks, and permanent deformations at and around the impact location. Sometimes, connection failure like fracture of the bolted connection and tearing of the girder web weld can also occur. Most of the typical damage types except for permanent deformations can be repaired using simple processes like grinding, welding, splicing, and replacing bolts etc.

The permanent plastic deformations produced by a collision can be described using the damage characterization scheme developed by Avent and Mukai (*1,2*), which includes strong axis (S), weak axis (W), torsional (T), and local buckling (L) damage shown in Figure 1.1.

The permanent deformations can be repaired by heat straightening, which is a structurally efficient and cost-effective repair process developed by steelworkers, fabricators, engineers, and researchers over the years (*3*). Heat straightening is normally composed of two stages of the repair process. In the first stage, restraining force opposite to the direction of damage is applied and then maintained through the second stage. In the second stage, heating is applied in appropriate patterns like Vee, strip, line, or spot on the damaged portions of the steel bridge using oxygen-fuel torches. The combination of restraining force and heating produces thermo-plastic strains and deformations that are opposite to the permanent deformations. Several repetitions of the combined restraining force and heating are required to reverse (repair) the permanent deformations to acceptable levels within tolerance (*2,4–6*).

Typical heating patterns used for conducting repair are shown in Figure 1.2. Vee heats are used to repair out-of-plane deformations of the flange, strip heats are used to repair web lateral deformations, line heats are used to repair weak axis deformations, and spot heats are used to repair the flange local buckling.

While implementing heat straightening repair process, field workers have to follow some restrictions to manage potentially detrimental side effects of heat straightening. The following are the major restrictions that need to be controlled carefully during heat straightening:

1. **Heating temperature.** To avoid the formation of martensite, which can cause brittle behavior of the repaired steel, the maximum heating temperature of mild carbon steel (e.g., A7, A36, A588 steel) has to be limited to 1200 °F (below the phase transition temperature of mild carbon steel—1340 °F) (*7*).
2. **Restraining force.** The yield stress of steel reduces significantly at elevated temperatures. The restraining force is limited to the value that would cause 50% of the plastic moment (M_p) of the damaged section (*7*). This is done to manage the stressed caused by the restraining force during heat straightening.
3. **Cooling method.** Ambient air cooling is recommended as the safest cooling method for heated steel. Rapid cooling can be detrimental if the steel is overheated and may produce brittle "hot spots" (*7*). Rapid cooling by compressed air or water mist can be applied when steel surface temperature is lower than 600 °F.
4. **Mechanical hot working.** Mechanical hot working, which is the combination of large restraining force and low

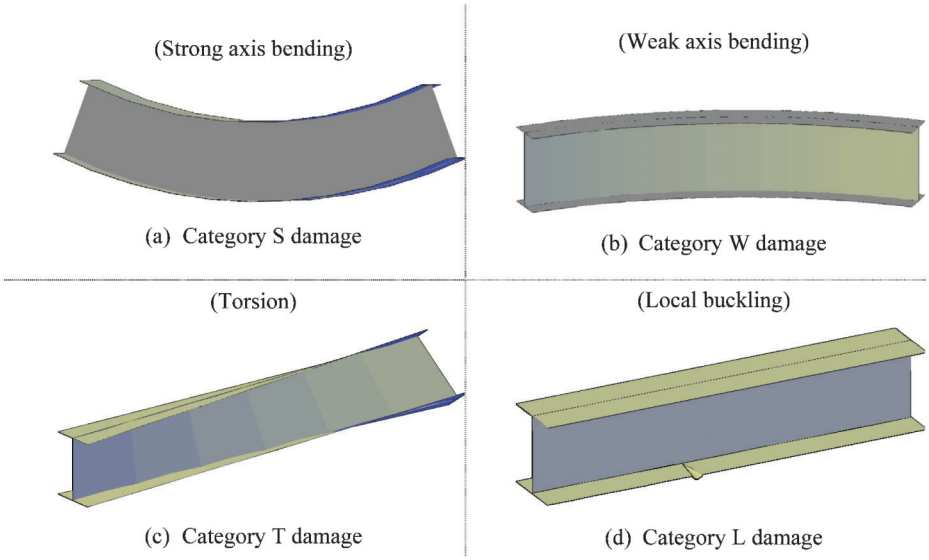

Figure 1.1 Fundamental damage categories for steel beams.

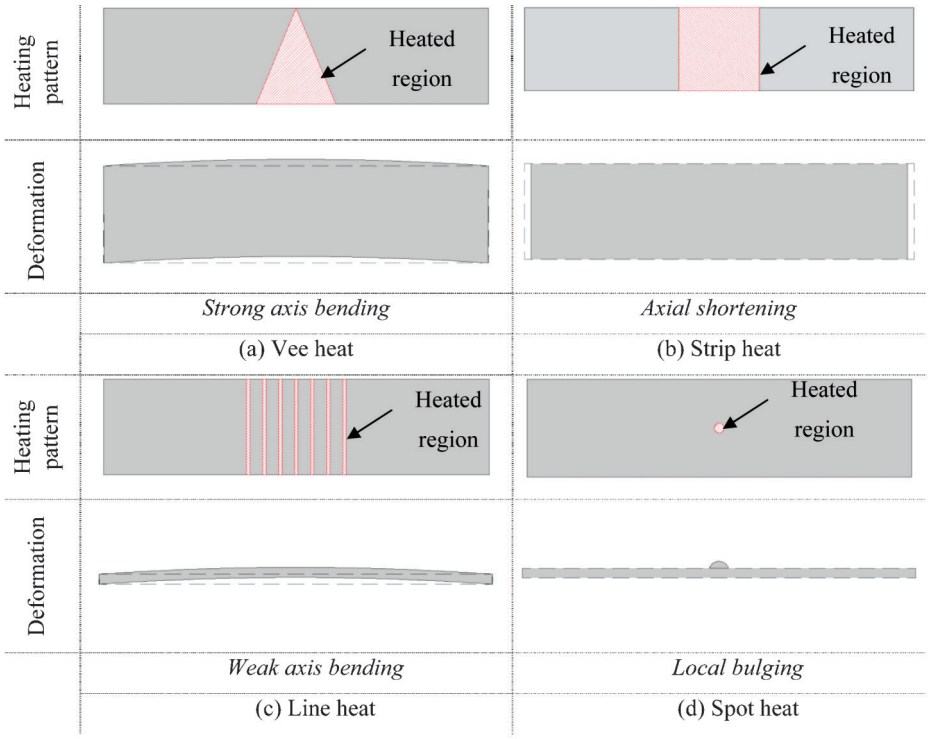

Figure 1.2 Typical heating patterns used for heat straightening repair.

heating temperature below 1200 °F, is not permitted because it can potentially degrade the material properties of repaired steel.

1.2 Problem Statement

Surveys from Varma et al. (*8*) indicated that only a small percentage of state highway agencies (SHAs) use the FHWA or NCHRP guidelines. Some SHAs develop and use their own set of guidelines for heat straightening repair. However, most SHAs do not have any guidelines for heat straightening repair. The survey also established that most SHAs believe that there is a significant need for additional research and more rational guidelines for multiple heat straightening of damaged bridges.

Heat straightening field visits to several repair sites revealed that real heat straightening repair process violated the limits and guidelines mentioned above (*9*), Most SHAs (including Indiana DOT) suspect that the heat straightening limits and guidelines are violated in the field due to time and economic issues. These violations include, but are not limited to: (a) under heating below 1200°F, (b) over heating above 1200°F, (c) over straining above the restraining force limit (0.5 M_p) and (d) multiple heat straightening of the same beam more than two times.

Currently, there is a lack of knowledge of the effects of these imperfections in the heat straightening repair process on the condition and serviceability of the damaged-repaired beams. This knowledge is needed to develop more realistic guidelines for evaluating and replacing bridge members subjected to damage followed by imperfect heat straightening repair. Bridge rehabilitation engineers need these guidelines to approve heat straightening implemented in the field and to develop confidence in the condition and serviceability performance of the bridge girder after repair.

1.3 Research Goal and Objectives

The overall goal of this research is to develop recommendations and guidelines for evaluating steel beam bridges in Indiana subjected to damage followed by heat straightening repair with imperfections (for example, overstraining, overheating, or multiple heat straightening).

The objectives of this research are:

1. To observe and report the realistic implementation of heat straightening repair (with imperfections) of steel bridges in Indiana with in situ field measurements;
2. To experimentally investigate the effects of heat straightening (with imperfections such as overheating, overstraining, and multiple heat straightening) on the structural properties and fracture toughness of small scale test beams;
3. To experimentally investigate the effects of realistic heat straightening (with imperfections such as overheating, overstraining, and multiple heat straightening) on the structural properties, fracture toughness, and serviceability performance of large scale test bridge; and
4. To develop recommendations and guidelines for evaluating steel beam bridges in Indiana subjected to realistic heat straightening with imperfections.

2. PREVIOUS RESEARCH AND GUIDELINES

This chapter provides the literature review of experimental and analytical investigations of previous heat straightening research. The provisions of the heat straightening repair process are also discussed in this chapter.

Previous studies of heat straightening repair on damaged steel beam bridges mainly focused on the following topics:

1. Structural properties of heat straightened steels
2. Techniques of heat straightening repair
3. Guidelines of heat straightening repair on damaged steels

2.1 Early Research

The plastic deformations (plastic rotations), thermal stresses, and applications of heat straightening in practical ways were mainly focused in early heat straightening studies.

Since the 1930's, thermal stress was used for dimensional modifications of steel members by steel fabricators (*3*). However, heat straightening was conducted by field workers with insufficient scientific backgrounds. Hence, the understanding of the thermal properties of steel was mainly focused in early studies (*10–12*). General procedures of heat straightening were also determined by the early researchers (*13*). One of the technical papers mainly focusing on thermal contraction and its effect on steel members was published by J. Holt in 1938. The procedure of heat straightening was also addressed in his publication. Later, the effect of restraining force on plastic rotation during the heat straightening process was added to his revised publication (*10*).

Three papers about heat straightening were published by R. Holt. In his first paper, the Vee heat applying procedure and visual inspection of steel at various temperatures were discussed (*13*). In the second, R. Holt addressed the effects of external restraints and various heating patterns (*13*). Local buckling and its relation to heating width were addressed in his third paper (*14*).

2.2 Previous Research

2.2.1 Experimental Research

Several experimental studies have been conducted to determine the effect of heat straightening on the deformation (plastic rotation) of heat straightened steel members, structural properties of heat straightened steels, and residual stresses caused by the heat straightening repair process.

2.2.1.1 Plastic rotations. The definition of plastic rotation is the change of the angle between the tangents from the opposite sides of the damage location.

Early studies mainly determined the plastic rotations induced by the edge heating, which can introduce smooth curvature (sweep) on a heated specimen, on undamaged steel plates, and on wide flange sections (*15–17*).

Vee heating, which can create sharp curvature on a heated specimen, is the fundamental heating pattern widely used in the real heat straightening repair process. Different parameters have been investigated to determine the influence on the plastic rotations of the Vee heated steel specimen. Weerth (*18*), Horton (*17*), Roeder (*3,22*), Avent et al. (*21,23*), and De Bejar (*24,25*) have conducted heat straightening experiments to find out the characteristics of plastic rotation in the heat straightening process with the following parameters: (i) Vee angle, (ii) Vee depth, (iii) geometric shape and size, (iv) yield stress, (v) maximum heating temperature, (vi) heating time, (vii) heating sequence and pattern, (viii) external restraining forces, (ix) internal restraining forces, and (x) quenching.

Weerth (*18*) has revealed following: (i) the angle of the Vee heat is directly related to the plastic rotation of the heated specimen in a proportional way; (ii) the plastic rotation of the heated specimen is positively affected by the full-depth Vee heats and the restraining force.

Horton (*17*) has concluded the following: (i) full-depth Vee heat is much more effective than half-depth Vee heat in the plastic rotation; (ii) effective heating pattern sequences of wide flange sections were determined; (iii) the plastic rotation of a heated specimen was merely increased by the water mist cooling method. Repair speed of the specimen was not significantly increased by the water mist cooling.

Roeder's (*3,22*) conclusions from his experiments are: (i) thermoplastic deformation is closely related to the temperature; (ii) surface damage to the steel, out-of-plane distortions, and plate buckling are produced by heating temperature higher than 1330 °F; (iii) local buckling can occur increasingly by the increased Vee angle; (iv) plastic rotation can be increased about 20–80% by quenching; (v) the tendency towards local buckling can be reduced by quenching; (vi) Vee heat can develop the plastic deformation primarily within the heated area; and (vii) the plastic rotation of the heated specimen can be increased by increasing the applied bending moment.

Avent et al. (*21,23*) have revealed that: (i) a linear relationship between the plastic rotation and Vee was found in plate and rolled shape specimens; (ii) slightly larger plastic rotations were produced by the Vee depth ratios of ¾ and 1 than a Vee depth ratio of ½; (iii) the plastic rotation was insignificantly affected by plate thickness and geometry; (iv) some temperature variation during heating was allowed by the maximum temperature of 1200 °F; (v) to determine the relationship between restraining forces and plastic rotation, more data are needed; and (vi) very little difference was found in the plastic rotations of undamaged and damaged specimens.

2.2.1.2 Residual stresses. Residual stresses can be produced from the damage and heat straightening repair cycle. Several experimental investigations have been conducted by Roeder (*22*) and Avent et al. (*21,23*) about the residual stresses resulting from the heat straightening of undamaged specimens. The residual stresses resulting from heat straightening on damaged plates and rolled shapes were determined in one research (*7*).

Brockenbrough and Ives (*15*) used the "sectioning method" to measure the residual stresses resulting from heat curving of a plate girder using line heats. The result of this study shows that the residual stress in the plate girder was reduced except at the middle width of the flange. At the heated edges of the flange, tensile residual stresses were close to the yield stress of the steel. The residual stresses in compression were found in the web area (*15*).

Roeder (*22*) determined the effects of residual stresses on heat straightening. The plastic rotations of test specimens with various heating cycles were compared to see the effects of residual stresses on heat straightening. An insignificant difference in the plastic rotation between the test specimens was found. As a result, the researcher concluded that the plastic rotation is not significantly affected by the residual stresses.

Avent and Fadous (*21*) determined the residual stresses produced in heat straightened A36 steel plates. In the results of the research, the Vee heated plates showed that the residual stresses of the edges were in tension and the centers were in compression. Compared with the undamaged specimen, these residual stresses were considerably significant. Additional experimental research of residual stresses about the magnitudes, distributions, and strain aging effects on heat straightened steel specimens was recommended by the authors to find out more detailed effects of the heat straightening repair on steel specimens.

The residual stress patterns in heat-straightened specimens including steel plates, angles, and beams were investigated by Avent et al. (*7*). The undamaged and damaged plates showed similar residual stress distributions as Roeder's (*22*) theoretical distribution of the residual stress. A significantly larger plastic rotation was determined during the first few heating cycles of the tested plates as opposed to further heating cycles. Similar residual stress patterns were developed in damaged and undamaged angle specimens. The effects of the Vee angle and load ratio on the residual stress patterns in beam specimens were insignificant. Residual stresses in the Vee heated beam specimens were increased compared with the unheated control specimen. In the flange regions of the beam specimens, the residual stress in compression was typically increased. This increase in compressive residual stress is unfavorable for column members. Finally, residual stresses in four weak axis damaged beam specimens and one strong axis damaged beam specimen were determined. The residual stress patterns subjected to one and two damage-repair cycles were similar. Also, four and eight times damaged repaired specimens showed similar residual stress patterns. The weak axis damaged beam specimens presented opposite residual stress patterns to those of undamaged beam specimens. These opposite residual stress patterns are favorable for the repair of column members. The strong axis damaged specimens showed similar residual stress patterns to those of the undamaged beam specimen. But the compressive residual stress was increased to some extent.

2.2.1.3 Thermal and structural properties. The yield stress, tensile stress, modulus of elasticity, ductility, fracture toughness, surface hardness, and fatigue strength are the structural properties mainly affected by the heat straightening repair process. Several studies were performed to investigate the effects of heat straightening on these structural properties. This section presents the effects of heat straightening repair on the thermal and structural properties of steels.

Yield stress. The yield stress of steel was influenced by the heat straightening in two ways. First, the yield stress of the steel reduces as the temperature of the steel increases. Figure 2.1 shows this relationship between the yield stress and steel temperature. In Figure 2.1, the relationship between the normalized yield stress and steel temperature is plotted using Equations 2.1–2.3 (*22*).

$$\frac{\sigma_{yt}}{\sigma_{yo}} = 1.0 \quad 0\ ^{\circ}\mathrm{F} \le T \le 100\ ^{\circ}\mathrm{F} \tag{2.1}$$

$$\frac{\sigma_{yt}}{\sigma_{yo}} = 1.0 - (T - 100)/5833 \quad 100\ ^{\circ}\mathrm{F} \le T \le 800\ ^{\circ}\mathrm{F} \tag{2.2}$$

$$\frac{\sigma_{yt}}{\sigma_{yo}} = -\left(720000 - 4200T + 2.75T^2\right) * 10^{-6} \quad T > 800\ ^{\circ}\mathrm{F} \tag{2.3}$$

Second, the yield stress is affected by the heat straightening repair process permanently after the steel is cooled down to ambient temperature. Previous research in material properties of heat straightened steel have indicated that the yield stress of most heated steels was increased (*5,26,27*).

Modulus of elasticity. As the temperature increases, similar to the yield stress described in the previous section, the modulus of elasticity decreases. Figure 2.2 shows this inverse relationship between the temperature and the modulus of elasticity. Equations 2.4–2.6 (*22*) are used for Figure 2.2 with an assumption that E_o is 30000 ksi. As shown in Figure 2.2, the modulus of the elasticity of steel at 1200 °F is close to half of its typical value (*28*).

$$\frac{E_t}{E_o} = 1.0 \quad 0\ ^{\circ}\mathrm{F} \le T \le 100\ ^{\circ}\mathrm{F} \tag{2.4}$$

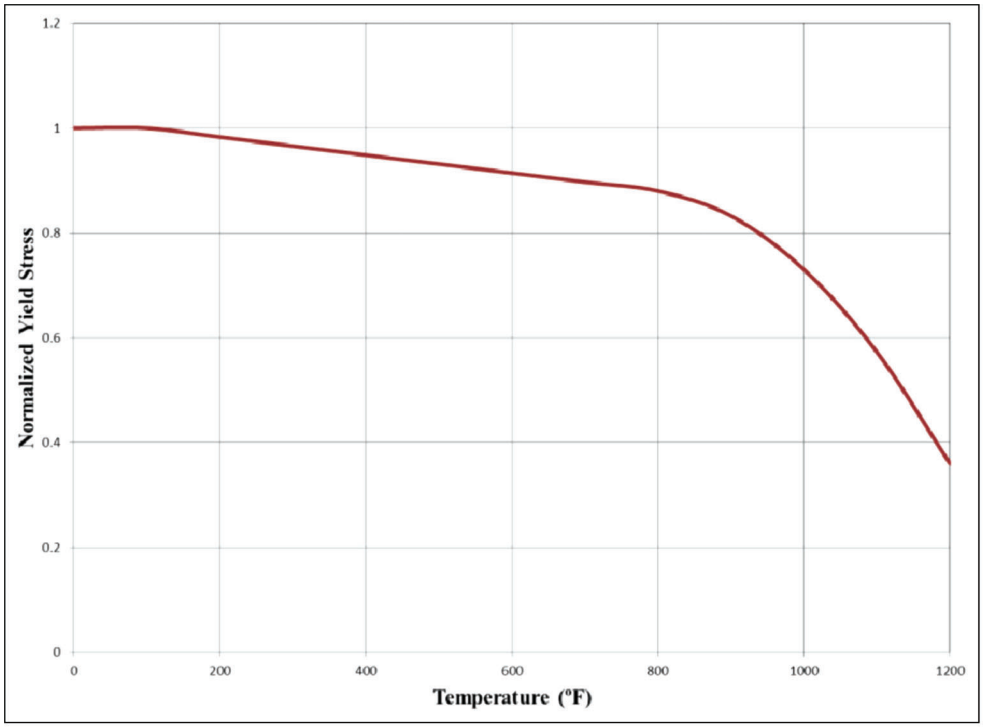

Figure 2.1 Normalized yield stress vs. temperature (*22*).

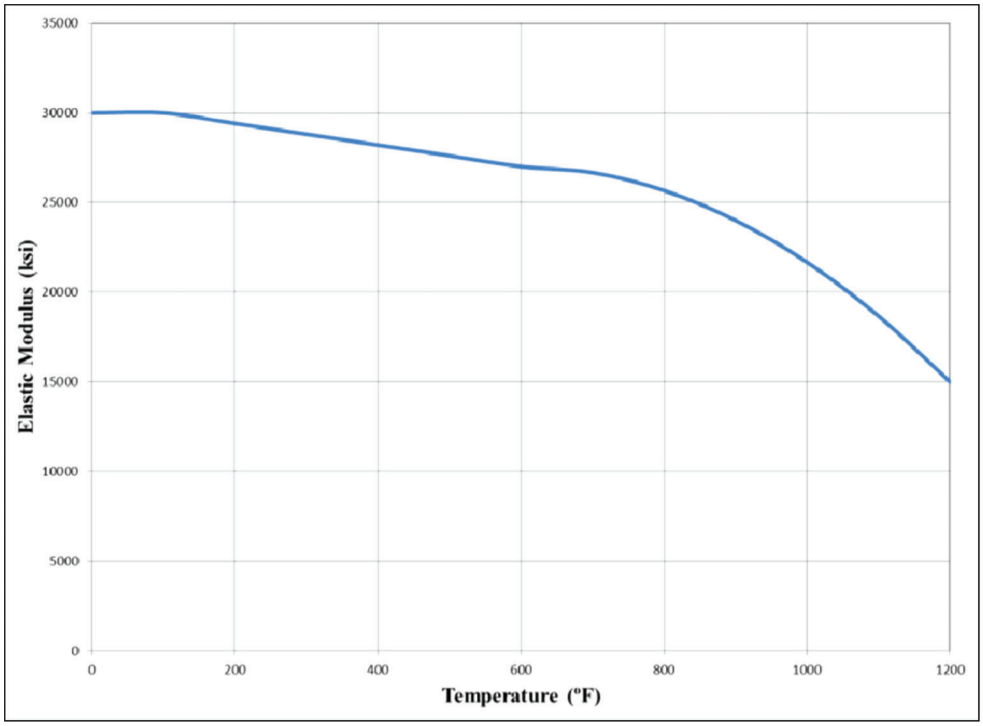

Figure 2.2 Modulus of elasticity vs. temperature (*3*).

$$\frac{E_t}{E_o} = 1.02 - 0.0002T \quad 100\ ^\circ F \le T \le 700\ ^\circ F \tag{2.5}$$

$$\frac{E_t}{E_o} = \left(500000 + 1333T - 1.1111T^2\right) * 10^{-6} \quad T > 700\ ^\circ F \tag{2.6}$$

Three heat straightening studies (*17,18,26*) indicated that the difference of the modulus of elasticity between the single Vee heated specimen and the unheated specimen was not so significant. All these studies were conducted on undamaged (straight) specimens. Avent et al. (*7*) revealed that the change in the modulus of elasticity is significant in a damaged specimen.

Thermal expansion. Thermal expansion enables the steel member to expand and contract in the desired direction. The coefficient of thermal expansion is described in the measure of the rate of strain per degree of temperature. The relationship of the coefficient of thermal expansion vs. temperature (*22*) for low carbon steel is shown in Figure 2.3. Roeder (*22*) has revealed that the coefficient of thermal expansion for Vee heats is increased up to 1600 °F for carbon steels. In the range of 250–1200 °F, the coefficient of thermal expansion has a linear relationship with the steel temperature (*3,11,26,29*).

Ductility. Previous research (*23*) presented that the ductility of the heat straightened steel plates (undamaged) was decreased about 10–20% of the unheated specimen. The ductility decrease in the heat straightened steel wide flange beams was 15–66% of the unheated specimen.

Puthericka1 (*30*) determined the mechanical properties of the steel bridge girder, which was heat straightened. A W30x108 steel bridge girder was removed from the serviced bridge by the Iowa Department of Transportation. From the material test results of the bridge, a reduction of the ductility in the web was 34% of the undamaged specimen and 28% of ductility loss was found in the flange.

Fracture toughness. The fracture toughness of steel at various temperatures is determined by the Charpy V-notch test (*31*). Another test method used to measure the fracture toughness of steel is the Drop Weight Tear test. There are three ways to measuring the fracture toughness of steel: (1) the Charpy V-notch fracture toughness energy, (2) T_{50} of upper shelf energy by the Charpy V-notch test, and (3) fracture transition temperature by the Drop Weight Tear test.

Several studies have been conducted on the notch toughness of heat straightened steel (*32–36*). Insignificant changes in the upper shelf energy absorption before and after the heat straightening repair was found from the various grades of steel plates (*28*). Pattee (*33*) used the Drop Weight Tear test to determine the toughness of several grades of steel (*33*). In this study, A517-A steel grade only showed a positive shift, which means an increase in fracture sensitivity.

Rockwell hardness. The surface hardness of a material can be measured from the Rockwell hardness test. Rockwell hardness tests were conducted on initially undamaged (straight) heat straightened specimens (*32–34,36*). The hardness values of undamaged steels were not significantly changed by the heat straightening (*32,33*). Till (*36*) indicated that heating the steel

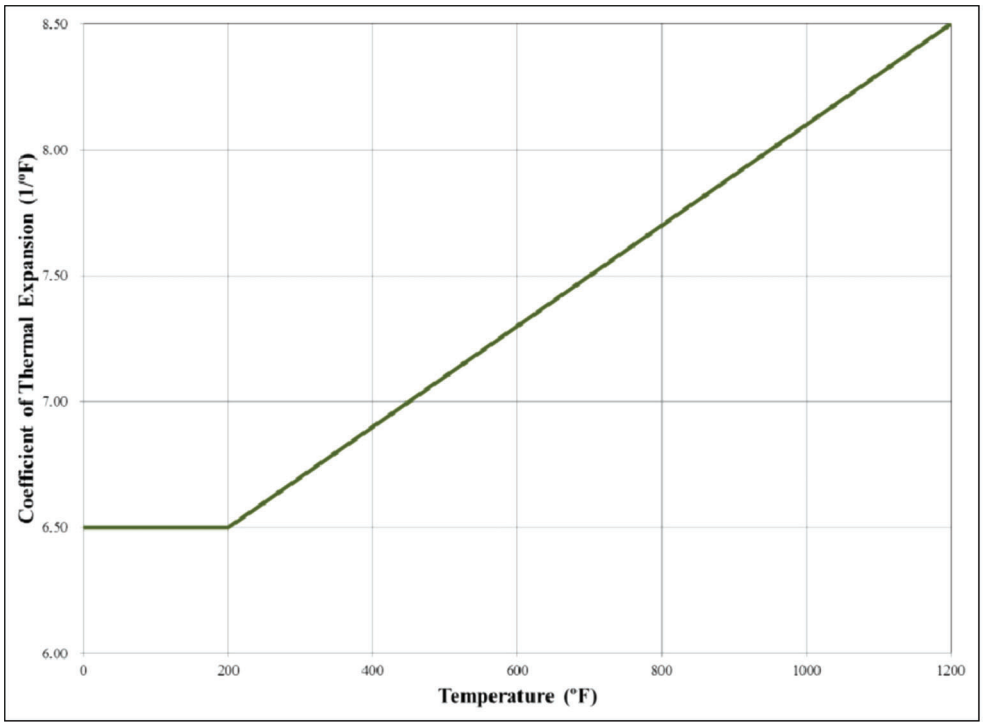

Figure 2.3 Coefficient of thermal expansion vs. temperature (*3*).

specimens to the temperature of 1100 °F to 1500 °F decreased the hardness of heated steel.

Fatigue life. Number of cycles of fluctuating stress and strain of steel to initiate cracks is the definition of fatigue life. Shanafelt and Horn (*37*) suggested that heat straightening repair should not be applied on non-redundant tension members. But they presented no scientific evidence in their report to prove their recommendation.

Microscopic investigations. While the material properties of heated steels revert to the pre cold-worked state, three processes occur in the steels–recovery, recrystallization, and grain growth.

Recovery relieves some stored internal energy caused in the previous cold work stage by the applied heat. Low temperatures and holding times are required for the recovery. Therefore, the recovery can occur during the heat straightening process.

The formation of a new set of free strained grains within cold worked steel is defined as recrystallization. The restoration of mechanical and physical properties of steel is completed during the recrystallization. The recrystallization also occurs in the heat straightening process.

The increase in average grain size of steels is referred to as grain growth. The grain growth generally occurs after the recovery and recrystallization. However, the grain growth needs longer holding time to occur and is not likely to happen in the heat straightening process.

The temperature required for the recrystallization in the steel is approximately 1000°F and must be kept one hour to complete (*38*). However, immediately after the heat is applied, the recovery and recrystallization begin.

2.2.2 Analytical Research

Development of the analytical models in heat straightening repair has focused on predicting the member behavior and the residual stress (in magnitude and pattern) caused by the heat straightening.

Many studies have been conducted experimentally to provide the data for the residual stress models with the purpose of development and calibration of the models (*16–18,23*). Other studies have been performed to analyze the behavior of the heat straightened members (plates and rolled shapes) during the repair process. Simple models to predict the member behavior during the heat straightening repair were developed (*13,19–21*). Computer models to predict the member behavior were also developed (*3,16–18,22*). All these models were mainly used by structural designers to find the required number of heating cycles to straighten the damaged steel member.

2.2.3 Full-Scale Research

Prototype bridge beam tests have been performed in the heat facility at Louisiana State University (LSU). This facility can create a controlled testing environment to the full scale test bridge beams and axially loaded (in compression) steel members. 20 ft. composite and non-composite specimen testing is available in this facility. Many studies have been performed at this facility to determine the characteristics of the heat straightening repair on damaged steel members. The plastic rotation, heating patterns and sequences, and damage assessment were mainly determined in this facility.

2.3 Recent Research

Kowalkowski and Varma (*8*) conducted an extensive research regarding the effects of multiple damage heat straightening repairs on the structural properties and serviceability of steel beam bridges. In this research, experimental and analytical investigations were performed to evaluate the effects of multiple heat straightening repairs on steel beam bridges.

Ninety-one laboratory scale specimens were tested to investigate the effects of multiple damage-heat straightening repair cycles on the structural properties of A36, A588, and A7 steel. The damage and repair parameters of the laboratory scale specimens were: (i) the damage strain ε_d, (ii) the restraining stress σ_r, (iii) the number of damage-repair cycles N_r, and (iv) the maximum heating temperature T_{max}. The effects of these parameters were evaluated on the structural properties including: (a) elastic modulus E, (b) yield stress σ_y, (c) ultimate stress σ_u, (d) % elongation, (e) surface hardness, (f) fracture toughness, and (g) microstructure.

The laboratory scale experimental results indicated that multiple damage-repair cycles did not have a significant influence on E, σ_y, σ_u, and surface hardness ($\pm$15%). However, they had a significant influence on the % elongation and fracture toughness.

Large scale beam specimens were tested to validate the conclusions from the laboratory scale tests. Six A36, A588, and A7 steel beam specimens were subjected to three damage-repair cycles. The results from the large scale tests matched well with the laboratory scale test results.

The experimental results of the laboratory and large scale tests indicated that: (1) A36 and A7 steel beams should be replaced after three damage-repair cycles, (2) A588 steel beams can be subjected to five damage-repair cycles, and (3) overheating the A36 steel to temperatures greater 1200 °F improves the fracture toughness of the damage-repaired steel significantly.

Analytical investigations were performed using a numerical approach for simulating the damage and the heat-straightening repair of composite steel bridge girders. This numerical approach was used to investigate the effects of damage followed by heat straightening repair on the residual stresses, serviceability, and ultimate load capacity of composite steel girders and bridges. Additionally, the effects of steel material and girder geometric properties, damage magnitude and location, and heating patterns and distribution were also evaluated.

The results of the analytical investigations indicated that: (1) damaged and damaged-repaired bridge beams are still capable of handling heavy traffic loads, (2) the welded connection between web stiffeners and the top flange of plate girder bridges are critical after damage and repair, and (3) concrete cracking or fracture may occur.

Connor et al. (*39*) have conducted research regarding the effect of damage and heat straightening repairs on the fatigue and fracture performance of steel girders. In this research, two cycles of damage-heat straightening repairs were recommended. After the third damage and repair cycle, a substantial decrease was discovered in the fatigue life of some details. A nondestructive testing inspection was performed to prove the recommendation. Treatment (e.g., simple grinding) of impact areas prior to heat straightening and reduction of restraining force were other important ways of increasing the fracture performance. Furthermore, during the repair of impacted points near transverse stiffeners, cracks were formed at the welded connection between the stiffener and the flange plates and extended into the flange. Connor et al. suggested that the whole stiffener or the portion of the stiffener near the flange being repaired should be removed prior to heat straightening repair to avoid this cracking. After completion of heat straightening repair, the removed stiffener might be reinstalled.

2.4 Heat Straightening Guidelines

Guidelines for conducting the heat straightening repair have been developed by the NCHRP (*37*) and the FHWA (*1*). These guidelines present procedures for estimating the damage magnitude and identify heating patterns and locations for repairing different types of damage.

The guidelines establish limits for: (a) the maximum damage that can be repaired (100 times the yield strain), (b) the maximum restraining force (50% of the section plastic moment), (c) the maximum heating temperature (650 °C/1200 °F for mild steels and 595°C/1100°F for quenched and tempered steels), and (d) the number of damage-heat straightening cycles at the same location (2 cycles of damage-heat straightening). The FHWA guidelines also identify the effects of damage and heat straightening repair on the residual stresses and the steel structural properties. These guidelines have been developed based on studies conducted over the years (*1,2*).

3. RESEARCH PLAN

The research objectives mentioned in the previous chapter will be achieved by conducting the following. General areas of this research are presented in the following sections. Sub-topics are also included within these general areas.

3.1 Evaluation of Heat Straightening in Indiana

This topic includes the evaluation of heat straightening in Indiana with a focus on its realistic implementation in the field. Additionally, heat straightening guidelines of the INDOT (Indiana Department of Transportation) are presented and reviewed. An analysis of Indiana's bridge hits database is performed to identify the bridge types, steel types, and maximum damage strains occurred in Indiana.

A heat straightening repair site (in Indiana) was visited to observe the realistic implementation of heat straightening in the field. Field measurements were performed to: (i) determine the damage location and magnitude, (ii) the restraining forces used in the repair process, and (iii) the maximum heating temperatures achieved using the oxy-fuel torches. The field measurements provide a summary of the realistic implementation of heat straightening in Indiana.

All findings from above topics are used to design and conduct the experimental investigations described in Sections 3.2 and 3.3.

3.2 Small Scale Experimental Investigations

Small scale experimental investigations are conducted to evaluate the effects of realistic heat straightening with imperfections on the structural properties of repaired steels. Small pieces of steel girders are fabricated and tested to explore the effects of various damage and repair parameters on realistic heat straightening repair. Test variables of the small scale test were identified from the database analysis in Section 3.1.

The small scale test setup focuses on the damage and repair of the bottom flange of steel beam girders. Figure 3.1 shows a schematic drawing of the small scale test. Six built-up section specimens were prepared and tested. A hydraulic actuator placed at the midspan shown in Figure 3.1 applies damage and restraining force to the test specimen. After the damage, Vee heat is applied on the plastically deformed region to repair the damage with restraining force. This damage and repair behavior is simulated by taking beam specimens with comparable flanges and subjecting them to weak axis bending.

The material properties including the structural properties, fracture toughness, and microstructure of

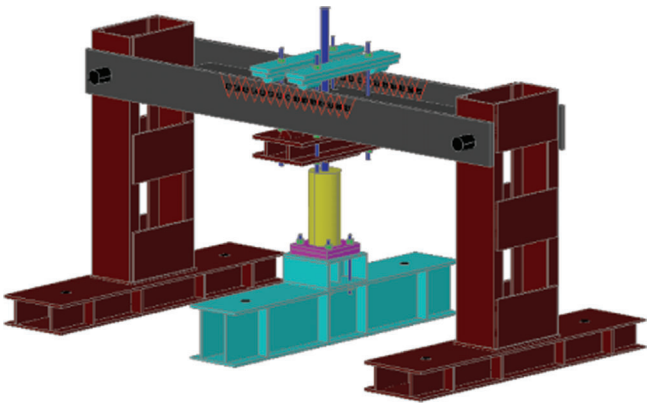

Figure 3.1 Small scale test setup.

the damaged and repaired specimens are determined and evaluated experimentally.

3.3 Large Scale Experimental Investigations

The large scale experimental investigations focus on evaluating the effects of heat straightening on damaged and heat straightened steel beam bridges. Similar to the small scale test, the test variables of the large scale test were also identified using the database analysis described in Section 3.1. Prior to the experimental investigations, finite element analysis of large scale test was conducted to estimate the bridge behavior during the damage and repair process of the large scale test.

Figure 3.2 shows the large scale test setup for conducting the experimental investigations. As shown, the test setup represents a large scale model of steel beam bridges damaged and repaired most frequently in Indiana. The test bridge is composed of two steel rolled beams and concrete slab deck. Two main girders were placed over six abutment blocks and will include four composite beam specimens like Figure 3.2.

All four beam spans in the test setup were subjected to damage and realistic heat straightening repair simulating field activities and conditions. The specimens were damaged at each midspan. After the damage, Vee heats were applied at the bottom flange of the girders to repair the damage. Hydraulic actuators attached to the midspan loading frames were used to apply the damage and restraining force to the specimen.

After the specimens were subjected to damage and heat straightening repair, the serviceability performance of the repaired bridge was determined by subjecting static loads simulating the AASHTO (*40*) live loading. As shown in Figure 3.2, two hydraulic actuators were attached to the midspan loading frames over the bridge specimen to apply concentrated loads to the bridge.

Finally, the material properties including the structural properties, fracture toughness, and microstructure of the damaged and repaired steel beam specimens were also determined and evaluated experimentally. These material properties were measured by conducting ASTM tests on standard coupons fabricated from material samples taken from each damaged repaired beam specimen.

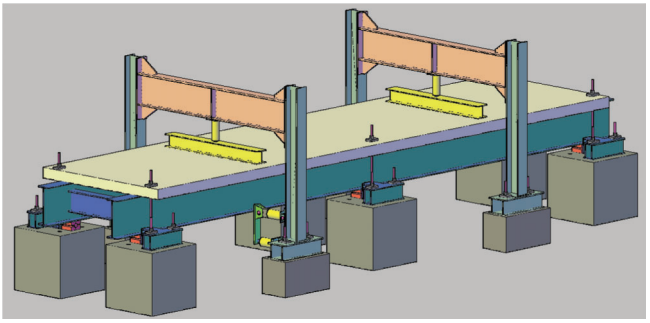

Figure 3.2 Large scale test setup.

3.4 Guidelines and Recommendations for Realistic Heat Straightening

Based on the findings and experimental results from above topics, heat straightening guidelines and recommendations are developed for steel beam bridges in Indiana. The main focus is on: (a) overstraining with restraining forces, (b) overheating beyond the recommended limit, and (c) multiple heat straightening repairs.

4. EVALUATION OF HEAT STRAIGHTENING IN INDIANA

This chapter evaluates the current status of the INDOT (Indiana Department of Transportation) heat straightening repair process and guidelines. Section 4.1 includes heat straightening guidelines of the INDOT. Section 4.2 analyses the Indiana heat straightening database. This is used to identify the steel bridge types and the maximum damage strains in real heat straightening repair. Section 4.3 describes the visit to the heat straightening site in Indiana. Some important problems found in the real heat straightening implementation site are also discussed in Section 4.3.

4.1 Review of the INDOT Guidelines

This section reviews the INDOT heat straightening guidelines (revised 3/13/08).

These guidelines provide the following required prequalifications for the contractor:

- At least five years of continuous work in heat straightening
- At least 10 heat straightening projects within the previous three-year period
- Experience documentation shall be presented (date, location, bridge owner, number and type of members, and duration)

The guidelines provide the following general requirements prior to heat straightening:

- Pre-heat straightening inspection (visual inspection, liquid dye penetration or magnetic particle testing when needed)
- Contractor's work proposal prior to heat straightening

  - applications of heating patterns and sequences
  - disconnecting, supporting, and adjusting steel, as required
  - the cleaning method and painting system to be used following the straightening

The guidelines acknowledge potential heat straightening equipment that may be used. For example:

- Equipment

  - All gas fueled heating equipment and force application devices
  - Fuel for heating shall be an oxygen fuel combination

- Propane, acetylene or other similar fuel
- Heat application shall be by single orifice tips only
- Jacks or "come-alongs" not exceeding 25 ton capacity
- Temperature measurements (Temperature sensitive crayons, pyrometer, infrared non-contact thermometer)

Heat straightening must be implemented with the following constraints:

- Temperature limitation
  - 1200 °F (640 °C) for Carbon Steels
  - 1100 °F (590 °C) for A514 and A709
  - 1050 °F (565 °C) for A709 (grade 70W) steel
- Triangular, Vee, and strip heat patterns are allowed
- The Vee heat pattern shall be located on the convex side of the beam
- 15 to 30 degrees of Vee angle and Max. base width of 12 inches
- Cooling with compressed air will only be under 600 °F
- Two torches shall be used over 1 inch thickness of the flange
- Restraining force shall not be increased during the heat cycle

The guidelines also provide acceptable local tolerances for straightness as follows:

- Horizontal Sweep: ⅜ inch per 20 feet of length (at the point of impact: ⅜ inch per 5 feet or ½ inch per 8 feet)
- Vertical Deflection: ¼ inch maximum
- Deflection of Web (out of plane of web): ¼ inch vertical or horizontal maximum

The guidelines also state about field supervision of repairs that the engineer shall routinely monitor heating temperatures and jacking forces to insure compliance with specified limits.

4.2 Indiana Heat Straightening Database

4.2.1 Heat Straightening Bridge Types

The Indiana heat straightening database was obtained from INDOT and analyzed to determine the steel bridge types and damage amount most relevant to this research. The database included only the information of damaged and heat straightened bridges in Indiana. This database did not include bridges in Indiana that have been damaged but not repaired. Researchers did not review inspection reports to identify all the damaged bridges in Indiana. The database analysis presented in this section is limited to the bridges that were damaged and then heat straightened under contract.

Twenty four heat straightening repair cases (19 bridges) in the database were evaluated. Three bridges had experienced two damage and heat straightening repair cycles at the same locations. Figure 4.1 and 4.2 present the database analysis results.

As seen in the Figure 4.1, sixteen out of nineteen damaged and heat straightened bridges in the database were made of A36 steel.

The composite continuous bridge was the most frequently damaged bridge type in the database. As shown in Figure 4.2, eleven bridges in the database were composite continuous bridges. The second most frequently damaged bridge type in the database was the non-composite continuous bridge.

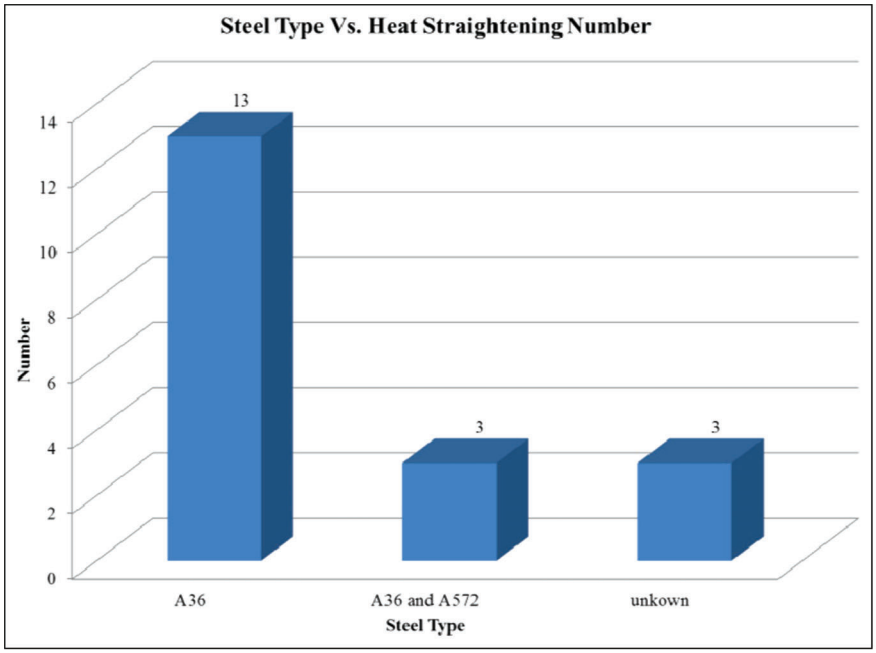

Figure 4.1 Steel type vs. number of heat straightening repairs.

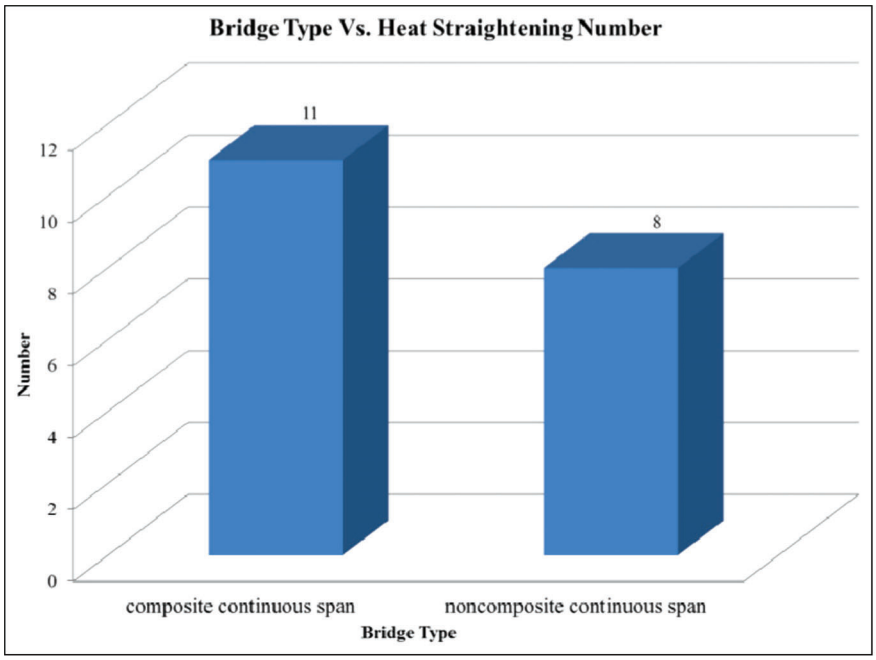

Figure 4.2 Bridge type vs. number of heat straightening repairs.

From all the above findings, researchers concluded that the composite continuous steel bridge with A36 steel was most relevant to this research project.

4.2.2 Maximum Damage Strain (ε_{max})

The maximum damage strain (ε_{max}) of each damage case was presumed using deformation diagrams from the drawings in the database. Twenty-four heat straightening cases from thirteen damage-repaired bridges presented a damage diagram to estimate the maximum damage strain (ε_{max}) of each case. Figure 4.3 shows one sample damage diagram from the I65-261-4904B bridge.

The offset method in the FHWA 1998 guidelines (*28*) was used to estimate the maximum damage strains (ε_{max}) in each damage case. Equation 4.2 ~ 4.4 with variables described in Figure 4.4 and 4.5 were used to determine the maximum damage strain.

To find out the yield strain (ε_y) of A36 steel, the maximum yield stress (σ_y) and young's modulus (E) were assumed to be 45 ksi and 30,000 ksi respectively. Using Equation 4.1, the yield strain (ε_y) of A36 steel was calculated as 0.0015 in./in. or 1500 με.

$$\varepsilon_y = \frac{\sigma_y}{E} \tag{4.1}$$

$$\varphi_d = \tan^{-1}\left(\frac{y_2 - y_1}{L_1}\right) + \tan^{-1}\left(\frac{y_3 - y_4}{L_2}\right) \tag{4.2}$$

$$R = \frac{C_d}{2\sin(\varphi_d/2)} \tag{4.3}$$

$$\varepsilon_{max} = \frac{1}{R} y_{max} \tag{4.4}$$

The ratio of the maximum damage strain to the yield strain, referred to as the strain ratio, μ, is presented in Table 4.1. As seen in the table, μ values were determined from about 15 to 35 with an average value of 28. In other words, the average maximum damage

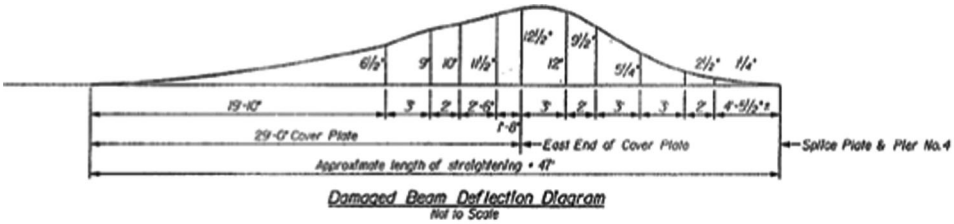

Figure 4.3 Damage diagram of I65-261-4904B bridge.

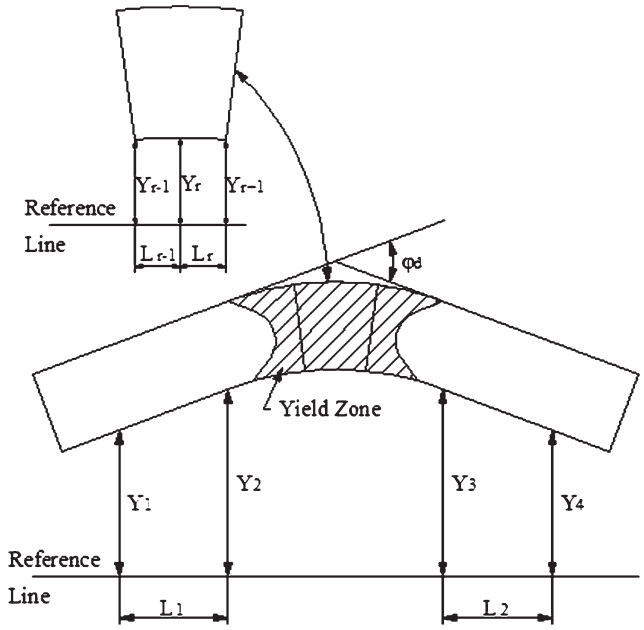

Figure 4.4 Offset measurements to calculate degree of damage and radius of curvature.

strain from the database analysis is about 28 times the yield strain (ε_y) value.

The ε_{max} described above was derived from the deformation data after elastic rebound of the damage deformation. In the real damage situation, the damage strain ε_d must be slightly larger to have permanent deformation corresponding to ε_{max}. Referring to previous research data (*8*), a 10% increase could be a reasonable increase. Therefore, μ value should be increased to 30 considering strain recovery due to the elastic rebound. Hence, maximum damage strain (ε_d) was targeted at 30 times the yield strain (ε_y).

4.3 Field Visit to Heat Straightening Repair Site

The heat straightening repair project on Allisonville Road, crossing over I465 eastbound near Indianapolis, was visited on October 20–21, 2009. Flame On, Inc., conducted heat straightening repair on the east-end girder (eastbound) damaged by an over-height truck. The damaged part of the steel girder had previously experienced another damage-repair process before this heat straightening repair. Two eastbound lanes on I465 were blocked for the repair process during night time work procedures.

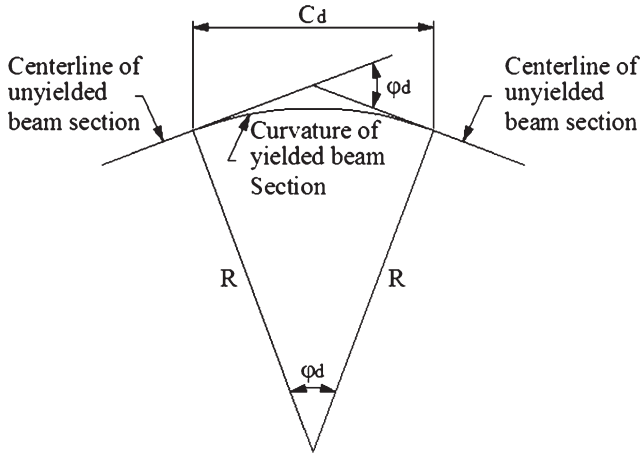

Figure 4.5 Relationship of degree of damage to radius of curvature and cord length.

TABLE 4.1
Maximum damage strain rate

Bridge Designation	μ = Max. Damage Strain/Yield Strain ($\varepsilon_{max}/\varepsilon_y$)
I65-261-4904B	14.9
31-71-5806C	14.7
I465-129-5277D	28.2
	29.8
	30.2
	29.4
I64-115-5663A	32.0
I465-129-5277C	26.3
	29.0
I65-124-4285 ENBL	34.1
	33.9
I465-125-5270JC SB	32.6
I64-25-5219H	30.9
	21.4
41-42-5081F	20.5
	23.9
	28.7
	32.2
I70-73-4647 DREC	34.8
I64-25-5219G	27.2
	36.0
I64-25-5219D	21.4
	35.6
Average	**28.2**

4.3.1 Damage Description

As shown in Figure 4.6, the east-end composite beam was hit by an over-height truck at 37 ft. from the south

Figure 4.6 Damage on Allisonville Road bridge.

abutment and various types of damages were found around the impact point. These damages included a 6 in. out-of-plane displacement (combined with distortion) of the bottom flange, formation of the web yield line, and the girder-to-diaphragm connection failure (including bolt fracture and bearing shear failure of the crossbeam).

The maximum out-of-plane damage occurred at the location with an additional cover plate, which was added in the previous damage-repair process. This is seen more clearly in Figure 4.7. Bearing shear failure that occurred in the end connection of one diaphragm is also shown in Figure 4.7. Yield lines also formed in the girder web close to the concrete slab following the girder direction. (See Damaged Girder video: http://dx.doi.org/10.4231/D3X63B541)

4.3.2 Repair Description

Figure 4.8 shows a hydraulic jack system installed by heat straightening repair technicians from Flame On, Inc. They used a 10 ton (20 kips) jack with a hydraulic hand pump to provide a restraining force prior to heating cycles. However, no pressure gages were attached to the system. They just assumed that the applied restraining force with the no-gauged hand pump was close to 10 kips.

A oxygen-propylene torch was used for the heating process. Initially, line heats were applied on the web of the girder close to the concrete slab. Figure 4.9 shows the line heat process being applied by a technician. After the line heat, Vee heats were applied on several damaged points of the beam as shown in Figure 4.10. As seen in Figure 4.10, half-depth and full-depth Vee heats were properly applied following the deformed shape of the bottom flange. The Vee angle was computed to be approximately 55°.

Three technicians from Flame On, Inc., performed the heating process using the oxygen-propylene torches. During the heating, the technicians did not use any temperature monitoring equipment like temperature indicating crayons or infrared thermometers. Technicians totally relied on their experience to reach their target temperature of 1200 °F.

The heating temperature was measured by the researchers using an infrared thermometer gun. In most of the heating cycles, technicians reached 1300 °F to 1530 °F as their maximum heating temperatures. These temperatures are higher than 1200 °F, which is

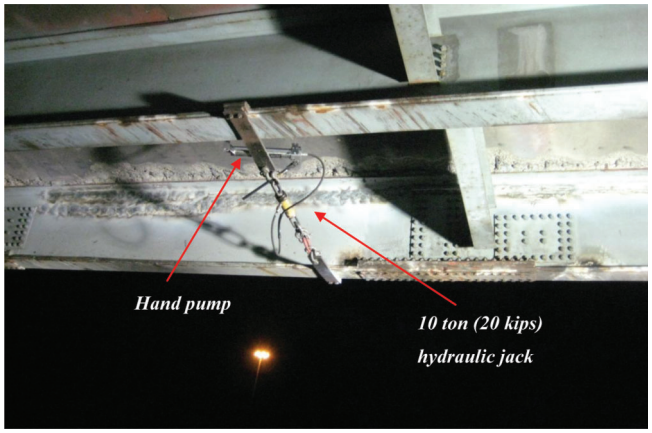

Figure 4.8 Hydraulic jack system for restraining force.

Figure 4.9 Line heat on the web of the girder.

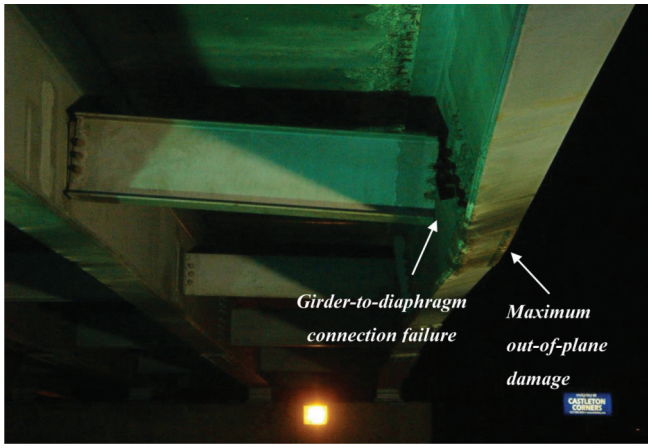

Figure 4.7 Close-up view of damaged region.

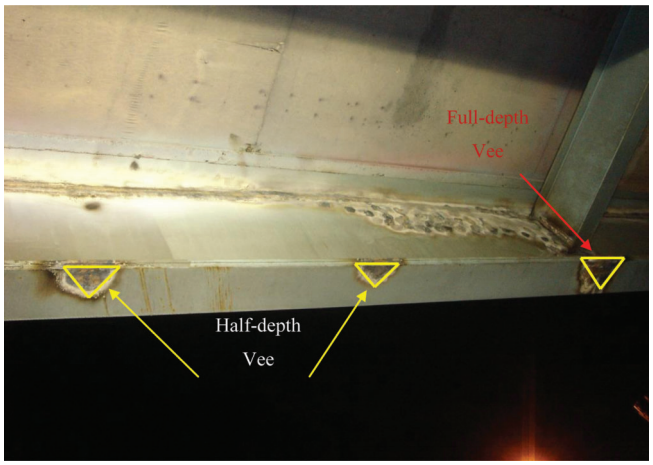

Figure 4.10 Vee heat locations of the bottom flange.

the maximum heating temperature recommended by the INDOT heat straightening guidelines.

The FHWA recommendation (*28*) allowed the steel to cool down to 250 °F before relieving the restraining force applied on the heated steel. But in this heat straightening process, the cooling temperature was not measured by any temperature measurement device. Technicians assumed 20 minutes was enough time to cool the steel down below 250 °F.

After nine heat straightening repair cycles, the damaged beam was almost straight with a ¼ in. tolerance. The damaged diaphragm was replaced with a new one after the heat straightening process was finished. (See Force System 1 video: http://dx.doi.org/10.4231/D3NS0KX8Z; Force System 2 video: http://dx.doi.org/10.4231/D3J09W45G; and Force System 3 video: http://dx.doi.org/10.4231/D30Z70W9F)

4.3.3 Imperfections in Field Implementations

As mentioned in the previous section, there were several deviations from the FHWA recommendations (*28*) for heat straightening repair at the actual site. These included the following:

- Unreliable restraining force on damaged beam
- Adjusting restraining force during the heat application
- No temperature measurements
- Overheating (heating temperature over 1200 °F)
- Inaccurate cooling time to cool down below 250 °F (no temperature measurement)

(See Temperature video: http://dx.doi.org/10.4231/D3D795B1Q; see Adjusting Force video: http://dx.doi.org/10.4231/D3SF2MC0W)

5. SMALL SCALE TEST: DESCRIPTION

This chapter focuses on the description of the test matrix, test setup and instrumentation, and test procedure of the small scale test. Six specimens were fabricated and tested. The test variables were developed based on the findings of previous chapters.

Section 5.1 includes the test matrix of the small scale test. Sections 5.2–5.4 include detailed descriptions of the test specimens, test setup, and test instrumentations. The small scale test procedures are described in Sections 5.5–5.6.

5.1 Small Scale Test Matrix

The damage and repair parameters considered in the small scale test were: (a) the damage magnitude, (b) the restraining force, (c) the maximum heating temperature, and (d) the number of multiple damage-repair cycles. The effects of these parameters on: (i) the structural properties including the yield stress, ultimate stress, and ductility, (ii) the fracture toughness, and (iii) the steel microstructure were evaluated experimentally.

Each test parameter included the following variations:

a. **Damage magnitude.** Following the findings in the INDOT heat straightening database analysis (Chapter 4), thirty times of the yield strain (30 ε_y) was used for the maximum damage magnitude in most of the test specimens. In order to see the effect of large damage on a test specimen, only one specimen was deformed to the maximum damage magnitude of sixty times of yield strain (60 ε_y).
b. **Damage and repair cycles.** The FHWA guidelines (*28*) recommended a maximum two times of damage and repair cycles at the same damage region. Otherwise, three times of damage and repair cycles for A36 steel was suggested in the previous research by Kowalkowski and Varma (*8*). Therefore, three times of damage-repair cycles were used in two test specimens to compare the difference with a onetime damaged and repaired specimen.
c. **Restraining moment.** Restraining force which can cause less than 50% of the plastic moment was allowed in the FHWA guidelines (*28*) to prevent unexpected yielding during the heating process. To follow this recommendation, restraining force equal to 40% of the plastic moment (0.4 M_p) at midpoint was used for most of the specimens. In one specimen, to see the overstraining effect, restraining force equivalent to 60% of M_p was applied.
d. **Maximum temperature.** The maximum heating temperature was strictly enforced to be 1200 °F in the control specimens following the FHWA guidelines (*28*). 1400 °F and 800 °F were used for the overheating and underheating cases.

The test matrix for the small scale test is shown in Table 5.1. Each small scale test specimen is identified by its name in Table 5.1. Table 5.1 also presents the damage-repair histories of the test specimens.

5.2 Small Scale Test Specimen

The small scale test setup was originally designed to damage and repair the W24 x 76 steel beams used in previous research (*8*). Therefore, the dimension of A36 steel sections needed to be equivalent to the W24 x 76

TABLE 5.1
Small scale test matrix

Specimen Name	Cycle (Number)	Damage Strain (ε_d)	Restraining Moment (M_r)	Maximum Temperature (T_{max})	Comment
1-1200-0.4-30	1	30 ε_y	0.40 M_p	1200 °F	Control specimen
3-1200-0.4-30	3	30 ε_y	0.40 M_p	1200 °F	Effects of multiple damage-repair cycles
3-1400-0.4-30	3	30 ε_y	0.40 M_p	1400 °F	Effects of multiple damage-repair cycles & overheating
1-1400-0.4-60	1	60 ε_y	0.40 M_p	1400 °F	Effects of large damage & overheating
1-1400-0.4-30	1	30 ε_y	0.40 M_p	1400 °F	Effects of overheating
1-800-0.6-30	1	30 ε_y	0.60 M_p	800 °F	Effects of overstraining & underheating

section. In this research, small scale beam specimens were fabricated using A36 steel plates because all rolled beams were made from A992 steel. The built-up cross-section of the A36 steel plates is shown in Figure 5.1.

Figure 5.2 provides fabrication details for the beam specimens to be tested. As seen in Figure 5.2, the total length of the specimen was 108 in. and the actual supporting length was 97 in. A 4 in. diameter hole for a 2 in. diameter threaded bar (for damaging force) to pass through and four slotted holes (2.00 x 1.00 in.) for ¾ in. diameter threaded bars (for restraining force) to pass through were fabricated in the central part of the webs as shown in Figure 5.2.

5.3 Small Scale Test Setup

Two built-up steel columns supported the test specimens during the damage and repair processes of the small scale test. Figure 5.3 shows the details of the column supports. As seen in Figure 5.3, each column was made from two C10 x 20 channels and six ¼ in. plates. The built-up section columns were welded to another built-up beam with 6 in. height and 15 in. width as shown in Figure 5.3. Those built-up beams were post-tensioned to the strong floor to provide support reactions.

Figure 5.4 shows a schematic diagram of the loading beam that was designed to apply the damaging and restraining forces at the midspan. The damaging (pushing upward) force was applied through two semi-circular shafts welded to the bottom loading beam. The restraining force (pulling downward) during heat straightening process was applied through four semi-circular shafts attached to the top loading beams.

Figures 5.5 and 5.6 show a detailed drawing and photograph of the small scale test setup.

5.4 Instrumentation

Figure 5.7 shows the front (flange A side) of the small scale test setup where the sensors were attached and Figure 5.8 shows the back (flange B side) of the setup. The left and right sides are decided from the frontal view (flange A side) of the test setup. The top of the beam specimen is the region where the Vee-heats are

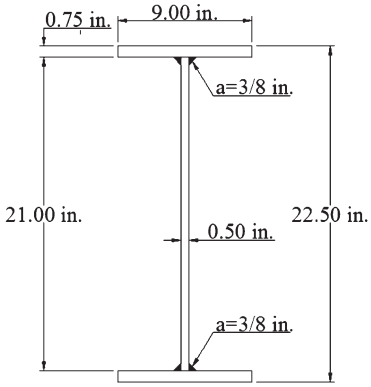

Figure 5.1 Small scale beam section.

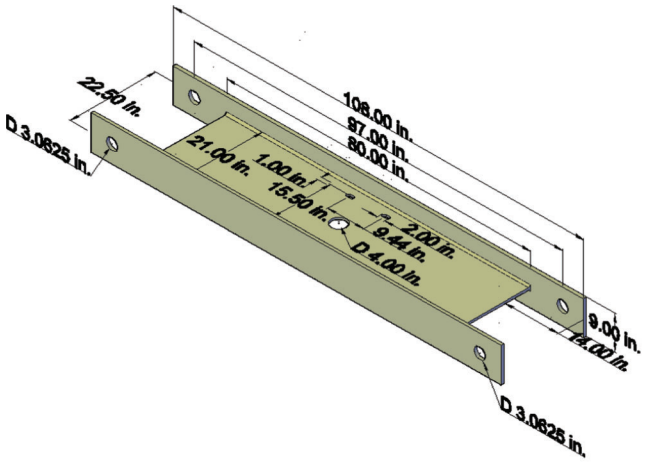

Figure 5.2 Small scale beam specimen dimension.

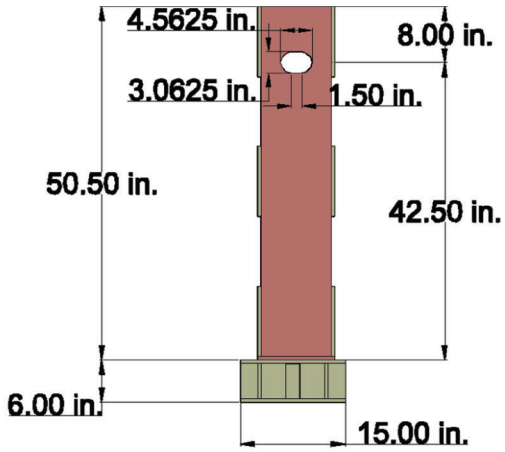

(a) Side view

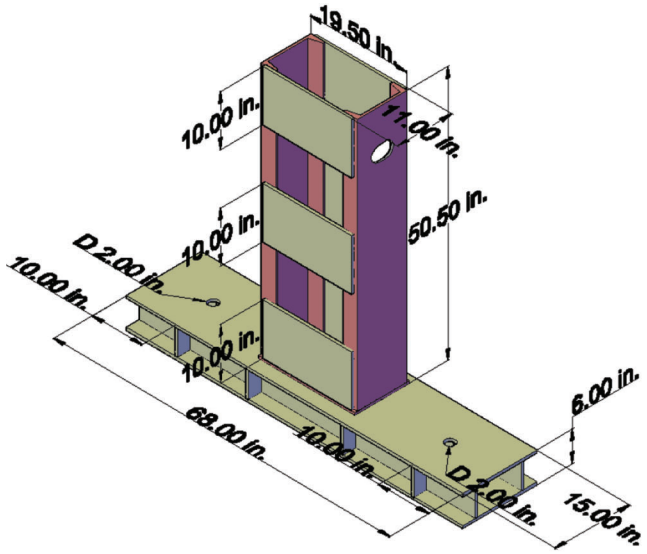

(b) Detailed dimension

Figure 5.3 Support column details.

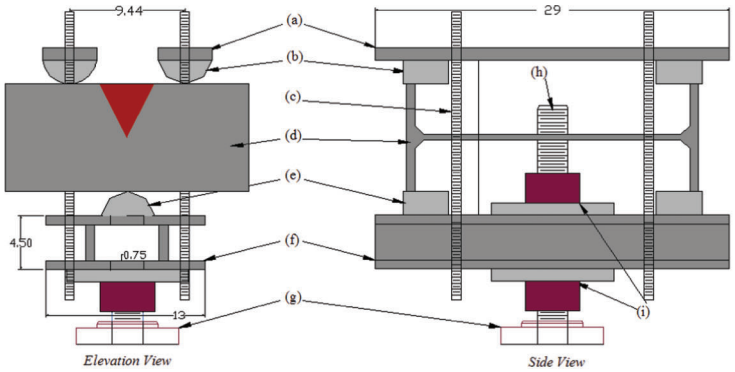

(a) Top plates
(b) Semi-circular contact shafts
(c) 0.75 in. threaded rods
(d) Beam specimen
(e) Semi-circular contact shafts
(f) Loading beam
(g) Hydraulic actuator
(h) 2.0 in. threaded rod
(i) Structural plates and nuts

Figure 5.4 Loading beam details.

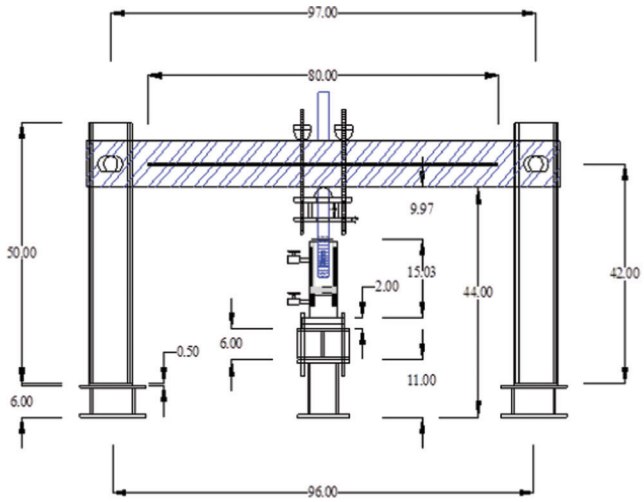

Figure 5.5 Detailed drawing of small scale test setup.

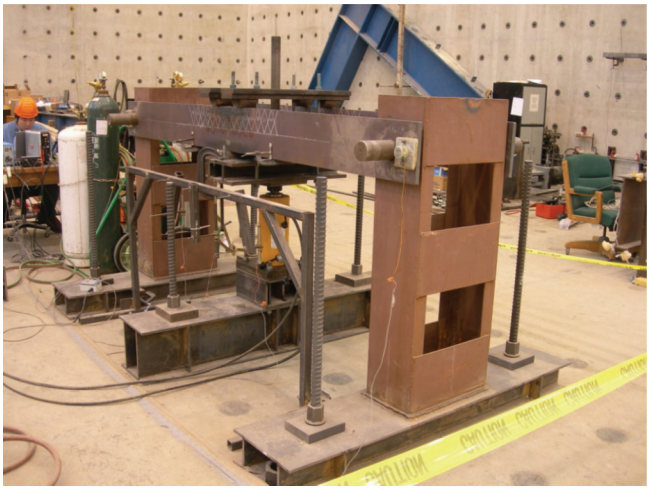

Figure 5.6 Photo of small scale test setup.

applied during the repair process. The bottom of the beam is referred to as the compression side where the concentrated force is applied during the damage process.

The instrumentation layout used for the small scale test is described in this section. Instruments (sensors) used in the small scale test include: (i) pressure transducers for force measurement, (ii) displacement transducers for deflection measurement, (iii) clinometers for rotation measurement, (iv) an infrared thermometer for temperature measurement, and (v) strain gages for strain measurement.

Pressure Transducers

A pressure transducer was used to measure the damaging and restraining forces during the small scale test. The transducer measured the pressure within the hydraulic line when the damaging and restraining forces were applied to the test specimen. The force was computed as the pressure multiplied by the effective cylinder area of the actuator (20.57 in^2 for the damaging force and 9.59 in^2 for the restraining

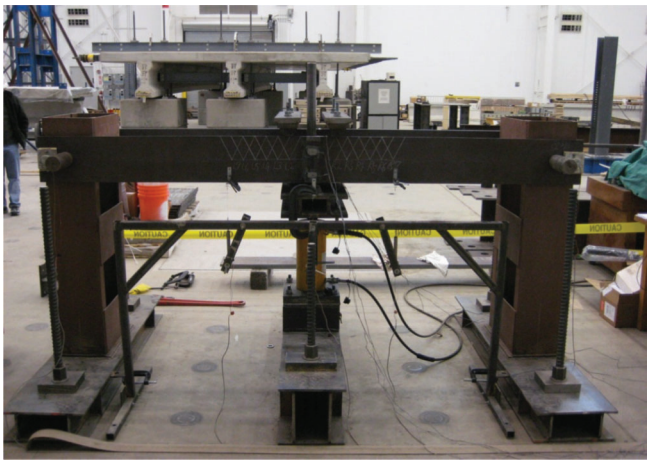

Figure 5.7 Photo of the front side of the small scale setup.

Figure 5.8 Photo of the back side of the small scale setup.

force). It was verified (calibrated) by using load cells with NIST traceable calibration.

Strain Gages

Six strain gages were used to measure the damage strains during the first damage cycle of each small scale specimen. These strain gages were attached to the midspan section of each specimen where the damaging force was applied. Figure 5.9 shows the location of the strain gages bonded to one flange (flange A or Flange B). The damage strain (ε_d) during the first damage cycle of each specimen was measured from the top strain gage shown in Figure 5.9.

Clinometers (rotation meters)

Two clinometers (rotation meters) were attached to each end of the front flange (flange A) to measure the rotations of the test specimens. As shown in Figure 5.9, these clinometers were located 3.5 in. from the beam supporting shafts. The symmetry of the test beam specimen was monitored from these clinometers during the damage and repair processes of each small scale test specimen.

Displacement transducers

Deflections of each small scale test specimen were measured by displacement transducers located at the beam midspan and at the one-third points along the length of the beam, located 33 in. from the end supports.

- The deflection at the beam midspan was measured using a 10 in. stroke displacement transducer that was connected to the front flange (flange A).
- The one-third point deflections were measured using two 6 in. stroke displacement transducers that were connected

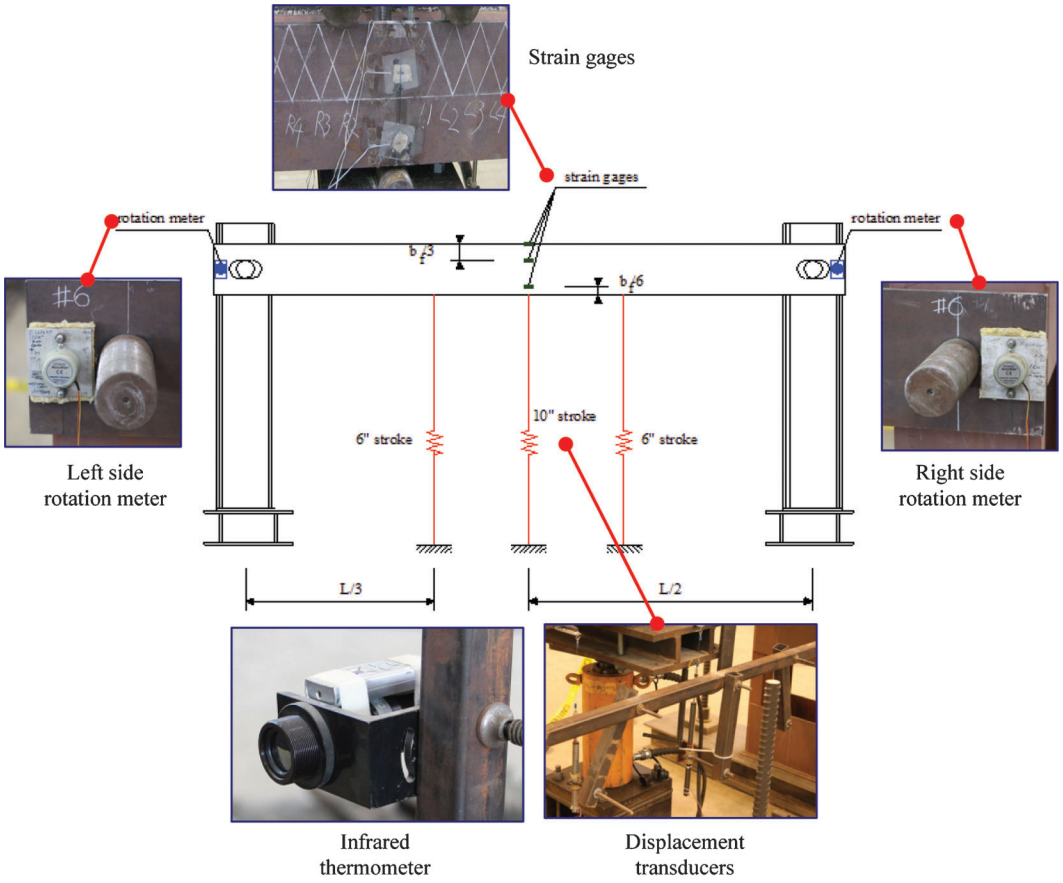

Figure 5.9 Small scale test sensor layout.

to the front flange (flange A). Figure 5.9 shows the location of these displace transducers.
- For multiple damage cycles, the magnitude of damage was measured by these displacement transducers.

Infrared Thermometer:

The surface temperature of each small scale specimen was measured using an infrared thermometer to get the time-temperature graph of each Vee heating cycle. The infrared thermometer was placed away from the heating region.

5.5 Experimental Procedure

Damage Procedure

A 100 ton capacity hydraulic actuator, which was connected to the loading beam explained in Section5.3, was used to damage the small scale beam specimens. The damaging force applied at the midspan by the hydraulic actuator was slowly increased until the targeted damage strain at the top strain gage was reached.

The behavior of each small scale specimen in the first damage cycle was carefully monitored by the top strain gages and displacement transducers shown in Figure 5.9. For multiple damage-repair specimens, subsequent damage cycles were finished when the midspan deflection reached the same amount of the first damage cycle.

Repair Procedure

1. Application of restraining forces. The restraining moment (M_r) was decided as 0.40 M_p or 0.60 M_p. M_p means the sectional plastic moment capacity of the specimen. Equation 5.1 shows the calculation of M_p, where Z_y is the plastic section modulus (31.7 in^3) and σ_y (45 ksi) is the yield stress of the A36 steel.

$$M_p = Z_y \times \sigma_y = 31.7 \times 45.0 = 1425.9 \text{ kip-in} \quad (5.1)$$

The maximum moment applied to each Vee heat region was computed from Equation 5.2. In Equation 5.2, X is the distance between the specific Vee region to the nearest supporting point and P is the applied force from the pressure transducer.

$$M = \frac{PX}{2} \quad (5.2)$$

2. Application of Vee heats. Oxygen-propylene torches were used for heating the small scale specimens. Two heating technicians simultaneously applied Vee heats to each flange (flange A or B) of the test specimen. Each technician used a hand-held infrared temperature gun to monitor the heating temperature of the steel. A spot heat was applied at the apex of the Vee to reach the targeted heating temperature. After reaching the targeted temperature, the heating torch was moved toward the flange edge following a serpentine way.

Vee heat regions of the small scale test specimens are shown in Figure 5.10. These Vee zones were located within the central plastic strain region of the specimen. The nomenclature of each Vee region is also shown in Figure 5.10. As seen in Figure 5.10, the Vee angle used for the small scale test was about 53°. This angle was similar to the Vee angle used in the heat straightening field visit in Section 4.3.

Photos of the whole damage and repair process are shown in Figure 5.11. This procedure includes: (a) setting up the undamaged specimen on the test bed, (b) damaging the beam to the desired strain level ($30\varepsilon_y$ or $60\varepsilon_y$) using the hydraulic actuator at the midspan, (c) heat straightening the specimen using the oxygen-propylene torch with downward restraining force, and (d) stopping the procedure with a ⅛ in. tolerance at the midspan.

5.6 Material Testing Procedures

For all small scale test specimens, uniaxial tension coupons were taken from the back flange (flange B) and Charpy v-notch coupons were taken from the front flange (Flange A). In addition to six small scale specimens, one undamaged steel plate (used for a flange plate) was prepared to take out additional undamaged material test coupons.

As shown in Figure 5.12, three uniaxial tension coupons were taken from the flange B of each specimen. Figure 5.13 shows the dimensions of the uniaxial tension coupon. All tension coupons were extracted from the central Vee regions (L1, C, and R1) of each back flange. The actual location and the nomenclature of each tensile coupon are also shown in Figure 5.12. Uniaxial tension specimens taken from the undamaged steel plate are shown in Figure 5.14. Figure 5.14 also shows the actual location and the nomenclature of each undamaged tensile coupon.

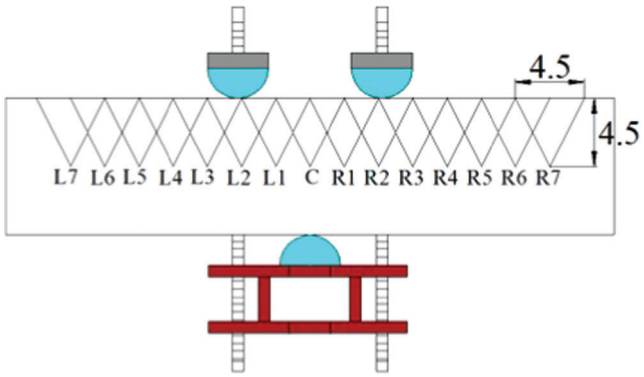

Figure 5.10 Vee heat locations and nomenclature.

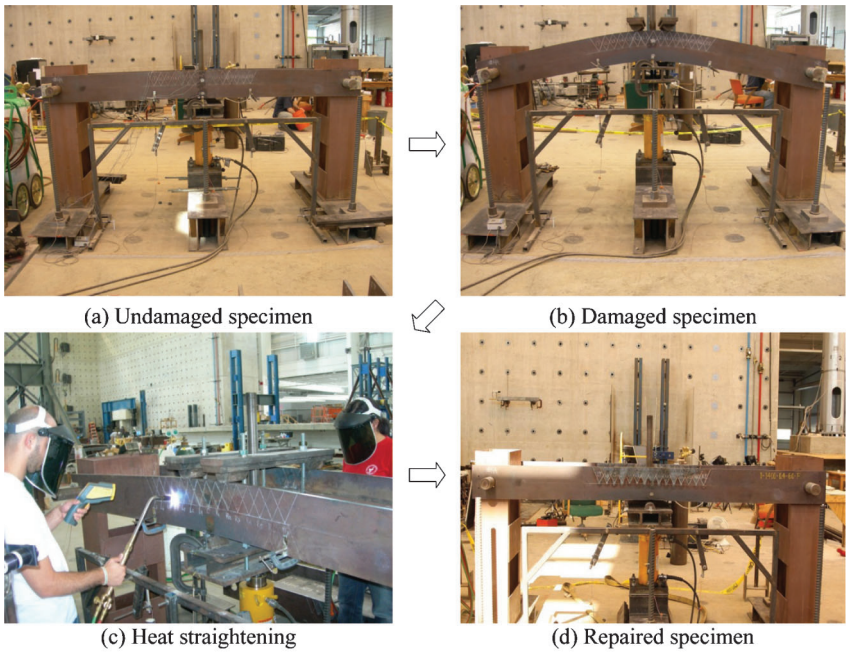

Figure 5.11 Heat straightening repair procedure of small scale test.

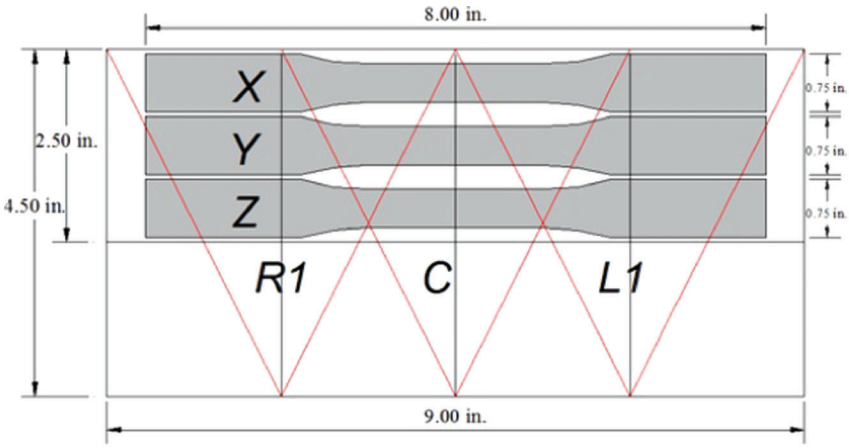

Figure 5.12 Nomenclature and location of damaged-repaired uniaxial tension coupons.

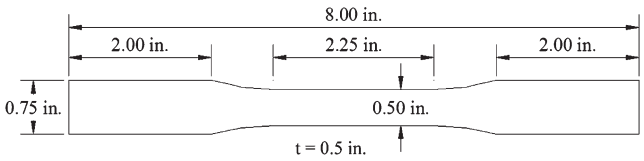

Figure 5.13 Uniaxial tension coupon detail.

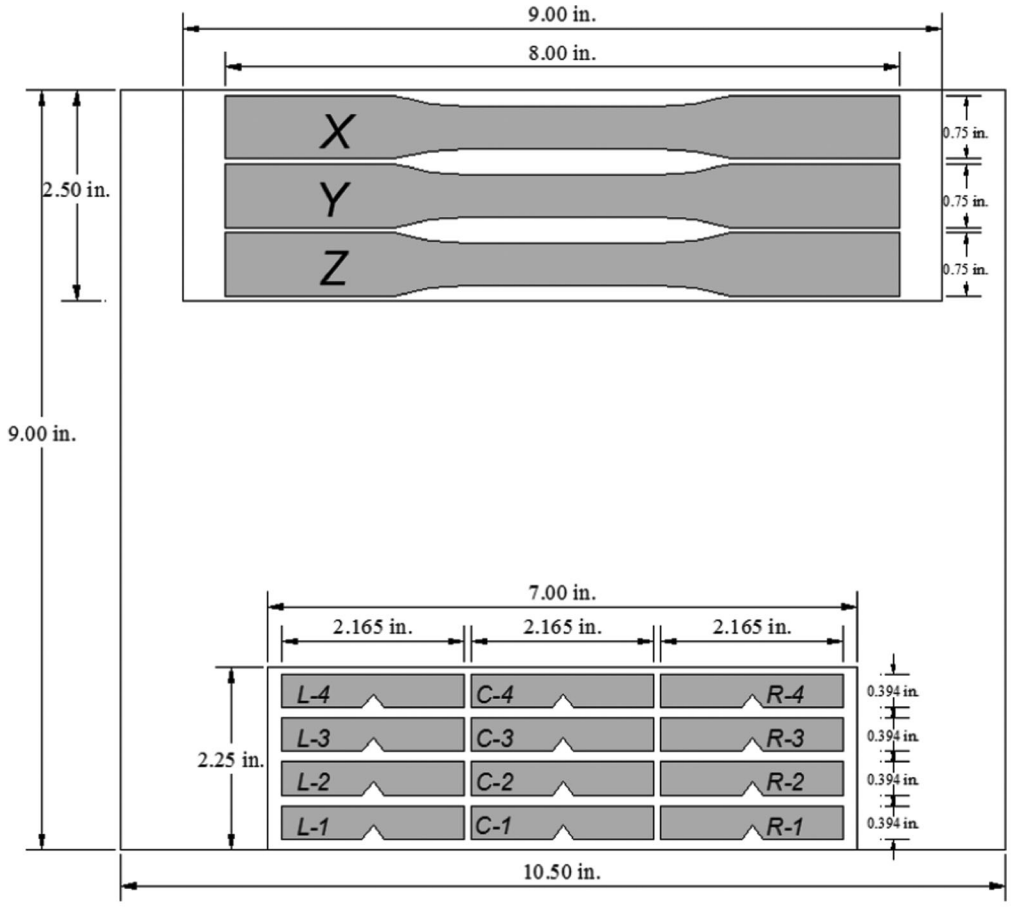

Figure 5.14 Material test coupons from the undamaged steel plate.

Fracture toughness tests, Rockwell hardness tests, and microstructure investigations were conducted on the Charpy coupons of each small scale specimen. The Charpy coupons of the small scale test specimens are shown in Figure 5.15. As seen in Figure 5.15, the v-notches of the Charpy coupons were fabricated facing the edge of the flange plate. The location and the nomenclature of each Charpy coupon are also shown in Figure 5.15. The Charpy specimens from the undamaged steel plate are shown in Figure 5.14. Figure 5.14

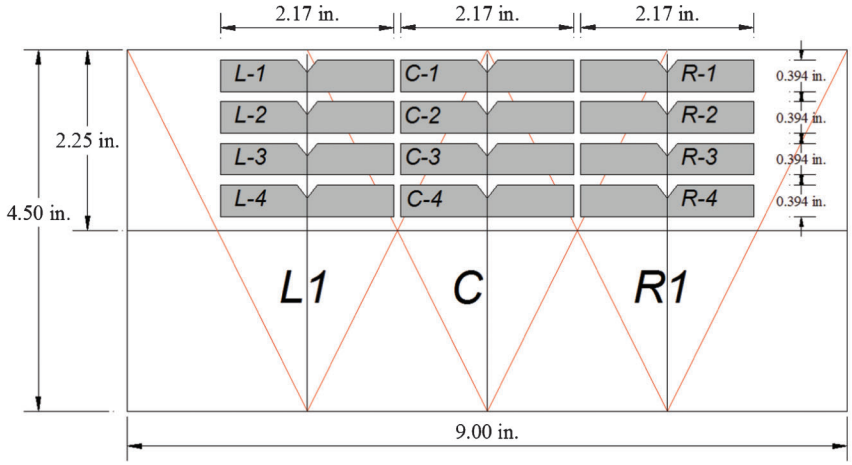

Figure 5.15 Nomenclature and location of damaged-repaired fracture toughness coupons.

also shows the actual location and the nomenclature of each undamaged Charpy coupon.

6. SMALL SCALE TEST: EXPERIMENTAL BEHAVIOR

This chapter presents the experimental behavior of the small scale test specimens during the damage and repair process. Six small scale beam specimens were tested by subjecting them to designed damage-heat straightening repair cycles. The damage and heat straightening repair parameters of these test specimens are presented in Table 5.1.

The experimental behavior of the beam specimens during each damage cycle is presented and discussed using the data measured by the instrumentation. The longitudinal strain gages worked well only during the first damage cycle. Hence, the load-strain P-ε behavior during the first damage cycle and the load-midspan deflection P-Δ and the load-end rotation P-θ during all damage cycles are presented. These comparisons indicate the change in strength and stiffness of the beam specimens. Photographs of the beam specimens before and after the damage cycle are provided. Other significant information noted during the experimental damage cycles is provided.

The behavior of the beam specimens during the repair cycles is presented using some of the data provided by the instrumentation. At least one figure which shows the force in the hydraulic actuator, the temperature at the surface of the Vee heated steel, and the deflections measured by the displacement transducers is provided for each specimen. The final condition of the damaged-repaired specimens are also shown and discussed. Finally, the number of Vee heats required to repair the damage of each cycle is also reported.

6.1 Damage process of Specimen #1 (1-1200-0.4-30)

All sensors were used to monitor specimen behavior during the damage procedure of the first specimen (1-1200-0.4-30). Strain sensors were located as described in Section 5.4.

Figure 6.1 shows the photographs of the beam specimen before (a) and after (b) the damage cycle. The beam specimen was damaged by monotonically increasing the concentrated force at the midspan. The damage was monitored using the longitudinal strain gages. The test was considered complete when one of the values of front top and back top strain gages reached 30 ε_y. The complete strain gage data for the damage cycle is shown in Figure 6.2.

P-Δ relationships for Specimen #1 is shown in Figure 6.3. The maximum plastic displacement at the midspan after the damage was measured as 3.5 in. The final damage displacement after elastic rebound was 2.8 in at the midspan.

Figure 6.4 shows the P-θ relationship of Specimen #1. The rotation angle of θ was measured close to the end point of the specimen following Section 5.4.

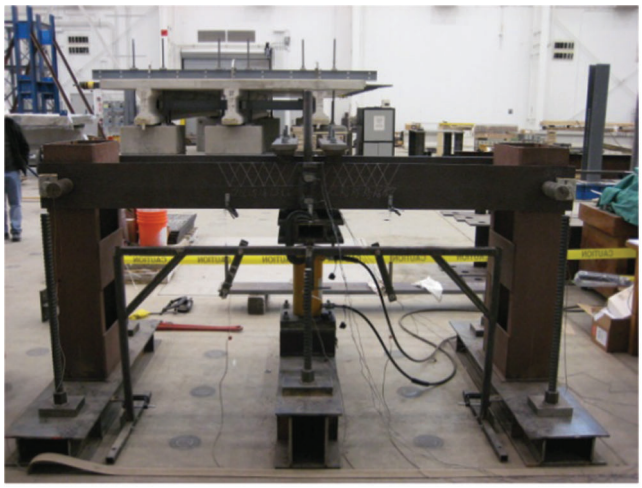

(a) Undamaged specimen

(b) Damaged specimen

Figure 6.1 Photographs of Specimen #1 before and after the damage.

6.2 Repair Process for Specimen #1 (1-1200-0.4-30)

Repair cycles of Specimen #1 were conducted by applying external forces causing restraining moments of 0.4 M_p at the midspan. The first repair cycle was conducted using simultaneous Vee heats applied at the center (C) Vee region of the front and back flanges shown in Figure 5.10. After that, other Vee regions (L1, R1-L6, R6) were heated to minimize out-of-plane distortion of damaged flange.

One hundred two (102) Vee heats were required to complete the repair cycle of Specimen #1. The frequency chart indicating the number of Vee heats applied to each location is shown in Figure 6.5. The photograph of the repaired beam is shown in Figure 6.6. After the final Vee heat repair, less than ⅛ in. of the midspan deflection was left.

Figure 6.7 shows the data of the initial eleven Vee heat repair cycles. This figure includes: (a) the displacements from three displacement transducers in inches, (b) the restraining force in the hydraulic

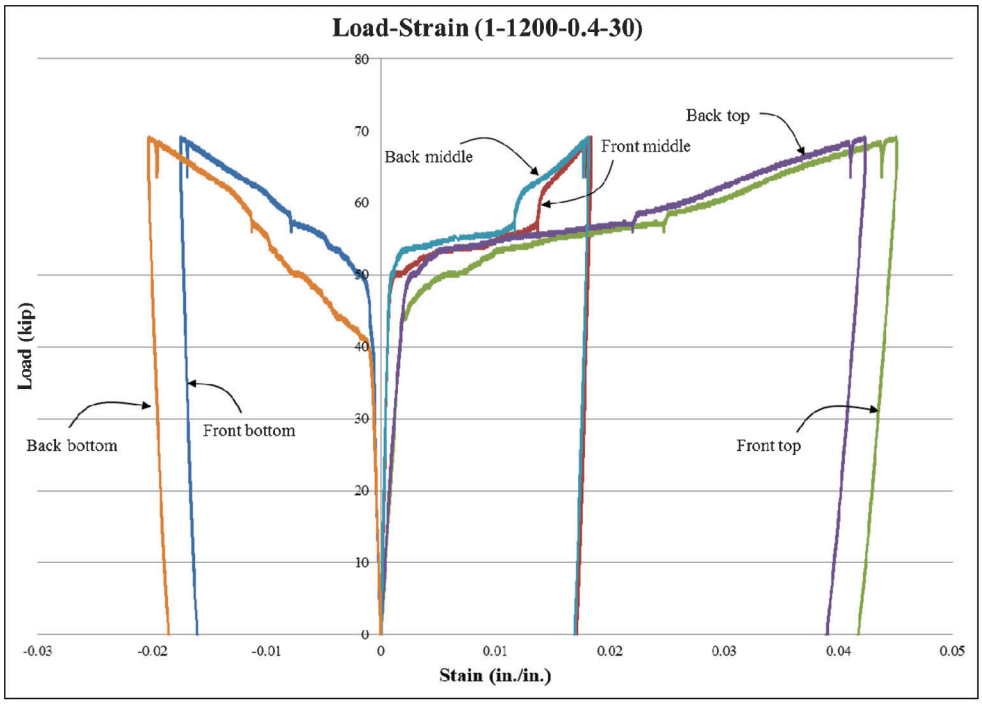

Figure 6.2 Load-strain diagram of Specimen #1 (1-1200-0.4-30).

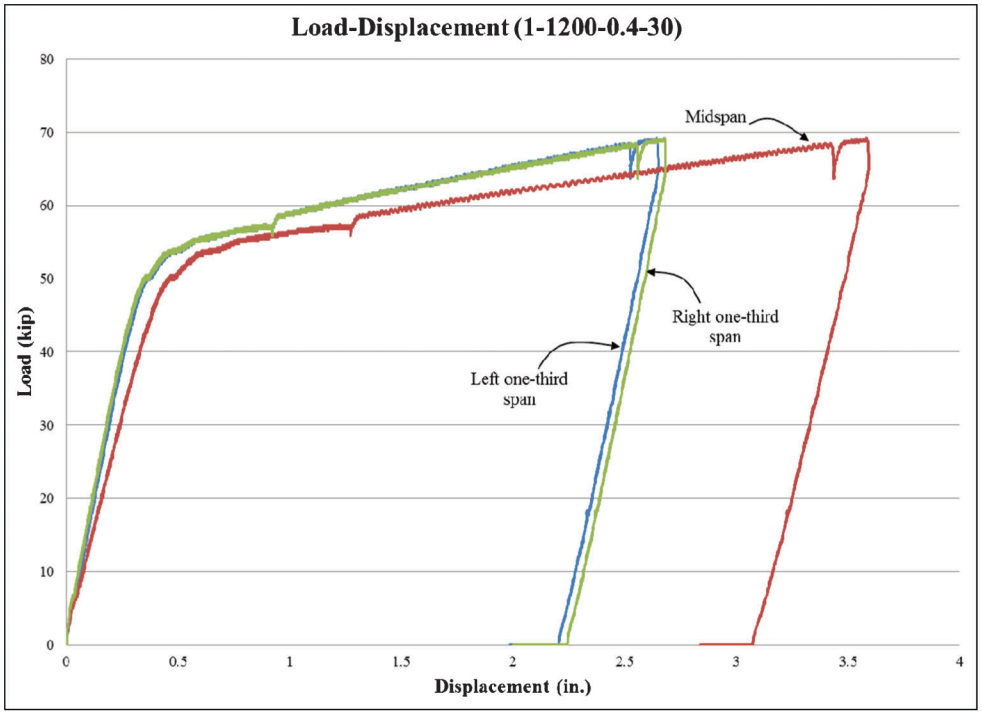

Figure 6.3 Load-displacement diagram of Specimen #1 (1-1200-0.4-30).

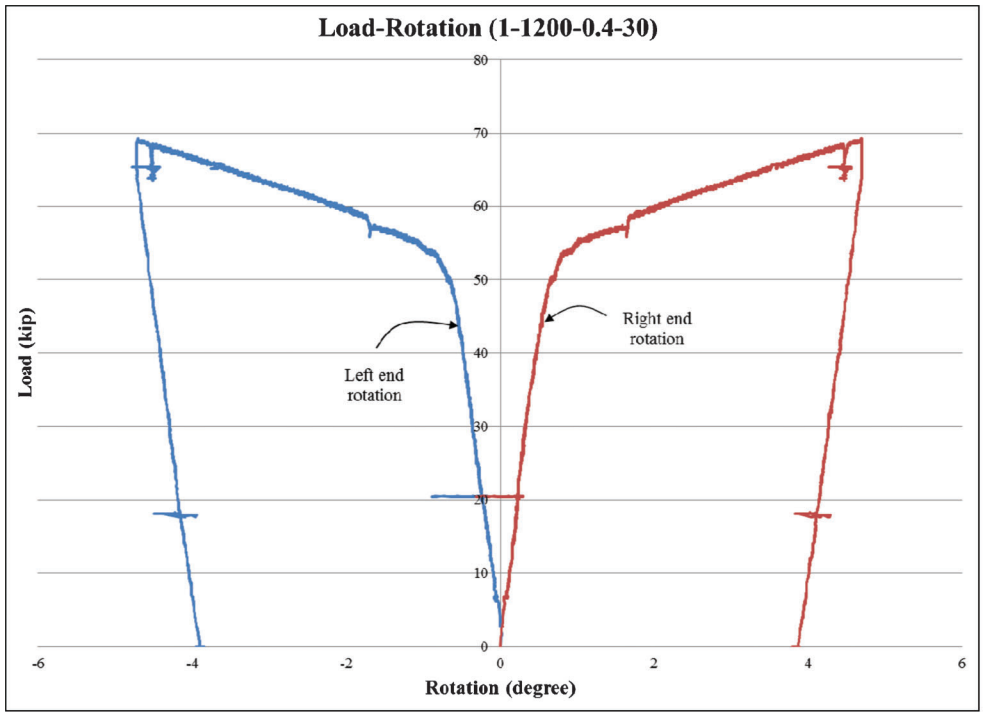

Figure 6.4 Load-rotation diagram of Specimen #1 (1-1200-0.4-30).

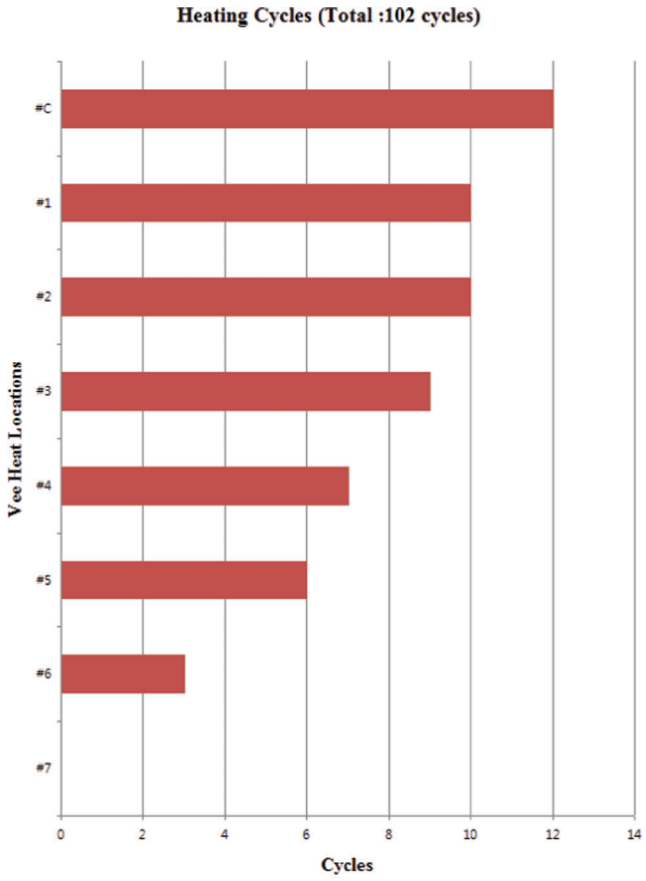

Figure 6.5 Vee heat frequency chart of Specimen #1.

Figure 6.6 Photograph of Specimen #1 after the heat straightening repair.

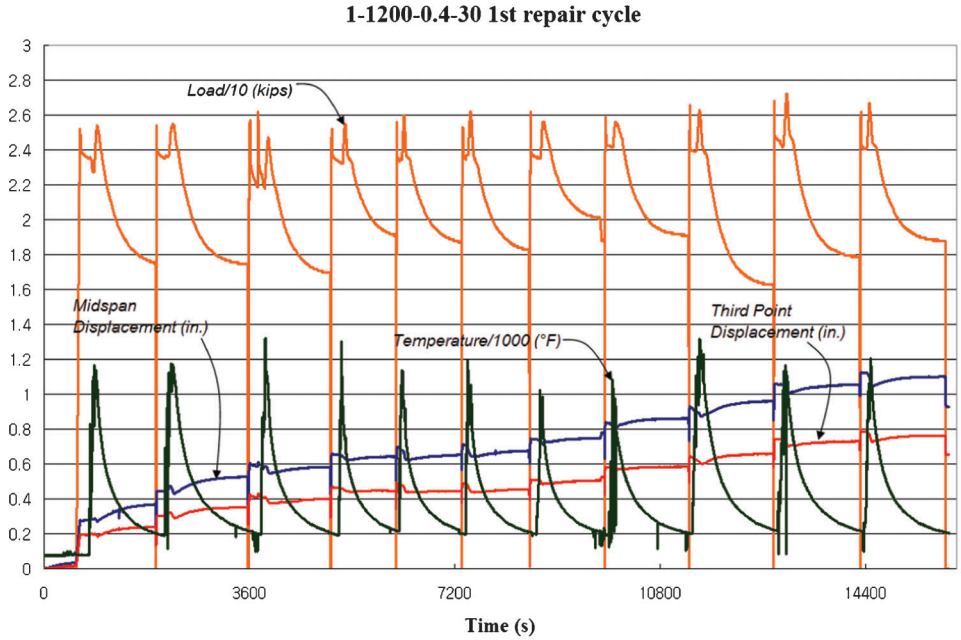

Figure 6.7 Instrument data during the repair cycle of Specimen #1.

actuator in kips, which is divided by 10 (i.e., 1.0 on the graph shows 10 kips of force), and (c) the temperature of the steel in F, which is divided by 1000 (i.e., 1.0 on the graph corresponds to 1000 °F).

6.3 Damage Process of Specimen #2 (3-1200-0.4-30)

Specimen #2 was subjected to three damage-repair cycles to determine the effect of multiple damage-repair cycles. Figure 6.8 shows the photographs of the beam specimen before and after each damage cycle. Each damage cycle corresponded to the damage strain of 30 ε_y (0.045 in./in.) at top strain gage. The damage strain in the first cycle was measured using the strain gage layout described Section 5.4. The strain gage data from the first damage cycle is provided in Figure 6.9.

Damage cycles 2 and 3 were conducted under displacement control, where the displacement at the midspan reached the required magnitude close to the result of the first damage cycle. Figure 6.10 compares the P-Δ behavior of all three damage cycles of Specimen #2. Figure 6.11 compares the P-θ behavior of all three damage cycles of Specimen #2.

As shown in Figures 6.10 and 6.11, the initial stiffness of the beam changed slightly after the first damage-repair event. The material became stronger after damage-repairs, which is clearly seen in Figures 6.10 and 6.11.

6.4 Repair Process for Specimen #2 (3-1200-0.4-30)

Repair cycles of Specimen #2 were conducted by applying external force corresponding to the restraining moment of 0.4 M_p. This restraining force in each repair cycle was equal to the force used for Specimen #1. The only difference was multiple damage-repair cycles (three times).

The total numbers of Vee heats required to straighten the specimen in each damage-repair cycle are shown in Figure 6.13. One hundred eighteen Vee heats on both flanges were required to complete the first repair cycle. The second repair cycle took one hundred and forty six Vee heats to complete. The third repair cycle needed two hundred eleven Vee heats to complete. Required numbers of the Vee heats to fully straighten the specimen were increased following the damage cycles. The final deflection at midspan after the third damage-repair cycle was less than ⅛ in. The final photograph of Specimen #2 after all repair cycles is shown in Figure 6.12.

Vee heats were applied to all Vee regions from the center (C) to the 7th (L7 or R7) heating locations to avoid excessive out-of-plane distortion.

Figure 6.14 shows the behavior of Specimen #2 in the initial several steps of each repair cycle. This figure includes: (a) the displacements from three displacement transducers in inches, (b) the restraining force in the hydraulic actuator in kips, which is divided by 10 (i.e., 1.0 on the graph shows 10 kips of force), and (c) the temperature of the steel in F, which is divided by 1000 (i.e., 1.0 on the graph corresponds to 1000 °F).

6.5 Damage Process of Specimen #3 (3-1400-0.4-30)

Specimen #3 was subjected to three damage-repair cycles with a heating temperature of 1400 °F to determine the effect of overheating and multiple damage-repair cycles. Figure 6.15 shows the photographs of the beam specimen before and after each

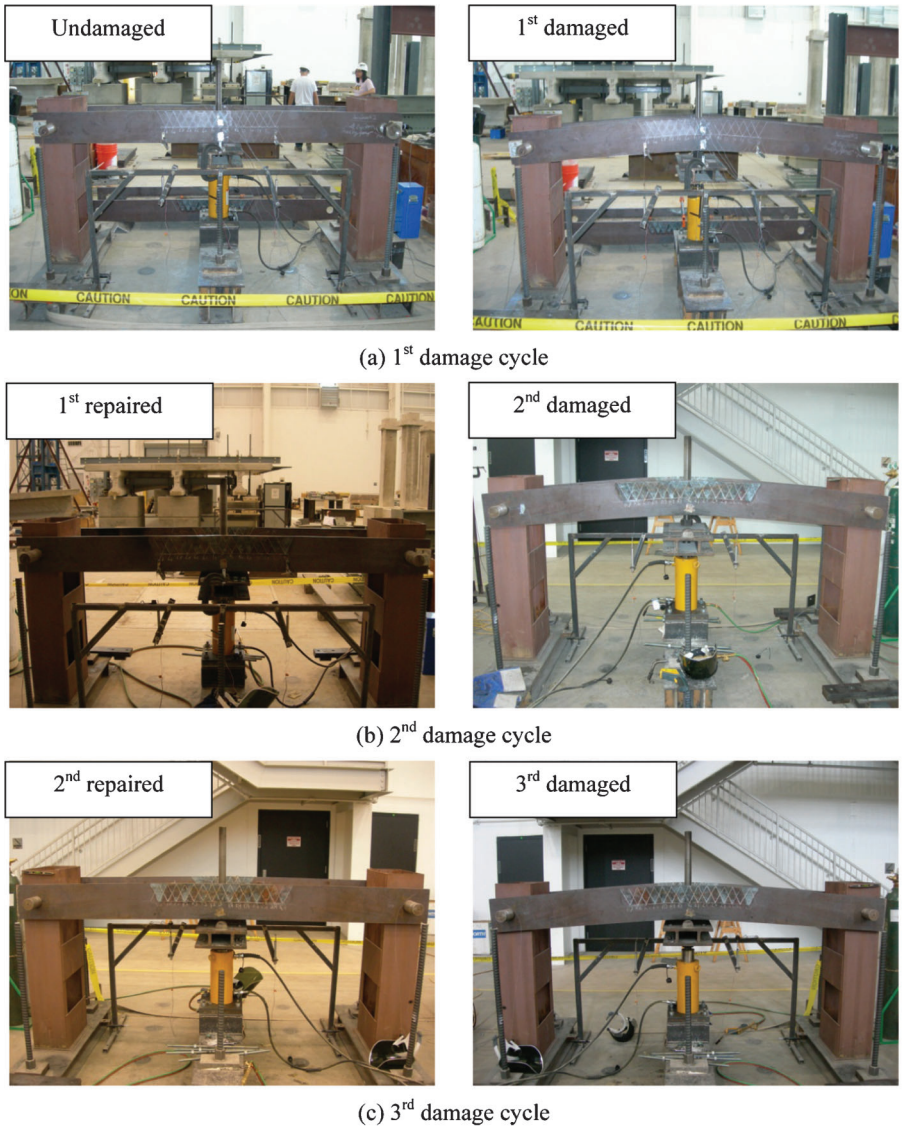

Figure 6.8 Photographs of Specimen #2 before and after the damage.

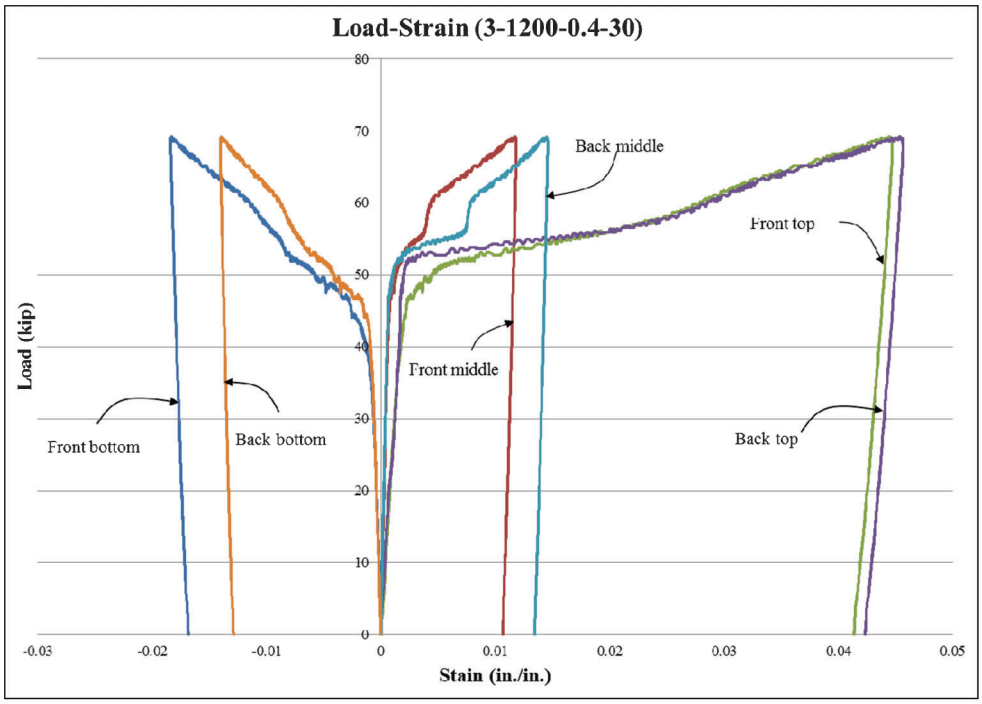

Figure 6.9 Load-strain diagram of Specimen #2 (1-1200-0.4-30).

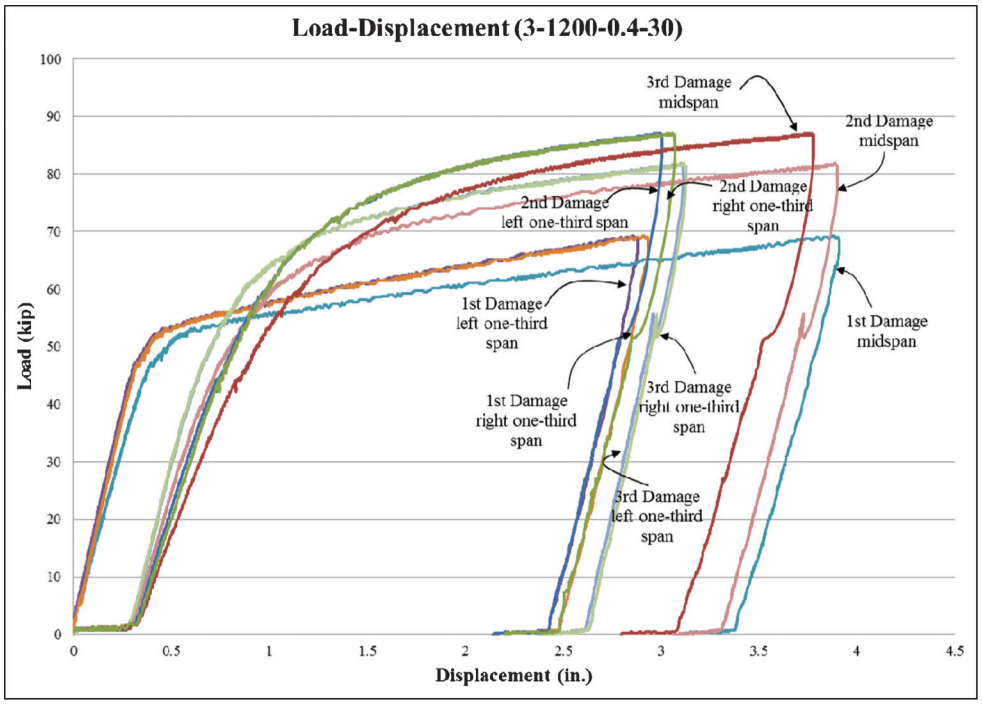

Figure 6.10 Load-displacement diagram of Specimen #2 (3-1200-0.4-30).

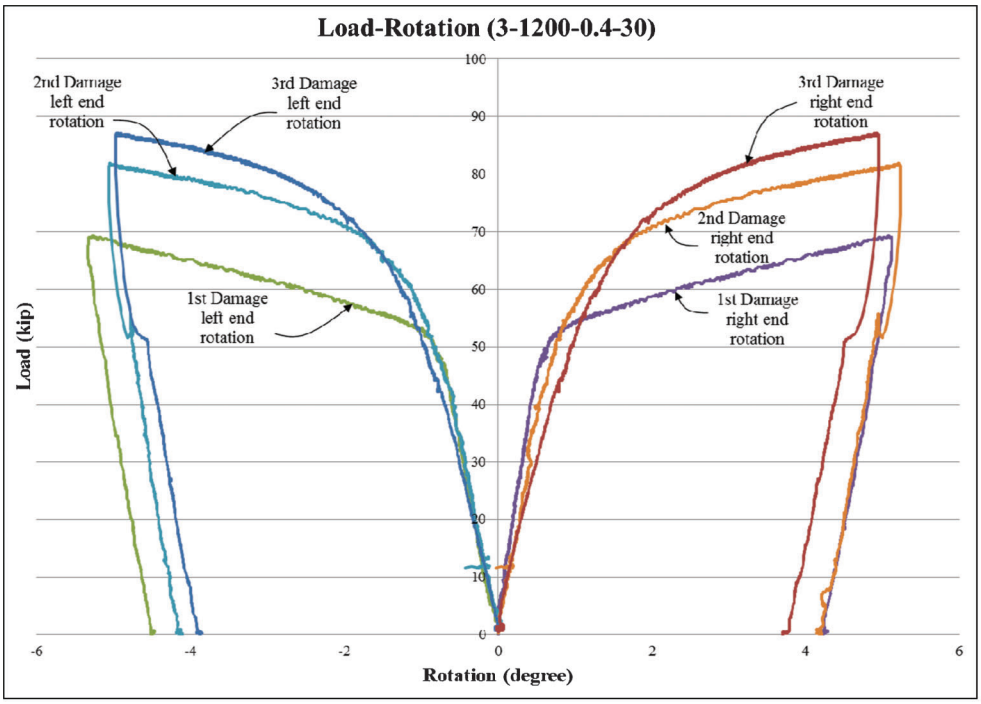

Figure 6.11 Load-rotation diagram of Specimen #2 (3-1200-0.4-30).

Figure 6.12 Photograph of Specimen #2 after the 3rd heat straightening repair.

damage cycle. Each damage cycle corresponded to the damage strain of 30 ε_y (0.045 in./in.) at the top strain gage. The damage strain in the first cycle was measured using the strain gage layout described Section 5.4. The strain gage data from the first damage cycle is provided in Figure 6.16.

Damage cycles 2 and 3 were conducted under displacement control, where the displacement at mid-span reached the required magnitude close to the result of the first damage cycle. Figure 6.17 compares the P-Δ behavior of all three damage cycles of Specimen #3. Figure 6.18 compares the P-θ behavior of all three damage cycles of Specimen #3.

As shown in Figures 6.17 and 6.18, the initial stiffness of the beam changed slightly after the first damage-repair event. The material became stronger after damage-repairs, which is clearly seen in Figures 6.17 and 6.18.

6.6 Repair Process for Specimen #3 (3-1400-0.4-30)

Repair cycles of Specimen #3 were conducted by applying external force corresponding to the restraining moment of 0.4 M_p which is similar to Specimen #2. The difference was that each Vee heat was subjected to a maximum temperature of 1400 °F. The color of the Vee at the maximum temperature of 1400 °F is shown in Figure 6.19 (b). For comparison, Figure 6.19 (a) shows the color of the Vee at the maximum temperature of 1200 °F.

The total numbers of Vee heats required to straighten the specimen in each damage-repair cycle are shown in Figure 6.20. Thirty nine Vee heats on both

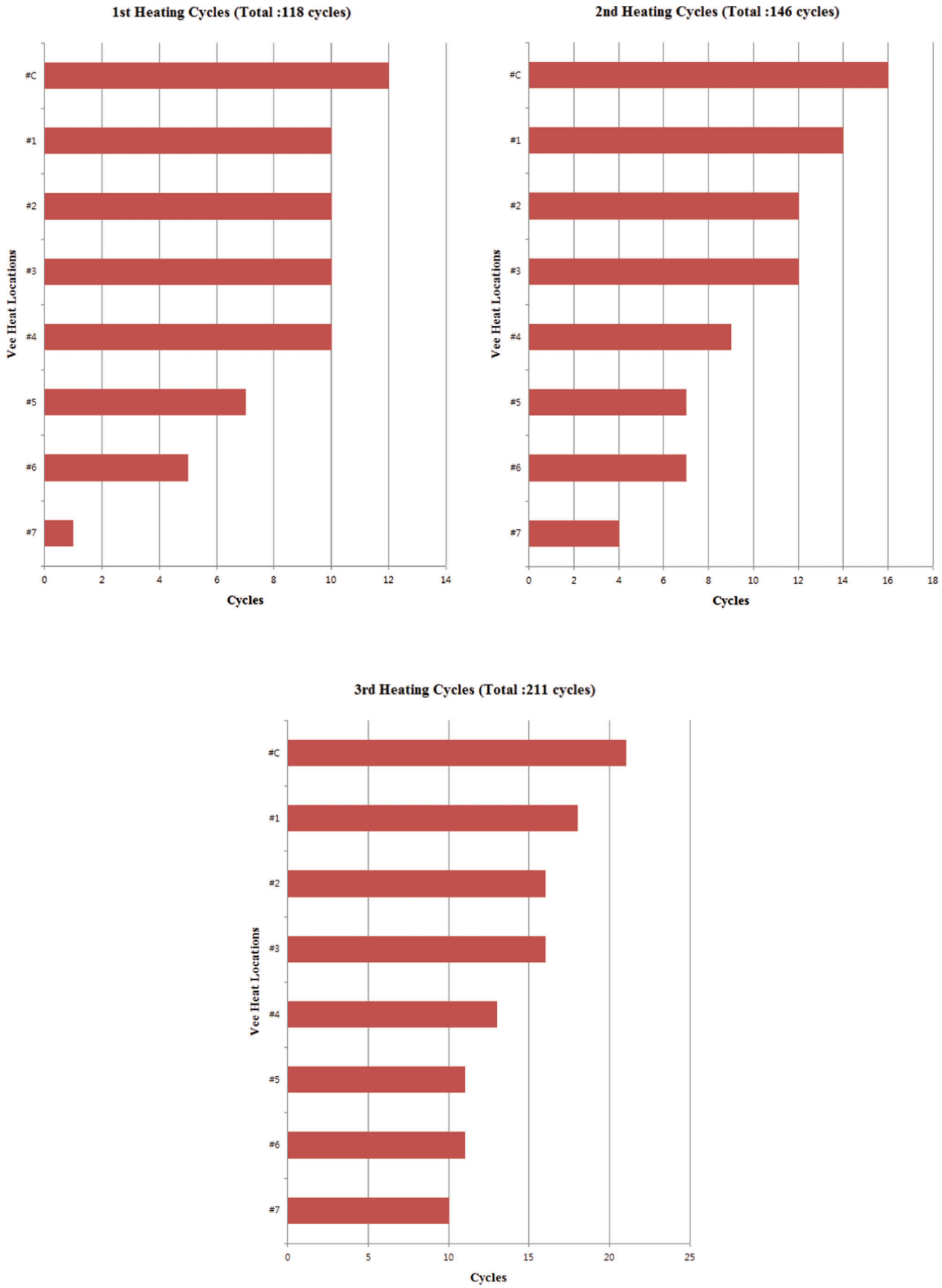

Figure 6.13 Vee heat frequency chart of Specimen #2.

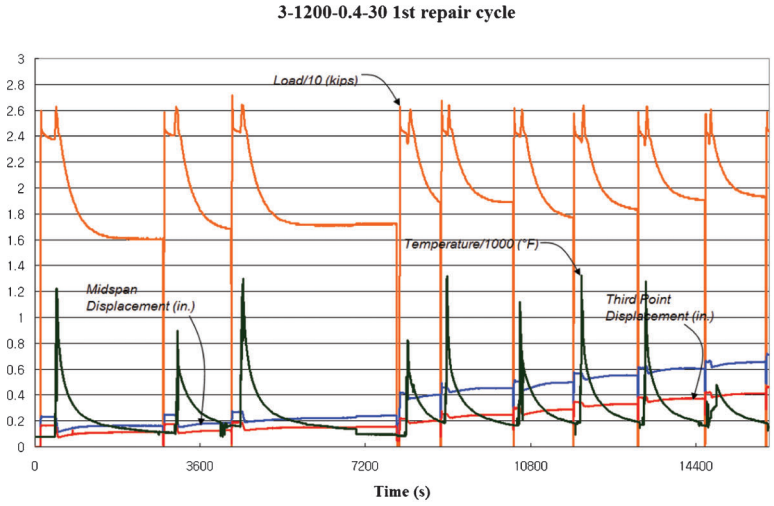

(a) 1st repair cycle

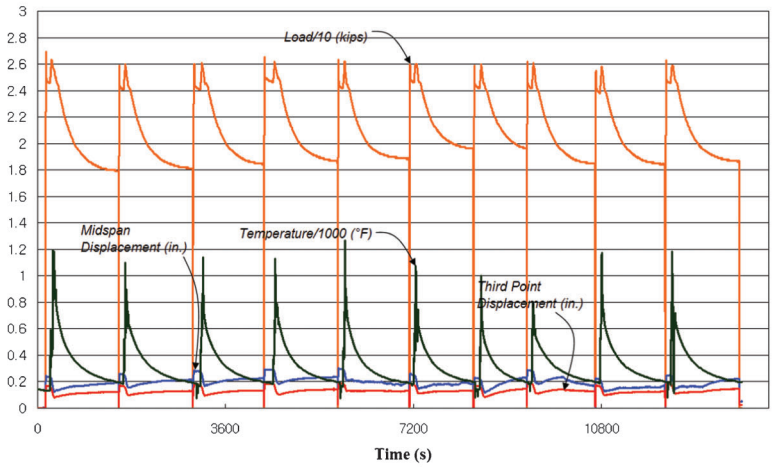

(b) 2nd repair cycle

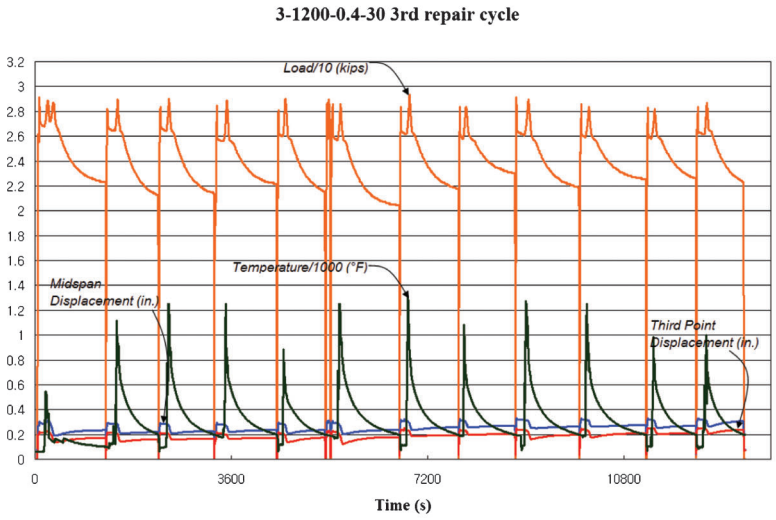

(c) 3rd repair cycle

Figure 6.14 Instrument data during the repair cycle of Specimen #2.

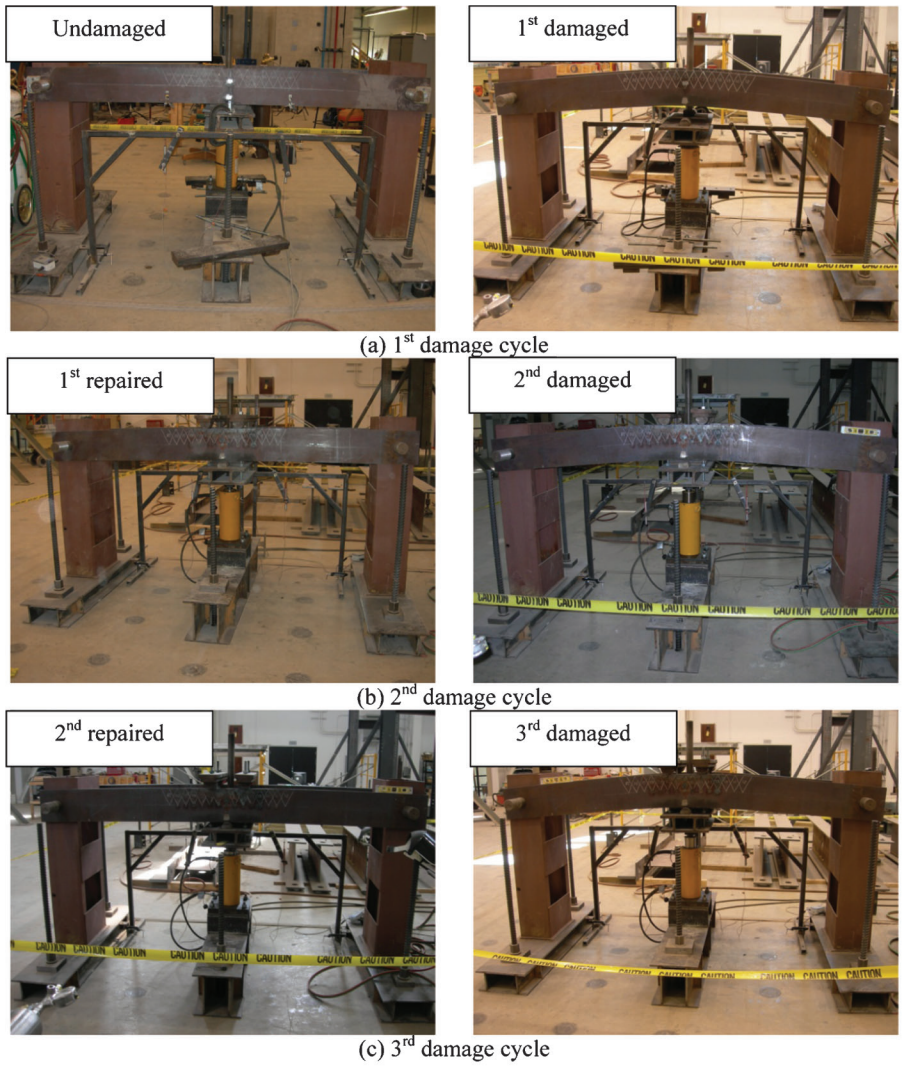

Figure 6.15 Photographs of Specimen #3 before and after the damage.

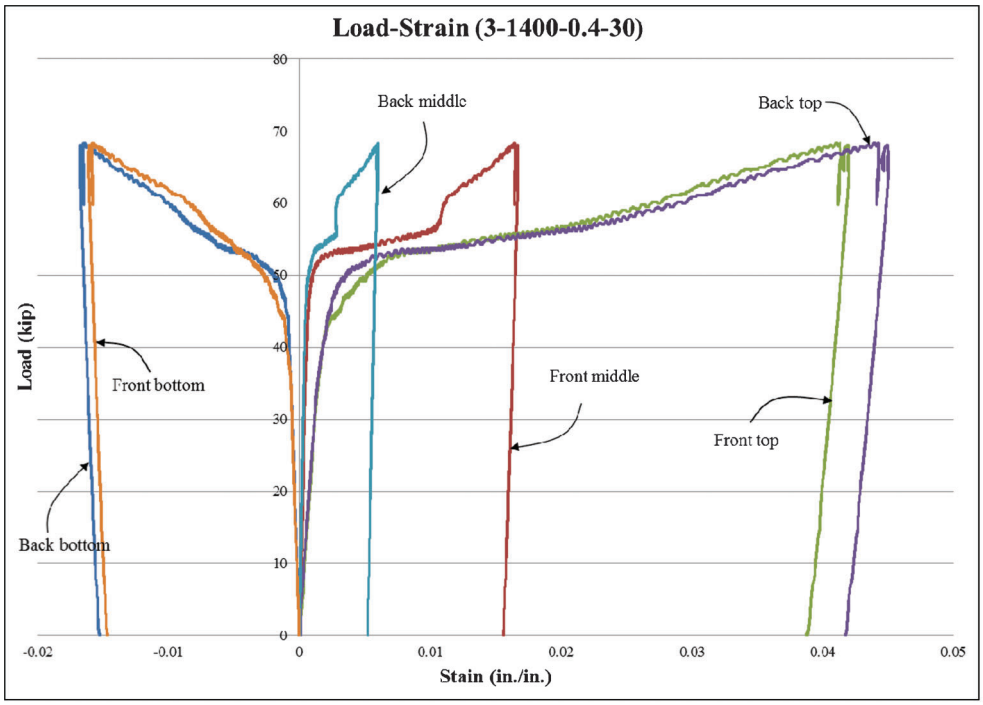

Figure 6.16 Load-strain diagram of Specimen #3 (1-1400-0.4-30).

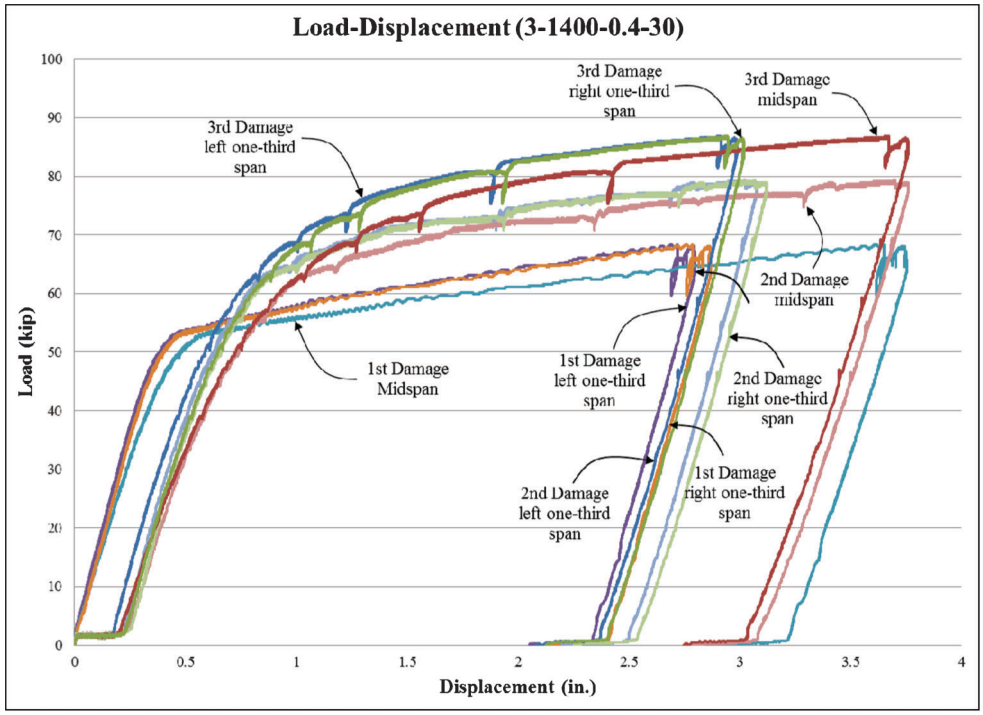

Figure 6.17 Load-displacement diagram of Specimen #3 (3-1400-0.4-30).

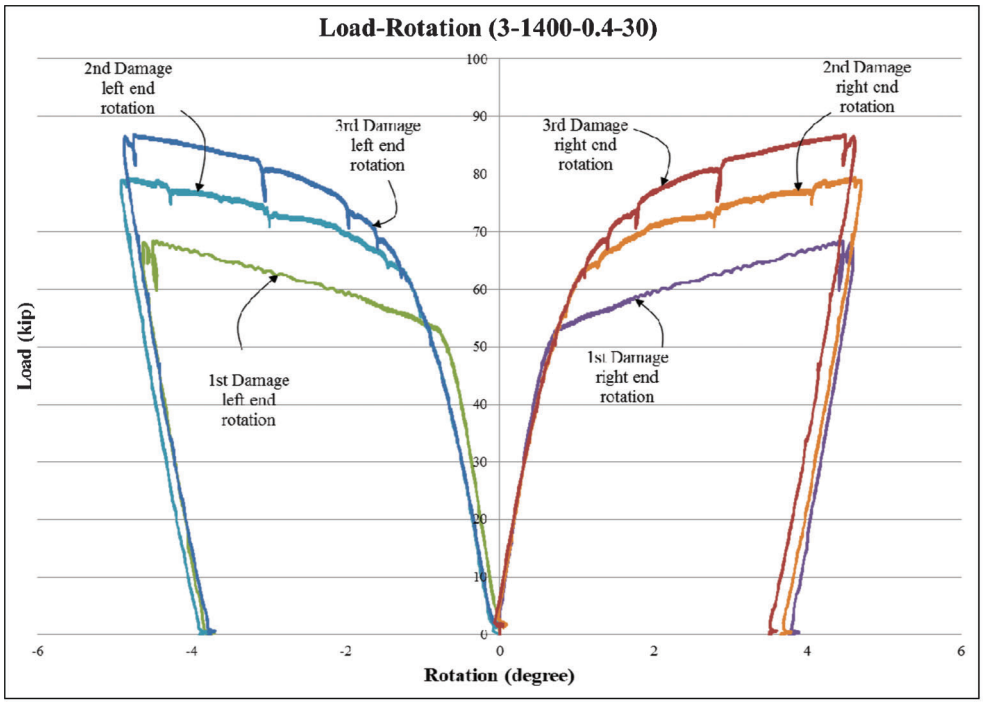

Figure 6.18 Load-rotation diagram of Specimen #3 (3-1400-0.4-30).

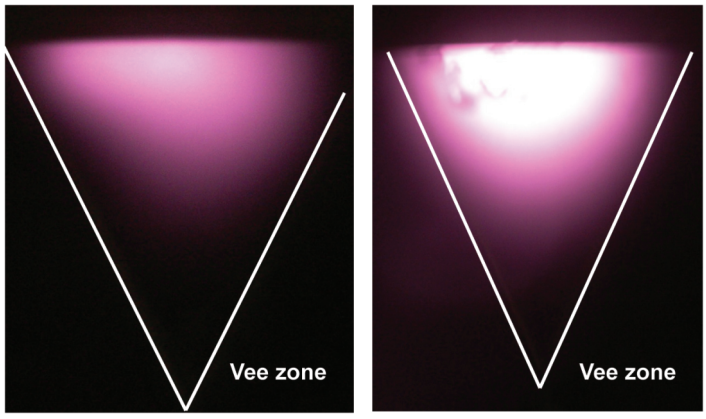

(a) 1200 °F (b) 1400 °F

Figure 6.19 Color of A36 steel at the maximum heating temperatures.

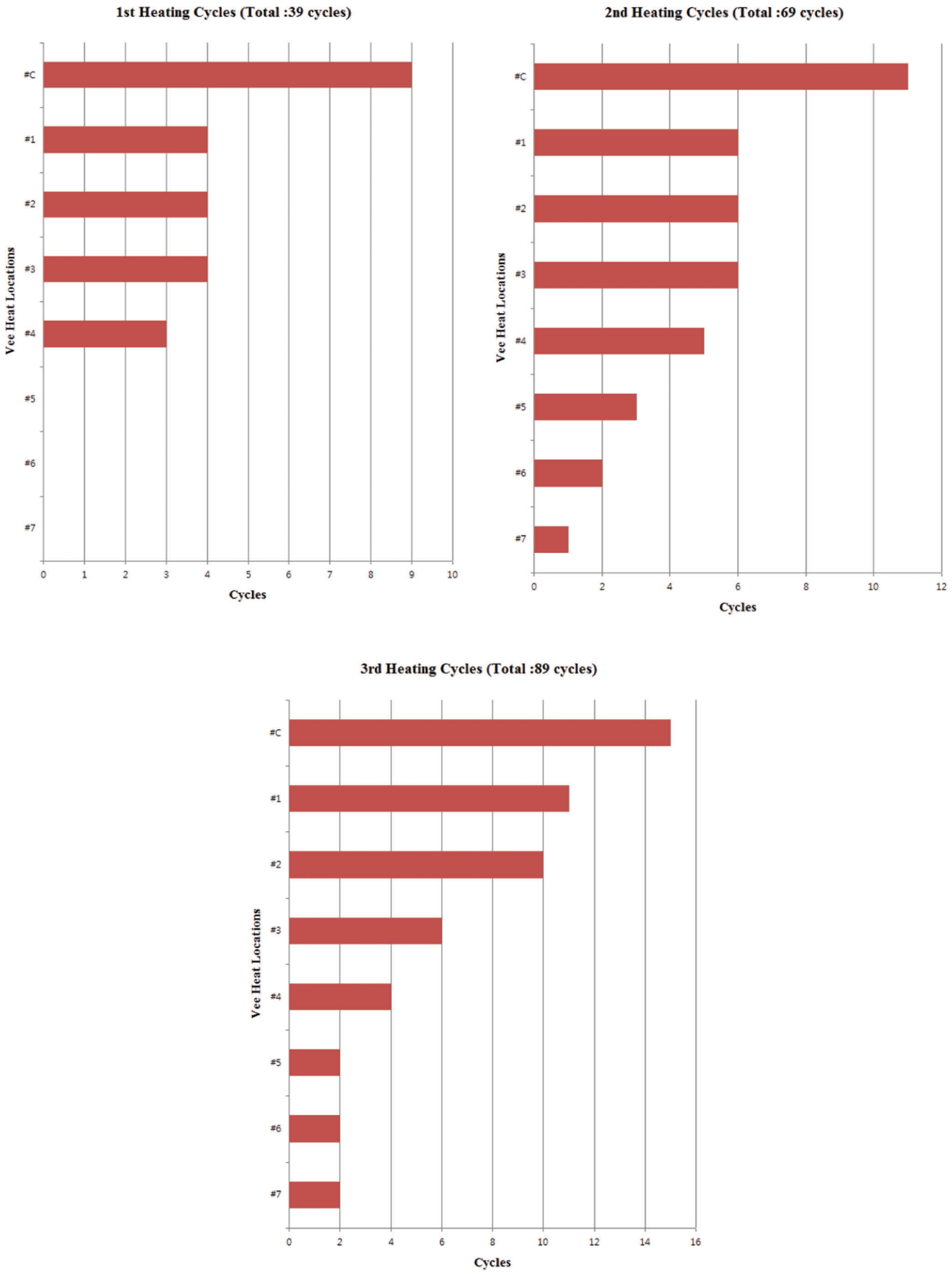

Figure 6.20 Vee heat frequency chart of Specimen #3.

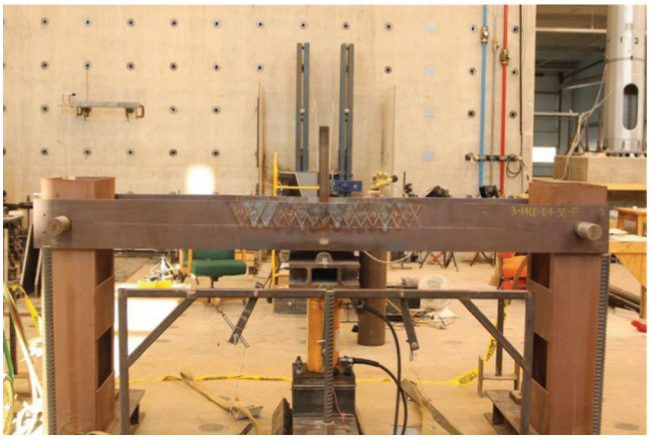

Figure 6.21 Photograph of Specimen #3 after the 3rd heat straightening repair.

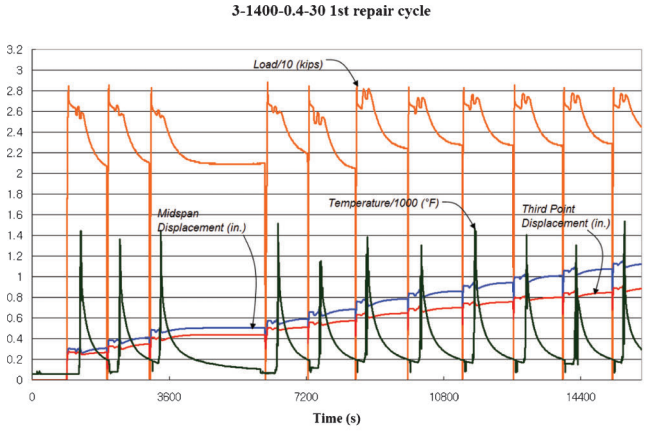

(a) 1st repair cycle

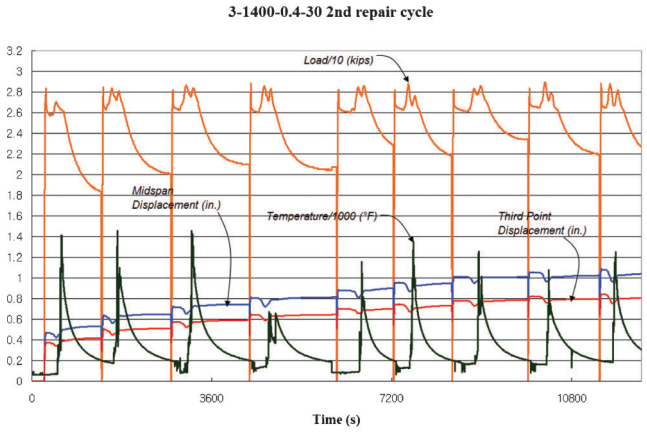

(b) 2nd repair cycle

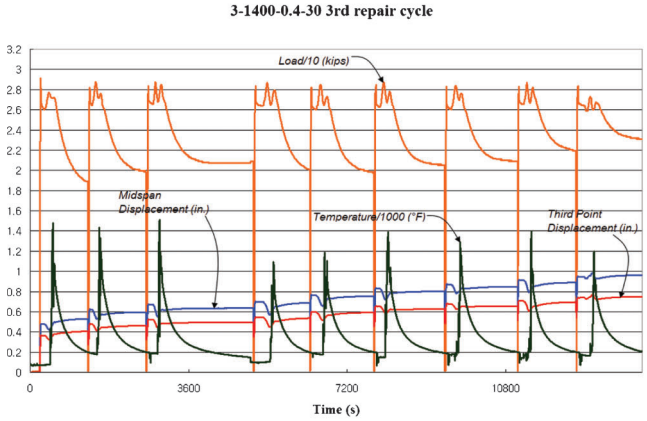

(c) 3rd repair cycle

Figure 6.22 Instrument data during the repair cycle of Specimen #3.

flanges were required to complete the first repair cycle. The second repair cycle took 69 Vee heats to complete. The third repair cycle needed 89 Vee heats to complete. Required numbers of Vee heats to fully straighten the specimen increased following multiple damage cycles, which was similar to Specimen #2. But the total numbers of Vee heats required in each damage-repair cycle reduced significantly as compared to Specimen #2. The final photograph of Specimen #3 after all repair cycles is shown in Figure 6.21.

Vee heats were applied to all Vee regions from the center (C) to the 7th (L7 or R7) heating locations to avoid excessive out-of-plane distortion.

Figure 6.22 shows the behavior of Specimen #3 in the initial several steps of each repair cycle. This figure includes: (a) the displacements from three displacement transducers in inches, (b) the restraining force in the hydraulic actuator in kips, which is divided by 10 (i.e., 1.0 on the graph shows 10 kips of force), and (c) the temperature of the steel in F, which is divided by 1000 (i.e., 1.0 on the graph corresponds to 1000 °F).

6.7 Damage Process of Specimen #4 (1-1400-0.4-60)

Specimen #4 used the same sensor layout as the previous specimens as shown in Section 5.4. This specimen was subjected to the larger damage strain of 60 ε_y during the damage process.

Figure 6.23 shows the photographs of the beam specimen before (a) and after (b) the damage cycle. The beam specimen was damaged by monotonically increasing the concentrated force at the midspan. The damage was monitored using the longitudinal strain gages. The test was considered complete when one of the values of the front top and back top strain gages reached 60 ε_y. The complete strain gage data for the damage cycle is shown in Figure 6.24.

The P-Δ relationship for Specimen #4 is shown in Figure 6.25. The maximum midspan plastic displacement at the damage process was measured as 8.7 in. The final damage displacement after elastic rebound was 7.5 in. at the midspan. Two displacement sensors located at the one-third point of each side were disconnected during the test because the displacements of the one-third point exceeded sensor capacity. Figure 6.25 shows only the

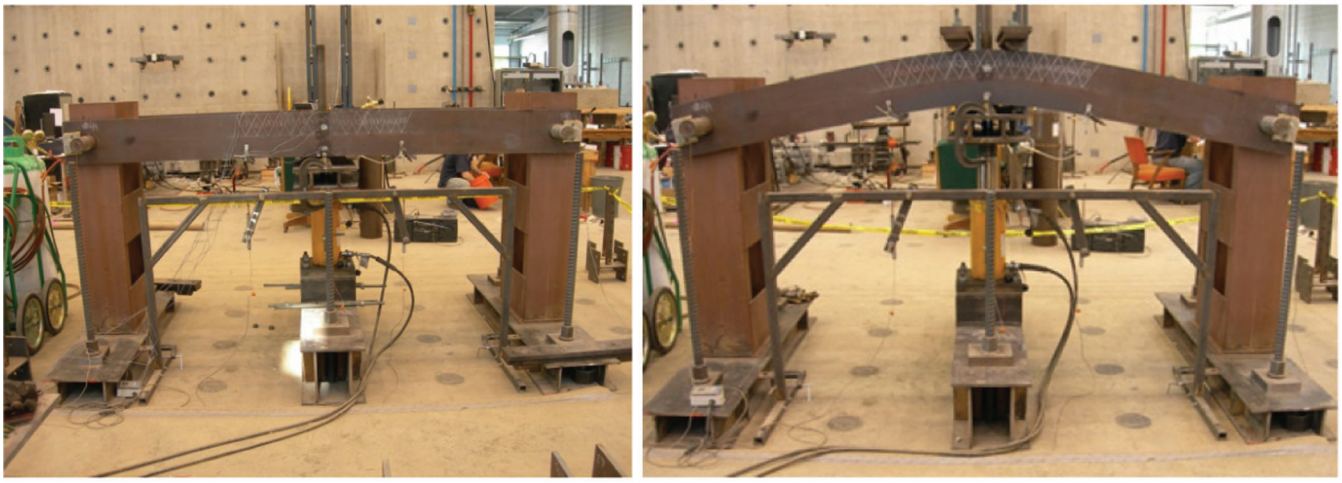

(a) Undamaged specimen (b) Damaged specimen

Figure 6.23 Photographs of Specimen #4 before and after the damage.

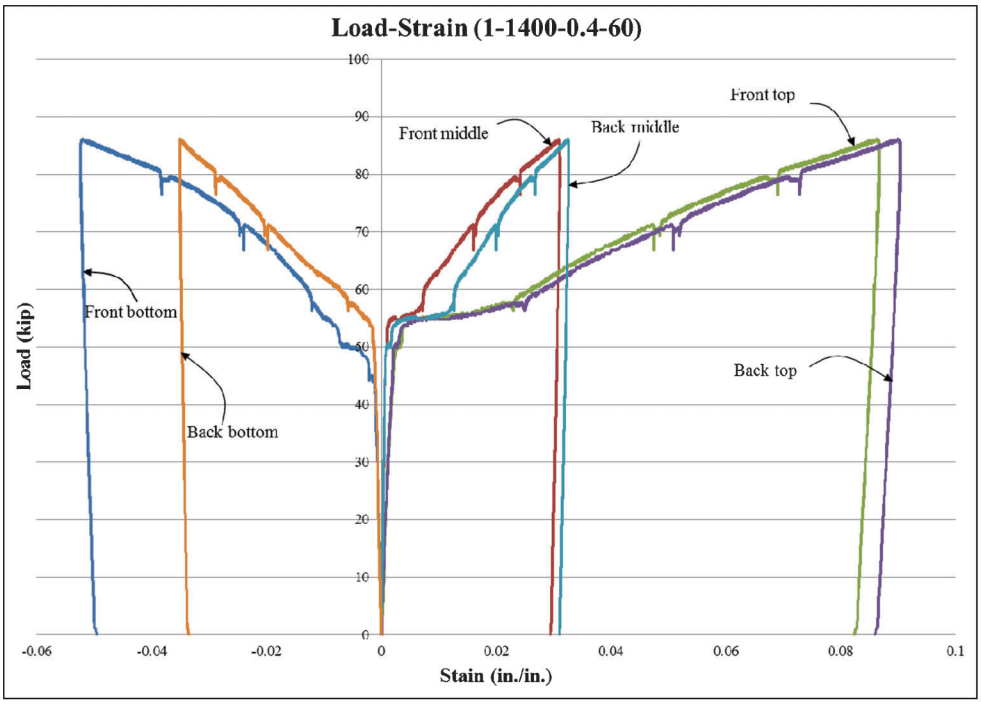

Figure 6.24 Load-strain diagram of Specimen #4 (1-1400-0.4-60).

midspan deflection behavior of Specimen #4 during the damage process.

Figure 6.26 shows the P-θ relationship of Specimen #4.

6.8 Repair Process for Specimen #4 (1-1400-0.4-60)

Repair cycles for Specimen #4 were conducted by applying external force corresponding to the restraining moment of 0.4 M_p with the Vee heat temperature of 1400 °F.

The photograph of the repaired beam is shown in Figure 6.27. After the final Vee heat repair, the remaining midspan deflection was less than ⅛ in. Two hundred seventy six Vee heats were required to complete the repair cycle of Specimen #4. The frequency chart indicating the number of Vee heats applied to each location is shown in Figure 6.28.

Figure 6.29 shows some of the initial data of the Vee heat repair cycles. This figure includes: (a) the displacements from three displacement transducers in inches, (b) the restraining force in the hydraulic actuator in kips, which is divided by 10 (i.e., 1.0 on the graph shows 10 kips of force), and (c) the temperature of the steel in F, which is divided by 1000 (i.e., 1.0 on the graph corresponds to 1000 °F).

6.9 Damage Process of Specimen #5 (1-1400-0.4-30)

Specimen #5 was tested to evaluate the effects of overheating. The Vee heat temperature was increased to 1400 °F to promote faster repair compared with Specimen #1. This specimen was also used as a comparison specimen for Specimen #3.

Figure 6.30 shows the photographs of the beam specimen before (a) and after (b) the damage cycle. The beam specimen was damaged by monotonically increasing the concentrated force at the midspan. The damage was monitored using the longitudinal strain gage. The test was considered complete when one of the values of the front top and back top strain gages reached 30 ε_y. The complete strain gage data for the damage cycle is shown in Figure 6.31.

P-Δ relationships for Specimen #5 is shown in Figure 6.32. Figure 6.33 shows the P-θ relationship of Specimen #5.

6.10 Repair Process for Specimen #5 (1-1400-0.4-30)

Repair cycles for Specimen #5 were conducted by applying external force corresponding to the restraining moment of 0.4 M_p with the Vee heat temperature of 1400 °F.

Fifty four Vee heats were required to complete the repair cycle of Specimen #5. The photograph of the repaired beam is shown in Figure 6.34. After the final Vee heat repair, the remaining midspan deflection was less than ⅛ in. The frequency chart indicating the number of Vee heats applied to each location is shown in Figure 6.35.

Figure 6.36 shows some of the initial data of Vee heat repair cycles. This figure includes: (a) the displacements from three displacement transducers in inches, (b) the restraining force in the hydraulic

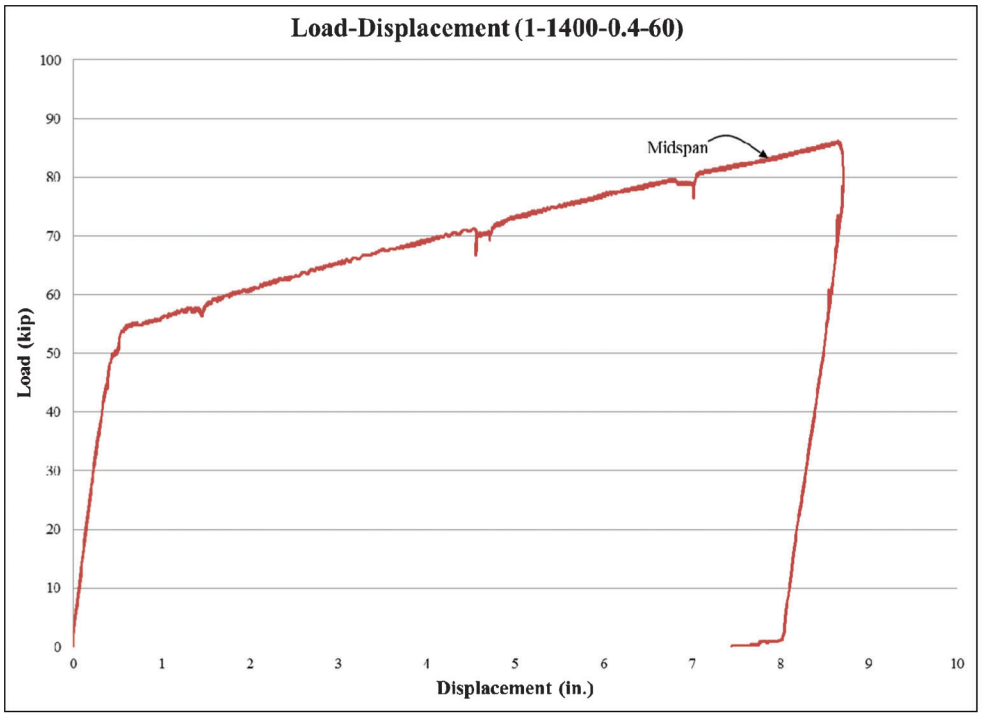

Figure 6.25 Load-displacement diagram of Specimen #4 (1-1400-0.4-60).

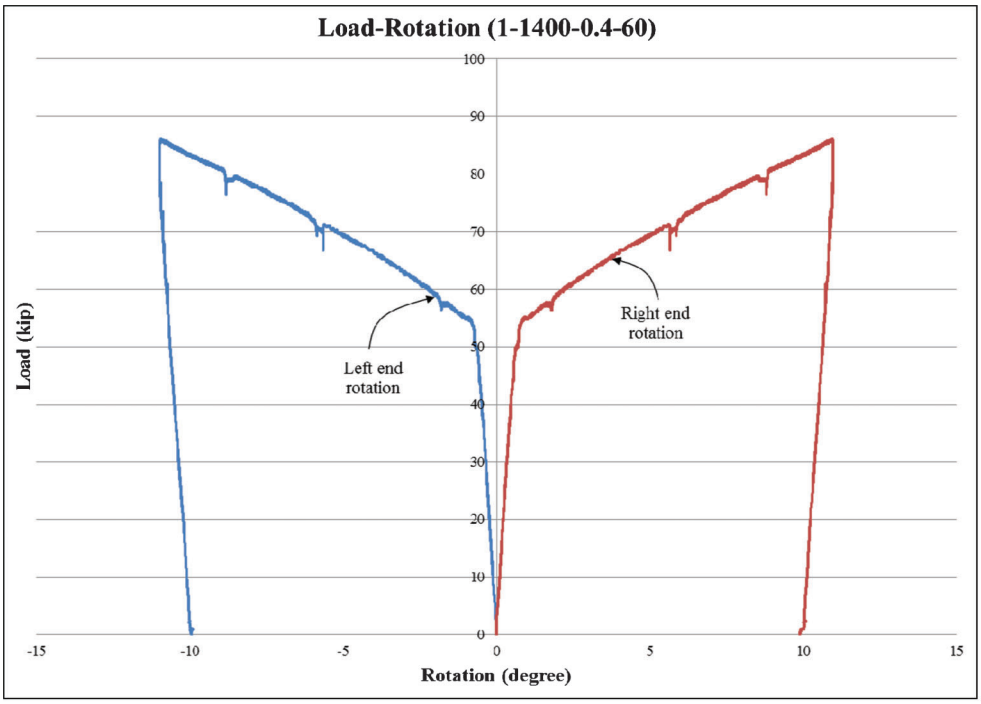

Figure 6.26 Load-rotation diagram of Specimen #4 (1-1400-0.4-60).

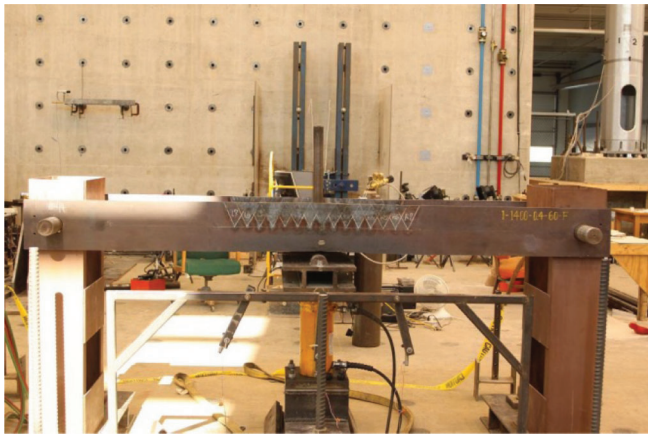

Figure 6.27 Photograph of Specimen #4 after the heat straightening repair.

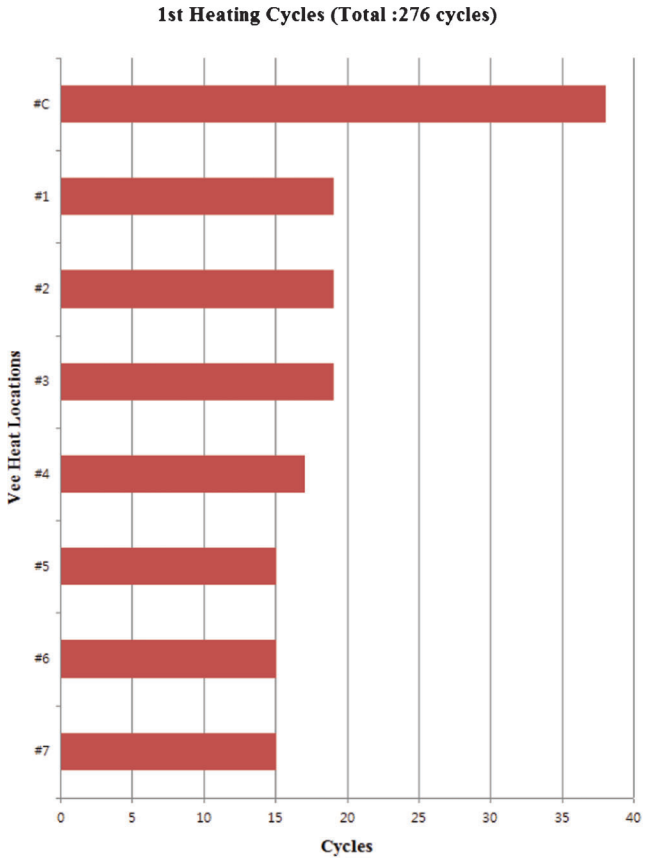

Figure 6.28 Vee heat frequency chart of Specimen #4.

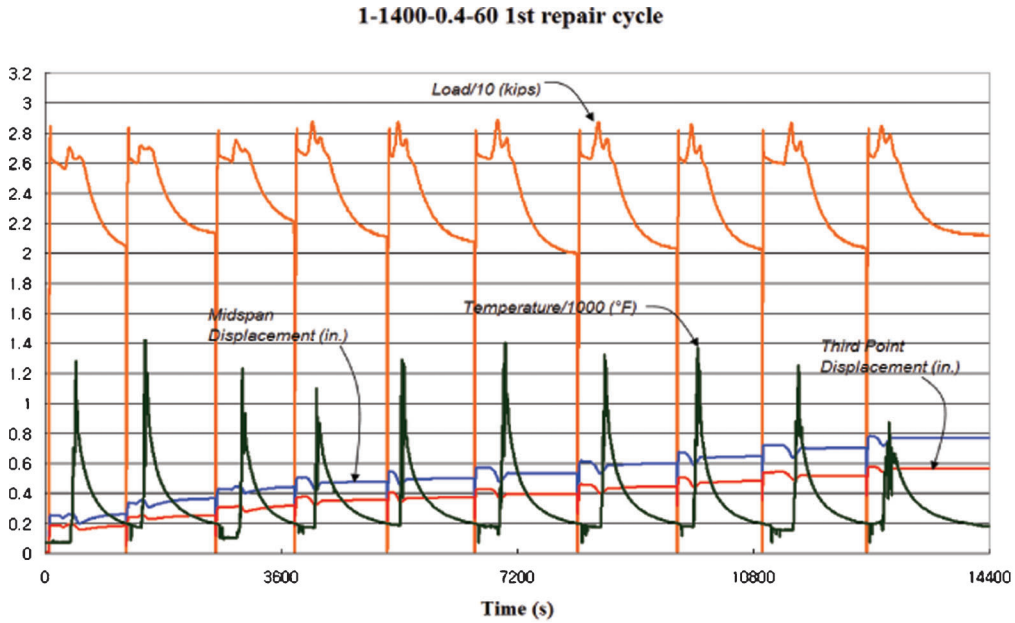

Figure 6.29 Instrument data during the repair cycle of Specimen #4.

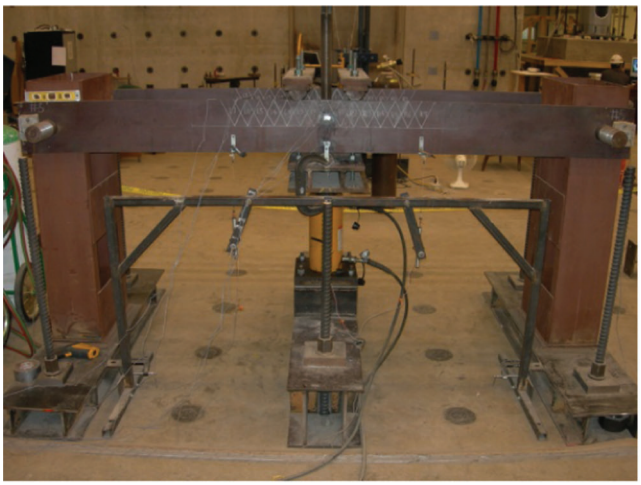

(a) Undamaged specimen

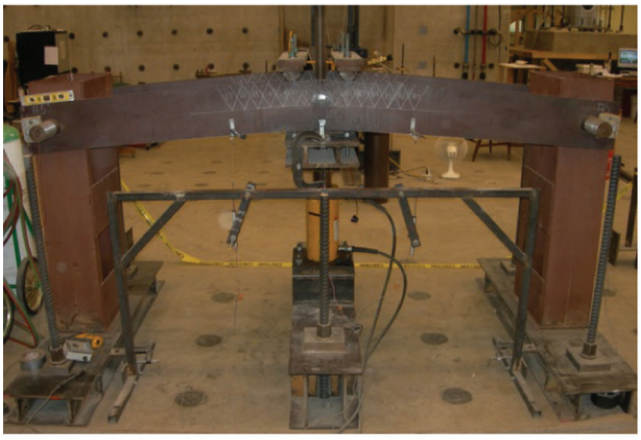

(b) Damaged specimen

Figure 6.30 Photographs of Specimen #5 before and after the damage.

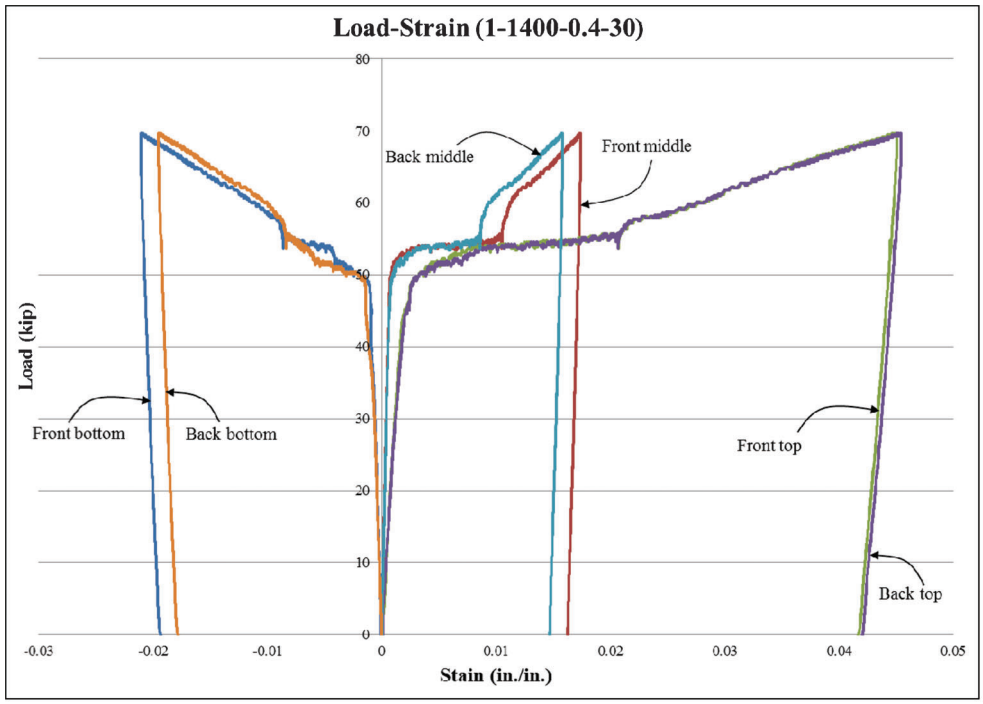

Figure 6.31 Load-strain diagram of Specimen #5 (1-1400-0.4-30).

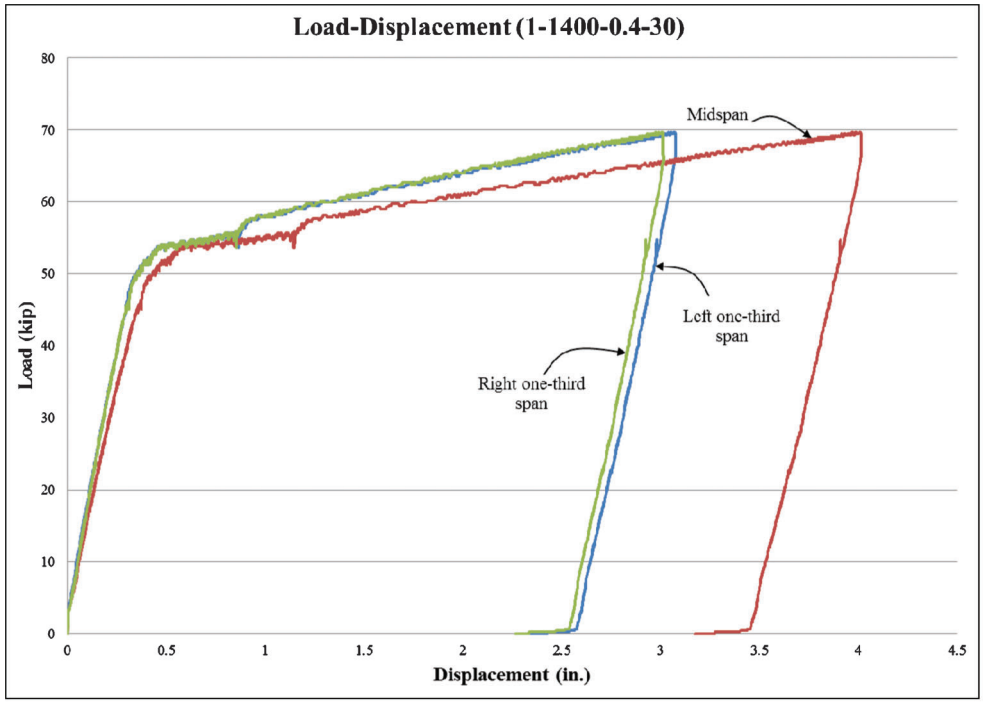

Figure 6.32 Load-displacement diagram of Specimen #5 (1-1400-0.4-30).

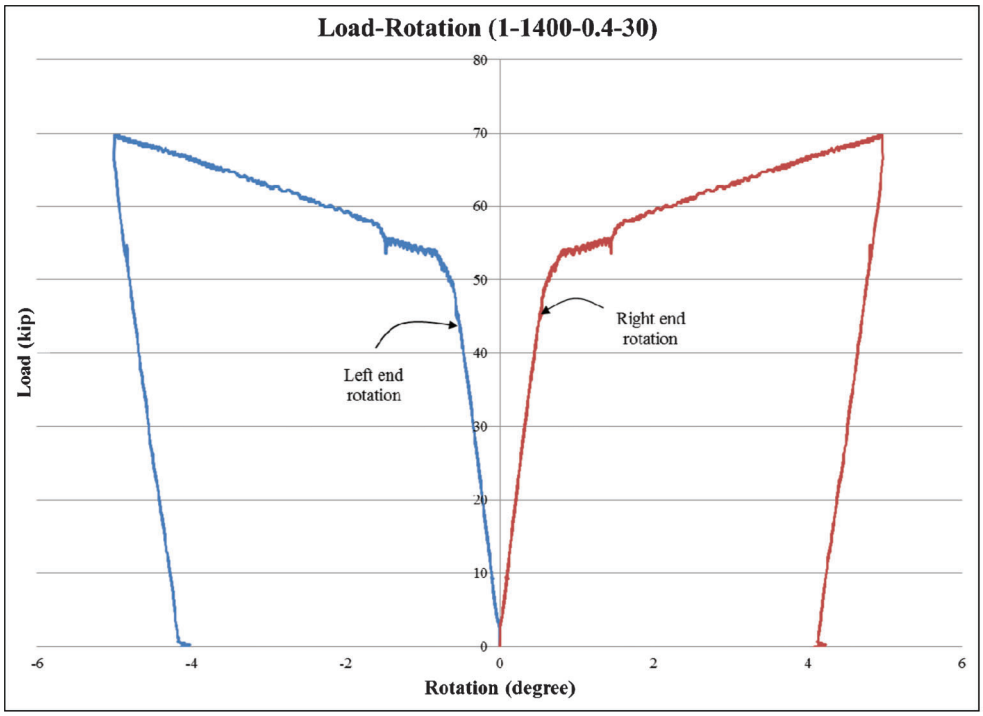

Figure 6.33 Load-rotation diagram of Specimen #5 (1-1400-0.4-30).

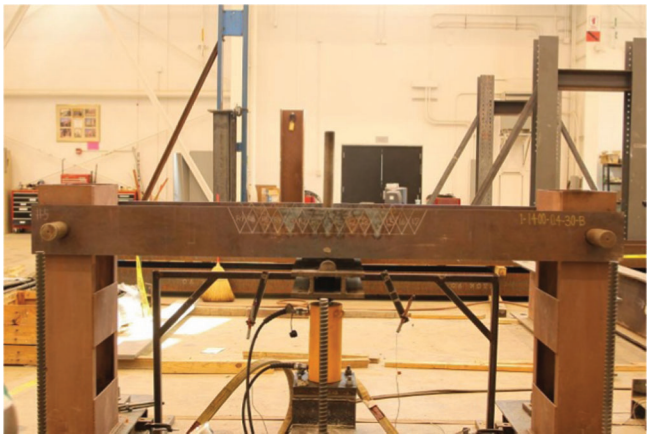

Figure 6.34 Photograph of Specimen #5 after the heat straightening repair.

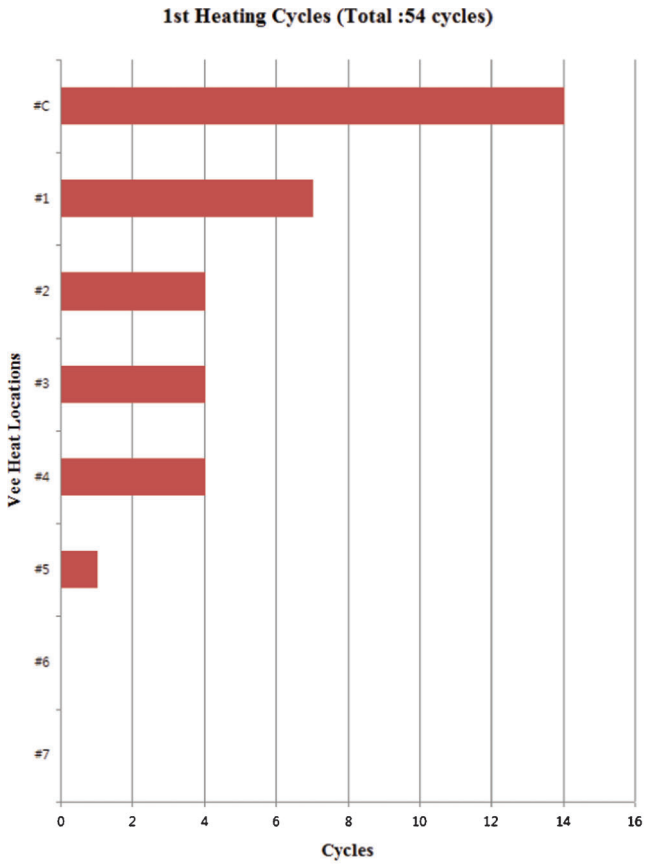

Figure 6.35 Vee heat frequency chart of Specimen #5.

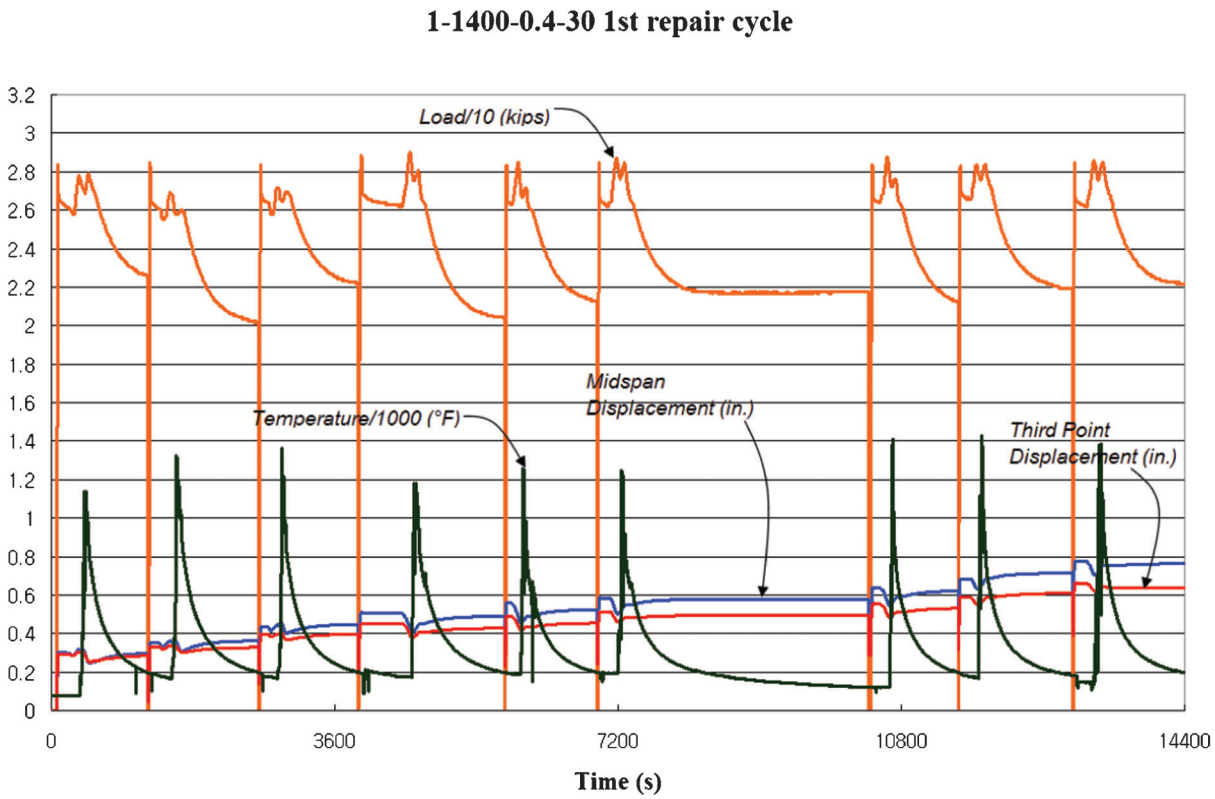

Figure 6.36 Instrument data during the repair cycle of Specimen #5.

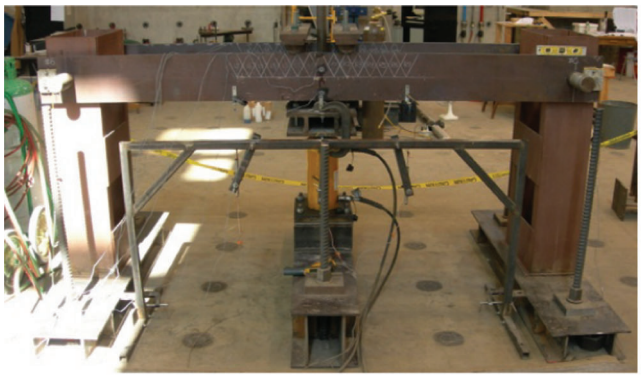

(a) Undamaged specimen

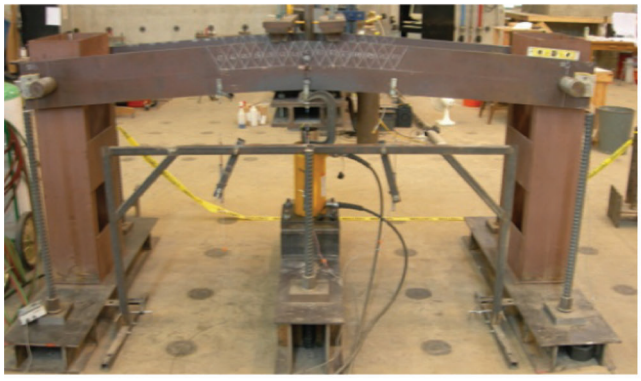

(b) Damaged specimen

Figure 6.37 Photographs of Specimen #6 before and after the damage.

actuator in kips, which is divided by 10 (i.e., 1.0 on the graph shows 10 kips of force), and (c) the temperature of the steel in F, which is divided by 1000 (i.e., 1.0 on the graph corresponds to 1000 °F).

6.11 Damage Process of Specimen #6 (1-800-0.6-30)

Specimen #6 was tested to evaluate the effects of underheating and overstraining.

Figure 6.37 shows the photographs of the beam specimen before (a) and after (b) the damage cycle. The beam specimen was damaged by monotonically increasing the concentrated force at the midspan. The damage was monitored using the longitudinal strain gage. The test was considered complete when one of the values of the front top and back top strain gages reached 30 ε_y. The complete strain gage data for the damage cycle is shown in Figure 6.38.

P-Δ relationships for Specimen #6 are shown in Figure 6.39. Figure 6.40 shows the P-θ relationship of Specimen #6.

6.12 Repair Process for Specimen #6 (1-800-0.6-30)

Repair cycles for Specimen #6 were conducted by applying external force corresponding to the restraining moment of 0.6 M_p with the maximum Vee heat temperature of 800 °F. Because of the low heating temperature, the cooling time was significantly reduced.

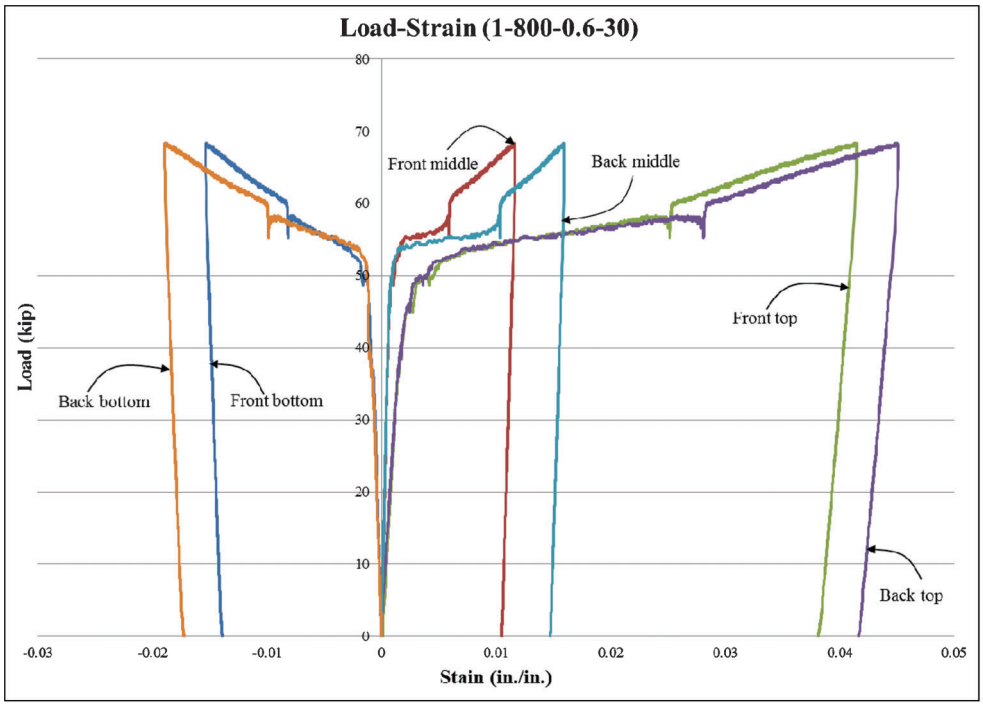

Figure 6.38 Load-strain diagram of Specimen #6 (1-800-0.6-30).

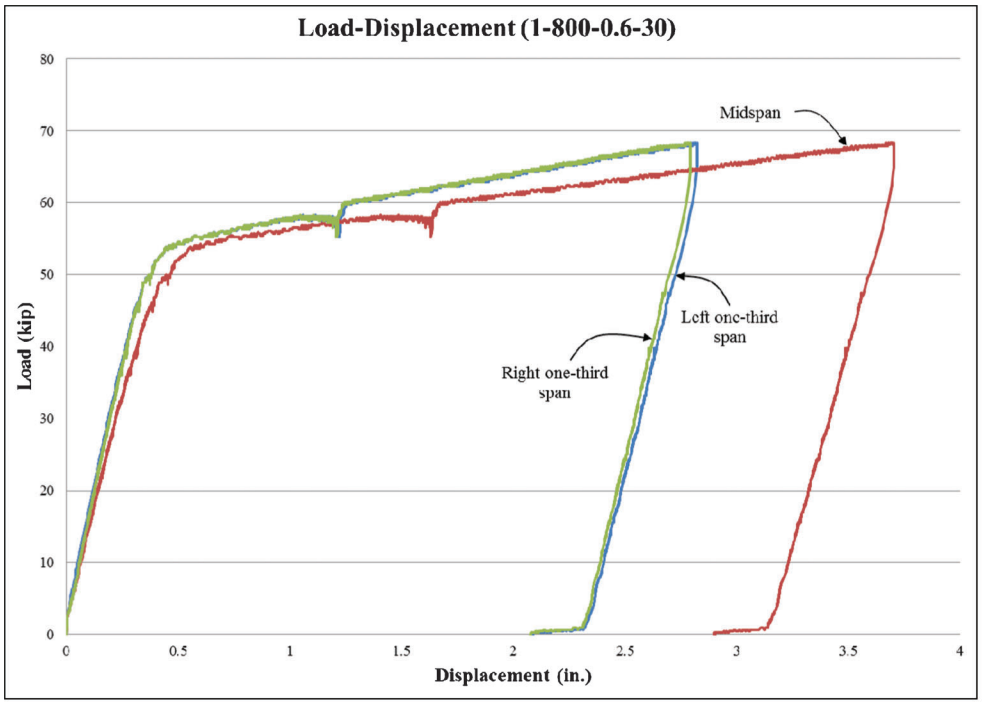

Figure 6.39 Load-displacement diagram of Specimen #6 (1-800-0.6-30).

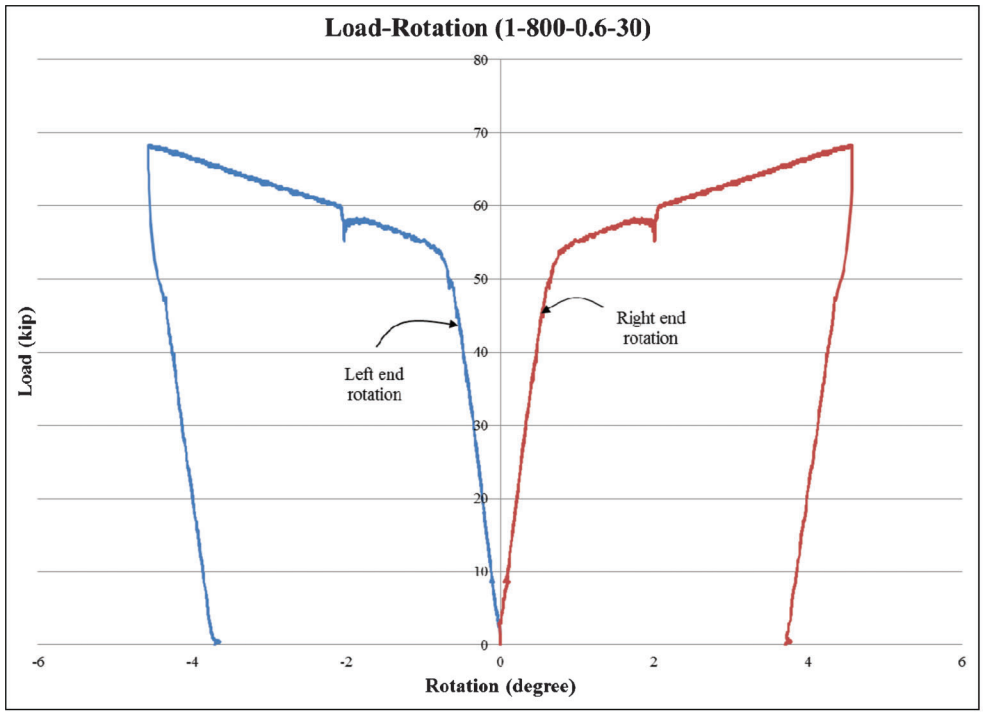

Figure 6.40 Load-rotation diagram of Specimen #6 (1-800-0.6-30).

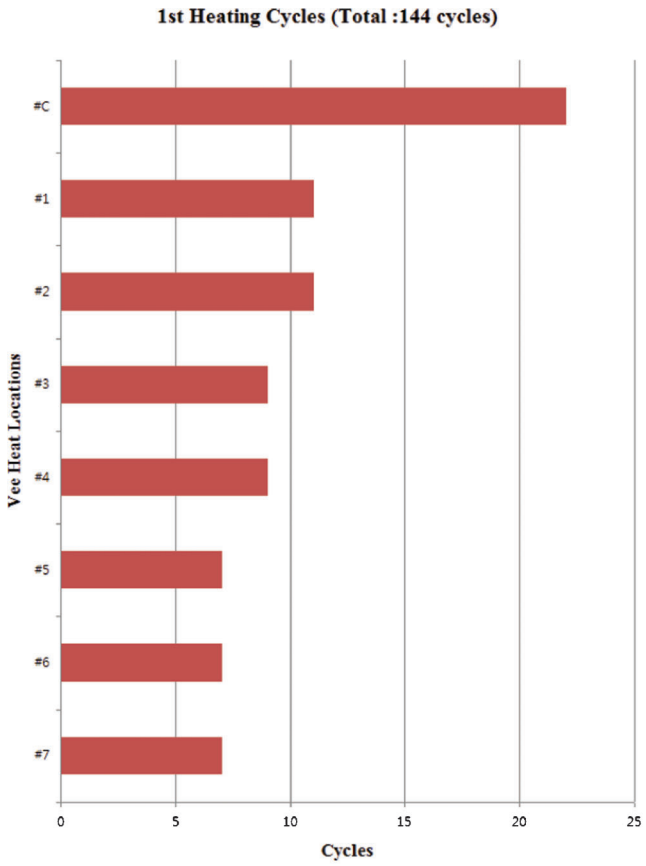

Figure 6.41 Vee heat frequency chart of Specimen #6.

Vee heats were re-applied when the steel was cooled down below 200 °F.

One hundred forty four Vee heats were required to complete the repair cycle of Specimen #6. After the final Vee heat repair, the remaining midspan deflection was less than ⅛ in. The frequency chart indicating the number of Vee heats applied to each location is shown in Figure 6.41. The photograph of the repaired beam is shown in Figure 6.42.

Figure 6.43 shows some of the initial data of the Vee heat repair cycles. This figure includes: (a) the displacements from three displacement transducers in inches, (b) the restraining force in the hydraulic actuator in kips, which is divided by 10 (i.e., 1.0 on the graph shows 10 kips of force), and (c) the temperature of the steel in F, which is divided by 1000 (i.e., 1.0 on the graph corresponds to 1000 °F).

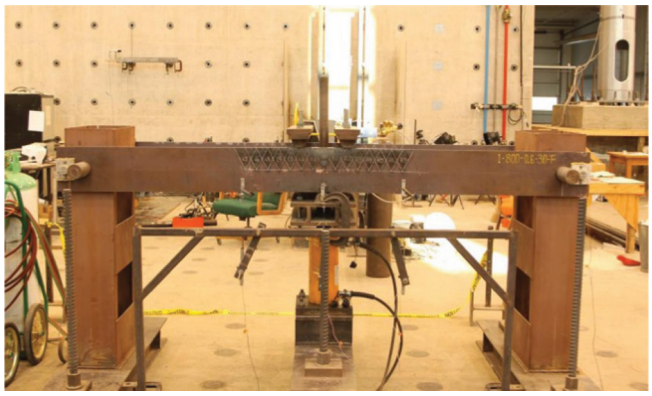

Figure 6.42 Photograph of Specimen #6 after the heat straightening repair.

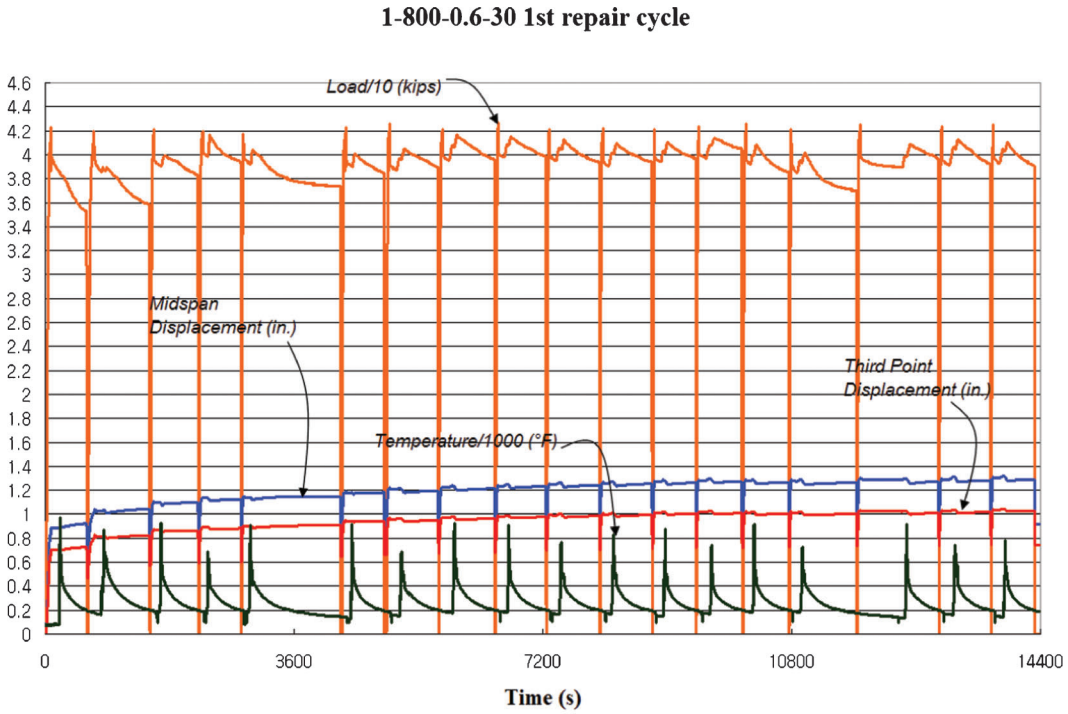

Figure 6.43 Instrument data during the repair cycle of Specimen #6.

7. SMALL SCALE TEST: MATERIAL TEST

This chapter presents the results of the material tests conducted on samples removed from the flanges of undamaged and damaged-repaired small scale test specimens. The material tests included: (a) uniaxial tension tests, (b) Charpy V-notch tests, (c) Rockwell hardness tests, and (d) microstructure investigations. The material tests were conducted following the ASTM standard test method that was applicable to each material test as explained earlier in Section 5.6.

7.1 Charpy Impact Fracture Toughness Tests

Initially, for each damaged-repaired beam specimen, twelve Charpy V-notch specimens in Figure 5.15 were planned to be removed from the front flange, identified as Flange A, and three uniaxial tensile coupons in Figure 5.12 were planned to be removed from the back flange, identified as Flange B.

Initial Charpy V-notch test results are shown in Table 7.1. As seen in the Table 7.1, Charpy V-notch test results conducted on the coupons from Flange A were fairly low. Even coupons from undamaged specimens (virgin material) were lower than the AASHTO bridge specification (2007) requirement of 25 ft·lbs. @ 40 °F.

Initial Charpy test results proved that Virgin A36 steel plates used to fabricate small scale test specimens did not satisfy the AASHTO bridge specification (2007) toughness requirements.

To get meaningful results from the Charpy V-notch test, a temperature-impact energy graph was developed with additional Charpy test results for the virgin material at different test temperatures. Figure 7.1 shows the temperature-impact energy graph developed using Charpy test results. As seen in Figure 7.1, the initial testing temperature of 40 °F was located over the transition region of the graph. Therefore, 70 °F (room temperature) was selected as the new Charpy impact test temperature.

The tensile coupons that were machined from the back flange of each damaged-repaired beam specimen were sacrificed to make new Charpy coupons as shown in Figure 7.2. Nine new Charpy impact test coupons were fabricated from the three tensile coupons of each small scale test specimen.

New Charpy V-notch test results are shown in Table 7.2. The comparisons of the averaged fracture toughness of all small scale test specimens at 40 °F and 70 °F of the test temperature are shown in Figure 7.3. The results are shown in the order of the fracture toughness magnitude with standard deviation error bars.

As seen in Table 7.2 and Figure 7.3, Charph V-notch test results at 70 °F were considerably higher than the 40 °F results.

The data of the Charpy impact fracture test presented in this section indicates that:

- The overall fracture toughness of the small scale tests was lower than the undamaged steel toughness.
- Compared with the control temperature (1200 °F), the fracture toughness of the overheated specimen (1400 °F) was slightly increased.

TABLE 7.1
Initial Charpy V-notch test results at 40 °F

Specimen Designation	Location	Charpy Results (ft·lbs.) L1	C	R1
1-1200-0.4-30	1	*47*	*31*	10
	2	*98*	*105*	13
	3	*101*	*92*	13
	4	*41*	*24*	11
	avg.		**11.75**	
3-1200-0.4-30	1	12	10	12
	2	10	10	8
	3	8	7	10
	4	6	7	7
	avg.		**8.92**	
3-1400-0.4-30	1	15	11	13
	2	8	10	11
	3	12	34	11
	4	10	6	6
	avg.		**12.25**	
1-1400-0.4-60	1	12	11	11
	2	10	10	12
	3	8	10	8
	4	7	5	8
	avg.		**9.33**	
1-1400-0.4-30	1	10	10	13
	2	15	9	11
	3	12	18	12
	4	7	9	10
	avg.		**11.33**	
1-800-0.6-30	1	5	5	6
	2	5	5	6
	3	6	6	6
	4	6	6	6
	avg.		**5.67**	
Virgin steel (undamaged)	1	16	26	21
	2	16	16	18
	3	18	15	20
	4	28	21	24
	avg.		**19.92**	

NOTE: Italicized values were ignored.

- The 1-800-0.6-30 specimen (underheating and overstraining) showed the lowest fracture toughness capacity.
- Multiple damage-repair cycles further reduced the fracture toughness of A36 steel.
- For all Charpy specimens, the fracture toughness values became smaller closer to the flange-web junction.

7.2 Uniaxial Tension Tests

Tensile coupon locations were changed due to new Charpy coupons taken from initial tensile coupons. Figure 7.4 shows new tensile coupon locations from the front flange of each damaged and repaired beam specimen. Totally, four new tensile coupons were fabricated from each small scale specimen.

Uniaxial tension tests were conducted according to ASTM E8 (*41*) on the tension coupons removed from each specimen. The detailed coupon dimension is shown in Figure 5.13. The test results of uniaxial tension tests are shown in Table 7.3, which includes the yield stress (σ_y), the ultimate stress (σ_t), the percent elongation, and the percent reduction (area).

Figures 7.5, 7.6, 7.7, and 7.8 show the normalized steel material properties (σ_y, σ_t, % elongation, and reduction in area) with respect to the corresponding undamaged steel material properties. Standard deviation error bars on each specimen are also shown in Figures 7.5–7.8.

The results of the uniaxial tension test presented in this section indicate that:

- Damage-repair cycles increased the yield stress of A36 steel (heated to 1200 °F & 1400 °F). Relative to the undamaged specimen, the yield stress of specimens with single damage-repair cycle specimens (Specimens 1 & 5) increased by 2–7%. Similarly for the specimens subjected to the multiple damage-repair cycles (Specimens 2 & 3), the yield stress increased by 19–23%.
- The ultimate strength of all specimens increased from 8% to 14%. But no specific relationships with test variables were found.
- Damage-heat straightening repairs reduced the percent elongation (ductility) of A36 steel. The ductility reduced to approximately 75–94% of the undamaged material.

7.3 Rockwell Hardness and Microstructure Investigations

Rockwell hardness tests were conducted on the Charpy v-notch impact test coupons according to ASTM E18 (*42*). Four points were taken on every specimen. Figure 7.9 shows Rockwell hardness points on one of the Charpy specimens. Table 7.4 shows Rockwell hardness test results and normalized values. Figure 7.10 shows normalized values of the Rockwell hardness test in the order of its magnitude with standard deviation error bars.

The Charpy specimens on which the Rockwell hardness tests were conducted were also used for the microstructure investigations. The Charpy specimen identified as C2 in every small scale specimen was used for the microstructure investigations. The specimens were prepared in accordance to the ASTM E3 (*43*).

The etched specimens were placed under a metallurgical microscope with a photo micrographic camera attached. A magnification of 300x was chosen for determining the grain sizes.

The grain size of each undamaged and damaged-repaired specimen was determined using the general line intercept procedure (Heyn Linear Intercept Procedure) outlined in ASTM E112 (*44*). In this method, a number of random lines are drawn with a known length and the number of grains that intercept each line are counted.

Figure 7.11 shows a photo of the undamaged specimen with twelve intercept lines. Each line represents 0.02 in. in real length. The grain size was measured by dividing the total length of the line (0.02 in.) by the grain numbers intercepting each line. The grain size of each specimen was computed by averaging the grain size of each line.

Microstructures of all specimens are shown in Figures 7.11 through 7.17. Table 7.5 shows the grain

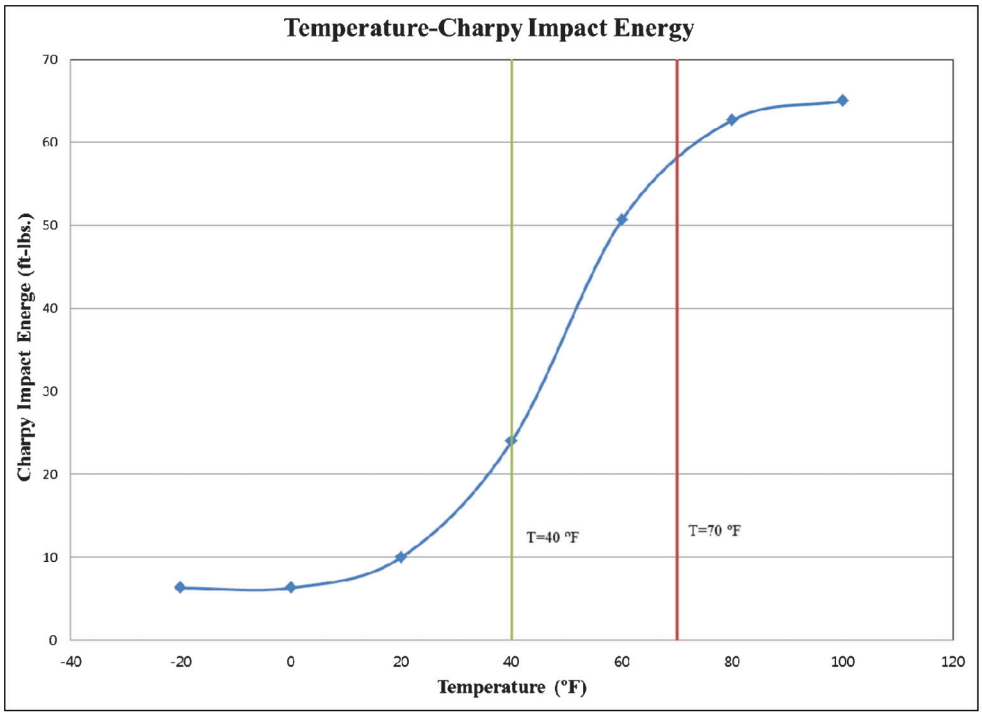

Figure 7.1 Temperature-Charpy impact energy graph of small scale specimen.

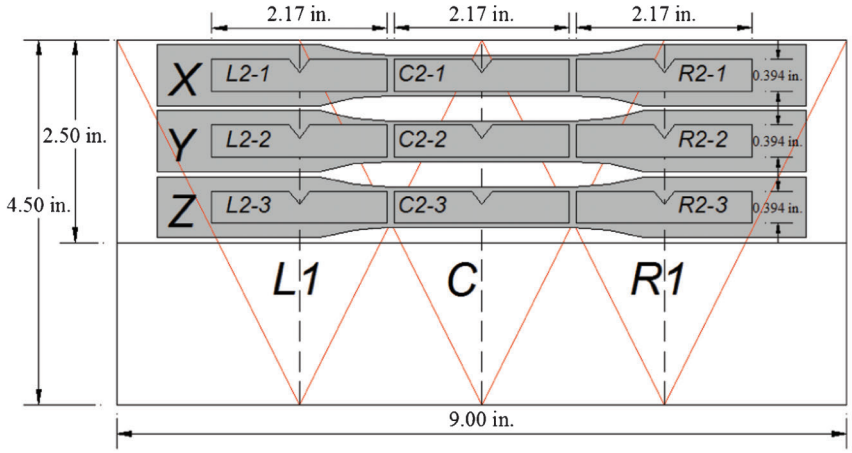

Figure 7.2 Nomenclature and location of new Charpy specimens.

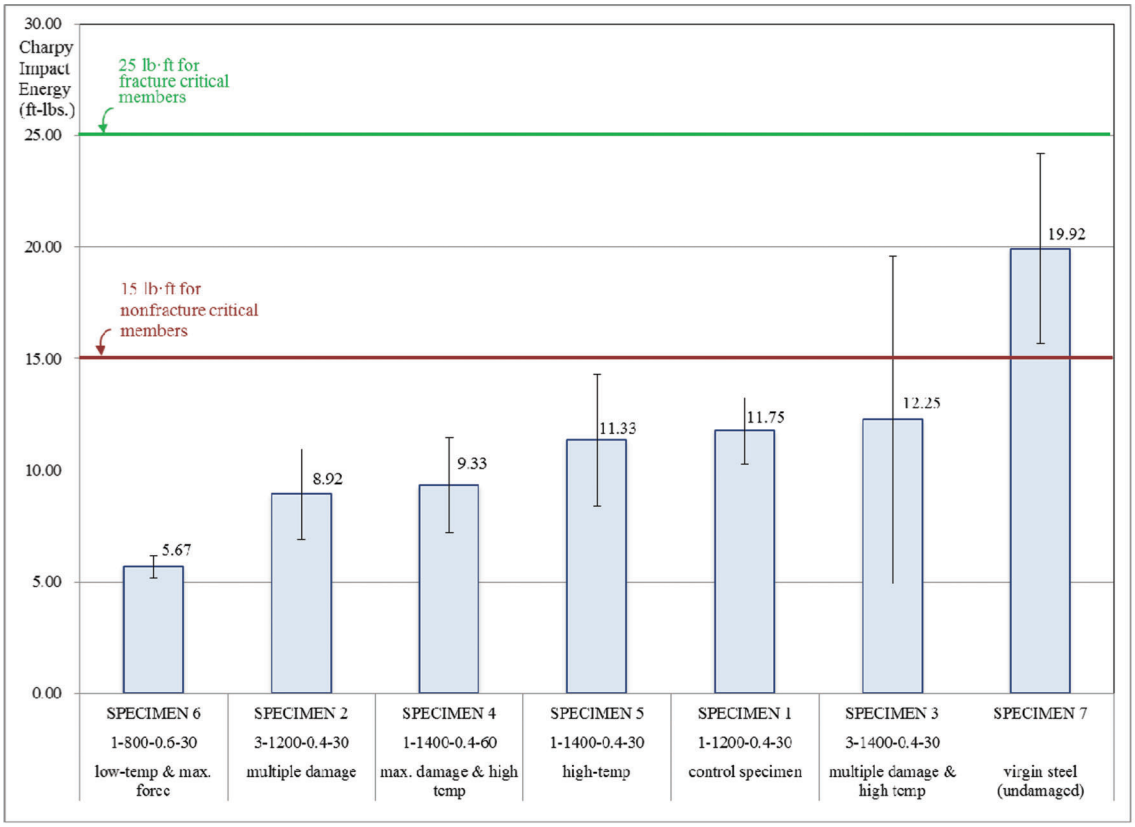

(a) Initial Charpy impact results

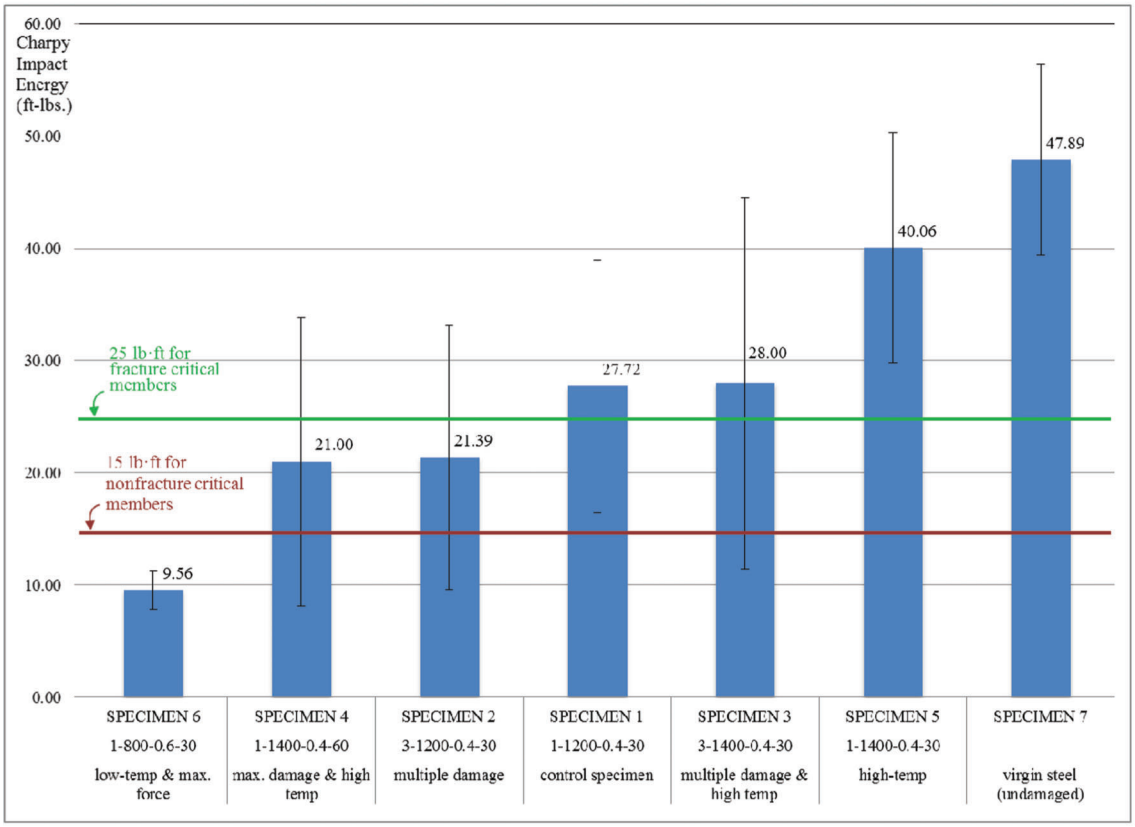

(b) New Charpy impact results

Figure 7.3 Initial and new Charpy impact results comparison.

TABLE 7.2
New Charpy V-notch test results at 70 °F

		Charpy Results (ft-lbs.)		
Specimen Designation	**Location**	**L1**	**C**	**R1**
1-1200-0.4-30	1	42	32.5	32.5
	2	34	31	15
	3	16	37	9.5
	avg.		**27.72**	
3-1200-0.4-30	1	43.5	15	22
	2	20	35	26
	3	9.5	11.5	10
	avg.		**21.39**	
3-1400-0.4-30	1	52	46	44.5
	2	28	13.5	32.5
	3	13.5	10.5	11.5
	avg.		**28.00**	
1-1400-0.4-60	1	35.5	44.5	29.5
	2	11	10.5	23
	3	14.5	10	10.5
	avg.		**21.00**	
1-1400-0.4-30	1	50	40	47
	2	51	41	40
	3	25	22	44.5
	avg.		**40.06**	
1-800-0.6-30	1	9.5	8	7.5
	2	9	8.5	10
	3	12	9	12.5
	avg.		**9.56**	
Virgin steel (undamaged)	1	59	36	62
	2	45	40	50
	3	46.5	42.5	50
	avg.		**47.89**	

TABLE 7.3
Uniaxial tension test results of small scale test

Specimen Designation	Coupon	Yield stress (ksi)	Ultimate stress (ksi)	% Elongation (%)	Reduction in area (%)
1-1200-0.4-30	1-XL	46.31	69.51	36.75	57.27
	1-XR	48.59	69.44	38.30	57.91
	1-YL	47.48	68.95	38.05	60.28
	1-YR	47.67	70.53	33.95	57.00
	avg.	**47.51**	**69.61**	**36.76**	**58.12**
3-1200-0.4-30	2-XL	49.65	72.47	30.80	59.58
	2-XR	50.41	73.46	28.55	53.45
	2-YL	50.73	73.56	30.90	55.62
	2-YR	68.31	75.51	26.70	56.36
	avg.	**54.78**	**73.75**	**29.24**	**56.25**
3-1400-0.4-30	3-XL	59.91	71.20	36.45	59.92
	3-XR	49.79	70.51	39.30	56.96
	3-YL	48.27	71.21	37.35	58.27
	3-YR	54.42	73.51	34.05	56.91
	avg.	**53.10**	**71.61**	**36.79**	**58.02**
1-1400-0.4-60	4-XL	51.09	71.32	37.50	57.24
	4-XR	50.88	69.89	34.45	57.61
	4-YL	65.52	73.15	35.45	54.70
	4-YR	52.20	71.62	31.35	58.02
	avg.	**54.92**	**71.50**	**34.69**	**56.89**
1-1400-0.4-30	5-XL	45.89	71.01	38.80	56.81
	5-XR	47.07	70.95	33.85	55.25
	5-YL	44.82	69.69	34.50	58.82
	5-YR	44.16	70.22	20.35	57.88
	avg.	**45.48**	**70.47**	**31.88**	**57.19**
1-800-0.6-30	6-XR	46.11	71.72	32.90	60.50
	6-XL	47.67	72.49	34.70	55.51
	6-YL	47.94	71.25	34.30	56.83
	6-YR	47.26	71.73	33.30	56.62
	avg.	**47.24**	**71.80**	**33.80**	**57.37**
Virgin steel-undamaged	7-X	43.94	58.77	41.60	55.88
	7-Y	45.37	68.08	39.35	55.91
	7-Z	44.09	67.41	36.65	56.89
	avg.	**44.46**	**64.75**	**39.20**	**56.23**

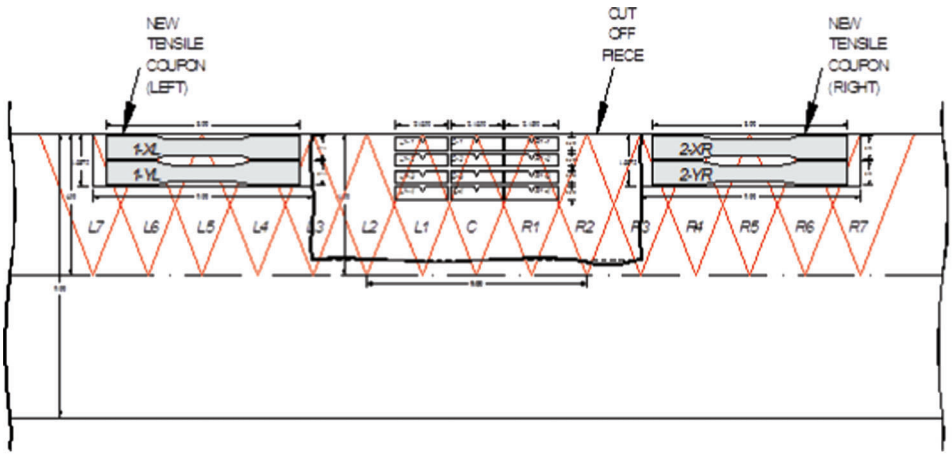

Figure 7.4 Nomenclature and location of new tensile specimens.

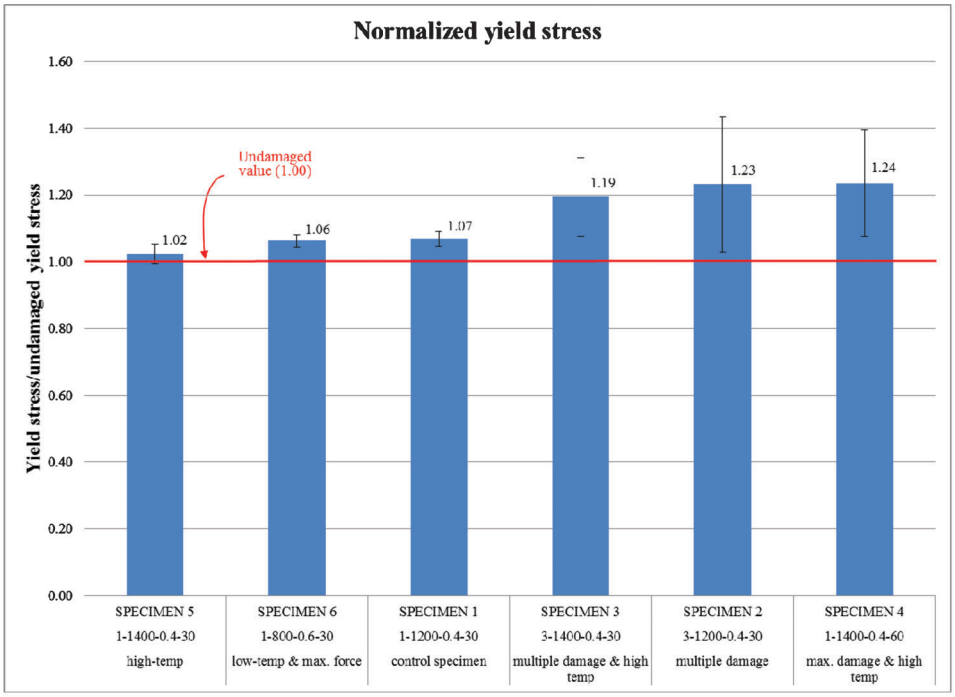

Figure 7.5 Normalized yield stresses of small scale specimens.

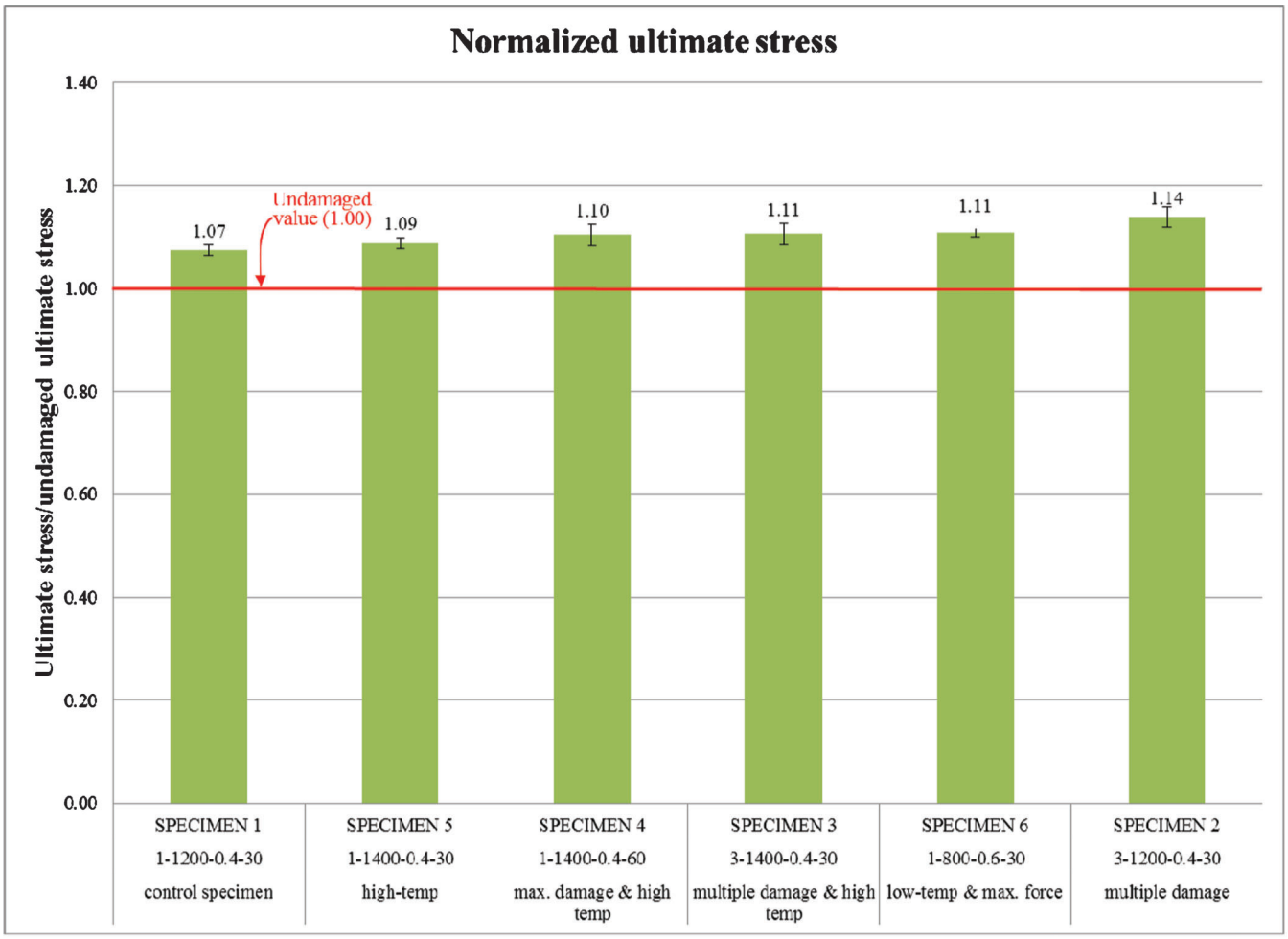

Figure 7.6 Normalized ultimate stresses of small scale specimens.

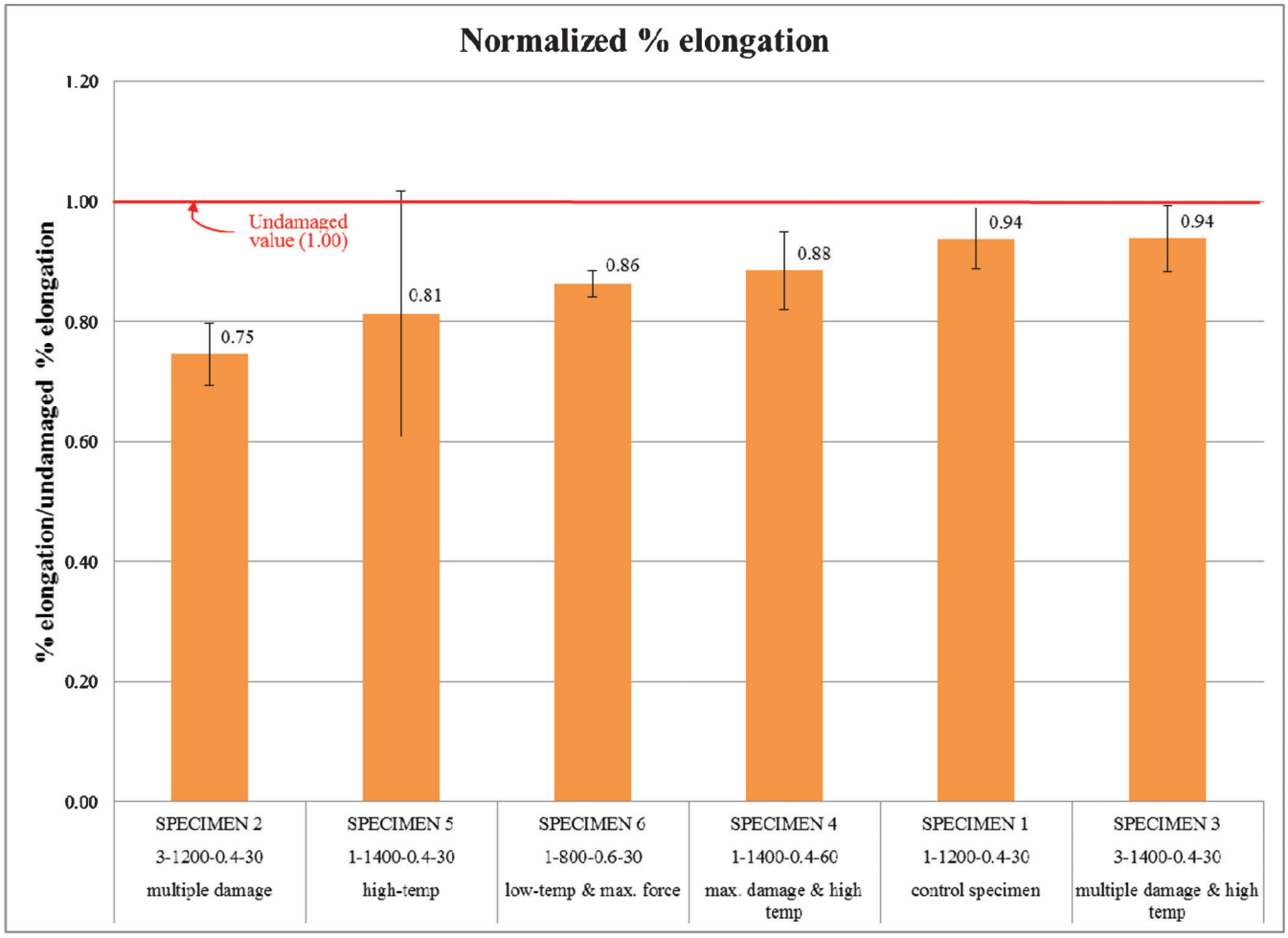

Figure 7.7 Normalized % elongations of small scale specimens.

TABLE 7.4
Rockwell hardness test results of small scale test

Specimen	Coupon	Rockwell Hardness Point				Avg.	Normalized Value
		1	2	3	4		
1-1200-0.4-30	1-C-2	82.7	82.5	80.7	84.5	82.6	1.12
3-1200-0.4-30	2-C-2	84.0	84.2	81.5	81.5	82.8	1.12
3-1400-0.4-30	3-C-2	82.0	80.5	80.5	80.7	80.9	1.10
1-1400-0.4-60	4-C-2	85.5	81.5	87.2	84.0	84.6	1.15
1-1400-0.4-30	5-C-2	82.0	83.5	85.5	87.2	84.6	1.15
1-800-0.6-30	6-C-2	88.0	89.6	89.5	89.7	89.2	1.21
Undamaged	7-C-2	73.2	75.3	73.5	73.0	73.8	1.00

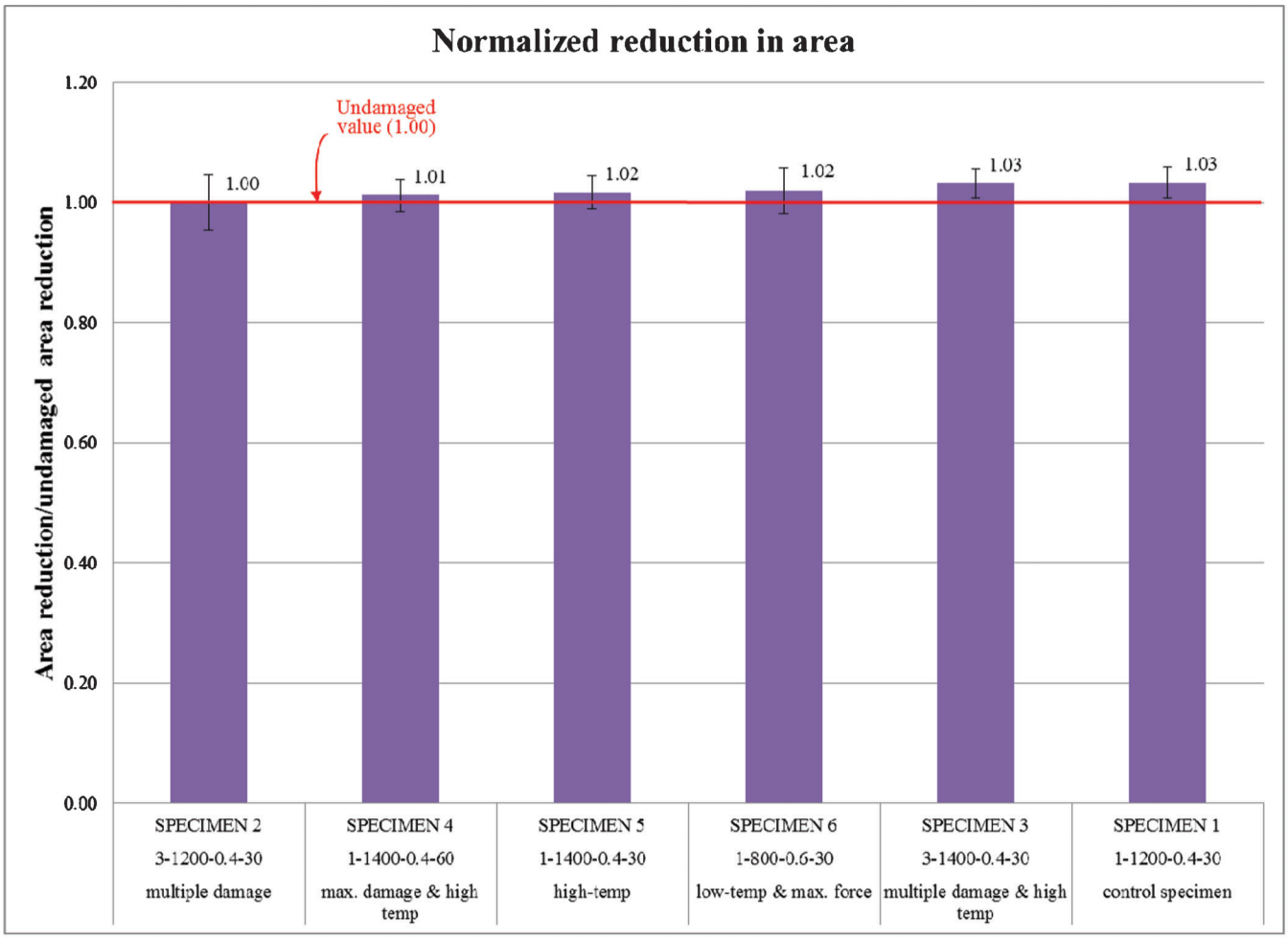

Figure 7.8 Normalized area reductions of small scale specimens.

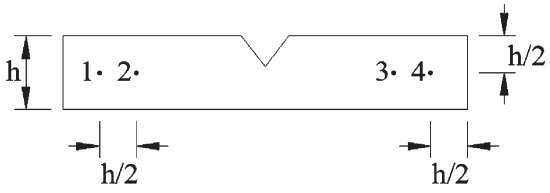

Figure 7.9 Rockwell hardness points.

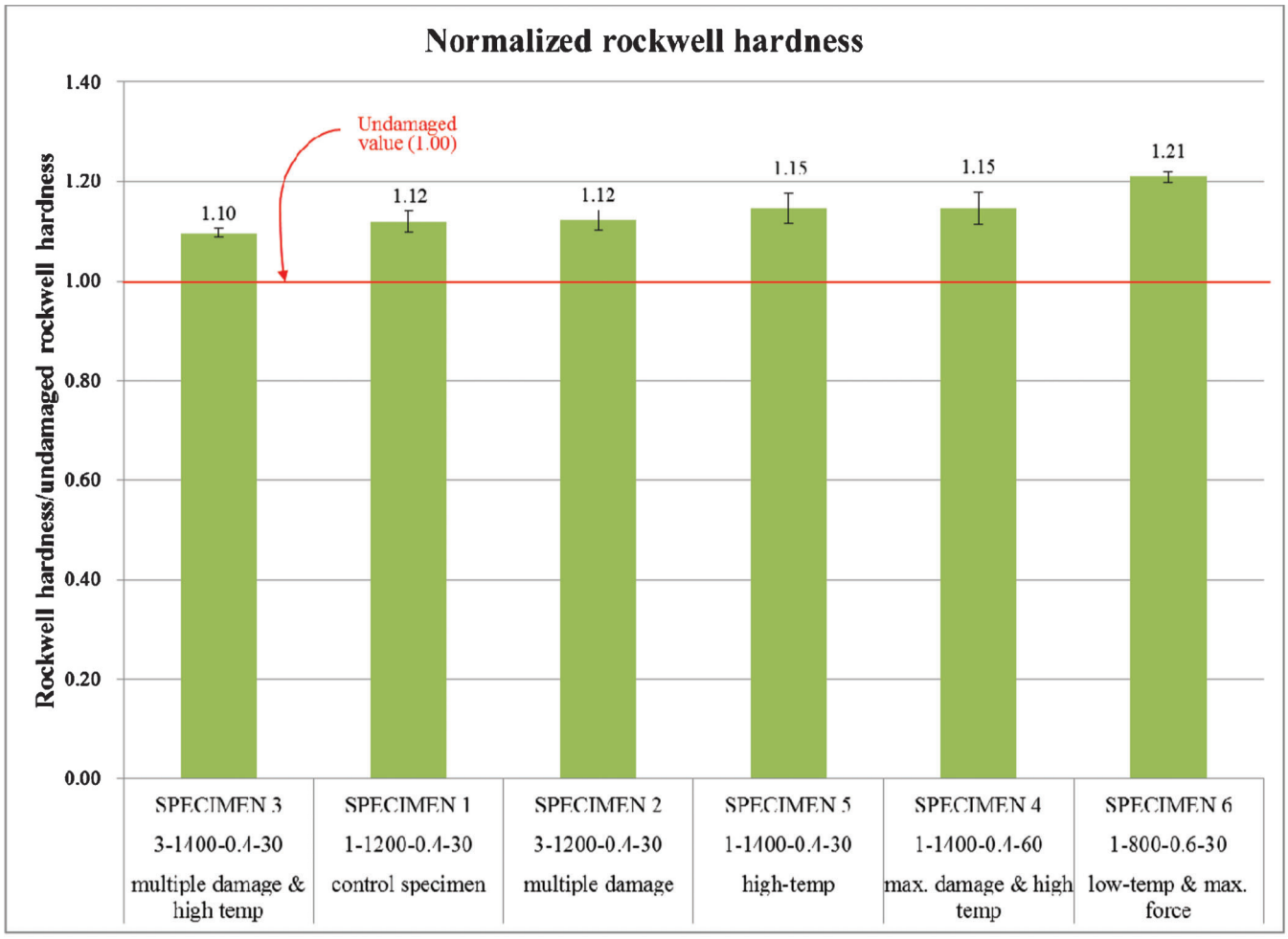

Figure 7.10 Normalized Rockwell hardness of small scale test.

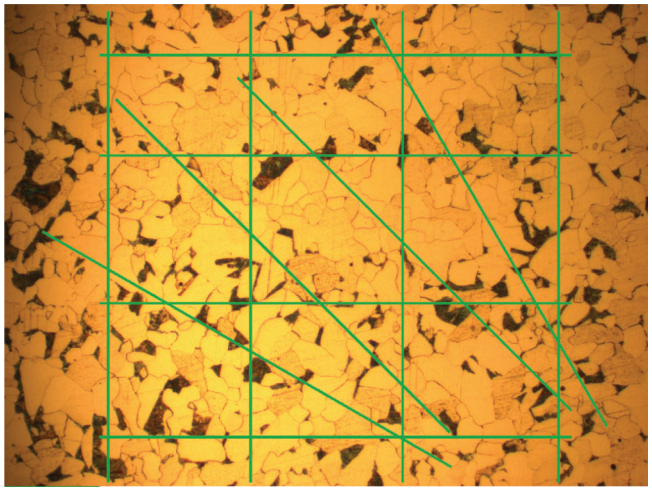

Figure 7.11 Heyn linear intercept procedure on Specimen #7 (undamaged)—300x.

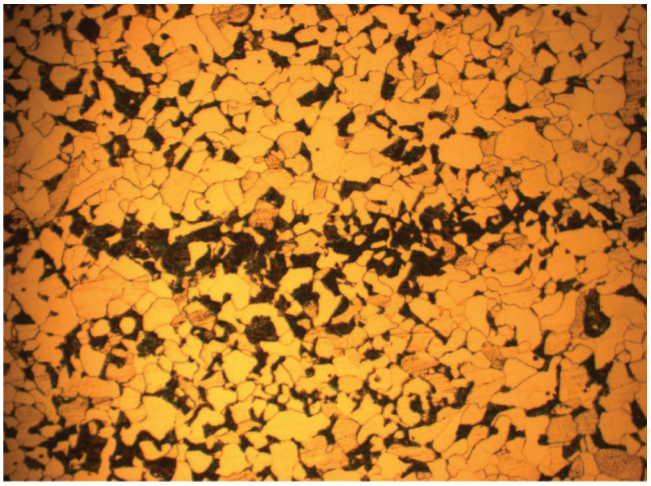

Figure 7.14 Microstructure of Specimen #3 (3-1400-0.4-30)—300x.

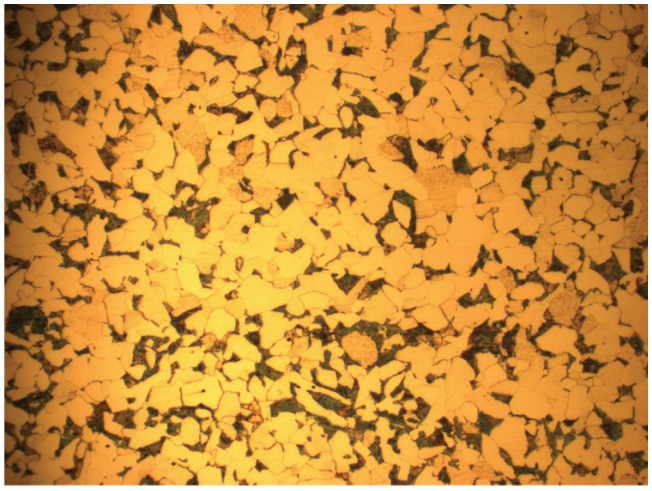

Figure 7.12 Microstructure of Specimen #1 (1-1200-0.4-30)—300x.

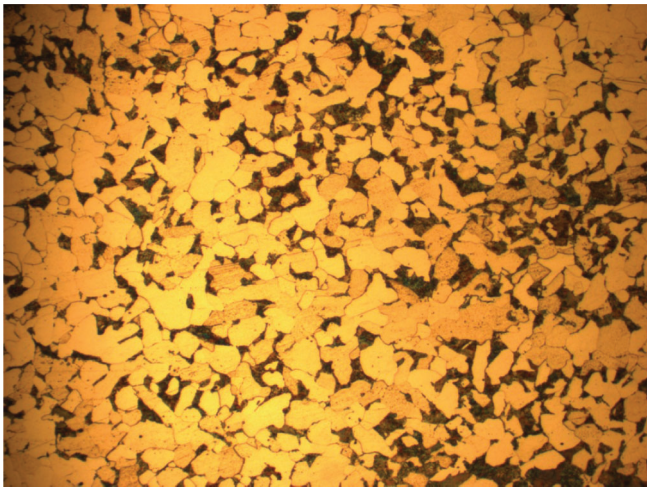

Figure 7.15 Microstructure of Specimen #4 (1-1400-0.4-60)—300x.

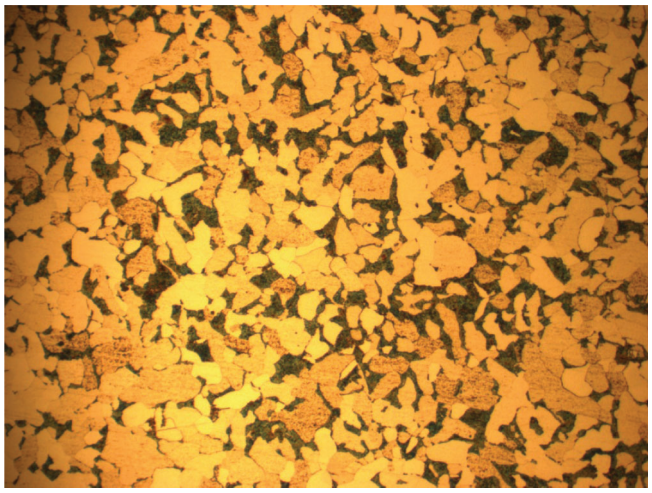

Figure 7.13 Microstructure of Specimen #2 (3-1200-0.4-30)—300x.

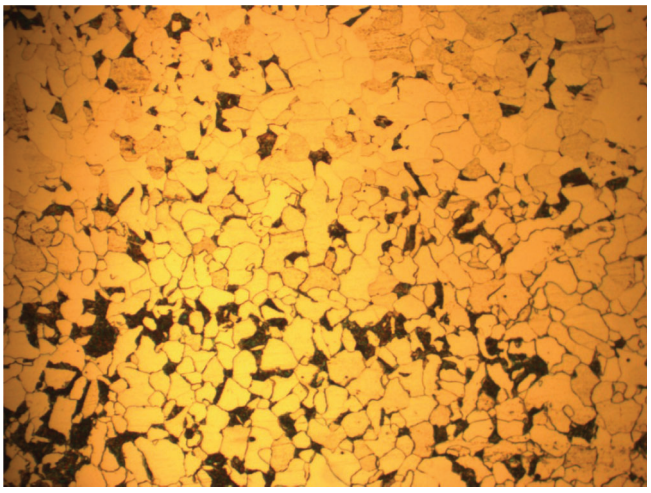

Figure 7.16 Microstructure of Specimen #5 (1-1400-0.4-30)—300x.

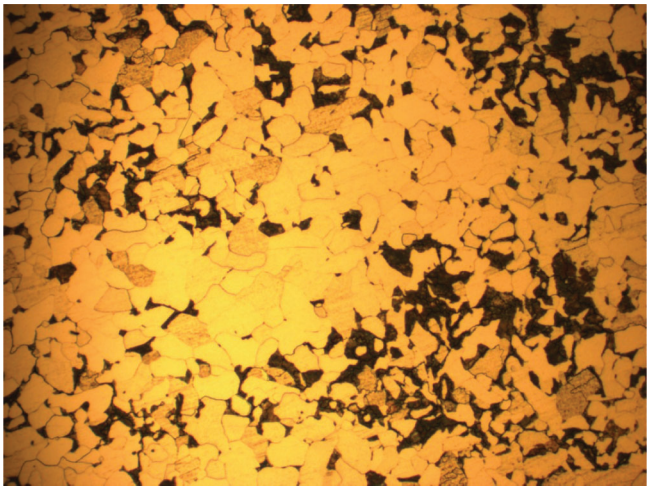

Figure 7.17 Microstructure of Specimen #6 (1-800-0.6-30)—300x.

size and percent pearlite of each specimen. Normalized values of all specimens compared with the undamaged specimen are also shown in Table 7.5. Normalized values with standard deviation error bars are also compared in Figures 7.18 and 7.19.

The data presented in this section indicate the followings:

- The Rockwell hardness of A36 steel was increased in all damage-repaired specimens (10–21%).
- Specimen 1-800-0.6-30 (low temp. & max. restraining force) showed a maximum increase of 21% in Rockwell hardness.
- Microstructure investigations indicated that brittle materials like bainite or martensite were not generated during heat straightening.
- Damage-repair cycles decreased the grain size of A36 steel to 86–99% of the undamaged material.
- The grain size decreased less when using multiple damage-repair cycles.
- Overheating did not show a clear relationship with the grain size.
- The percent pearlite of A36 steel decreased to 75–99% of the undamaged steel.
- The impact of multiple damage-repair cycles and overheating to the percent pearlite of A36 steel did not have any clear trend.

7.4 Chemical Composition Analysis

Chemical composition of A36 steel used for the small scale specimen was determined according to ASTM E415 (*45*). The chemical composition of undamaged steel was measured three times to get more accurate results. Table 7.6 presents the chemical composition of the undamaged small scale test specimen. In Table 7.6, the chemical requirements of ASTM A36 (*46*) steel (same as AASHTO M270 requirements) are also shown. As seen in the table, all three test results are very similar to each other and also meet the ASTM A36 requirements.

From the chemical composition of the steel, the eutectoid temperature (A_{c1}) and the stable austenite temperature (A_{c3}) can be determined by the empirical equations.

A_{c1} is the lower phase transition temperature where the body centered cubic molecular structure begins to assume a face centered cubic form. When the heated steel cools below the A_{c1} temperature, the steel tries to return to a body centered structure. This process requires sufficient time to complete. Therefore, fast cooling may not allow the steel to complete this process (phase change) and may cause martensite which is a hard and brittle phase of steel (*28*). As recommended in many heat straightening guidelines, the maximum heating temperature of 1200 °F was decided with about 150 °F safety margin from the A_{c1} temperature to avoid the formation of martensite which may cause reduced ductility and fatigue resistance.

A_{c3} is the upper phase transition temperature where the molecular change in structure is complete. This is the temperature where the steel changed to a uniform solution called austenite. Between the A_{c1} and A_{c3} temperature, hot rolling and hot working can be possible.

The following equations can predict the A_{c1} and A_{c3} temperatures using the percent component of the chemical elements:

Krauss (*47*):

$$A_{c1}[^{\circ}C] = 723 - 10.7(\%Mn) - 16.9(\%Ni) + 29.1(\%Si) + 16.9(\%Cr) + 290(\%As) + 6.38(\%W) \quad (7.1)$$

TABLE 7.5
Microstructure investigation results of small scale test

		Average Grain Size		% Pearlite	
Specimen	**Coupon**	**Real Value (in.)**	**Normalized Value**	**Real Value (%)**	**Normalized Value**
1-1200-0.4-30	1-C-2	0.000672	0.86	27.415	0.96
3-1200-0.4-30	2-C-2	0.000771	0.99	22.533	0.79
3-1400-0.4-30	3-C-2	0.000731	0.94	22.177	0.78
1-1400-0.4-60	4-C-2	0.000739	0.95	26.495	0.93
1-1400-0.4-30	5-C-2	0.000692	0.89	21.360	0.75
1-800-0.6-30	6-C-2	0.000763	0.98	27.125	0.95
Undamaged	7-C-2	0.000778	1.00	28.491	1.00

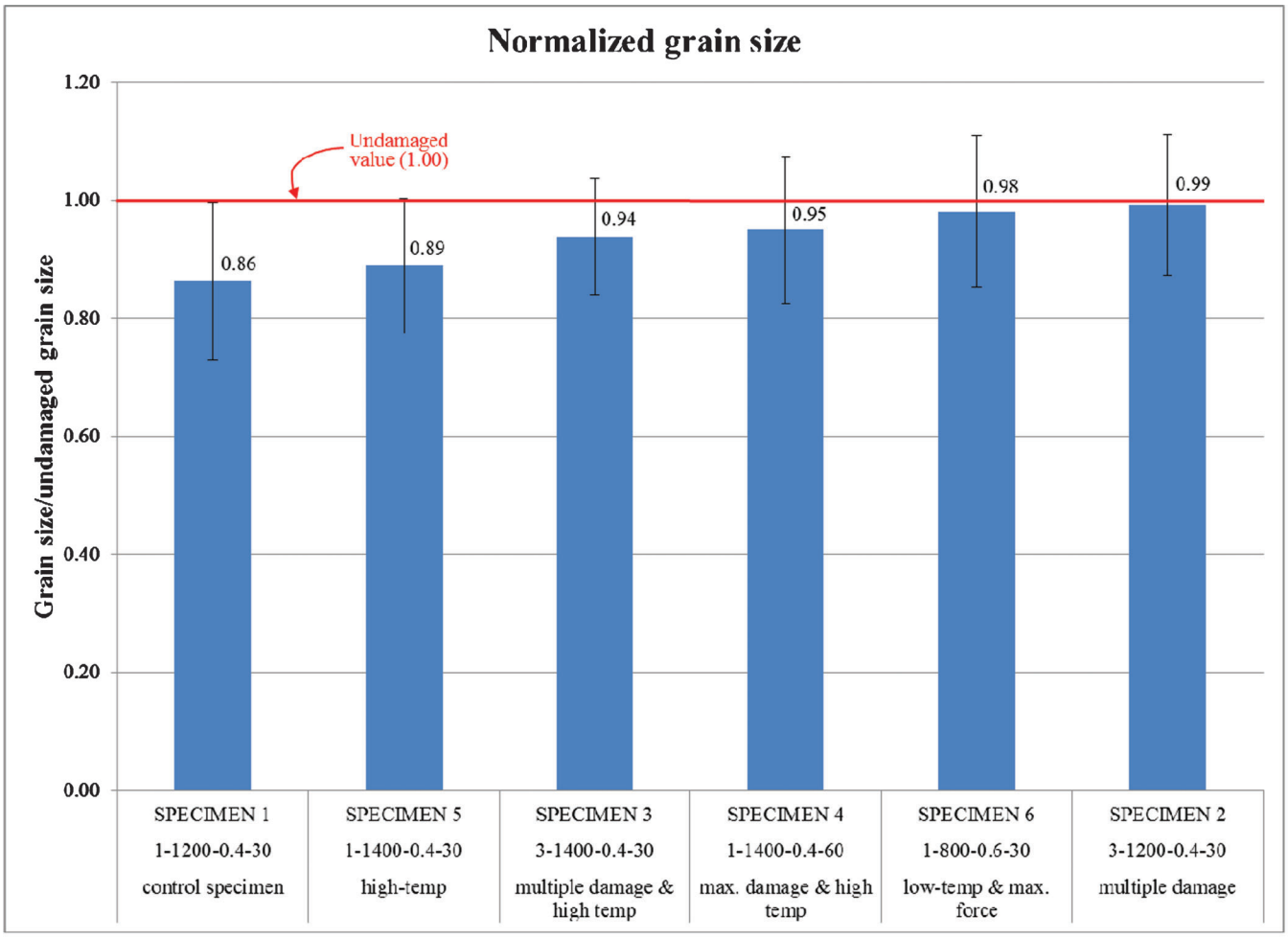

Figure 7.18 Normalized grain size of small scale test.

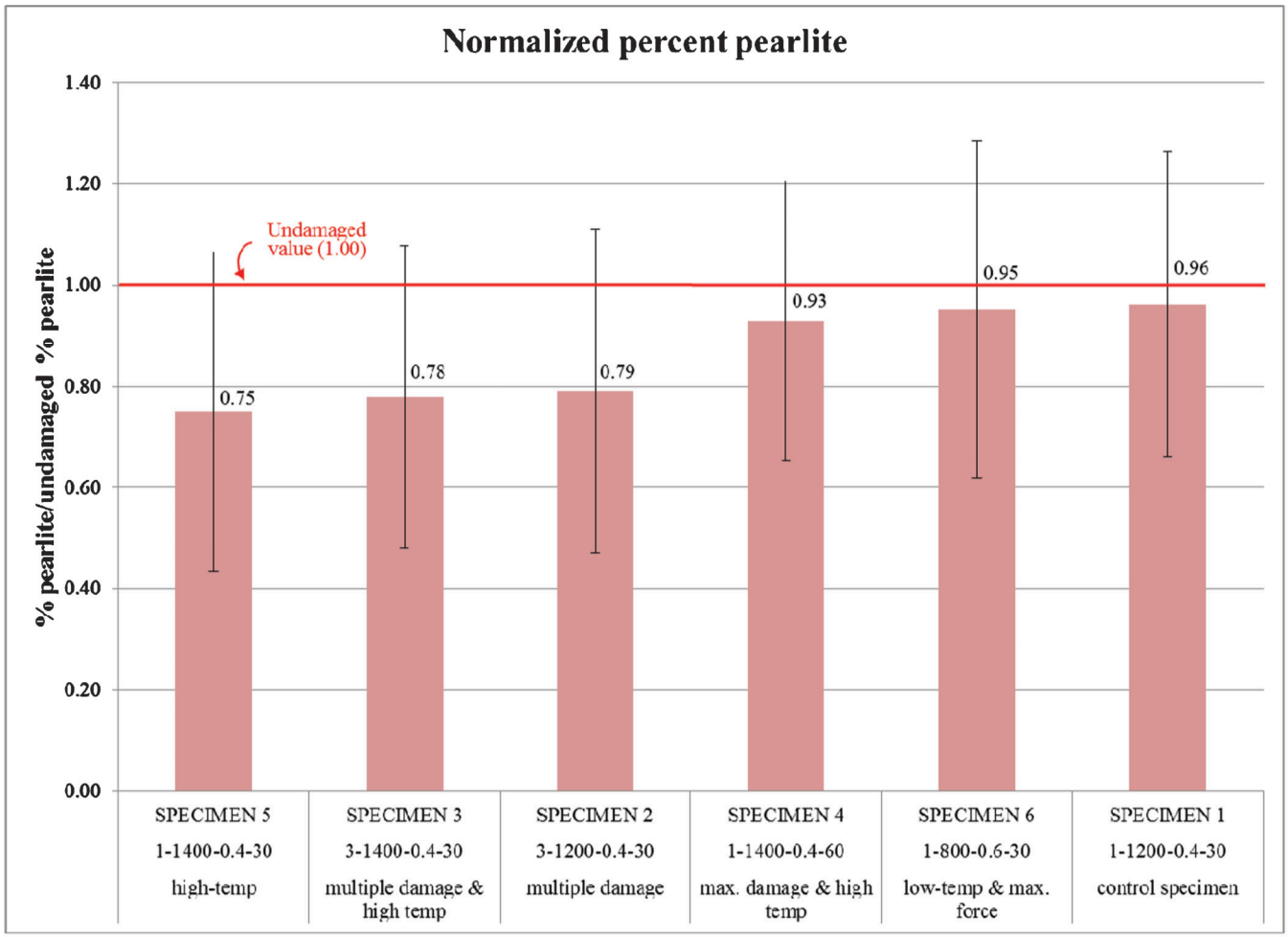

Figure 7.19 Normalized percent pearlite of small scale test.

$$A_{c3}[^{\circ}C] = 910 - 203\sqrt{(\%C)} - 15.2(\%Ni) + 44.7(\%Si) + 104(\%V) + 31.5(\%Mo) + 13.1(\%W) \quad (7.2)$$

Trzaska and Dobrzan'ski (*48*):

$$A_{c1}[^{\circ}C] = 739 - 22.8(\%C) - 6.8(\%Mn) + 18.2(\%Si) + 11.7(\%Cr) - 15(\%Ni) - 6.4(\%Mo) - 5(\%V) - 28(\%Cu) \quad (7.3)$$

$$A_{c3}[^{\circ}C] = 937.3 - 224.5\sqrt{(\%C)} - 17(\%Mn) + 34(\%Si) - 14(\%Ni) + 21.6(\%Mo) + 41.8(\%V) - 20(\%Cu) \quad (7.4)$$

TABLE 7.6
Chemical composition of small scale test steel

	Small Scale Test			ASTM A36 (AASHTO M270)
	Test 1	Test 2	Test 3	
C	0.190	0.190	0.190	Max 0.25
Cb	0.003	0.002	0.002	
Cr	0.075	0.080	0.080	
Cu	0.250	0.210	0.210	
Mn	0.540	0.510	0.500	
Mo	0.037	0.054	0.054	
Ni	0.100	0.100	0.100	
P	0.010	0.010	0.010	Max 0.04
S	<0.01	0.010	0.010	Max 0.05
Si	0.040	0.040	0.040	Max 0.4
V	0.003	0.004	0.004	

TABLE 7.7
A_{c1} & A_{c3} temperatures of small scale test

		Small Scale Test		
		Test 1	Test 2	Test 3
Krauss (*47*)	**A_{c1} [°F]**	1330.0	1331.1	1331.4
	A_{c3} [°F]	1588.5	1591.0	1591.7
Trzaska & Dobrzan'ski (*48*)	**A_{c1} [°F]**	1339.0	1341.9	1341.6
	A_{c3} [°F]	1613.7	1614.1	1614.8

The computed A_{c1} and A_{c3} values are presented in Table 7.7. As seen in Table 7.7, empirical equations of A_{c1} & A_{c3} from different researchers showed results similar to each other.

8. LARGE SCALE TEST: DESCRIPTION

The large scale test focuses on experimental investigations to evaluate the effects of realistic heat straightening with imperfections on the condition and serviceability of a steel beam bridge.

This chapter presents detailed description of the test matrix, test setup and instrumentation, and test procedure for the large scale test. The large scale test bridge was constructed following the findings from the INDOT database analysis in Chapter 4.2. The large scale tests were conducted using: (a) A36 W30x90 steel beams for the main bridge girder, (b) full composite continuous bridge, (c) 20 ft. span length (equivalent to the cross beam distance), (d) 8 in. concrete slab thickness, and (e) 30 ε_y of maximum damage strain (ε_d).

Section 8.1 includes the design procedure for the test bridge. Detailed descriptions of the test matrix, test setup, and test instrumentations are presented in Sections 8.2–8.4. The large scale test procedure is described in Sections 8.5–8.6.

8.1 Large Scale Bridge Design

A large scale test setup was designed following the AASHTO bridge specification (2007). A fully composite steel beam bridge using W30x90 rolled beams with an 8 in. concrete slab was fabricated to be damaged and repaired by the heat straightening repair process, while incorporating typical imperfections observed in the field.

As shown in Figure 8.1 (a), two W30x90 rolled beams were used as main girders of the test bridge and W20x57 rolled beams were used as cross beams (diaphragm) with 20 ft. spacing. Figure 8.1 (b) shows sectional details of the large scale bridge specimen. ¾ in. diameter A325 bolts were used for the web-to-girder connection. ¾ in. diameter with 4 in. length shear studs were distributed along the main girder direction with 5 in. spacing to develop composite section behavior.

Figure 8.2 shows reinforcement drawings at the positive and negative moment regions and the drawing

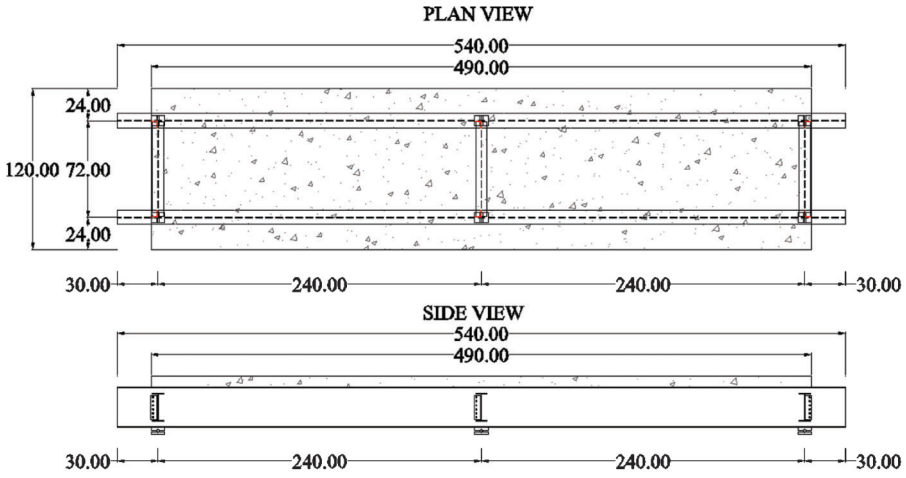

(a) Plan and side view of large-scale specimen

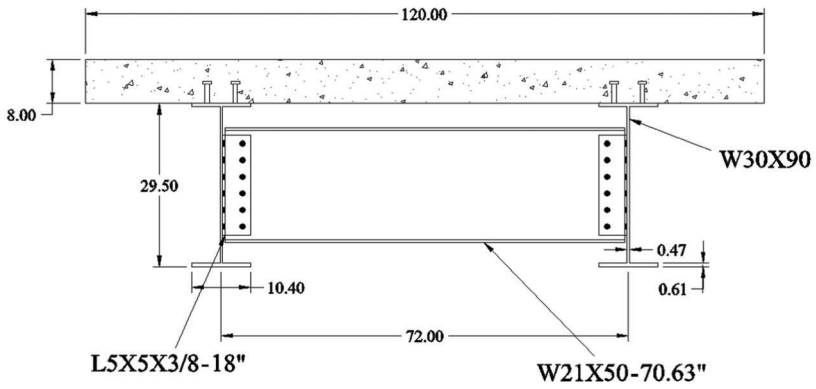

(b) Sectional view of large-scale specimen

Figure 8.1 Drawings of large scale specimen.

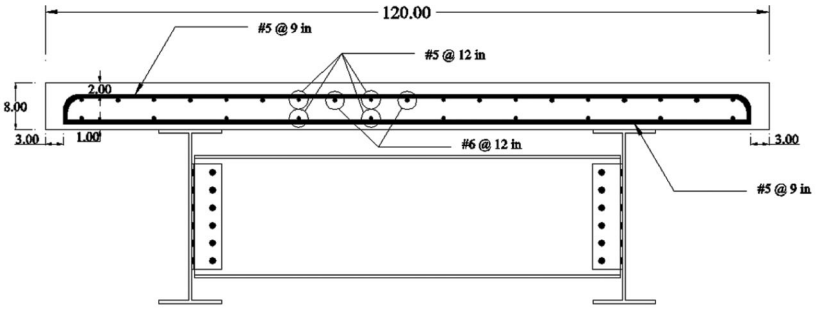

(a) Negative region reinforcement drawing

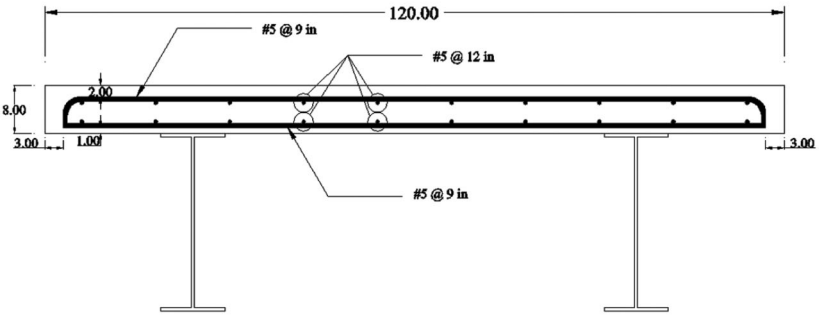

(b) Positive region reinforcement drawing

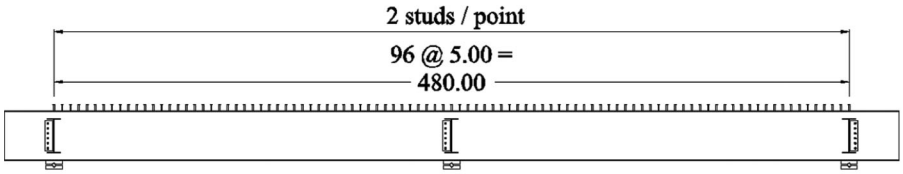

(c) Shear stud distribution

Figure 8.2 Slab reinforcements and shear stud drawings.

of shear stud distribution. #5 steel rebar with 9 in. spacing were placed as the main reinforcement in the transverse direction. In the positive moment region, #5 bars with 12 in. spacing were used as longitudinal reinforcement. In the negative moment region, #6 rebars with 12 in. spacing were added between the top #5 longitudinal bars. All these rebars satisfied the AASHTO 2007 specification for slab reinforcement design requirements. Normal weight concrete with 4000 psi compressive strength (f'_c) was used for the slab.

8.2 Large Scale Test Matrix

Similar to the small scale test, the damage and repair parameters considered in the large scale test were: (a) the damage magnitude, (b) the restraining force, (c) the maximum heating temperature, and (d) the number of multiple damage-repair cycles.

Each test parameter included the following variations:

a. **Damage magnitude.** Following the findings from the INDOT heat straightening database analysis (Chapter 4), thirty times of yield strain (30 ε_y) was used for the maximum damage magnitude in all of the test specimens.
b. **Damage and repair cycles.** The FHWA guidelines (1998) (*28*) recommended a maximum of two times of damage and repair cycles at the same damage region. Otherwise, three times of damage and repair cycles for A36 steel was suggested in the previous research by Varma and Kowalkowski (2004) (*8*). Therefore, for comparison, three times of damage-repair cycles were used in two specimens.
c. **Restraining moment.** Restraining force which can cause less than 50% of the plastic moment was recommended in the FHWA guidelines (1998) (*28*) to prevent unexpected yielding during the heating process. To follow this recommendation, a restraining force equal to 40% of the plastic moment (0.4 M_p) was used for most of the specimens. Restraining force causing 60% of M_p was applied in one specimen to see the effect of overstraining.
d. **Maximum temperature.** The maximum heating temperature applied during the repair process was 1200 °F in the normal-heating specimen. 1400 °F and 800 °F were used for overheating and underheating cases.

Figure 8.3 shows specimen designation for each test specimen. Designation "S" means southern span and "N" means northern span of the test bridge. "1" means eastern girder and "2" means western girder of the test bridge. For example, S1 means the specimen located at the southeast side of the test bridge.

The test matrix for the large scale test is shown in Table 8.1. Each large scale specimen is identified by its name in Table 8.1. Table 8.1 also presents the damage-repair histories.

8.3 Large Scale Test Setup

Two portal frames made up of one A572 Gr 50 W24x103 beam and two A572 Gr 50 W12x53 columns were fabricated to apply midspan serviceability loadings. These frames were also designed to provide reactions to the lateral damage and repair forces of the main bridge girders. To achieve a proper height for the heat straightening process, concrete blocks (24 in. x 27 in. x 42 in.) were fabricated and placed underneath the portal frames. Figures 8.4 and 8.5 show the details of the portal loading frames.

A specially designed loading frame shown in Figure 8.6 was used to apply damaging force at the bottom flange located at the midspan of each specimen. As shown in Figure 8.6, two 100 ton hydraulic actuators applied damaging force to the main girders of the test bridge. One end of the upper hydraulic actuator was pin connected to the loading beam composed of a 2 in. diameter semicircular shaft and ¾ in. thickness plate. The other end was also pin connected to the loading frame to eliminated unexpected bending moments during the damaging process. The extension of the upper hydraulic actuator mainly applied damaging force to the bottom flange of the main girders. The other actuator attached to the lower side of the damaging system was controlled to keep the loading beam perpendicular to the laboratory floor. By keeping the loading beam perpendicular to the ground floor, damaging force could be applied parallel to the ground.

A572 Gr 50 steel was used for all specially designed structures including loading beam, pin connection components, and the reaction base for the lower actuator. A325 structural bolts and nuts were used to connect the damaging system and the loading frame.

During the heat straightening process, a specially designed restraining system shown in Figure 8.7 was used to apply restraining force to the damaged point of each specimen. As shown in Figure 8.7, the restraining system was composed of a restraining grip, connection chain, and hydraulic actuator. Restraining force was applied to the damaged bridge specimen by a specially designed restraining grip which was connected to the 100 ton hydraulic actuator through ⅝ in. shackles (10 kip capacity) and ⅝ in. chains (18 kip capacity).

The restraining grip was made up of four 6 × 6 × ½ (A572 Gr50 steel) angles and two 1 in. thickness steel bars (A572 Gr 50 steel). As shown in Figure 8.7, the restraining grip was fabricated to provide Vee heating region within the grip distance. 6 × 6 × ½ angles were bolted to the 1 in. thickness steel bars with a 15 in. gap distance between the angles to expose the plastically deformed region of the bottom flange for Vee heat application.

Six specially designed built-up counter blocks provided lateral reaction to the test bridge during the damage and repair process. Each block was fabricated from 0.75 in thickness steel plates (A572 Gr 50 steel)

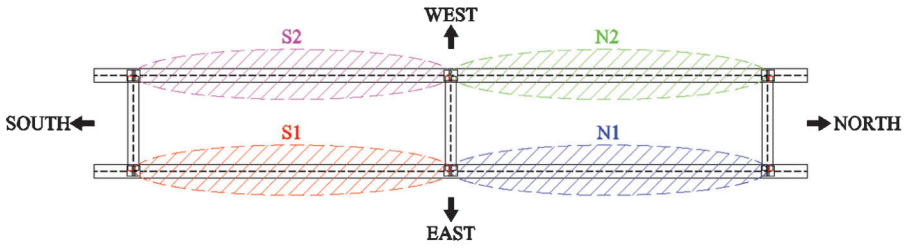

Figure 8.3 Specimen designation.

TABLE 8.1
Large scale test matrix

Specimen Name	Span Name	Cycle (Number)	Damage Strain (ε_d)	Restraining Moment (M_r)	Maximum Temperature (T_{max})	Comment
3-1400-0.4-30	S1	3	30 ε_y	0.40 M_p	1400 °F	Effects of multiple damage-repair cycles & overheating
1-1400-0.4-30	S2	1	30 ε_y	0.40 M_p	1400 °F	Control specimen (overheating)
3-1200-0.4-30	N1	3	30 ε_y	0.40 M_p	1200 °F	Effects of multiple damage-repair cycles
1-800-0.6-30	N2	1	30 ε_y	0.60 M_p	800 °F	Effects of overstraining & underheating

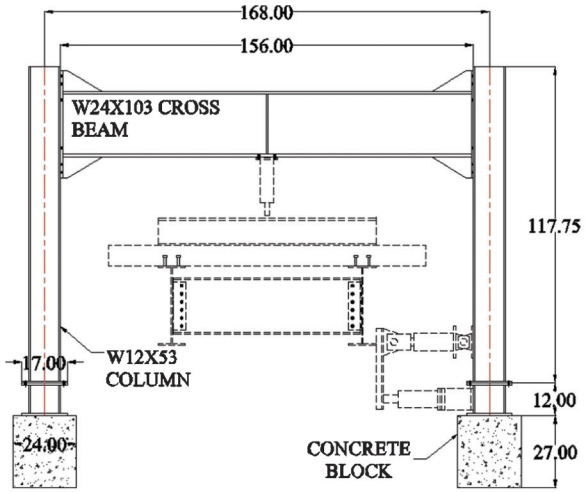

Figure 8.4 Dimensions of the loading frame.

and post-tensioned to the laboratory floor with a total force of 240 kips. Assuming that the friction coefficient (μ) between the concrete and steel is 0.3, each counter block could provide 72 kips of the lateral reaction force. Figure 8.8 shows the detailed drawing and the location of the counter blocks.

Photographs of the large scale test bridge in each construction stage are shown in Figure 8.9. The large scale test bridge was constructed as follows: (i) steel members (main girders and cross beams) were assembled on the laboratory floor and lifted up on the abutment blocks (Figure 8.9 (a)), (ii) slab formworks were attached to steel members and steel reinforcements (including shear studs) were placed at the designed position (Figure 8.9 (b)), (iii) 4000 psi concrete was cast and cured (Figure 8.9 (c)), and (iv) other test setups including loading frames and counter

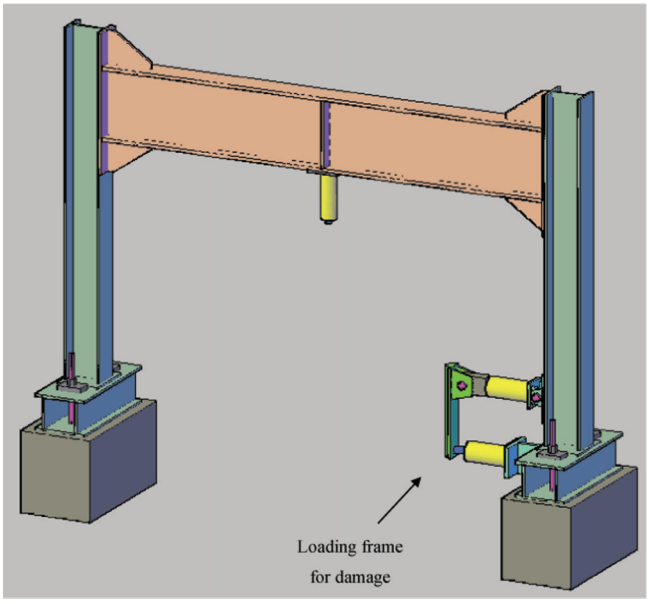

Figure 8.5 Loading frame detail.

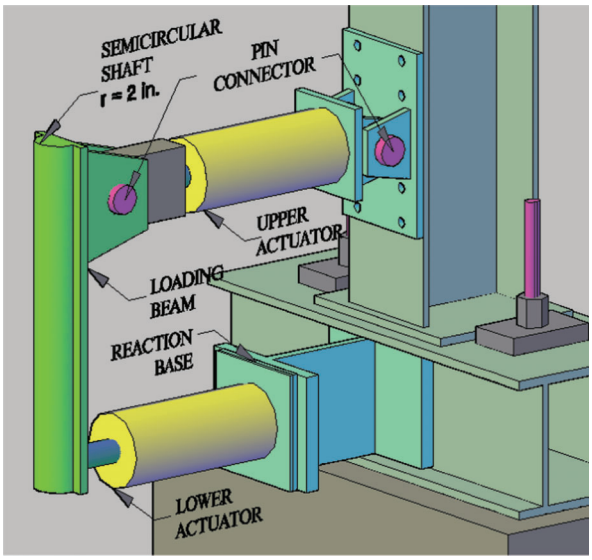

Figure 8.6 Plan of the damaging system.

blocks were placed and post-tensioned to the laboratory floor (Figure 8.9(d)).

Six concrete cylinders (6 in. x 12 in.) were cast from the same concrete mix used for the bridge slab. Actual concrete compressive stresses (f'_c) at 28 days are presented in Table 8.2. The average compressive strength of concrete (f'_c) was 5400 psi, which was 35% larger than 4000 psi of designed concrete compressive strength.

8.4 Large Scale Instrumentation

Instruments (sensors) used for the large scale test include: (a) pressure transducers for force measurement, (b) displacement transducers for measuring vertical and lateral deflections, (c) rotation meters for measuring span end rotations, (d) an infrared thermometer for temperature measurement, and (e) strain gages for strain measurement.

Figure 8.10 shows sensor layouts for the large scale test when the S1 specimen was damaged and repaired. As seen in Figure 8.10, compared with other specimens, additional sensors were added to the test specimen (S1) to measure the detailed behavior of the test specimen during the damage and repair process.

Each sensor was named after its type and location. Figure 8.11 shows the naming rules of the sensors for the large scale bridge test.

Pressure Transducers

The force applied by each hydraulic actuator in every test stage was measured using pressure transducers attached to the hydraulic network. The force to damage and repair the bridge specimen was applied using a 100 ton capacity hydraulic actuator. The applied load was computed as the measured pressure from the pressure transducer multiplied by the effective cylinder area of

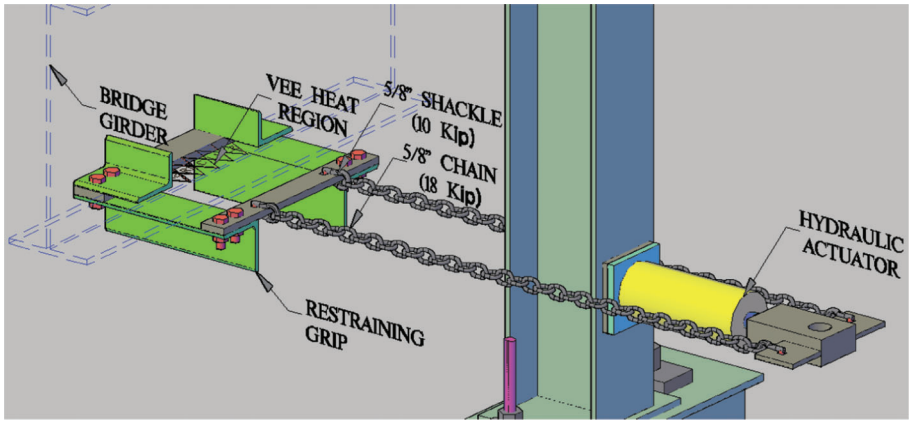

Figure 8.7 Plan of the restraining system.

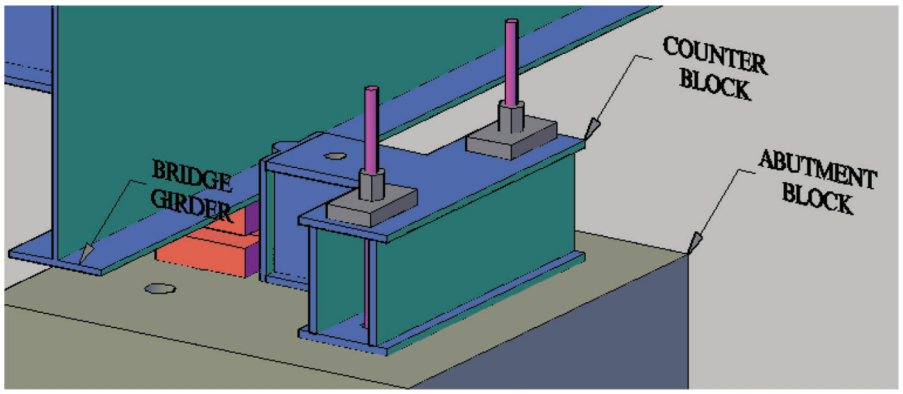

(a) Counter block detail

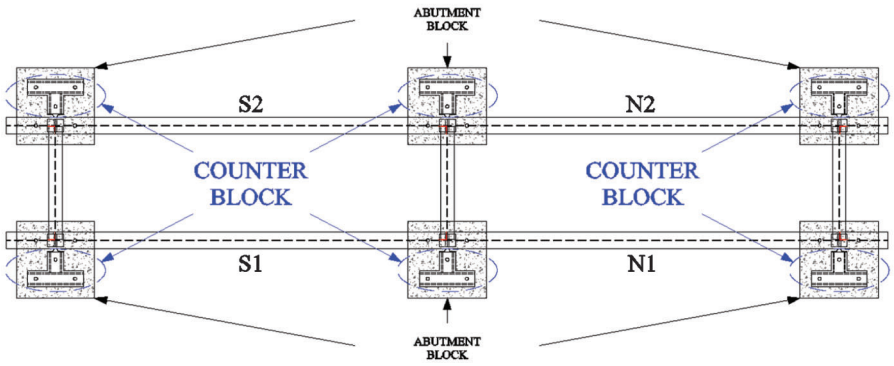

(b) Counter block location

Figure 8.8 Plan of the counter block.

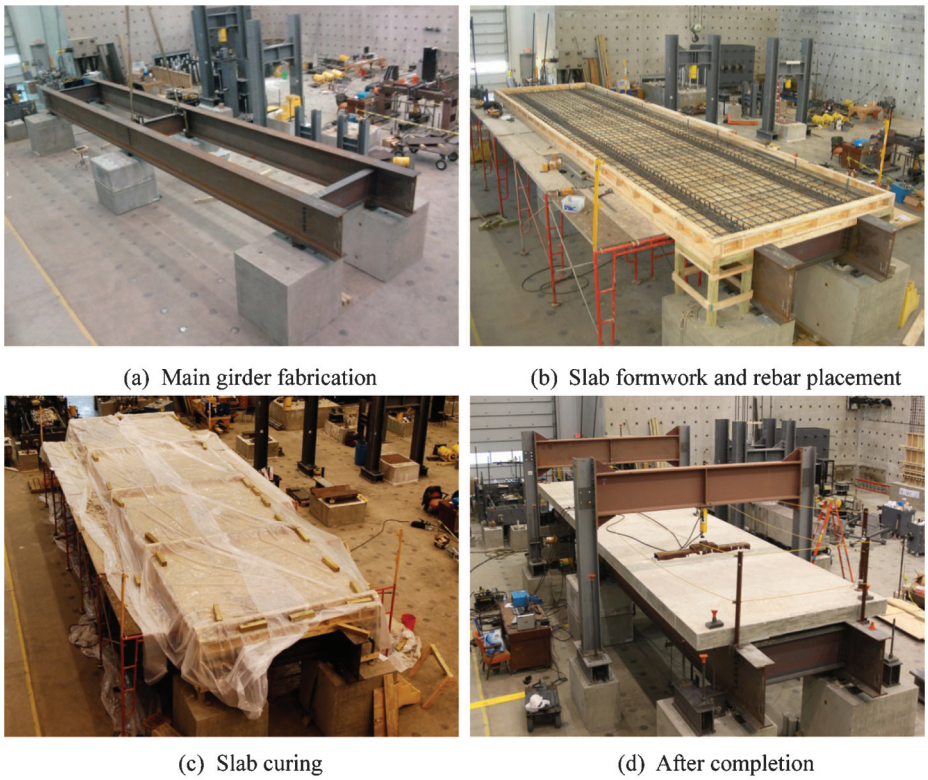

(a) Main girder fabrication (b) Slab formwork and rebar placement

(c) Slab curing (d) After completion

Figure 8.9 Large scale test bridge construction.

the actuator specified by the manufacturer (20.57 in^2). A 50 ton capacity hydraulic actuator was used to apply loads to check the serviceability performance of the large scale test bridge. The force applied by the 50 ton capacity hydraulic actuator was calculated by multiplying the measured pressure with manufacturer specified effective cylinder area of 11.81 in^2.

Strain Gages

Several strain gages were used to measure the strains in the tested bridge specimen during the first damage cycle of each specimen. Figure 8.10 shows the detailed location of the strain gages attached to the tested specimen. As shown in Figure 8.10, three strain gages were bonded to the inside (tension side) of the tested specimen. The strain gage bonded at the midspan of the tested specimen was used to monitor the damage strain (ε_d) during the first damage cycle of each specimen. Four strain gages were bonded to the outside of the tested specimen to monitor the behavior of the test specimen during the damage process.

TABLE 8.2
Strength of the slab concrete at 28 days

Cylinder Specimen	Concrete Strength at 28 Days f'_c (psi)
1	5276
2	5253
3	4984
4	5717
5	5528
6	5643
Avg.	**5400**

Clinometers (Rotation Meters)

The rotations of each span (specimen) were measured by two rotation meters, where two rotation meters were placed at 40 in. (⅙ of the span length) from the bridge supporting bearings. The main purpose of these rotation meters was to compare the serviceability of the test bridge in each test stage. However, the rotations of all specimens during the service load application were too small to be measured by the rotation meters. Therefore the measured rotations did not show a clear difference between each test process and were neglected.

Displacement Transducers

Displacement transducers were used to measure the vertical and lateral deflections of the bridge specimen during all test stages. Figure 8.10 shows the detailed locations of all displacement transducers. During the damage and repair process, lateral deflections were monitored and recorded to see the behaviors of the test specimen, while vertical deflections were mainly used to check the serviceability performance of the test bridge

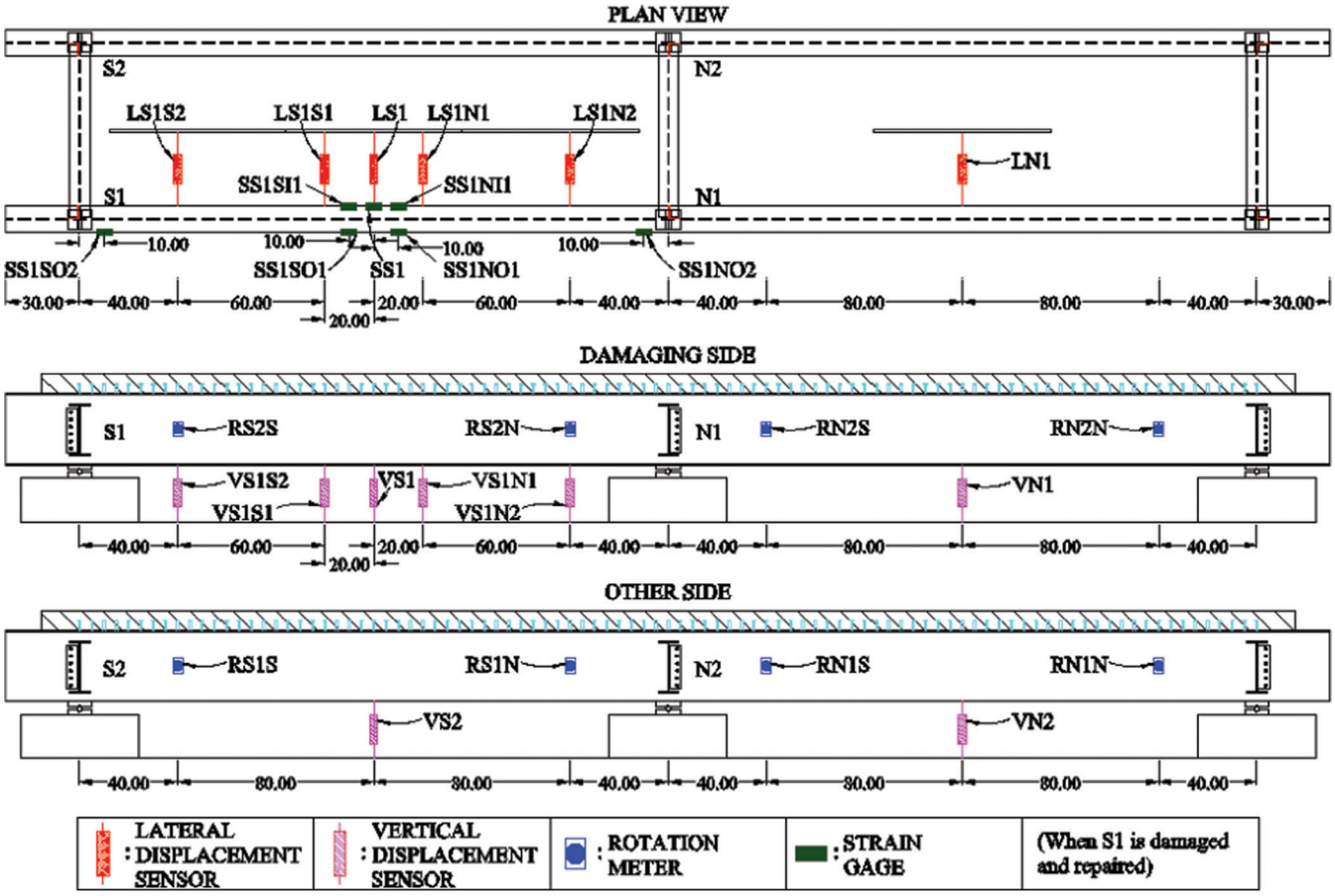

Figure 8.10 Large scale test sensor layout (S1 damage and repair).

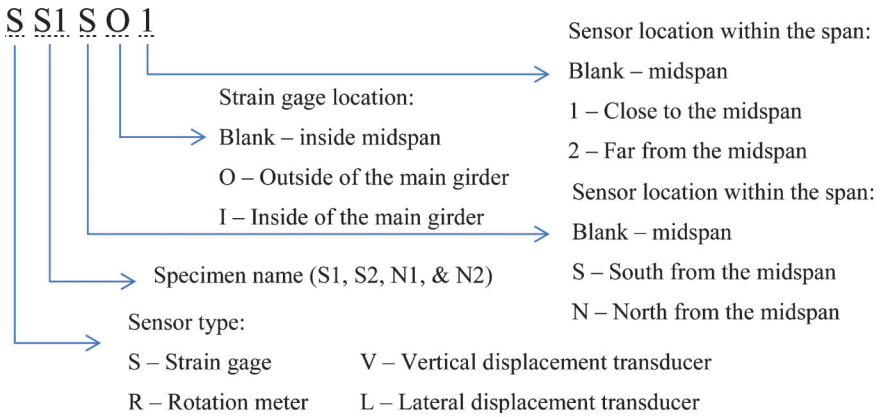

Figure 8.11 Naming of sensors.

specimens. For multiple damage cycles, the magnitude of damage was measured by these displacement transducers.

Infrared Thermometer

The surface temperature of each large scale specimen was measured using an infrared thermometer to get the time-temperature graph of each Vee heating cycle. The infrared thermometer was placed away from the heating region of the bridge.

8.5 Large Scale Experimental Procedure

Damage Procedure

As mentioned in Section 8.3, a specially designed loading beam, which was connected to two 100 ton capacity hydraulic actuators, was used to damage the bottom flange of the test specimen. The two actuators were acting together to create lateral force to damage the test specimen horizontally. A photograph of this damaging system is shown in Figure 8.12. The actual damage operation of this system is shown in Figure 8.13.

The damage of the bridge specimen during the first damage cycle was carefully monitored using a strain gage and displacement transducer attached to the midspan of each specimen. The damaging force applied at the midspan by the hydraulic actuators was slowly increased until the targeted damage strain at the midspan was reached.

For multiple damage and repair specimens (S1 and N1), subsequent damage cycles were controlled by the lateral displacement at the midspan. The subsequent damage cycles were finished when the lateral displacement of the midspan reached the same amount of maximum lateral displacement of the first damage cycle.

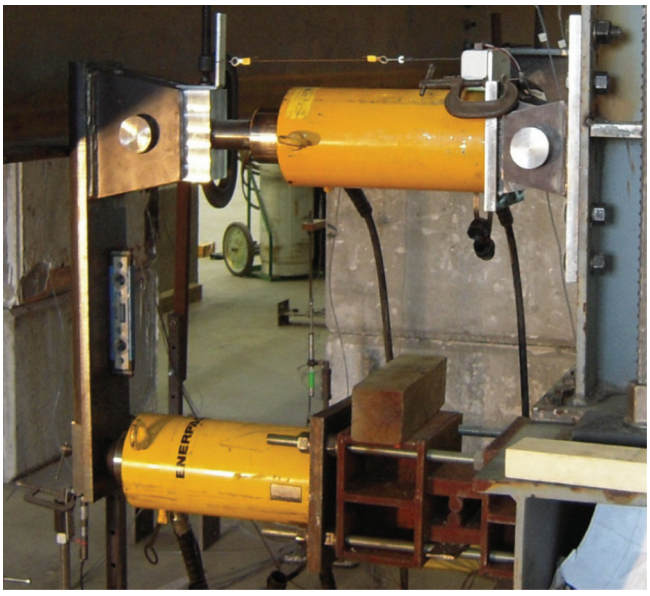

Figure 8.12 Damaging system.

Figure 8.13 Actual damage of large scale specimen.

Repair Procedure

1. Application of restraining forces. The restraining moment (M_r) was decided as 0.40 M_p or 0.60 M_p. M_p means the sectional plastic moment capacity of the specimen. However, it is very difficult to find out the actual M_p of a damaged bridge section because of its geometric complexities. The FHWA heat straightening guidelines (*28*) recommended $M_p/3$ of the bottom flange moment as the upper limit of the restraining force instead of 0.5 M_p of the whole damaged section. $M_p/3$ of the bottom flange could be reached when the maximum compression stress of the bottom flange became 50 percent of its yield stress.

A finite element model of the test bridge was developed by using the ABAQUS 6.10 analysis program to calculate the restraining force which could lead to 50 percent of yield stress at the maximum compression point of the bottom flange. Figure 8.14 shows the ABAQUS bridge model to determine the maximum restraining force. Figure 8.15 shows the

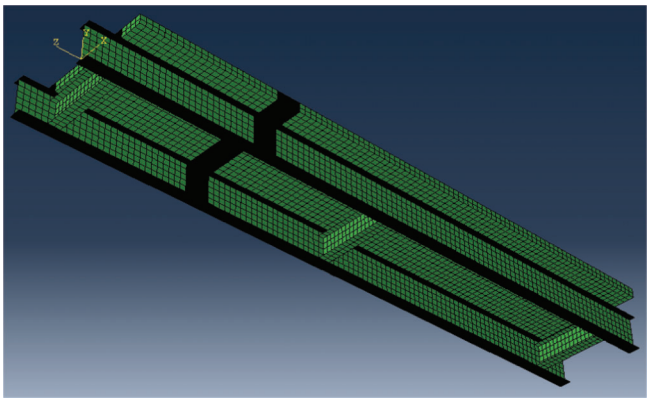

Figure 8.14 Finite model of the large scale test bridge.

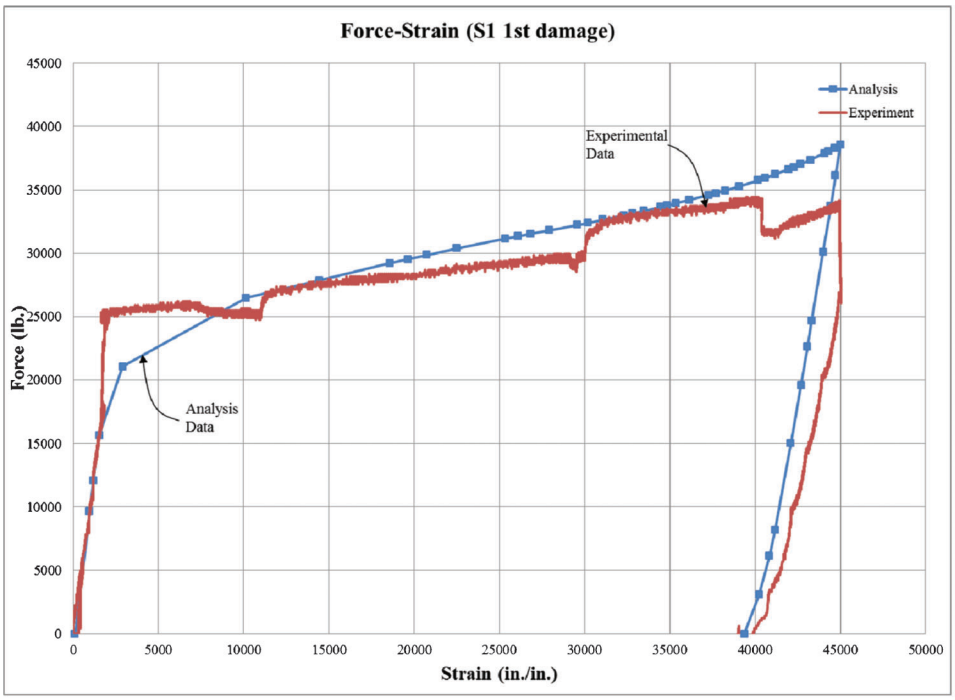

Figure 8.15 Analysis and experimental data comparison (S1 damage).

comparison of the finite element model prediction with the experimental result for S1 specimen (Force-Strain relationship of the 1st damage cycle). As shown in Figure 8.15, the experimental data compares reasonably well with the finite element model.

Assuming the steel yield stress to be 45 ksi, the ABAQUS model was used to determine that 7.9 kips of restraining force produces 22.5 ksi of maximum compressive stress. Figure 8.16 shows the results of the ABAQUS model. 7.9 kips of restraining force was selected as the maximum restraining force producing approximately 0.5 M_p on the whole damaged section. The restraining forces that can cause 0.4 M_p and 0.6 M_p were determined using the ABAQUS model as 6.32 kips and 9.48 kips respectively (80 percent and 120 percent of 7.9 kips).

However, in the first two Vee heating cycles of all repair processes, the restraining force of 0.25 M_p (3.95 kips) was applied on the damaged specimen. The FHWA heat straightening guidelines (*28*) recommended ¼ M_p of the restraining force in the first two cycles of Vee heating to release residual stress caused by the damage process.

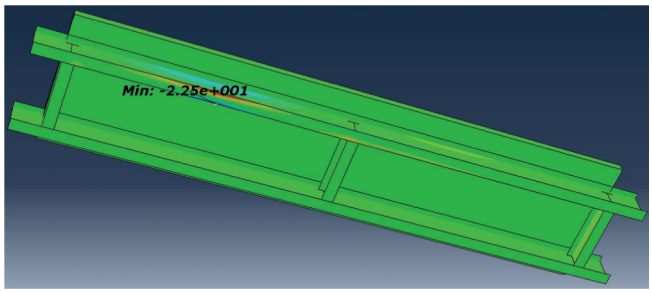

Figure 8.16 Maximum compression stress when applying 0.5 M_p of restraining force.

2. Application of heat straightening. An oxygen-propylene torch was used for heating the large scale specimens. The heating technician used a hand-held infrared temperature gun to monitor the heating temperature of the steel. A spot heat was applied at the apex of the Vee to reach the targeted heating temperature. After reaching the targeted temperature, the heating torch was moved toward the flange edge following a serpentine way. Vee heat was only applied on the top surface of the bottom flange during the first couple of cycles. After excessive upward direction distortion was noticed, Vee heat was also applied on the bottom surface of the bottom flange to reduce the distortion.

Vee heat regions of the large scale test specimens are shown in Figure 8.17. These Vee zones were located within the central plastic strain region of the bridge specimen. The nomenclature of each Vee region is also shown in Figure 8.17. As seen in Figure 8.17, the Vee angle used for the small scale test was about 53°. This angle was similar to the Vee angle used in the heat straightening field visit in Section 4.3.

The actual Vee heat application is shown in Figure 8.18. Figure 8.18 (a) shows the actual restraining system used to apply restraining force to the damaged specimen. Figure 8.18 (b) shows the Vee heat application

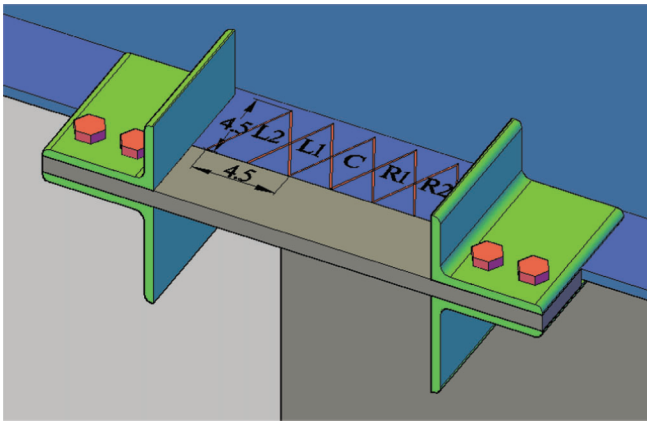

Figure 8.17 Vee heat locations and nomenclature.

using the oxygen-propylene heating torch. A non-contact infrared thermometer gun to check the applied temperature during the Vee heat application is shown in Figure 8.18 (b).

After the damaged bridge specimen was fully straightened by the Vee heat application, flange bulges (L category damage: localized damage) remained in and outside of the bottom flange. The outside bulge was caused by the damaging force at the contact point with the loading beam, and the inside bulge was initiated from the Vee heat application. Figure 8.19 shows an actual photo of the localized bulge damage on the bottom flange of the bridge specimen and line heat repair. All localized damages were also fixed by using the localized line heat repair method.

(a) Restraining system

(b) Vee heat application

Figure 8.18 Heat straightening application (Vee heat).

The required restraining force for the line heat repair process was computed from the yield line analysis method in the FHWA heat straightening guidelines (*28*). Figure 8.20 shows the yield line analysis for the idealized flange bulge geometry. Equations 8.1–8.5 were used to find out the required jacking force (P_j) of each test specimen.

$$M_p = \frac{F_y t^2}{4} \tag{8.1}$$

Where, F_y = yield stress, t = flange thickness.

The work done, W_e, by external loads, W_u, is

$$W_e = \left(W_u \frac{ac}{2}\right)(0.75\delta_u) \tag{8.2}$$

The internal work done, W_I, is computed from the following equation using the geometry coming from Figure 8.20 (a).

$$W_I = M_p\left(\frac{a\delta_u}{c} + \frac{2c\delta_u}{b} + \frac{2c\delta_u}{b} + \frac{2b\delta_u}{c}\right) \tag{8.3}$$

Equating external and internal work done,

$$W_u = \frac{8}{3}\frac{M_p}{ac}\left(\frac{a}{c} + \frac{4c}{b} + \frac{2b}{c}\right) \tag{8.4}$$

A load ratio of 50% was used and the required jacking force on the bulge was computed using the following equation.

$$P_j = \frac{W_u ac}{4} \tag{8.5}$$

The required jacking force (restraining force) was determined by using Equation 8.5. Variables used for the equation were selected conservatively to reduce the unexpected harmful effect of overstraining. Actual values of the variables used to calculate the restraining force were as follows:

F_y = 36 ksi, t = 0.61 in., a = 0.001 in., b = 2.5 in., and c = 5 in.

With all above variables, the calculated P_j value using Equation 8.5 was 20.09 kips. However, this jacking force (restraining force) was reduced to 10.05 kips, which was about 50 percent of the calculated value to prevent overstraining of the bottom flange.

3. Evaluation of serviceability performance. After the specimens were damaged and heat straightening repaired, the serviceability performance of the

(a) Outside local damage (b) Line heat application (outside)

(c) Inside local damage (d) Line heat application (inside)

Figure 8.19 Heat straightening application (Line heat).

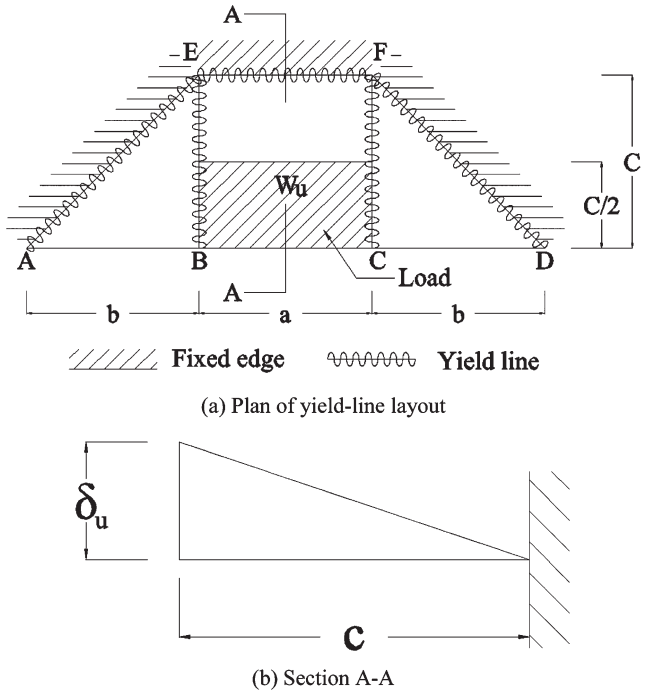

Figure 8.20 Yield line analysis for idealized flange bulge geometry.

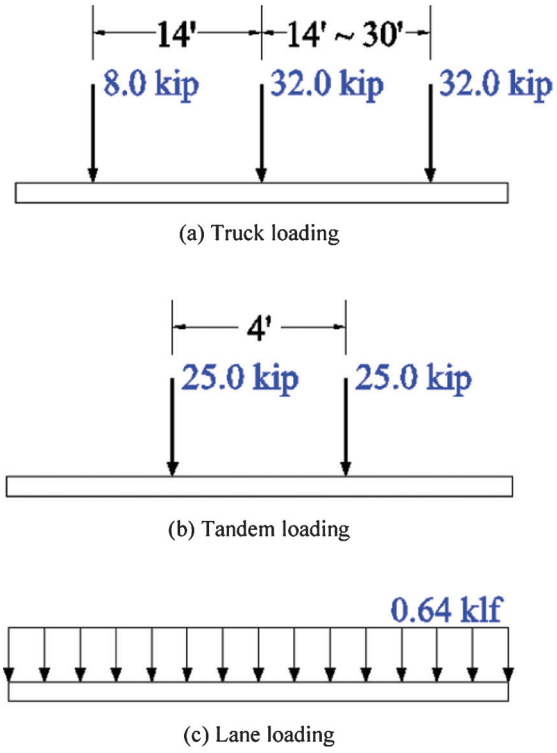

Figure 8.21 HL-93 live loadings of the AASHTO 2007 specification.

repaired beams was determined by subjecting them to static loads simulating the AASHTO 2007 HL-93 live load which can cause the maximum moment at each midspan (damaged and repaired point).

SAP 2000 structural analysis program was used to determine the maximum live load effect on the test bridge. A 20 ft. two-span frame model was developed to apply the AASHTO 2007 HL-93 live load. HL-93 truck loading, tandem loading, and lane loading described in the AASHTO 2007 specification were applied on the analysis model. Details of these live loads are shown in Figure 8.21.

Following the AASHTO 2007 design procedure, the truck loading or tandem loading was combined with the lane loading and applied on the bridge model. The maximum HL-93 live load moment diagram obtained from the SAP 2000 linear analysis is shown in Figure 8.22. As seen in Figure 8.22, the maximum moment at the midspan by the applied HL-93 live load was 2123.5 kip·in.

A static load which can cause 2123.5 kip·in moment at each midspan was also determined by the SAP 2000 analysis program. Figure 8.23 shows 55.8 kips of static load applied at each midspan and a corresponding bending moment diagram of the analysis model. As seen in Figure 8.23, 2123.5 kip·in of the moment value was developed at each midspan by 55.8 kips of static load. Therefore, 55.8 kips of static midspan load was decided as the maximum live load to determine the serviceability performance of the test bridge.

8.6 Large Scale Material Testing Procedures

Charpy V-notch coupons and uniaxial tension coupons were taken from the damaged and heat straightening repaired flange area of each specimen. In addition to the four damaged and repaired specimens, one steel plate from the undamaged bottom flange was prepared to take out additional material test coupons.

As shown in Figure 8.24, two uniaxial tension coupons were taken from the midspan of each test specimen. The dimensions of the uniaxial tension coupons are shown in Figure 5.13. All tension coupons were taken from the Vee heated regions at the midspan (L1, C, and R1) between 1.6 in. and 3.4 in. from the outer surface of the bottom flange. The actual location and the nomenclature of each tensile coupon are also shown in Figure 8.24.

Fracture toughness tests, Rockwell hardness tests, and microstructure investigations were conducted on the Charpy coupons of each large scale specimen. The Charpy coupons of the large scale test specimens are shown in Figure 8.24. The Charpy specimens were removed within a distance of 1.6 in. of the flange edge. As seen in Figure 8.24, the v-notches of the Charpy coupons were fabricated facing the edge of the bottom flange plate. The location and the nomenclature of each Charpy coupon are also shown in Figure 8.24.

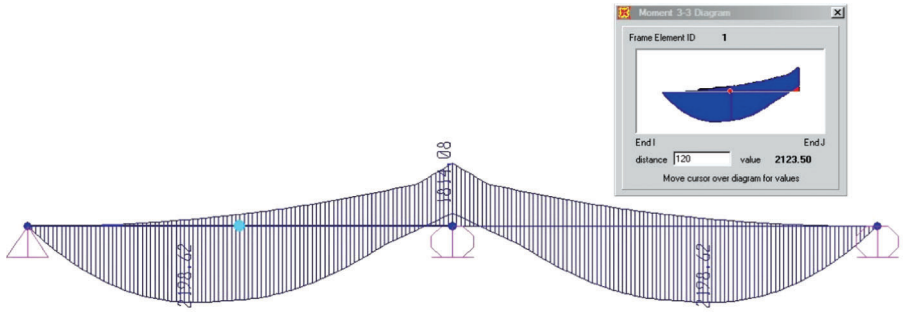

Figure 8.22 Bending moment diagram of HL-93 live load analysis.

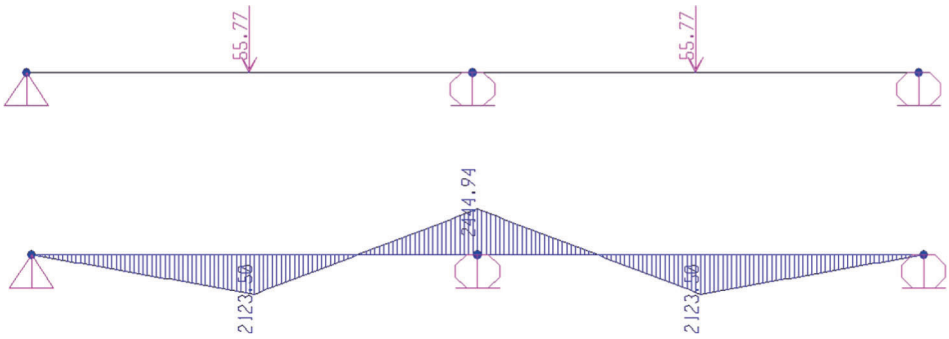

Figure 8.23 Static load and bending moment diagram for serviceability checkup.

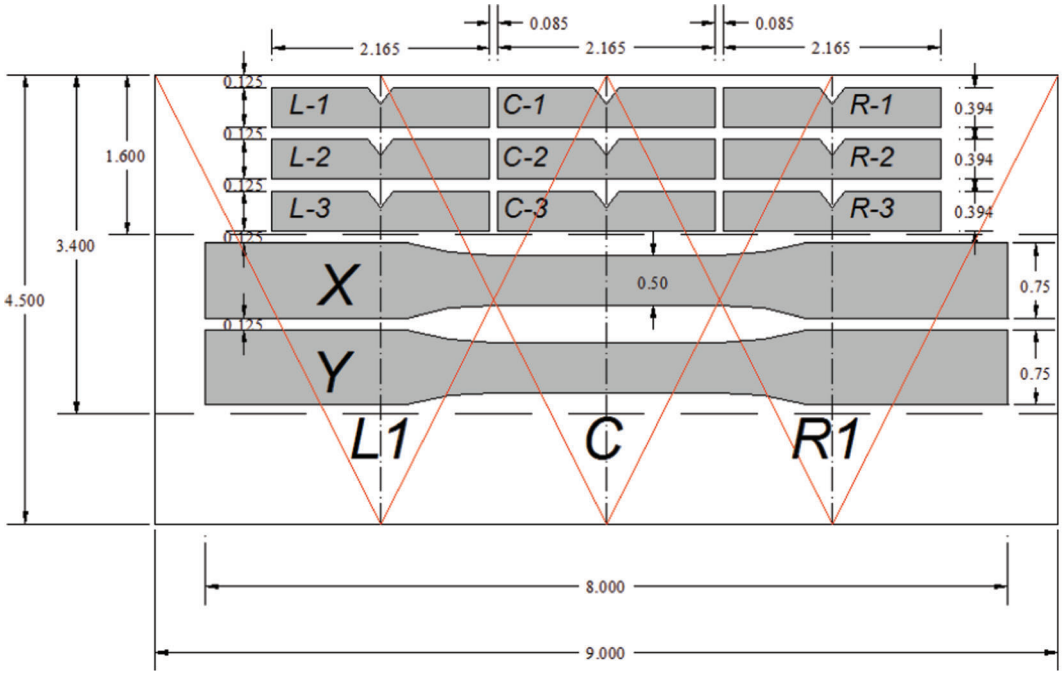

Figure 8.24 Nomenclature and location of large scale material coupons.

9. LARGE SCALE TEST: EXPERIMENTAL BEHAVIOR

Four large scale composite beam specimens from the large scale bridge were tested by subjecting them to damage-heat straightening repair cycles. The damage and heat straightening repair parameters of these test specimens are presented in Table 8.1.

The experimental behavior of the beam specimens during the damage cycles is presented and discussed using the data provided by the instrumentations (sensors). As mentioned previously, the longitudinal strain gages worked well during the first damage cycle only. Hence, the load-strain P-ε behavior during the first damage cycle and the load-midspan deflection P-Δ during all damage cycles are shown. These comparisons indicate the change in strength and stiffness of the beam after the previous damage-repair event. Photographs of the bridge specimens before and after the damage cycle are provided. Other significant information noted during the experimental damage cycles is provided.

The behavior of the test specimens during the repair cycles is presented using the data measured by the instrumentation. At least one figure which shows the force in the hydraulic actuator, the temperature at the surface of the Vee heated steel, and the deflections measured by the displacement transducers is provided for each specimen. The final condition of the damaged-repaired beam specimens is also shown and discussed. Finally, the number of Vee heats required to repair the damage of each cycle is reported.

9.1 Damage Process of S1 Specimen (3-1400-0.4-30)

Several sensors were used to monitor the specimen behavior during the first damage procedure of the first specimen (3-1400-0.4-30). Strain gages were located at the planned location shown in Section 8.4. After the first damage cycle, all the sensors except for the strain gages were reattached to the test bridge specimen to monitor the behavior of the following cycles.

In the initial test plan, the S1 specimen was to be subjected to three damage-repair cycles to evaluate the effect of multiple damage cycles and overheating. However, during the first repair cycle, an unexpected error occurred in the data acquisition system and 10 times larger than intended restraining force close to 70 kips was applied to the damaged S1 specimen. By this accidental restraining force, the test specimen was fully straightened without any Vee heat application. After this accident, the original test plan was still implemented and specimen S1 was subjected to three more damage-repair cycles. As a result, S1 specimen was subjected to one damage-force repair cycle and three damage-heat repair cycles.

Figure 9.1 shows photographs of the beam specimen before and after the first damage cycle. As mentioned previously, the first damage was repaired by excessive restraining force which was close to 70 kips. Three

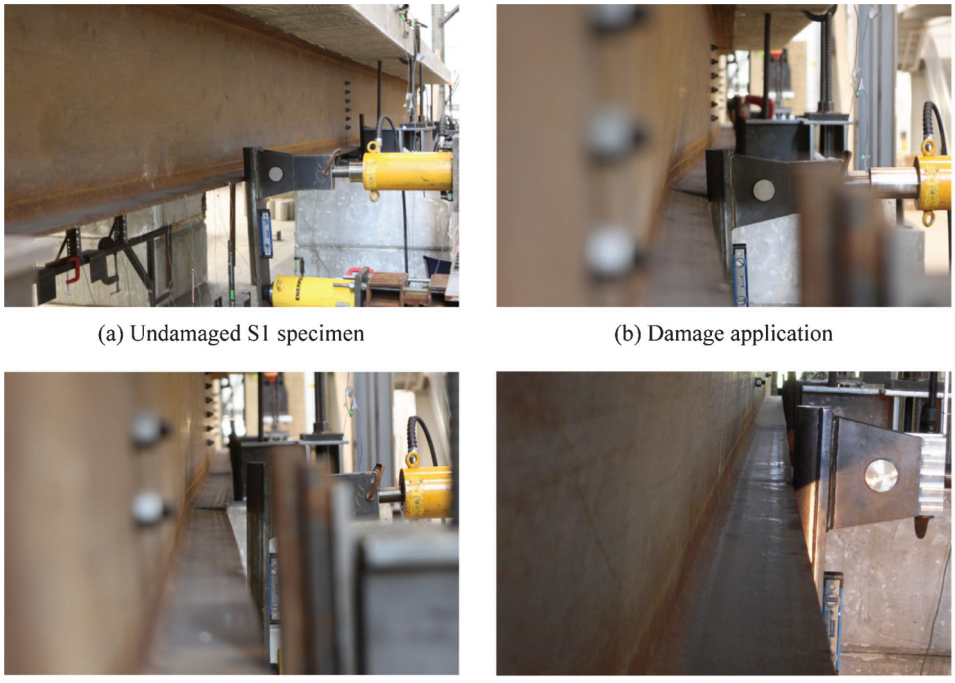

(a) Undamaged S1 specimen

(b) Damage application

(c) S1 after 1st damage

(d) After force repair (cold work)

Figure 9.1 Photographs of 1st damage-repair cycle (S1 specimen).

additional damage-heat straightening repair cycles were applied on the S1 specimen after the first force repair as shown in Figure 9.2.

Each damage cycle corresponded to the damage strain of 30 ε_y (0.045 in./in.) at the midspan strain gages. The damage strain in the first cycle was measured using the strain gage layout described in Section 8.4 The strain gage data from the first damage cycle is provided in Figure 9.3.

Damage cycles 2, 3 and 4 were conducted under displacement control, where the displacement at the midspan was monitored and controlled to reach the displacement from the first damage cycle. Figures 9.4–9.7 show the lateral displacement behavior in each damage cycle. The maximum lateral displacements at each damage cycle corresponding to the maximum damage strain of 30 ε_y are shown in Table 9.1. The permanent deformations left in S1 specimen after elastic rebound are also presented in Table 9.1. These permanent deformations were the final damage magnitude to be fixed by the heat straightening process.

Figure 9.8 compares the P-Δ behavior of all four damage cycles of the S1 specimen. All four graphs in Figure 9.8 show similar P-Δ behavior in all damage cycles. Therefore, the stiffness of the S1 specimen in each damage-repair cycle was not affected significantly by the damage-repair process. (See S-1 Span Damage video: http://dx.doi.org/10.4231/D3RJ48V2G)

9.2 Repair Process of S1 Specimen (3-1400-0.4-30)

Repair cycles of the S1 specimen were conducted by applying external force corresponding to the restraining moment of 0.4 M_p described in Section 8.5. Vee heats were initially applied at the center (C) Vee region of the bottom flange shown in Figure 8.17. After that, other Vee regions (L1, R1-L2, R2) were heated to minimize out-of-plane distortion of the damaged flange. Each Vee region was heated to a maximum temperature of 1400 °F to see the overheating effect.

The total numbers of Vee heats required to straighten the specimen in each damage-repair cycle

(a) S1 after 2nd damage

(b) S1 after 2nd repair

(c) S1 after 3rd damage

(d) S1 after 3rd repair

(e) S1 after 4th damage

(f) S1 after 4th repair

Figure 9.2 Photographs of S1 specimen before and after the damage.

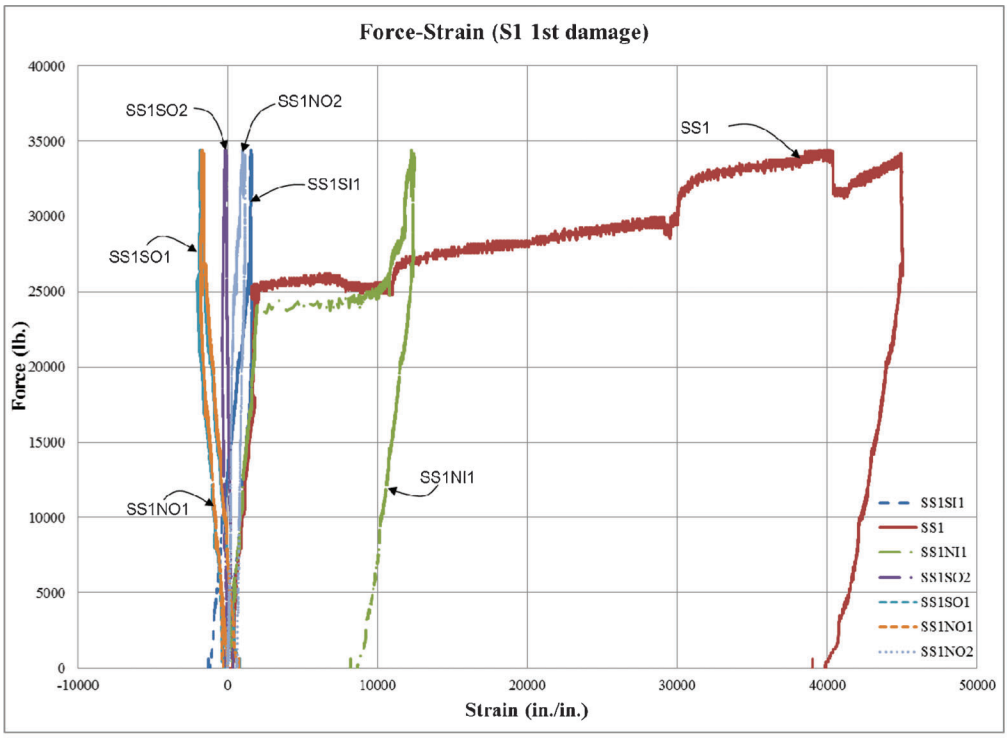

Figure 9.3 Load-strain diagram of S1 specimen.

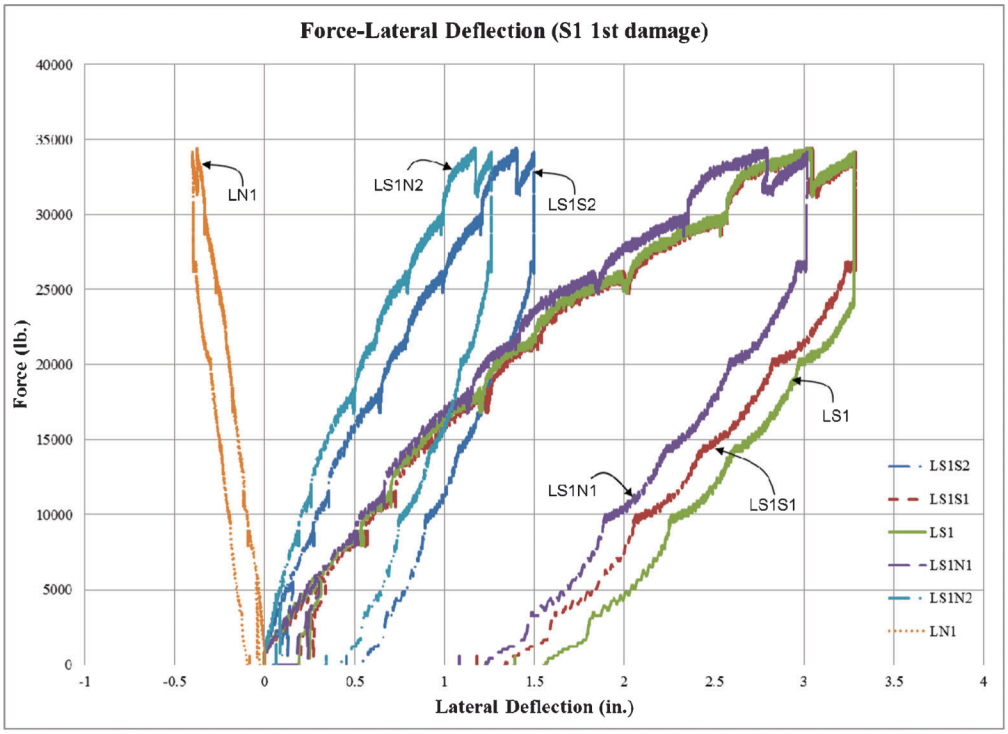

Figure 9.4 Load-displacement diagram of S1 specimen (1st damage).

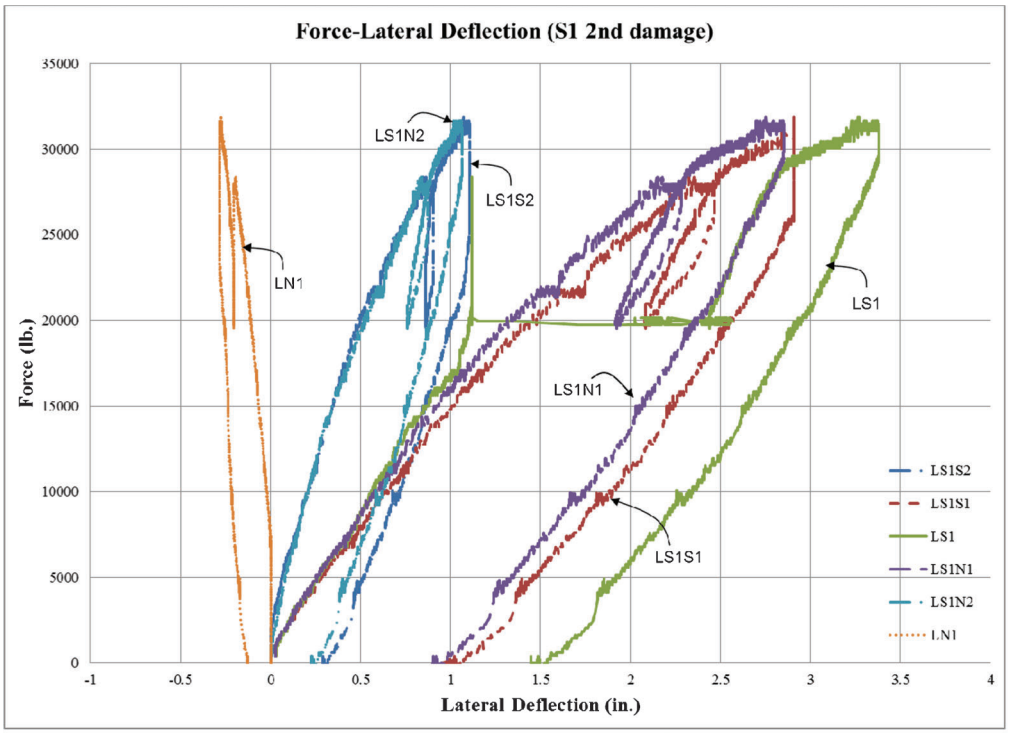

Figure 9.5 Load-displacement diagram of S1 specimen (2nd damage).

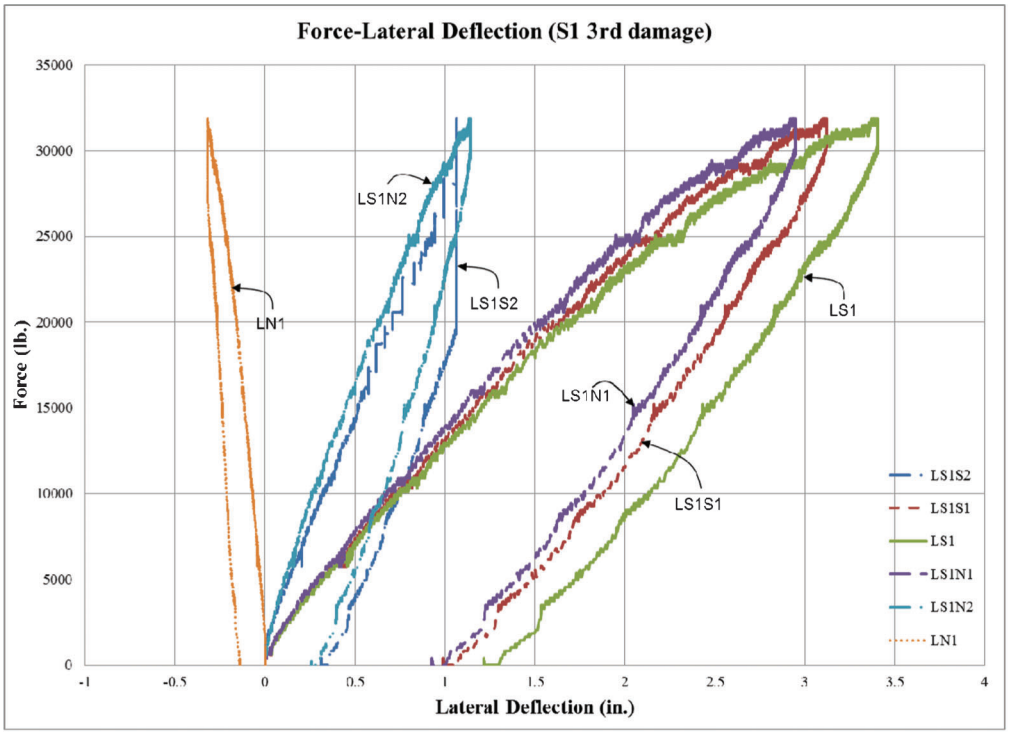

Figure 9.6 Load-displacement diagram of S1 specimen (3rd damage).

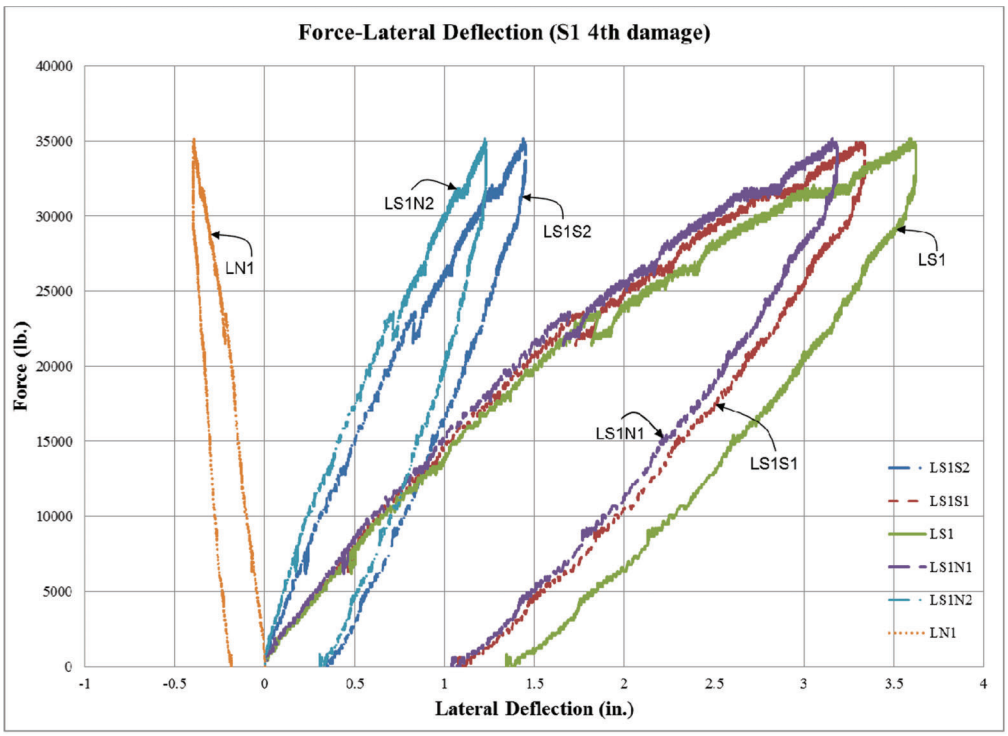

Figure 9.7 Load-displacement diagram of S1 specimen (4th damage).

TABLE 9.1
Maximum midspan deflection of S1 specimen

Damage Cycle	At the Maximum Damage (in.)	After the Damage (in.)
1st	3.29	1.39
2nd	3.38	1.45
3rd	3.40	1.22
4th	3.62	1.35
Avg.	**3.42**	**1.35**

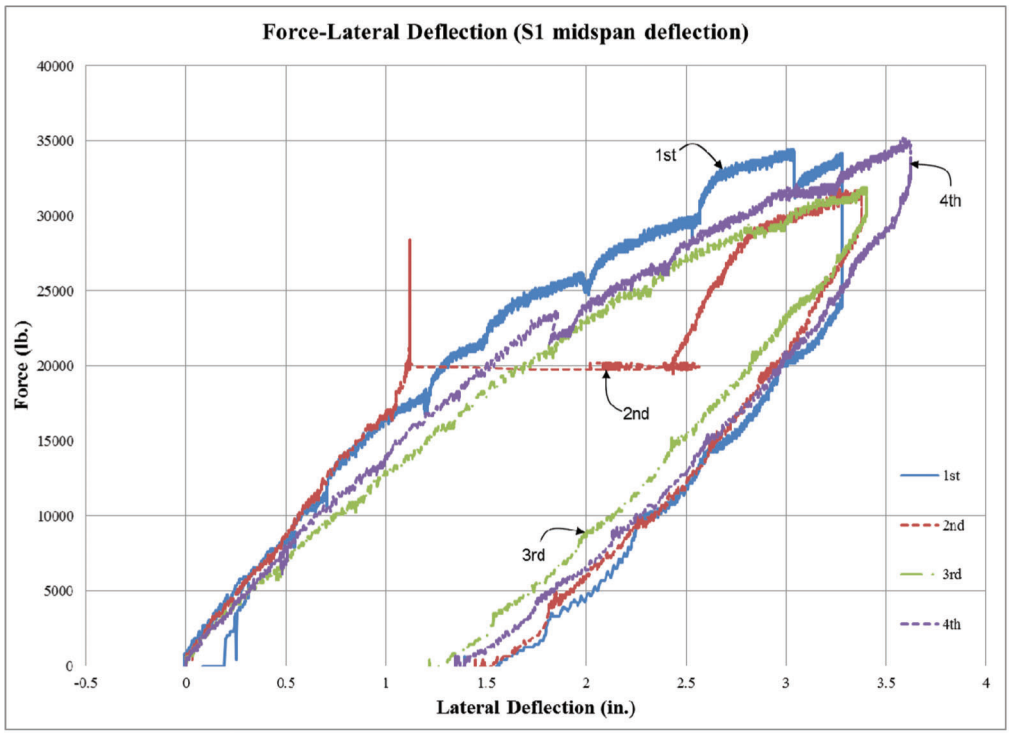

Figure 9.8 Midspan load-displacement diagram of S1 specimen (all damages).

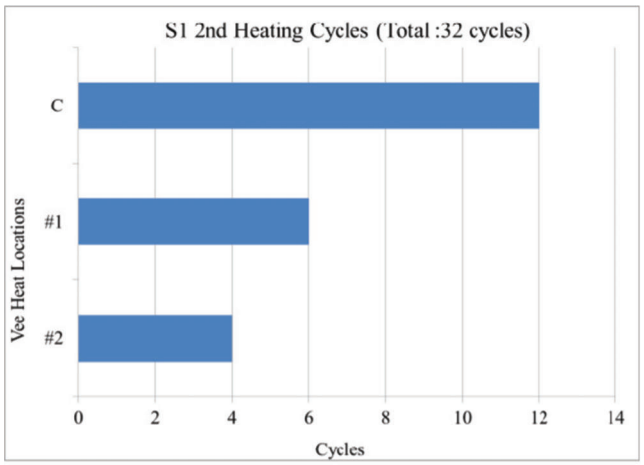

(a) Vee heat frequency of 2nd repair cycle

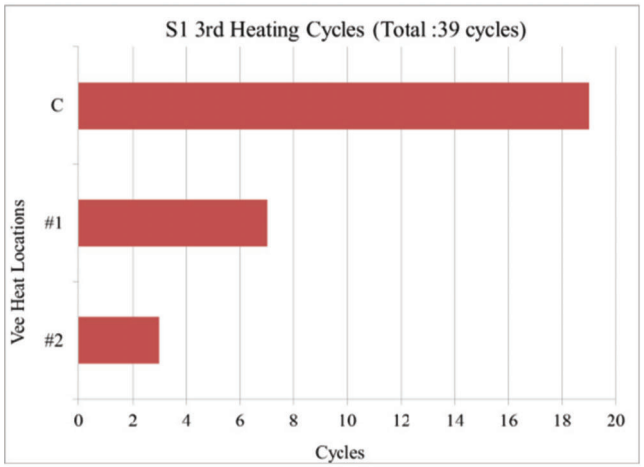

(b) Vee heat frequency of 3rd repair cycle

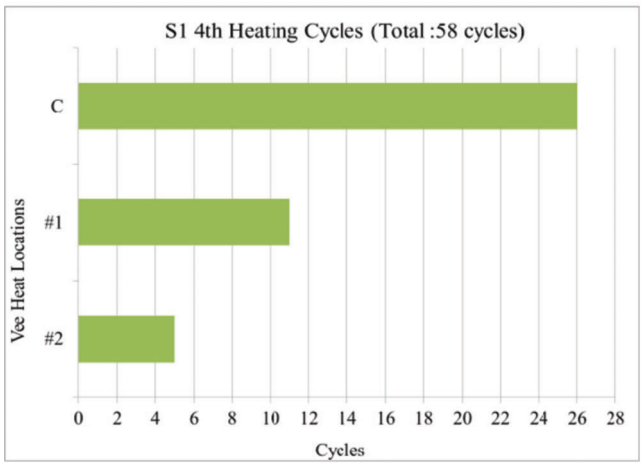

(c) Vee heat frequency of 4th repair cycle

Figure 9.9 Vee heat frequency chart of S1 specimen.

are shown in Figure 9.9. Thirty-two Vee heats on the bottom flange were required to complete the first repair cycle. The second repair cycle took 39 Vee heats to complete. The third repair cycle needed 58 Vee heats to complete. The required numbers of the Vee heats to fully straighten the specimen increased following multiple damage cycles.

After applying Vee heats to straighten the specimen, localized damage of the flange bulge was still left at the midspan of the specimen. This localized damage was repaired by the line heat method with additional jacking force described in Section 8.5. Table 9.2 presents the local damage amount of the flange bulge and applied line heat frequency in each repair cycle.

The final photographs of the S1 specimen after all repair cycles are shown in Figure 9.10. As seen Figure 9.10, the specimen was fully straightened after all repair processes. The surface of the repaired region was ground smoothly to deter undesired stress concentrations.

Figure 9.11 shows the behavior of the S1 specimen in the initial several steps of each repair cycle. These figures include: (a) the displacements from three inside displacement transducers in inches, (b) the restraining force in the hydraulic actuator in kips, which is divided by 3 (i.e., 1.0 on the graph shows 3 kips of force) and (c) the temperature of the steel in °F, which is divided by 1000 °F (i.e., 1.0 on the graph corresponds to 1000 °F).

9.3 Serviceability Behavior of S1 Specimen (3-1400-0.4-30)

The serviceability performance of the test bridge during the S1 damage-repair process was determined by simultaneously subjecting each midspan of test bridge to 56 kips of static loading. All vertical midspan displacements of the test bridge were measured and compared to determine the serviceability difference between each damage-repair cycle. Figure 9.12 shows the serviceability test using two 50 ton capacity hydraulic actuators attached to the midspan loading frames.

The AASHTO 2007 bridge specification limited live-load deflections to L/800 for ordinary bridges and L/1000 for bridges in urban areas that are subject to pedestrian use. Using these limitations with a 20 ft. (240 in.) span length, allowable maximum deflection values of the test bridge were 0.3 in. (L/800) and 0.24 in. (L/1000).

Figure 9.13 shows the serviceability behavior of the test bridge before and after the S1 damage-repair process. The maximum midspan deflections in all cases were not bigger than 0.035 in. which is much smaller than the AASHTO deflection limit of 0.3 in. or 0.24 in. Therefore, the maximum midspan deflection after the S1 damage-repair process was within the AASHTO specification deflection limit.

Figure 9.14 shows the measured maximum midspan deflection values after each damage-repair cycle. All the maximum deflections were within the AASHTO specification deflection limit. The final serviceability deflections of the S1 repair were not changed significantly from the undamaged serviceability deflection.

TABLE 9.2
Local damage and line heat frequency of S1 specimen

Repair Cycle	Local Damage of Inside Flange (Upward—in.)	Line Heat Frequency (Inside—Cycles)	Local Damage of Outside Flange (Downward—in.)	Line Heat Frequency (Outside—Cycles)
2nd	9/16	6	5/16	10
3rd	7/16	7	5/16	6
4th	3/16	8	1/4	3

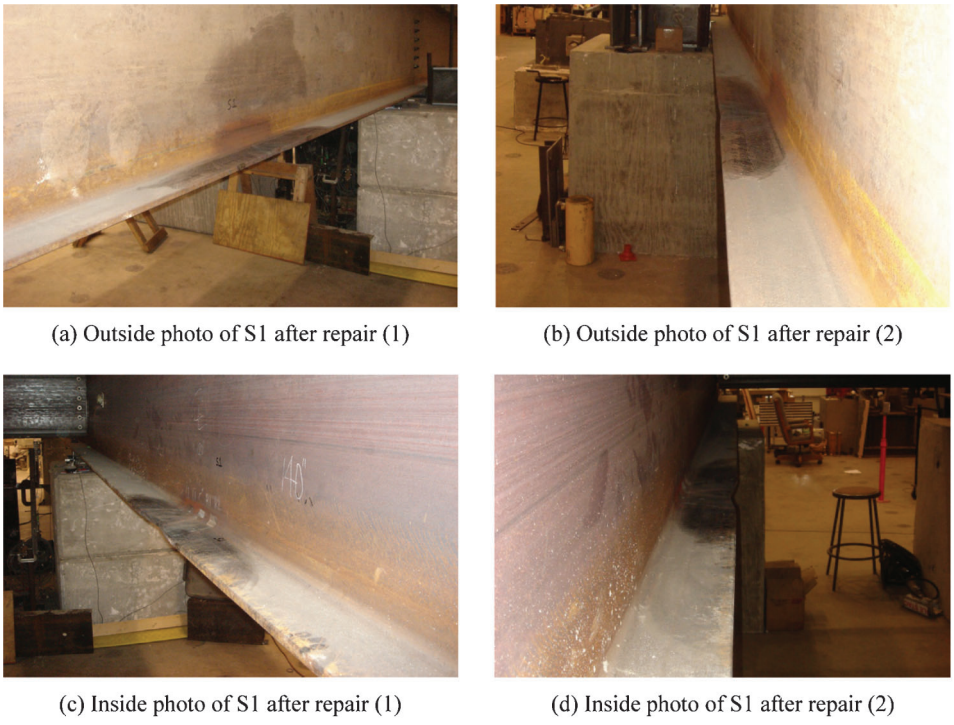

(a) Outside photo of S1 after repair (1)

(b) Outside photo of S1 after repair (2)

(c) Inside photo of S1 after repair (1)

(d) Inside photo of S1 after repair (2)

Figure 9.10 Photographs of S1 specimen after all repair processes.

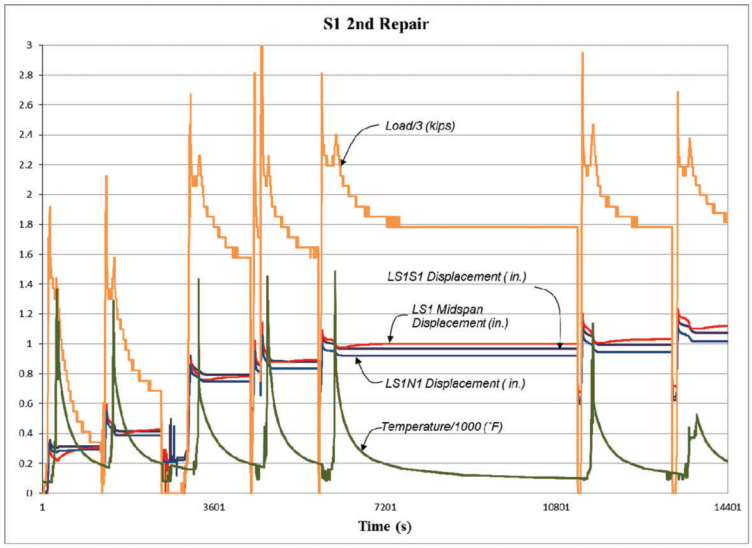

(a) 2nd repair cycle

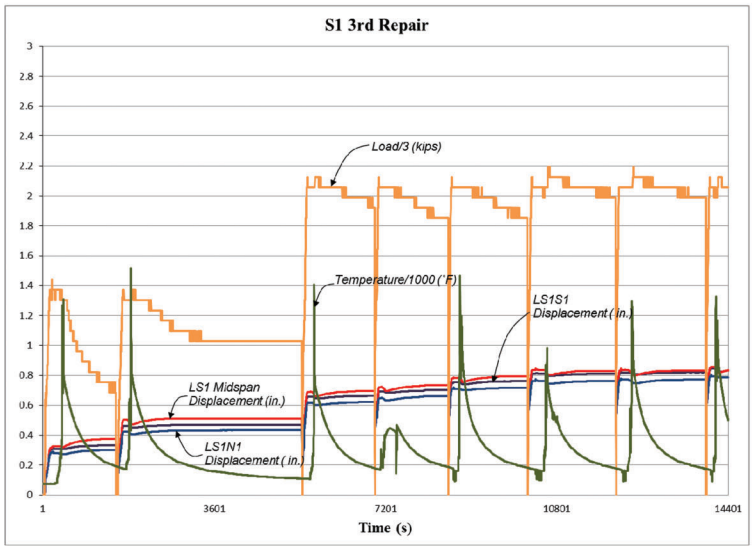

(b) 3rd repair cycle

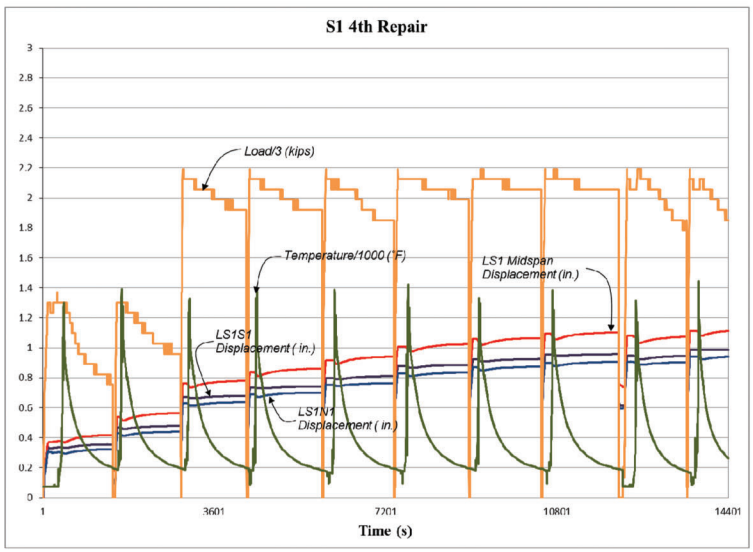

(c) 4th repair cycle

Figure 9.11 Instrument data during the repair cycles of S1 specimen.

Figure 9.12 Photograph of serviceability test.

9.4 Damage Process of S2 Specimen (1-1400-0.4-30)

Several sensors were used to monitor specimen behavior during the damage procedure of the S2 specimen (1-1200-0.4-30). Strain gages were located at the planned location described in Section 8.4.

Figure 9.15 shows the photographs of the beam specimen before and after the damage cycle. The beam specimen was damaged by monotonically increasing the concentrated force at the midspan. The damage was monitored by using the longitudinal strain gages. The test was considered complete when the strain gage located at the midspan of the specimen reached 30 ε_y. The complete strain gage data for the damage cycle is shown in Figure 9.16.

P-Δ relationships for the S2 specimen are shown in Figure 9.17. The plastic displacement at the maximum damage was found to be 3.70 in. The final damage displacement after elastic rebound was 1.54 in. (See S-2 Span Damage video: http://dx.doi.org/10.4231/D34Q7QQ3T)

9.5 Repair Process of S2 Specimen (1-1400-0.4-30)

The repair cycle of the S2 specimen was conducted by applying external force corresponding to the restraining moment of 0.4 M_p described in Section 8.5. Vee heats were initially applied at the center (C) Vee region of the bottom flange shown in Figure 8.17. After that, other Vee regions (L1, R1-L2, R2) were heated to minimize the out-of-plane distortion of the damaged flange. Each Vee region was heated to a maximum temperature of 1400 °F to see the over-heating effect.

Twenty-four Vee heats were required to complete the repair cycle of the S2 specimen. The photographs of the repaired beam are shown in Figure 9.18. The surface of the repaired region was ground smoothly to deter undesired stress concentrations. The specimen straightness was confirmed by the tout line method which used a tout line to measure the gap distance from the specimen to the tout line. The frequency chart indicating the amount of the Vee heats applied to each Vee location is shown in Figure 9.19.

After applying Vee heats to straighten the specimen, localized damage of the flange bulge was still left in the midspan at the specimen. This localized damage was repaired by the line heat method with additional jacking force described in Section 8.5. Table 9.3 presents the local damage amount of the flange bulge and applied line heat frequency in the repair cycle of the S2 specimen.

Figure 9.20 shows the behavior of the S2 specimen in the initial several steps of the repair cycle. This figure includes: (a) the displacements from three inside displacement transducers in inches, (b) the restraining force in the hydraulic actuator in kips, which is divided by 3 (i.e., 1.0 on the graph shows 3 kips of force), and (c) the temperature of the steel in °F, which is divided by 1000 °F (i.e., 1.0 on the graph corresponds to 1000 °F).

9.6 Serviceability Behavior of S2 Specimen (1-1400-0.4-30)

The serviceability performance of the test bridge during the S2 damage-repair process was determined by simultaneously subjecting each midspan of test bridge to 56 kips of static loading. All vertical midspan displacements of the test bridge were measured and compared with previous serviceability performance results.

Figure 9.21 shows serviceability behavior of the test bridge after the S2 damage and the S2 repair process. The maximum midspan deflections in all cases were not bigger than 0.035 in. which is much smaller than the AASHTO deflection limit of 0.3 in. or 0.24 in. Therefore, the maximum midspan deflection after the S2 damage-repair process was within the AASHTO specification deflection limit. However, the S1 deflection in Figure 9.21 (b) shows unreliable behavior. It is presumed that an error occurred in the measurement of the S1 displacement transducer at the serviceability test of the S2 repair.

Figure 9.22 shows the measured maximum midspan deflection values after each damage-repair cycle. The final serviceability deflections of the S2 repair (except for the S1 deflection) were not changed significantly from the undamaged serviceability deflection.

9.7 Damage Process of N1 Specimen (3-1200-0.4-30)

Several sensors were used to monitor specimen behavior during the first damage procedure of the N1 specimen (3-1200-0.4-30). Strain gages were located at the planned location shown in Section 8.4. After the first damage cycle, all the sensors except for the strain gages were reattached to the test bridge specimen to monitor the behavior of the following cycles. Figure 9.23 shows photographs of the bridge specimen before and after each damage cycle.

The N1 specimen was planned to be subjected to three damage-repair cycles to determine the effect of multiple damage cycles. Each damage cycle corresponded to the damage strain of 30 ε_y (0.045 in./in.) at the midspan strain gages. The damage strain in the first

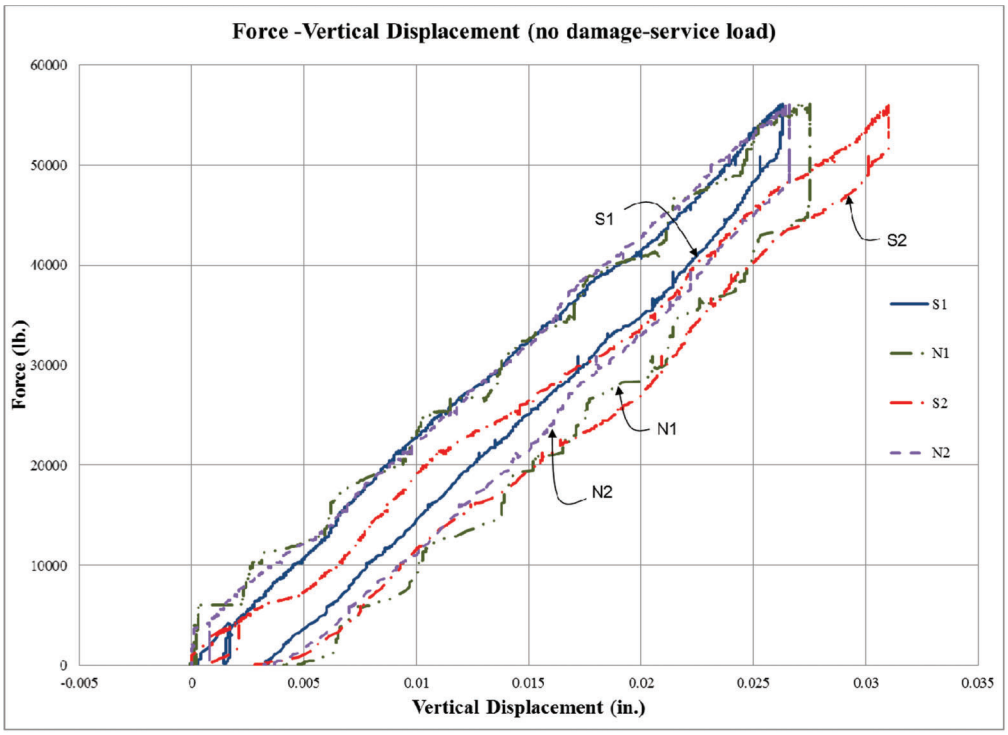

(a) Force-vertical displacement of undamaged bridge

(b) Force-vertical displacement of S1 4th repaired bridge

Figure 9.13 Service load-vertical displacement behavior of S1 test.

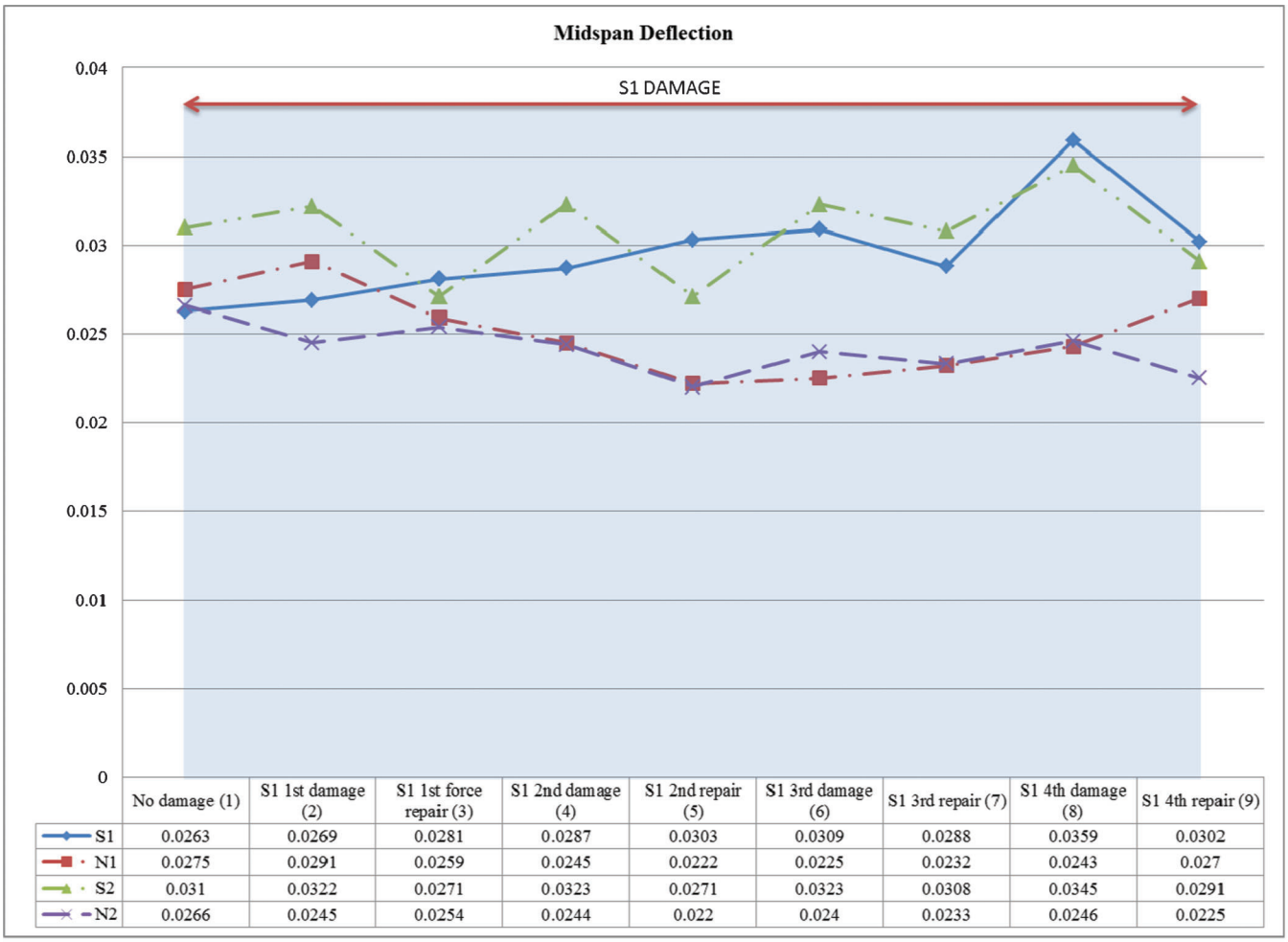

	No damage (1)	S1 1st damage (2)	S1 1st force repair (3)	S1 2nd damage (4)	S1 2nd repair (5)	S1 3rd damage (6)	S1 3rd repair (7)	S1 4th damage (8)	S1 4th repair (9)
S1	0.0263	0.0269	0.0281	0.0287	0.0303	0.0309	0.0288	0.0359	0.0302
N1	0.0275	0.0291	0.0259	0.0245	0.0222	0.0225	0.0232	0.0243	0.027
S2	0.031	0.0322	0.0271	0.0323	0.0271	0.0323	0.0308	0.0345	0.0291
N2	0.0266	0.0245	0.0254	0.0244	0.022	0.024	0.0233	0.0246	0.0225

Figure 9.14 Midspan displacements of S1 test.

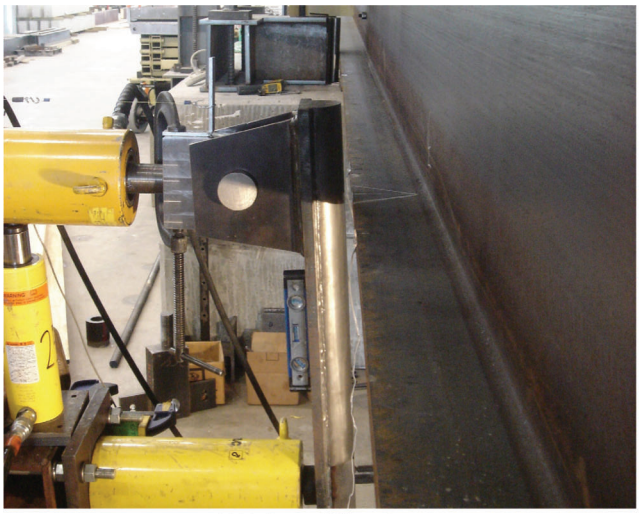

(a) Undamaged S2 specimen

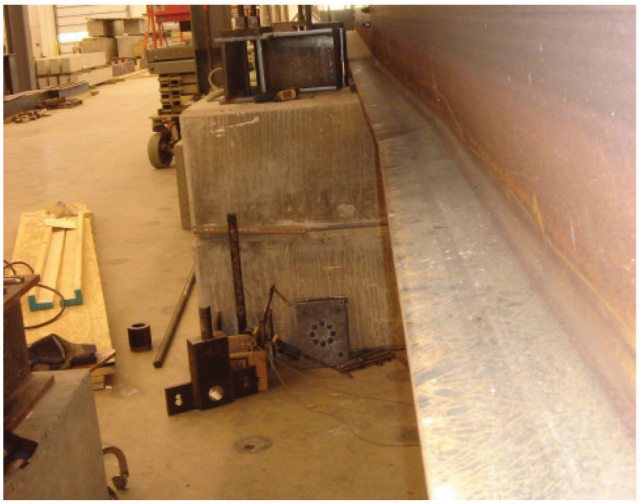

(b) Damaged S2 specimen

Figure 9.15 Photographs of S2 specimen before and after the damage.

cycle was measured using the strain gage layout described Section 8.4. The strain gage data from the first damage cycle is provided in Figure 9.24.

Damage cycles 2 and 3 were conducted under displacement control, where the displacement at the midspan was monitored and controlled to reach the displacement from the first damage cycle. Figures 9.25–9.27 show the lateral displacement behavior in each damage cycle. The maximum lateral displacement at each damage cycle corresponding to the maximum damage strain of 30 ε_y is shown in Table 9.4. The permanent deformations left in the N1 specimen after elastic rebound are also presented in Table 9.4. These permanent deformations were the final damage magnitude to be fixed by the heat straightening process.

Figure 9.28 compares the P-Δ behavior of all three damage cycles of the N1 specimen. All three graphs in Figure 9.28 show similar P-Δ behavior in all damage cycles. Therefore, the stiffness of the N1 specimen in each damage-repair cycle was not affected too much by the damage-repair process. (See N-1 Span Damage video: http://dx.doi.org/10.4231/D3W66984S)

9.8 Repair Process of N1 Specimen (3-1200-0.4-30)

Repair cycles of the N1 specimen were conducted by applying external force corresponding to the restraining moment of 0.4 M_p described in Section 8.5. Vee heats were initially applied at the center (C) Vee region of the bottom flange shown in Figure 8.17. After that, other Vee regions (L1, R1-L2, R2) were heated to minimize the out-of-plane distortion of the damaged flange. Each Vee region was heated to a maximum temperature of 1200 °F.

The total numbers of Vee heats required to straighten the specimen in each damage-repair cycle are shown in Figure 9.29. Forty-two Vee heats on the bottom flange were required to complete the first repair cycle. The second repair cycle took 50 Vee heats to complete. The third repair cycle needed 66 Vee heats to complete. The required numbers of Vee heats to fully straighten the specimen were increased following multiple damage cycles.

After applying Vee heats to straighten the specimen, localized damage of the flange bulge was still left in the midspan at the specimen. This localized damage was repaired by the line heat method with additional jacking force described in Section 8.5. Table 9.5 presents the local damage amount of the flange bulge and applied line heat frequency in each repair cycle.

The final photographs of the S1 specimen after all repair cycles are shown in Figure 9.30. As seen in Figure 9.30, the specimen was fully straightened after all repair processes. The surface of the repaired region was ground smoothly to deter undesired stress concentrations.

Figure 9.31 shows the behavior of the S1 specimen in the initial several steps of each repair cycle. These figures include: (a) the displacements from three inside displacement transducers in inches, (b) the restraining force in the hydraulic actuator in kips, which is divided by 3 (i.e., 1.0 on the graph shows 3 kips of force), and (c) the temperature of the steel in °F, which is divided by 1000 °F (i.e., 1.0 on the graph corresponds to 1000 °F).

9.9 Serviceability Behavior of N1 Specimen (3-1200-0.4-30)

The serviceability performance of the test bridge during the N1 damage-repair process was determined by simultaneously subjecting each midspan of test bridge to 56 kips of static loading. All vertical midspan displacements of the test bridge were measured and compared to determine the serviceability difference between each damage-repair cycle.

Figure 9.32 shows the serviceability behavior of the test bridge after the N1 1st damage and the N1 3rd

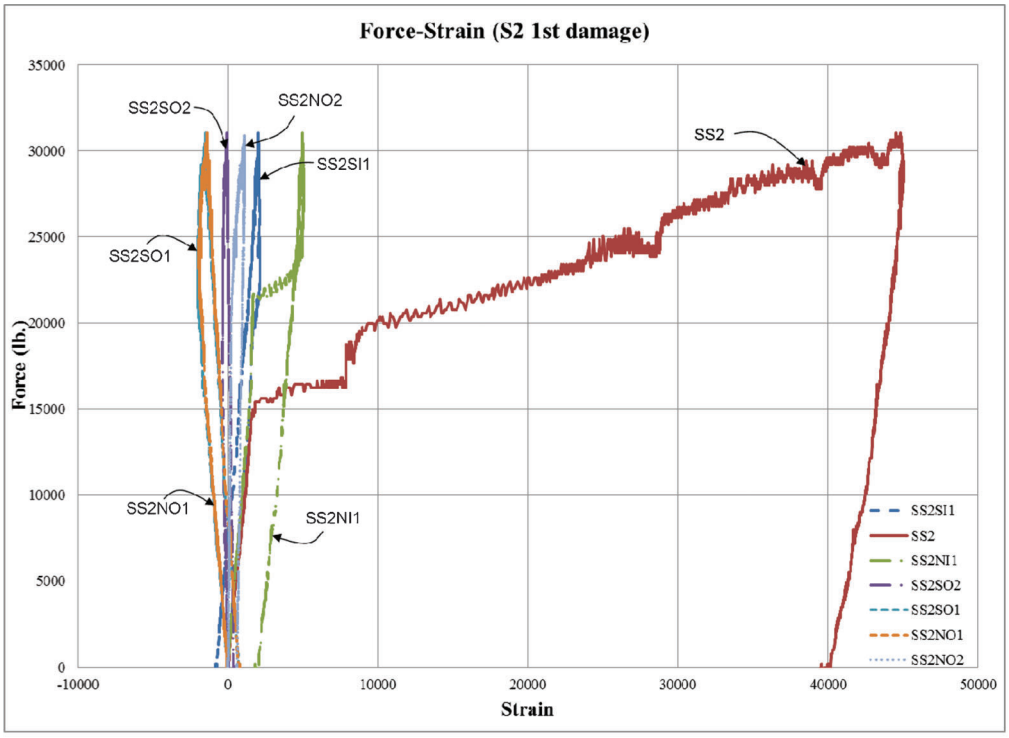

Figure 9.16 Load-strain diagram of S2 specimen.

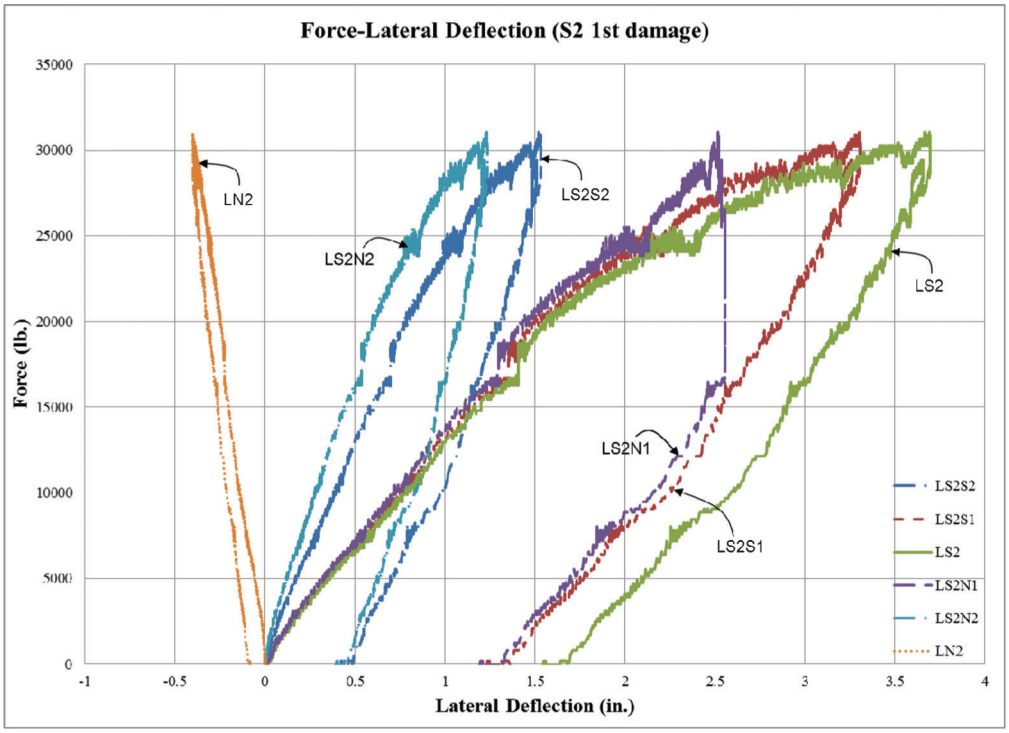

Figure 9.17 Load-displacement diagram of S2 specimen.

(a) Outside photo of S2 after repair (1)

(b) Outside photo of S2 after repair (2)

(c) Inside photo of S2 after repair (1)

(d) Inside photo of S2 after repair (2)

Figure 9.18 Photographs of S2 specimen after the repair process.

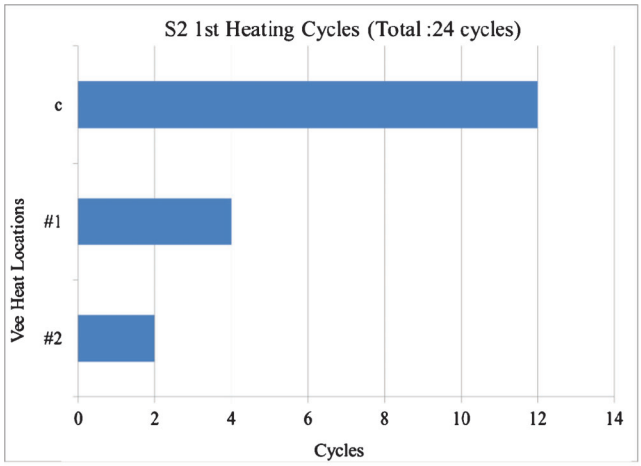

Figure 9.19 Vee heat frequency chart of S1 specimen.

TABLE 9.3
Local damage and line heat frequency of S2 specimen

Repair Cycle	Local Damage of Inside Flange (Upward—in.)	Line Heat Frequency (Inside—Cycles)	Local Damage of Outside Flange (Downward—in.)	Line Heat Frequency (Outside—Cycles)
1st	3/8	8	1/4	4

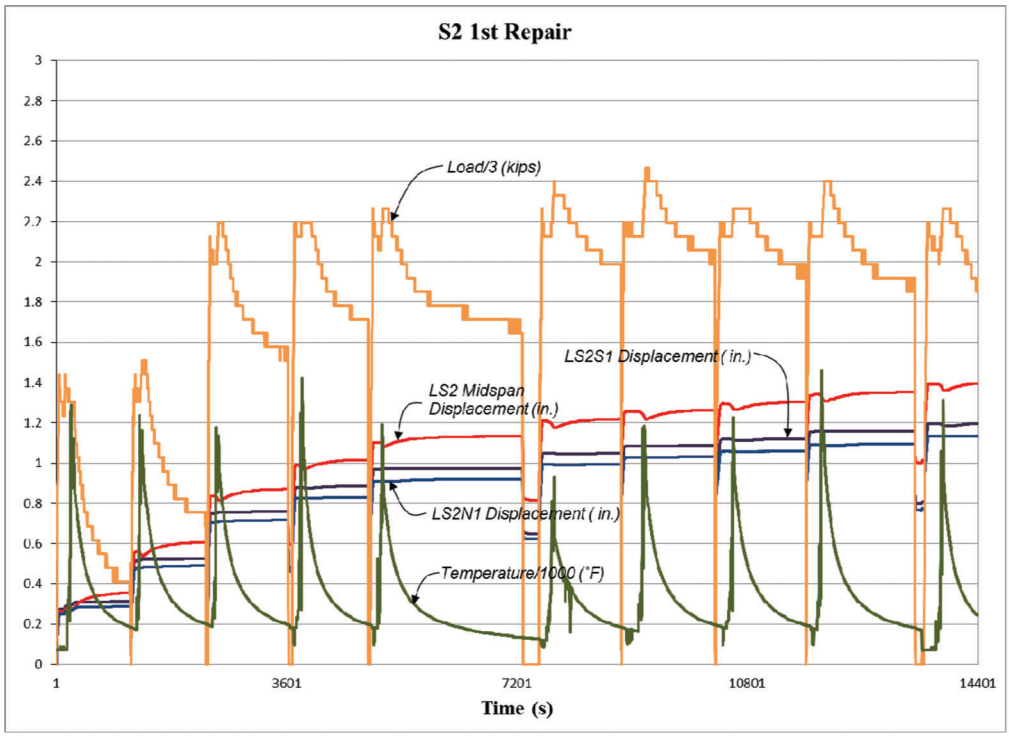

Figure 9.20 Instrument data during the repair cycle of S2 specimen.

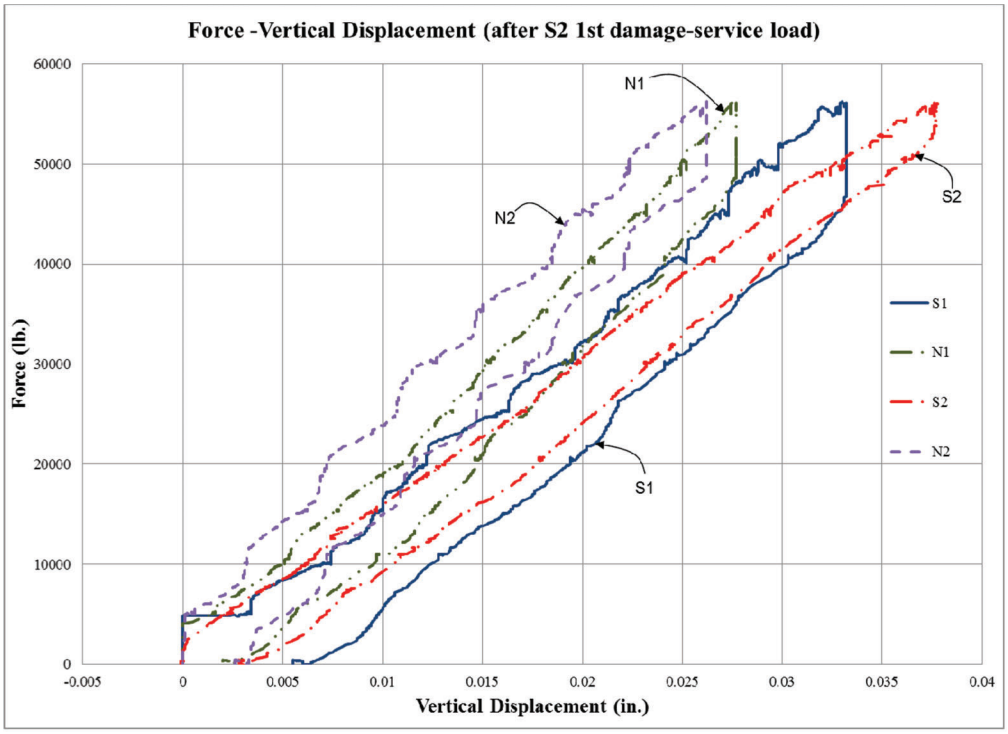

(a) Force-vertical displacement after S2 damage

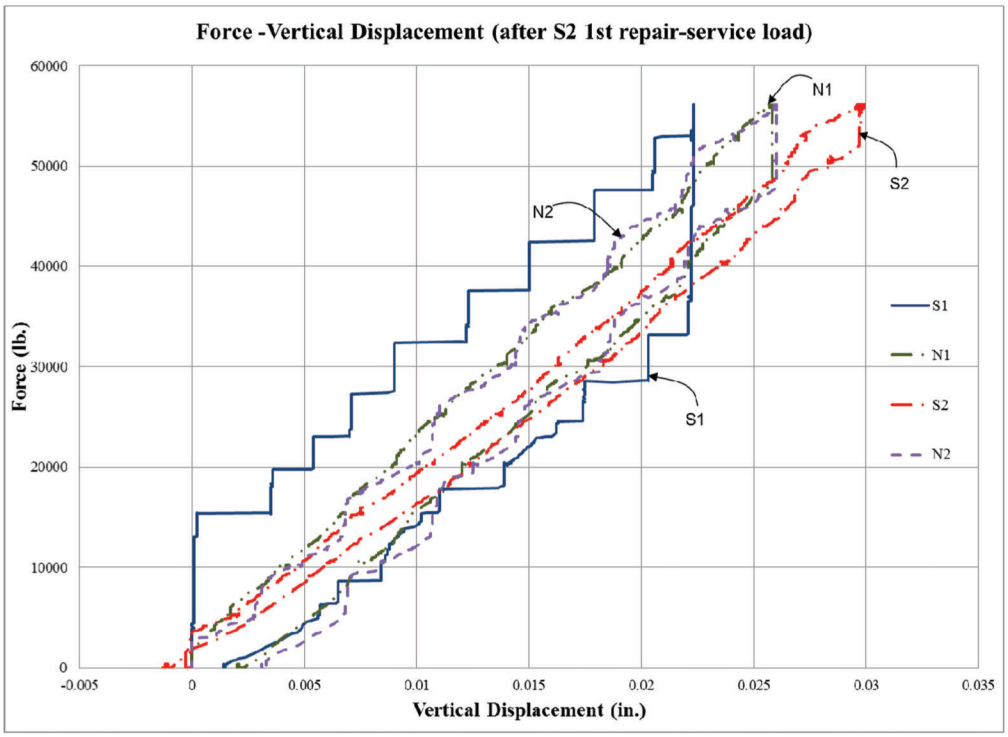

(b) Force-vertical displacement after S2 repair

Figure 9.21 Service load-vertical displacement behavior of S2 test.

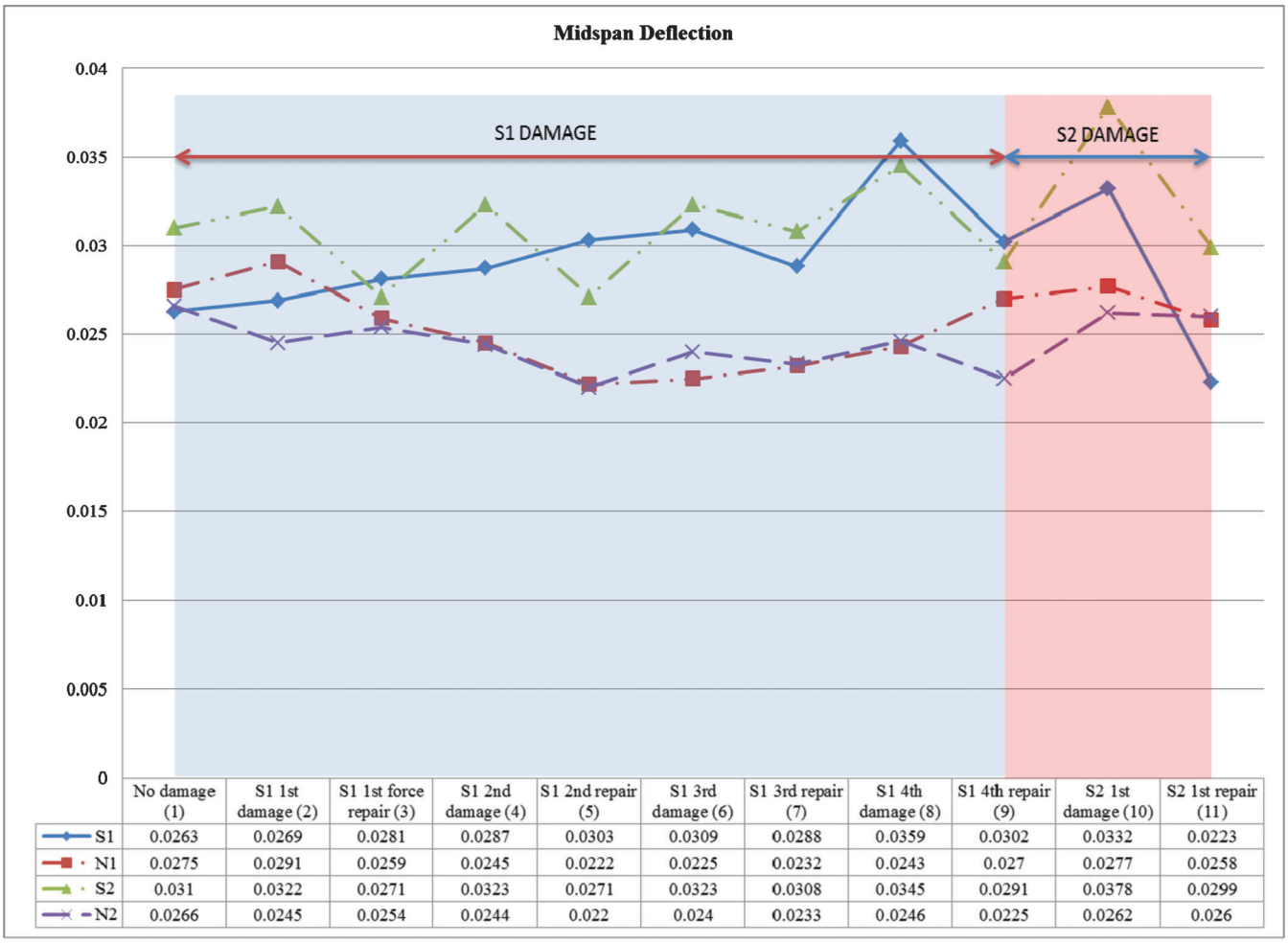

	No damage (1)	S1 1st damage (2)	S1 1st force repair (3)	S1 2nd damage (4)	S1 2nd repair (5)	S1 3rd damage (6)	S1 3rd repair (7)	S1 4th damage (8)	S1 4th repair (9)	S2 1st damage (10)	S2 1st repair (11)
S1	0.0263	0.0269	0.0281	0.0287	0.0303	0.0309	0.0288	0.0359	0.0302	0.0332	0.0223
N1	0.0275	0.0291	0.0259	0.0245	0.0222	0.0225	0.0232	0.0243	0.027	0.0277	0.0258
S2	0.031	0.0322	0.0271	0.0323	0.0271	0.0323	0.0308	0.0345	0.0291	0.0378	0.0299
N2	0.0266	0.0245	0.0254	0.0244	0.022	0.024	0.0233	0.0246	0.0225	0.0262	0.026

Figure 9.22 Midspan displacements of S1 and S2 test.

(a) N1 after 1st damage

(b) N1 after 1st repair

(c) N1 after 2nd damage

(d) N1 after 2nd repair

(e) N1 after 3rd damage

(f) N1 after 3rd repair

Figure 9.23 Photographs of N1 specimen before and after the damage.

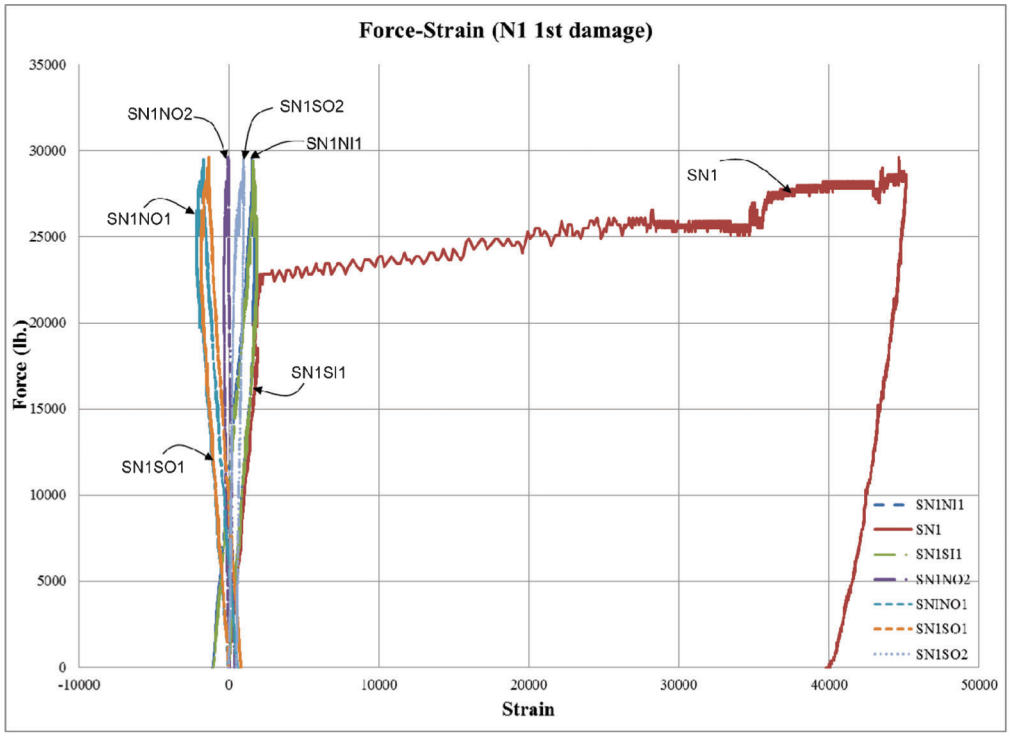

Figure 9.24 Load-strain diagram of N1 specimen.

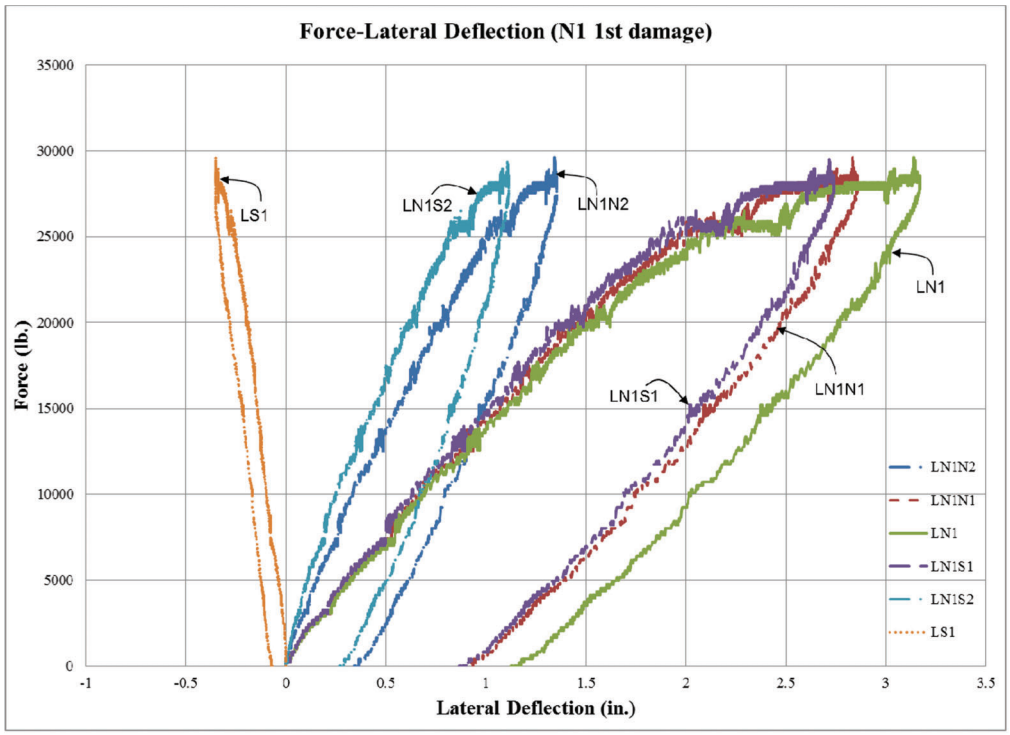

Figure 9.25 Load-displacement diagram of N1 specimen (1st damage).

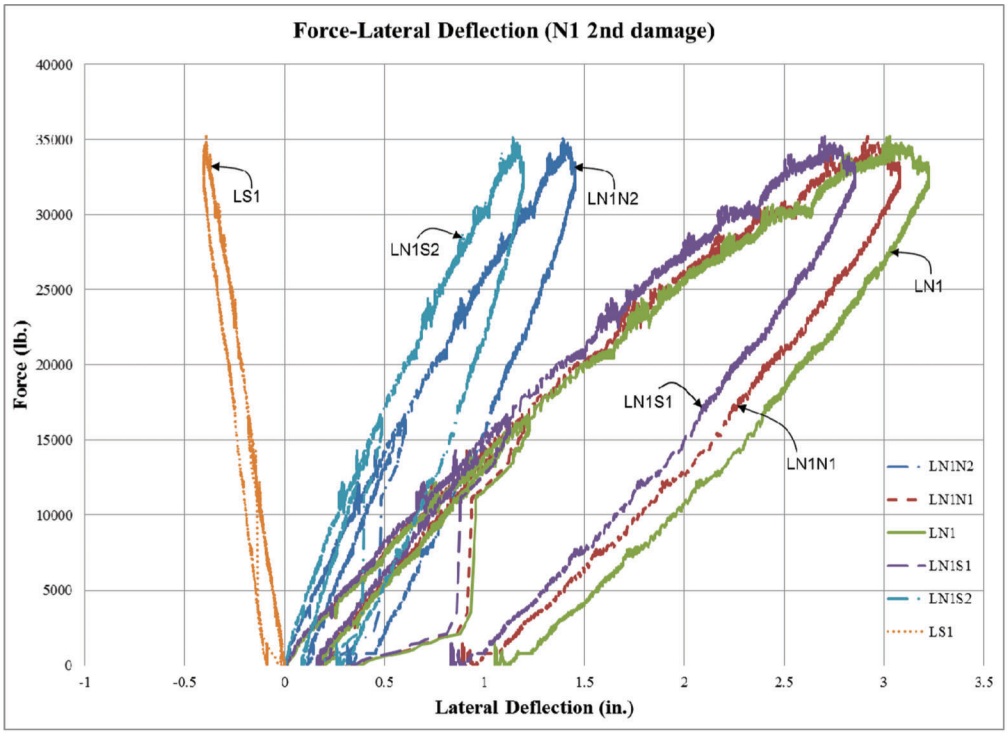

Figure 9.26 Load-displacement diagram of N1 specimen (2nd damage).

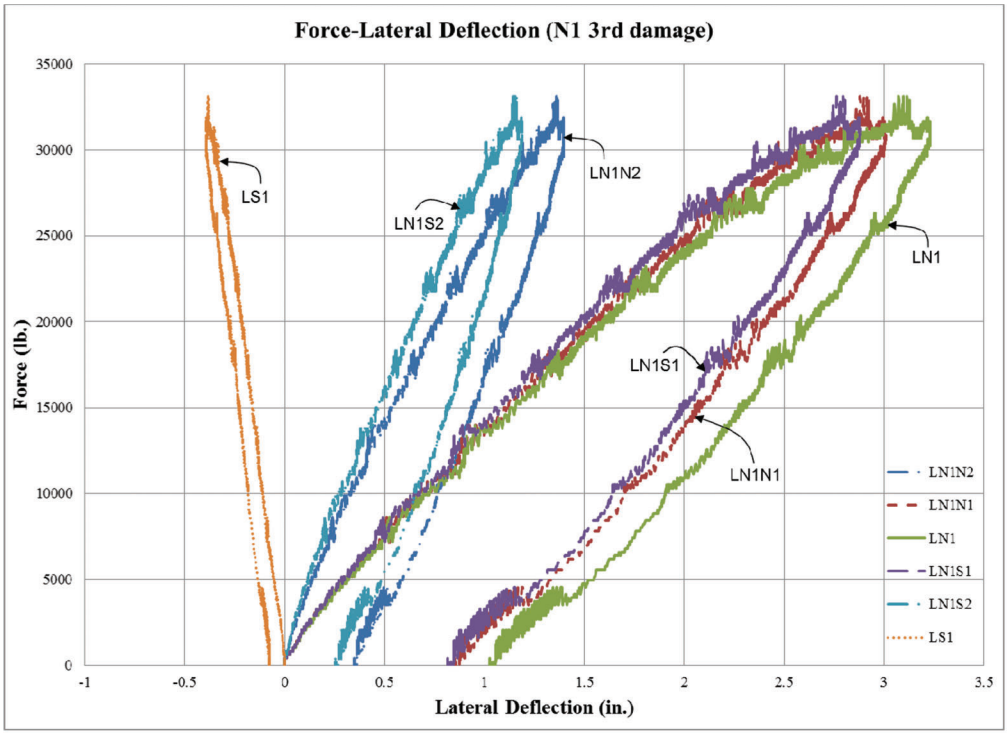

Figure 9.27 Load-displacement diagram of N1 specimen (3rd damage).

TABLE 9.4
Maximum midspan deflection of N1 specimen

Damage Cycle	At the Maximum Damage (in.)	After the Damage (in.)
1st	3.17	1.12
2nd	3.22	1.05
3rd	3.23	1.03
Avg.	**3.21**	**1.07**

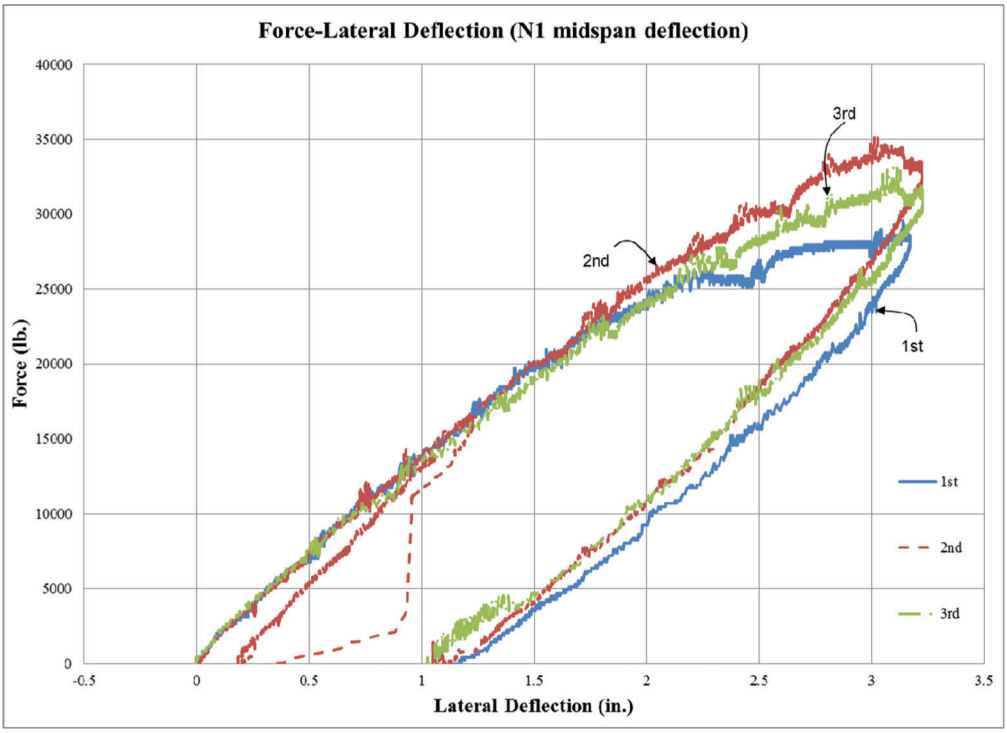

Figure 9.28 Midspan load-displacement diagram of N1 specimen (all damages).

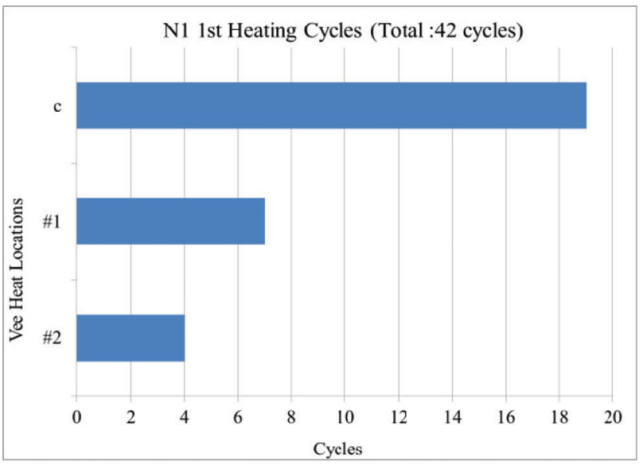

(a) Vee heat frequency of 1st repair cycle

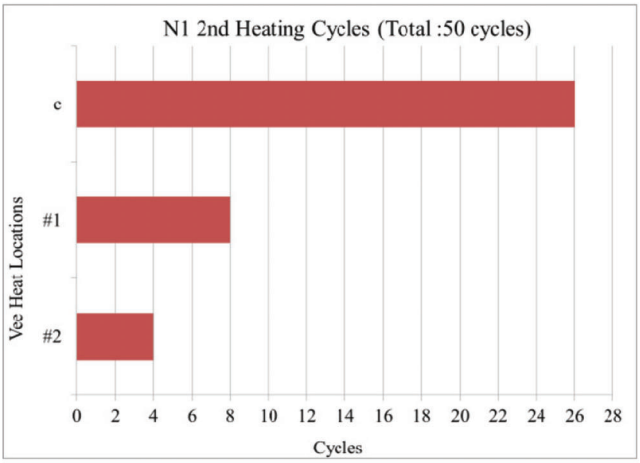

(b) Vee heat frequency of 2nd repair cycle

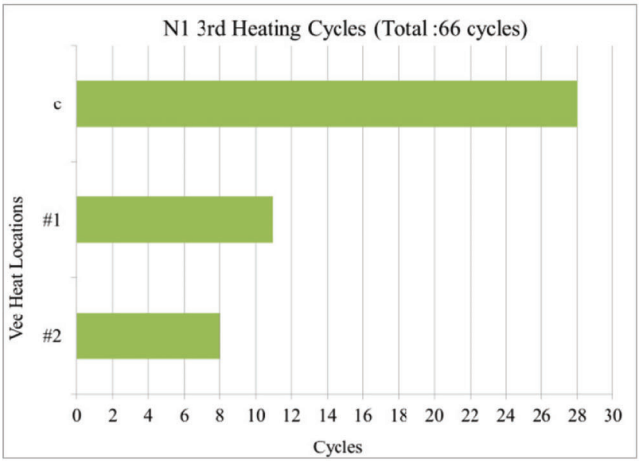

(c) Vee heat frequency of 3rd repair cycle

Figure 9.29 Vee heat frequency chart of N1 specimen.

repair process. The maximum midspan deflections in all cases were not bigger than 0.035 in. which is much smaller than the AASHTO deflection limit of 0.3 in. or 0.24 in. Therefore, the maximum midspan deflection after the N1 damage-repair process was within the AASHTO specification deflection limit.

Figure 9.33 shows the measured maximum midspan deflection values after each damage-repair cycle. The final serviceability deflections of N1 repair were not changed significantly from the undamaged serviceability deflection.

9.10 Damage Process of N2 Specimen (1-800-0.6-30)

Several sensors were used to monitor specimen behavior during the damage procedure of the N2 specimen (1-800-0.6-30). Strain sensors were located at the planned location described in Section 8.4.

Figure 9.34 shows the photographs of the beam specimen during the damage cycle. The beam specimen was damaged by monotonically increasing the concentrated force at the midspan. The damage was monitored using the longitudinal strain gages. The test was considered complete when the strain gage located at the midspan of the specimen reached 30 ε_y. The complete strain gage data for the damage cycle is shown in Figure 9.35.

P-Δ relationships for the N2 specimen are shown in Figure 9.36. The plastic displacement at the maximum damage was found to be 4.51 in. The final damage displacement after elastic rebound was 2.32 in. (See N-2 Span Damage video: http://dx.doi.org/10.4231/D38G8FH7Z)

9.11 Repair Process of N2 Specimen (1-800-0.6-30)

The repair cycle of the N2 specimen was conducted by applying external force corresponding to the restraining moment of 0.6 M_p described in Section 8.5. Vee heats were initially applied at the center (C) Vee region of the bottom flange shown in Figure 8.17. After that, other Vee regions (L1, R1-L2, R2) were heated to minimize the out-of-plane distortion of the damaged flange. Each Vee region was heated to a maximum temperature of 800 °F to see the under-heating effect combined with overstraining.

Four hundred and ten Vee heats were required to complete the repair cycle of the N2 specimen. The photographs of the repaired beam are shown in Figure 9.37. The surface of the repaired region was ground smoothly to deter undesired stress concentrations. The specimen straightness was confirmed by the tout line method which used a tout line to measure the gap distance from the specimen to the tout line. The frequency chart indicating the amount of Vee heats applied to each Vee location is shown in Figure 9.38.

After applying Vee heats to straighten the specimen, localized damage of the flange bulge was still left in the midspan at the specimen. This localized damage was repaired by the line heat method with additional jacking force described in Section 8.5. Table 9.6 presents the local damage amount of the flange bulge and the applied line heat frequency in the repair cycle of the N2 specimen.

TABLE 9.5
Local damage and line heat frequency of N1 specimen

Repair cycle	Local Damage of Inside Flange (Upward—in.)	Line Heat Frequency (Inside—Cycles)	Local Damage of Outside Flange (Downward—in.)	Line Heat Frequency (Outside—Cycles)
1st	1/2	17	1/4	4
2nd	17/16	24	1/4	5
3rd	3/16	1	5/16	6

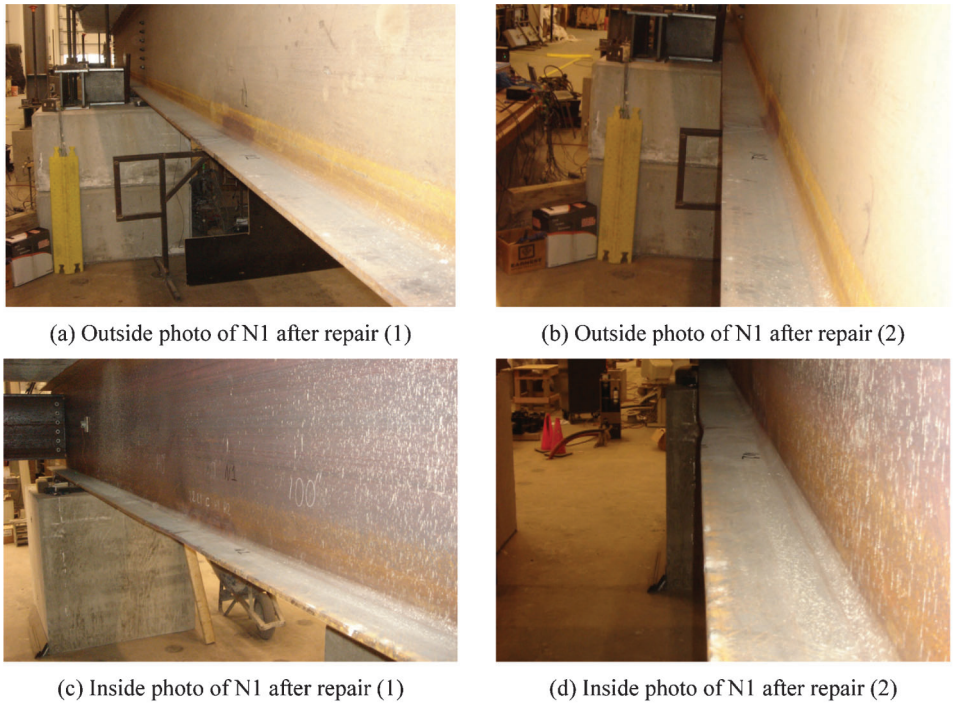

(a) Outside photo of N1 after repair (1)

(b) Outside photo of N1 after repair (2)

(c) Inside photo of N1 after repair (1)

(d) Inside photo of N1 after repair (2)

Figure 9.30 Photographs of N1 specimen after all repair processes.

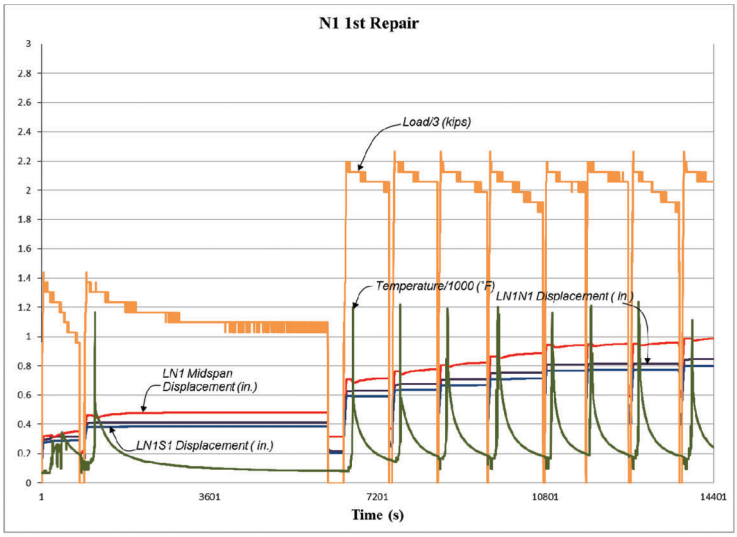

(a) 1st repair cycle

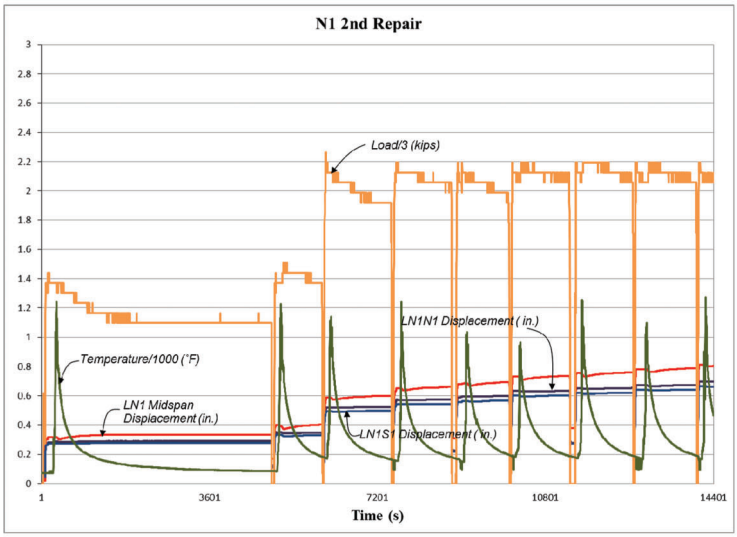

(b) 2nd repair cycle

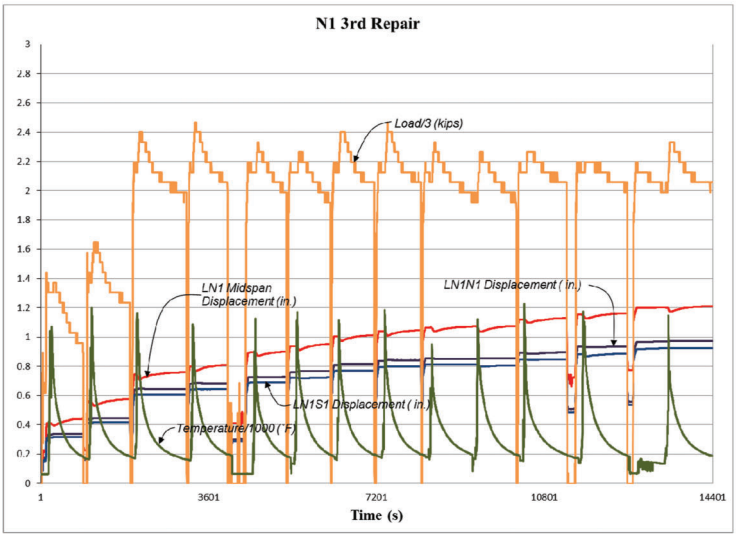

(c) 3rd repair cycle

Figure 9.31 Instrument data during repair cycles of N1 specimen.

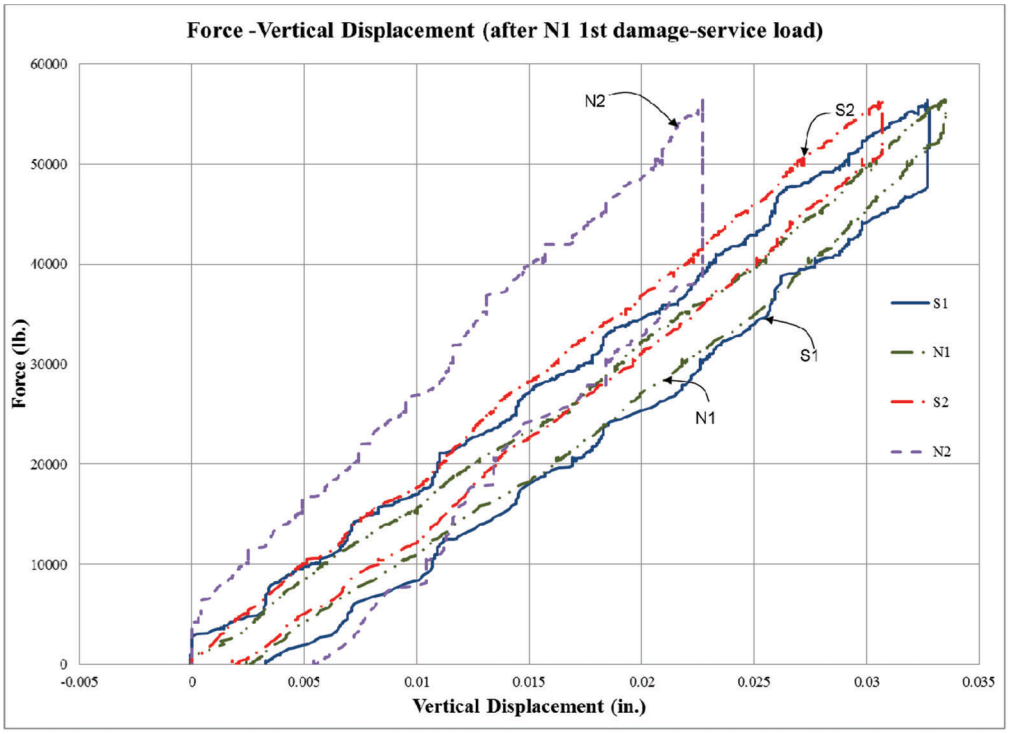

(a) Force-vertical displacement after N1 1st damage

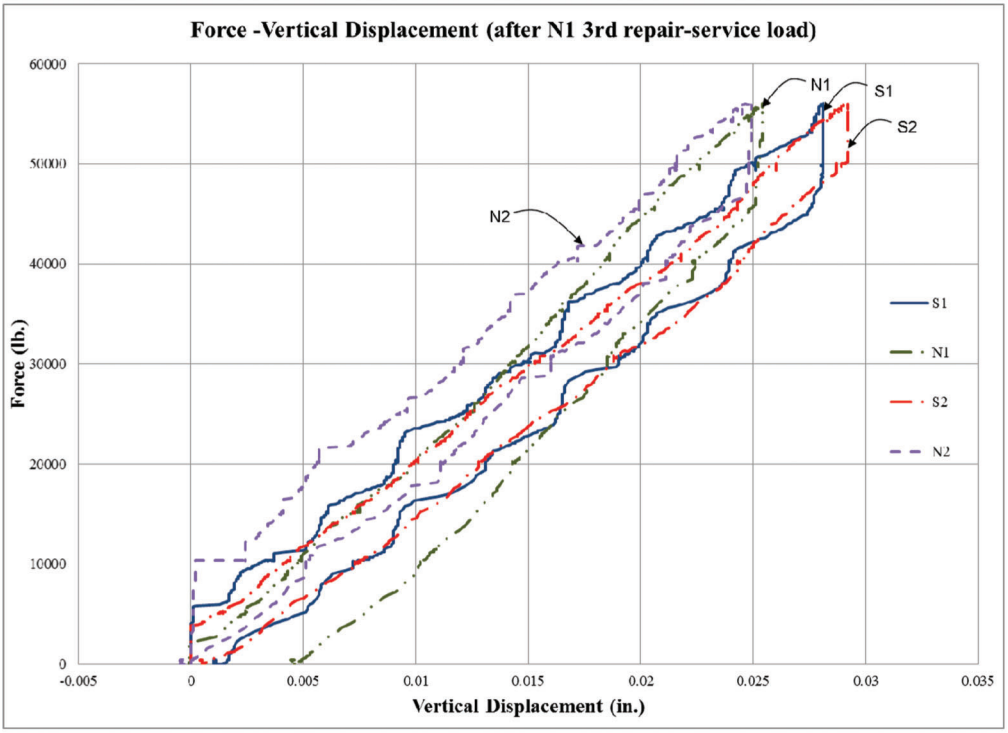

(b) Force-vertical displacement after N13rd repair

Figure 9.32 Service load-vertical displacement behavior of N1 test.

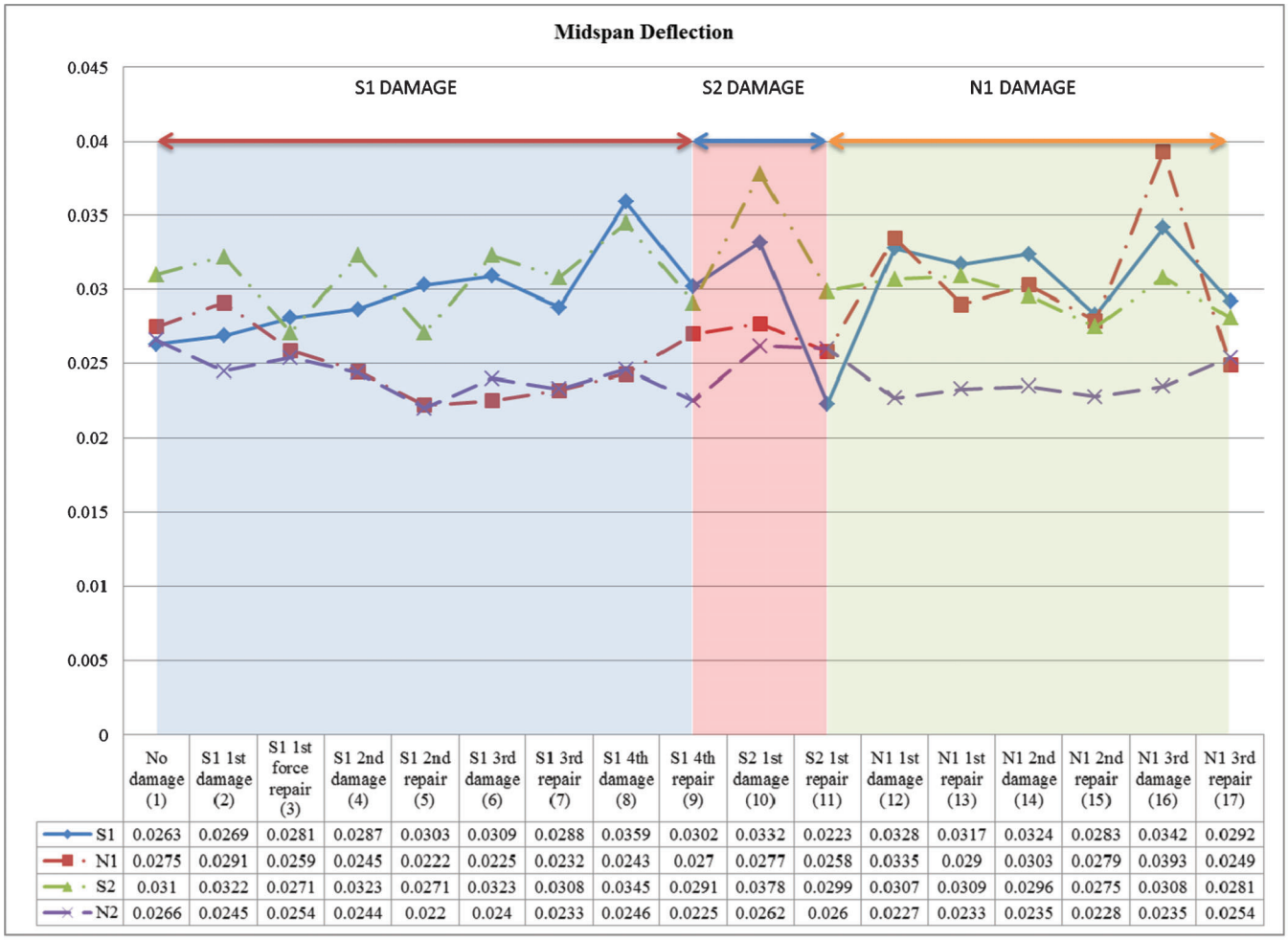

	No damage (1)	S1 1st damage (2)	S1 1st force repair (3)	S1 2nd damage (4)	S1 2nd repair (5)	S1 3rd damage (6)	S1 3rd repair (7)	S1 4th damage (8)	S1 4th repair (9)	S2 1st damage (10)	S2 1st repair (11)	N1 1st damage (12)	N1 1st repair (13)	N1 2nd damage (14)	N1 2nd repair (15)	N1 3rd damage (16)	N1 3rd repair (17)
S1	0.0263	0.0269	0.0281	0.0287	0.0303	0.0309	0.0288	0.0359	0.0302	0.0332	0.0223	0.0328	0.0317	0.0324	0.0283	0.0342	0.0292
N1	0.0275	0.0291	0.0259	0.0245	0.0222	0.0225	0.0232	0.0243	0.027	0.0277	0.0258	0.0335	0.029	0.0303	0.0279	0.0393	0.0249
S2	0.031	0.0322	0.0271	0.0323	0.0271	0.0323	0.0308	0.0345	0.0291	0.0378	0.0299	0.0307	0.0309	0.0296	0.0275	0.0308	0.0281
N2	0.0266	0.0245	0.0254	0.0244	0.022	0.024	0.0233	0.0246	0.0225	0.0262	0.026	0.0227	0.0233	0.0235	0.0228	0.0235	0.0254

Figure 9.33 Midspan displacements of S1, S2, and N1 test.

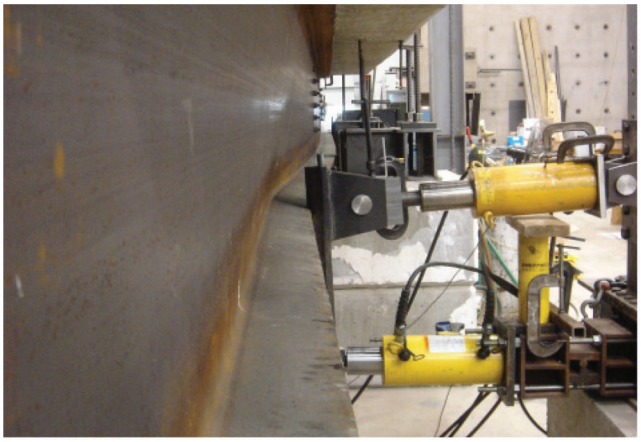

(a) Damage application of N2 specimen

(b) Damaged N2 specimen

Figure 9.34 Damage photographs of N2 specimen (1-800-0.6-30).

Figure 9.39 shows the behavior of the N2 specimen in the initial several steps of the repair cycle. This figure includes: (a) the displacements from three inside displacement transducers in inches, (b) the restraining force in the hydraulic actuator in kips, which is divided by 3 (i.e., 1.0 on the graph shows 3 kips of force), and (c) the temperature of the steel in °F, which is divided by 1000 °F (i.e., 1.0 on the graph corresponds to 1000 °F).

9.12 Serviceability Behavior of N2 Specimen (1-800-0.6-30)

The serviceability performance of the test bridge during the N2 damage-repair process was determined by simultaneously subjecting each midspan of test bridge to 56 kips of static loading. All vertical midspan displacements of the test bridge were measured and compared with previous serviceability performance results.

Figure 9.40 shows the serviceability behavior of the test bridge after the N2 damage and the N2 repair process. The maximum midspan deflections in all cases were not bigger than 0.045 in. which is much smaller than the AASHTO deflection limit of 0.3 in. or 0.24 in. Therefore, the maximum midspan deflection after the N2 damage-repair process was within the AASHTO specification deflection limit.

Figure 9.41 shows the measured maximum midspan deflection values after each damage-repair cycle. The final serviceability deflections of the N2 repair were not changed significantly from the undamaged serviceability deflection.

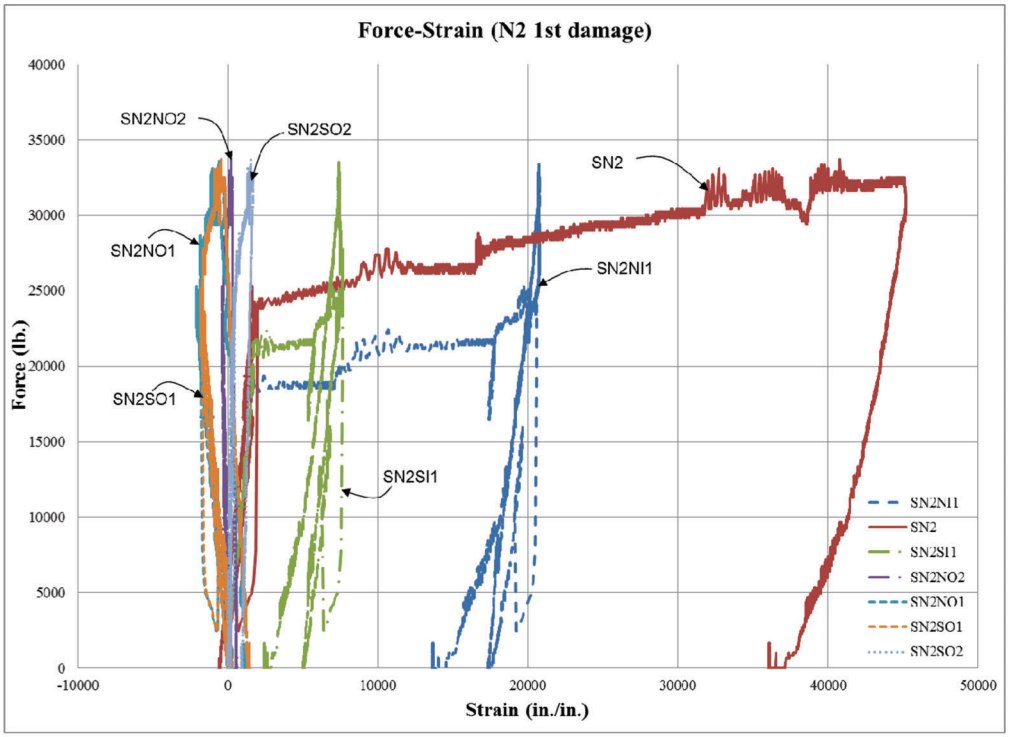

Figure 9.35 Load-strain diagram of N2 specimen.

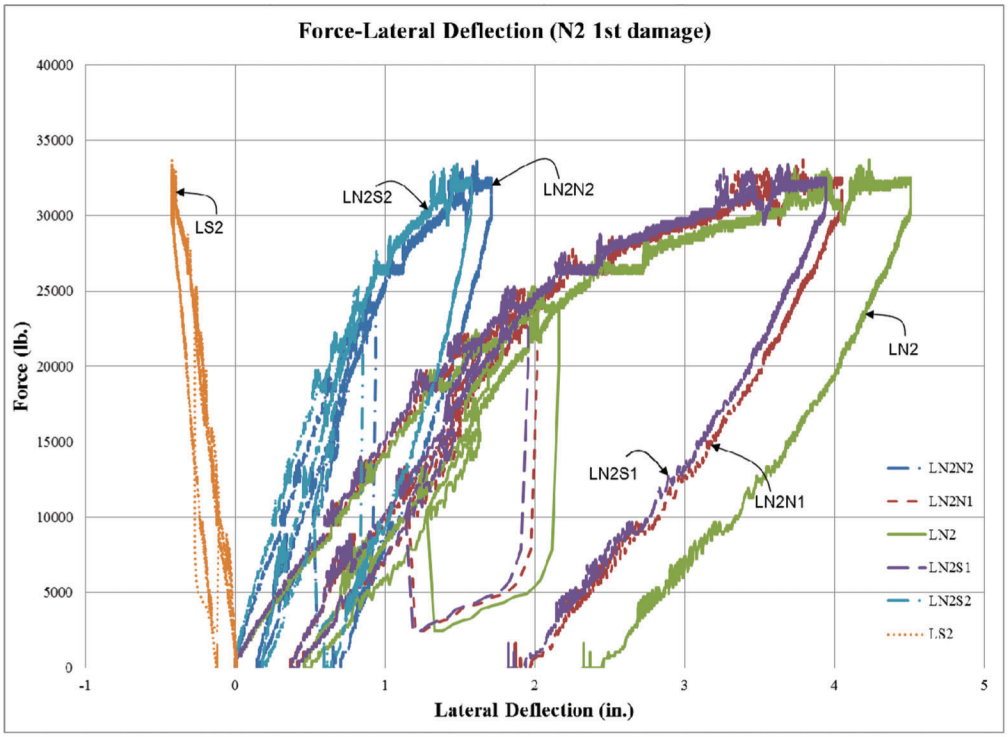

Figure 9.36 Load-displacement diagram of N2 specimen.

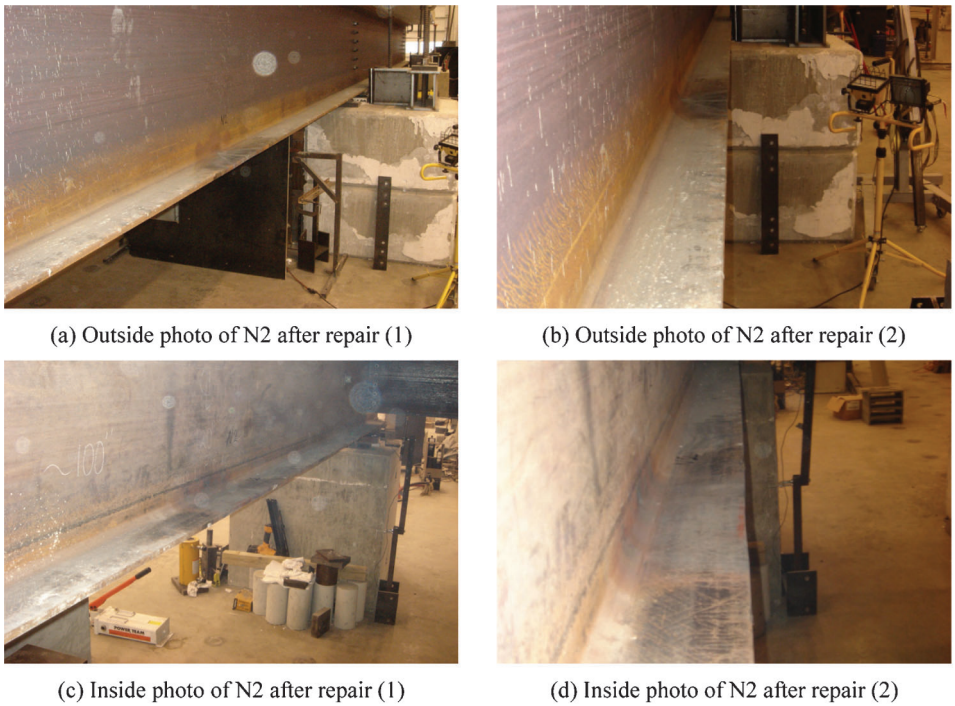

(a) Outside photo of N2 after repair (1)

(b) Outside photo of N2 after repair (2)

(c) Inside photo of N2 after repair (1)

(d) Inside photo of N2 after repair (2)

Figure 9.37 Photographs of N2 specimen after the repair process.

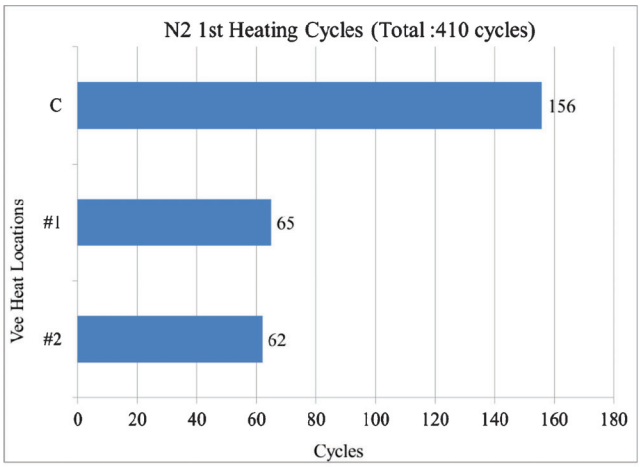

Figure 9.38 Vee heat frequency chart of N2 specimen.

TABLE 9.6
Local damage and line heat frequency of N2 specimen

Repair cycle	Local Damage of Inside Flange (Upward—in.)	Line Heat Frequency (Inside—Cycles)	Local Damage of Outside Flange (Downward—in.)	Line Heat Frequency (Outside—Cycles)
1st	5/16	37	1	17

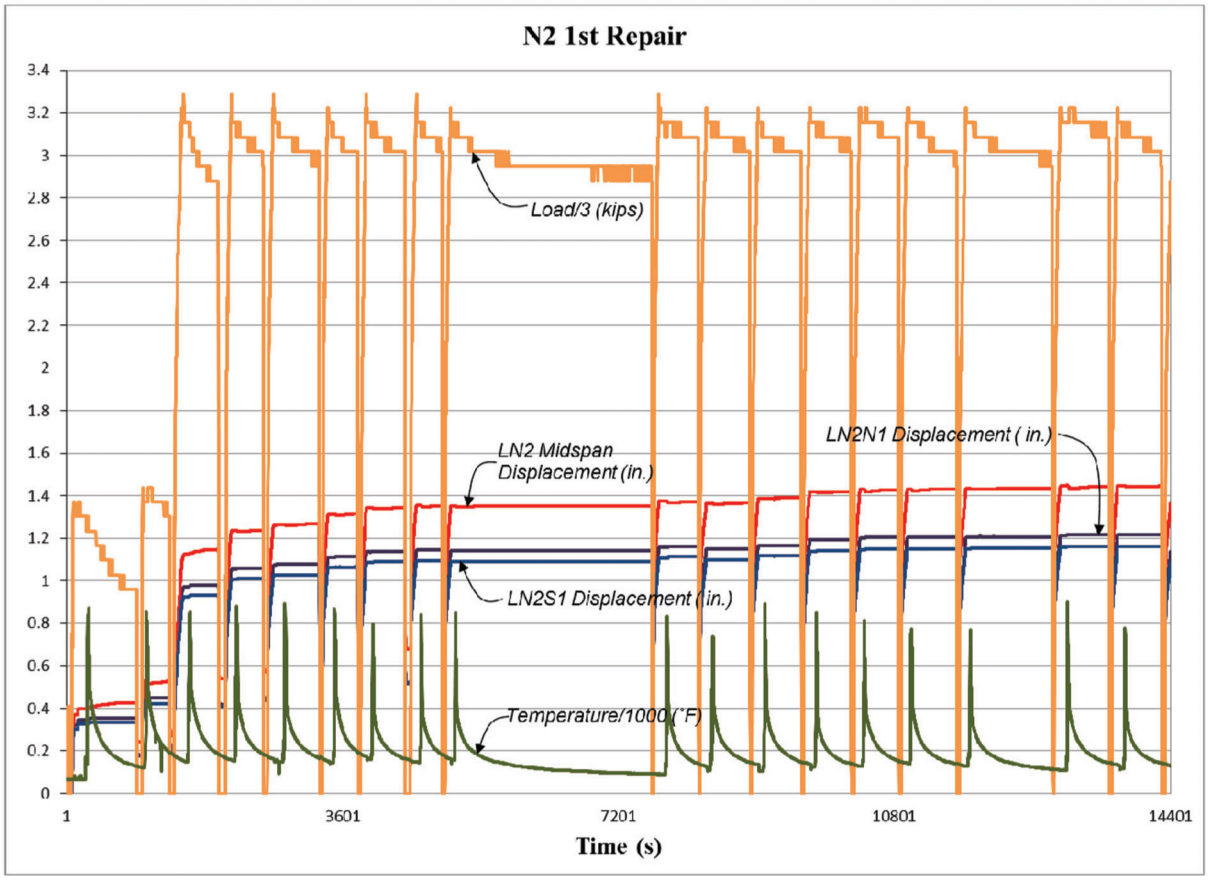

Figure 9.39 Instrument data during the repair cycle of N2 specimen.

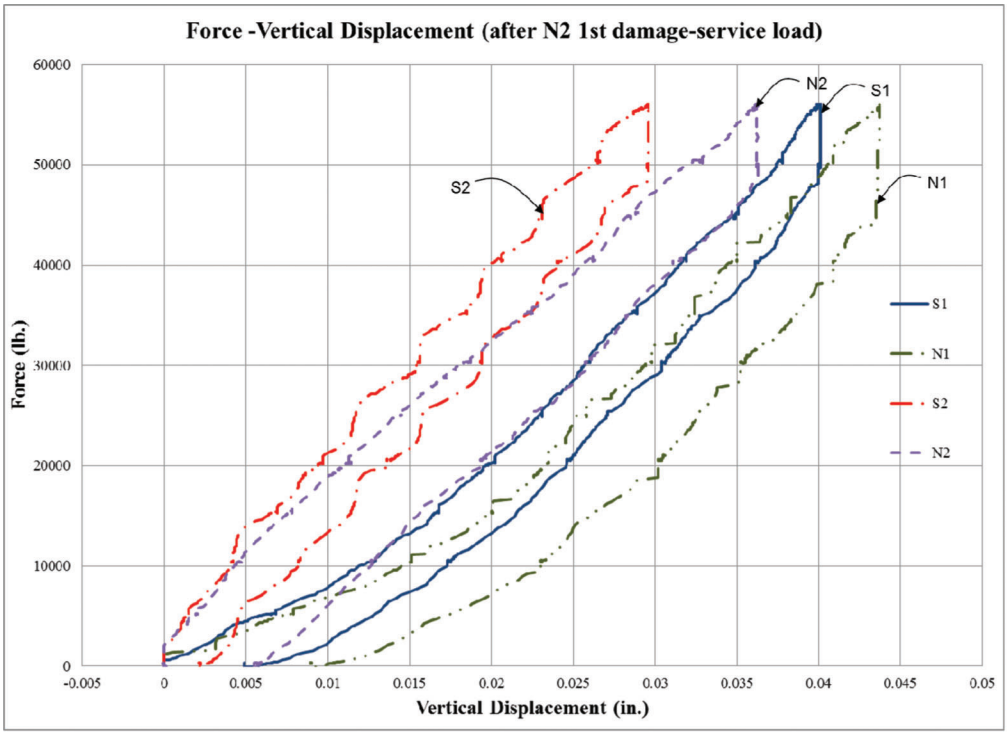

(a) Force-vertical displacement after N2 damage

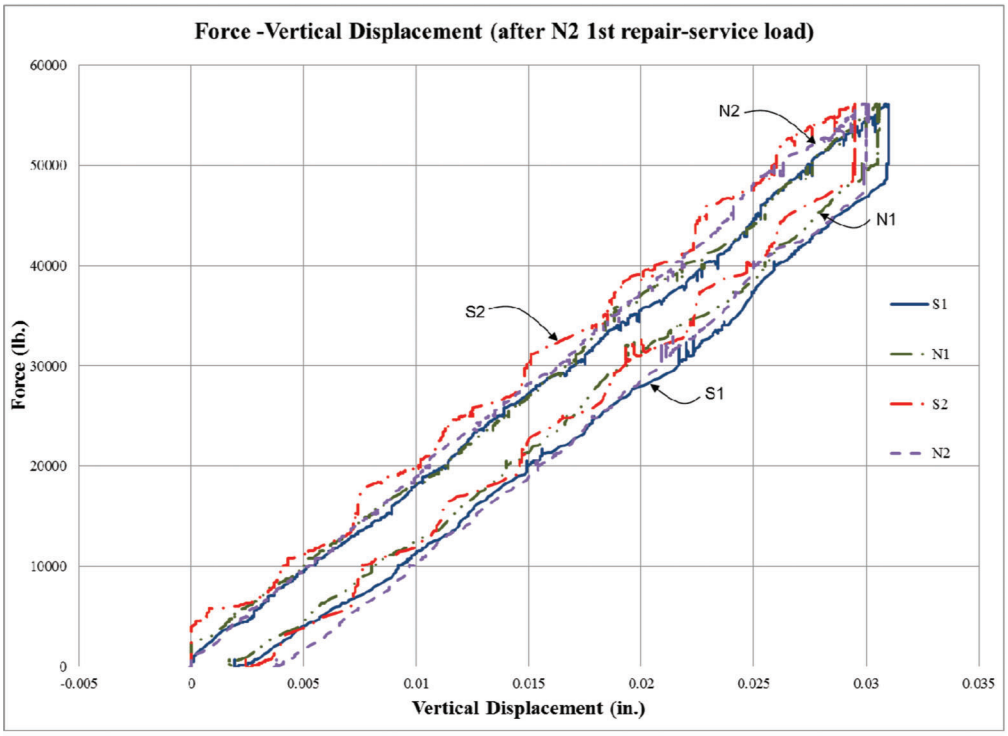

(b) Force-vertical displacement after N2 repair

Figure 9.40 Service load-vertical displacement behavior of N2 test.

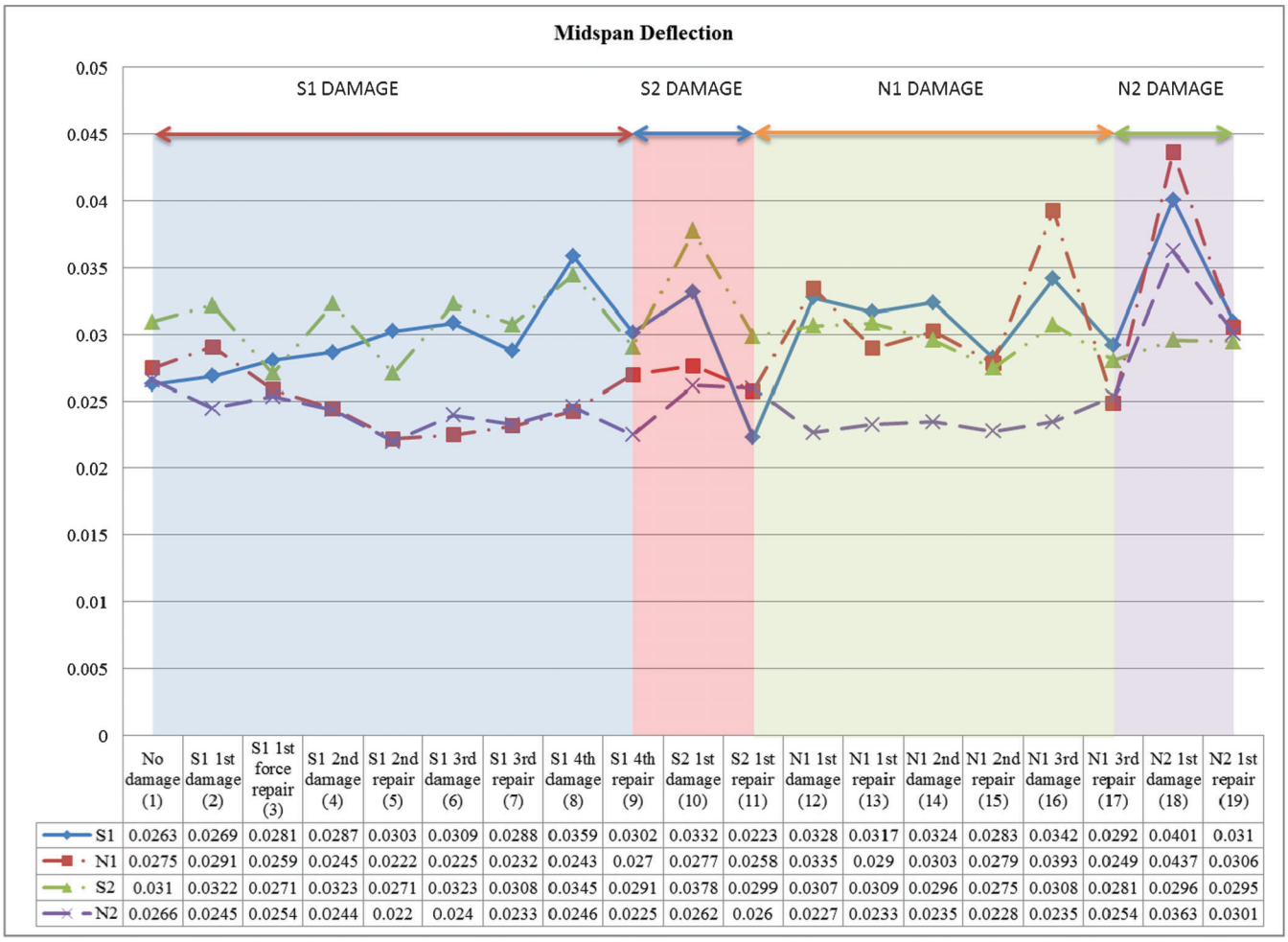

	No damage (1)	S1 1st damage (2)	S1 1st force repair (3)	S1 2nd damage (4)	S1 2nd repair (5)	S1 3rd damage (6)	S1 3rd repair (7)	S1 4th damage (8)	S1 4th repair (9)	S2 1st damage (10)	S2 1st repair (11)	N1 1st damage (12)	N1 1st repair (13)	N1 2nd damage (14)	N1 2nd repair (15)	N1 3rd damage (16)	N1 3rd repair (17)	N2 1st damage (18)	N2 1st repair (19)
S1	0.0263	0.0269	0.0281	0.0287	0.0303	0.0309	0.0288	0.0359	0.0302	0.0332	0.0223	0.0328	0.0317	0.0324	0.0283	0.0342	0.0292	0.0401	0.031
N1	0.0275	0.0291	0.0259	0.0245	0.0222	0.0225	0.0232	0.0243	0.027	0.0277	0.0258	0.0335	0.029	0.0303	0.0279	0.0393	0.0249	0.0437	0.0306
S2	0.031	0.0322	0.0271	0.0323	0.0271	0.0323	0.0308	0.0345	0.0291	0.0378	0.0299	0.0307	0.0309	0.0296	0.0275	0.0308	0.0281	0.0296	0.0295
N2	0.0266	0.0245	0.0254	0.0244	0.022	0.024	0.0233	0.0246	0.0225	0.0262	0.026	0.0227	0.0233	0.0235	0.0228	0.0235	0.0254	0.0363	0.0301

Figure 9.41 Midspan displacements of S1, S2, N1, and N2 test

10. LARGE SCALE TEST: MATERIAL TEST

This chapter presents the results of the material tests conducted on samples machined from the flanges of undamaged and damaged-repaired large scale test specimens. The material tests included: (a) uniaxial tension tests, (b) Charpy V-notch tests, (c) Rockwell hardness tests, and (d) microstructure investigations. The material tests were conducted following the ASTM standard test method that was applicable to each material test as described in Section 8.6.

10.1 Charpy Impact Fracture Toughness Tests

Charpy V-notch specimens were removed from the midspan of the bottom flange of all test specimens as shown in Figure 8.24. One additional flange plate from the undamaged part of the test bridge was prepared to fabricate additional Charpy test coupons to determine the undamaged fracture toughness of the test bridge. The Charpy V notch impact fracture test was conducted at 40 °F as recommended for zone 2 by AASHTO (*40*).

The results of the fracture toughness tests on CVN specimens taken from the large scale test specimens are listed in Table 10.1. Averages and standard deviations were taken both across the width of the flanges (i.e., averages of 1, 2, and 3) and along the flange length (i.e., averages of L1, C, and R1). The overall average values and standard deviations of all nine Charpy specimens are also provided in Table 10.1. These fracture toughness values were normalized with respect to the average (mean) fracture toughness of the undamaged plate, which is also presented in Table 10.1.

Table 10.2 provides the means, standard deviations, 95% confidence intervals for the actual mean, medians, and absolute average deviations from the median for the nine Charpy specimens removed from each specimen.

Figure 10.1 shows the average Charpy fracture toughness test results of all specimens with standard deviation error bars. The results are shown in the order of the magnitude of fracture toughness values. The AASHTO requirements for Zone 2 fracture critical (25 ft·lb @ 40 °F) and nonfracture critical members (15

TABLE 10.1
Fracture toughness test results of large scale test

	S1 Specimen					Normalized S1				
	L1	**C**	**R1**	**Avg.**	**Std. Dev.**	**L1**	**C**	**R1**	**Avg.**	**Std. Dev.**
1	98	56	64	72.7	18.21	0.40	0.23	0.26	0.30	0.07
2	220	26	63	103.0	84.10	0.90	0.11	0.26	0.42	0.34
3	41	15	12	22.7	13.02	0.17	0.06	0.05	0.09	0.05
Avg.	119.7	32.3	46.3	**66.1**		0.49	0.13	0.19	**0.27**	
Std. Dev.	74.67	17.33	24.28		**60.18**	0.31	0.07	0.10		**0.25**
	S2 Specimen					**Normalized S2**				
1	95	92	100	95.7	3.30	0.39	0.38	0.41	0.39	0.01
2	59	104	94	85.7	19.29	0.24	0.43	0.39	0.35	0.08
3	39	74	49	54.0	14.72	0.16	0.30	0.20	0.22	0.06
Avg.	64.3	90.0	81.0	**78.4**		0.26	0.37	0.33	**0.32**	
Std. Dev.	23.17	12.33	22.76		**22.70**	0.10	0.05	0.09		**0.09**
	N1 Specimen					**Normalized N1**				
1	73	71	17	53.7	25.94	0.30	0.29	0.07	0.22	0.11
2	84	83	40	69.0	20.51	0.34	0.34	0.16	0.28	0.08
3	33	34	12	26.3	10.14	0.14	0.14	0.05	0.11	0.04
Avg.	63.3	62.7	23.0	**49.7**		0.26	0.26	0.09	**0.20**	
Std. Dev.	21.91	20.85	12.19		**26.65**	0.09	0.09	0.05		**0.11**
	N2 Specimen					**Normalized N2**				
1	103	84	153	113.3	29.10	0.42	0.34	0.63	0.46	0.12
2	25	91	99	71.7	33.16	0.10	0.37	0.41	0.29	0.14
3	9	55	82	48.7	30.14	0.04	0.23	0.34	0.20	0.12
Avg.	45.7	76.7	111.3	**77.9**		0.19	0.31	0.46	**0.32**	
Std. Dev.	41.06	15.58	30.27		**40.84**	0.17	0.06	0.12		**0.17**
	Undamaged Specimen					**Normalized Undamaged**				
1	246	238	248	244.0	4.32	1.01	0.98	1.02	1.00	0.02
2	235	249	249	244.3	6.60	0.96	1.02	1.02	1.00	0.03
3	234	247	249	243.3	6.65	0.96	1.01	1.02	1.00	0.03
Avg.	238.3	244.7	248.7	**243.9**		0.98	1.00	1.02	**1.00**	
Std. Dev.	5.44	4.78	0.47		**5.97**	0.02	0.02	0.00		**0.02**

TABLE 10.2
Statistical values of fracture toughness test results

Statistical Property	**S1**	**S2**	**N1**	**N2**	**Undamaged**
Mean	66.1	78.4	49.7	77.9	243.9
Std. Dev.	63.8	24.1	28.3	43.3	6.3
95% High	115.2	97.0	71.4	111.2	248.8
95% Low	17.0	59.9	27.9	44.6	239.0
Median	56.0	92.0	40.0	84.0	247.0
Average Absolute From Median	39.0	19.1	23.9	30.6	4.7

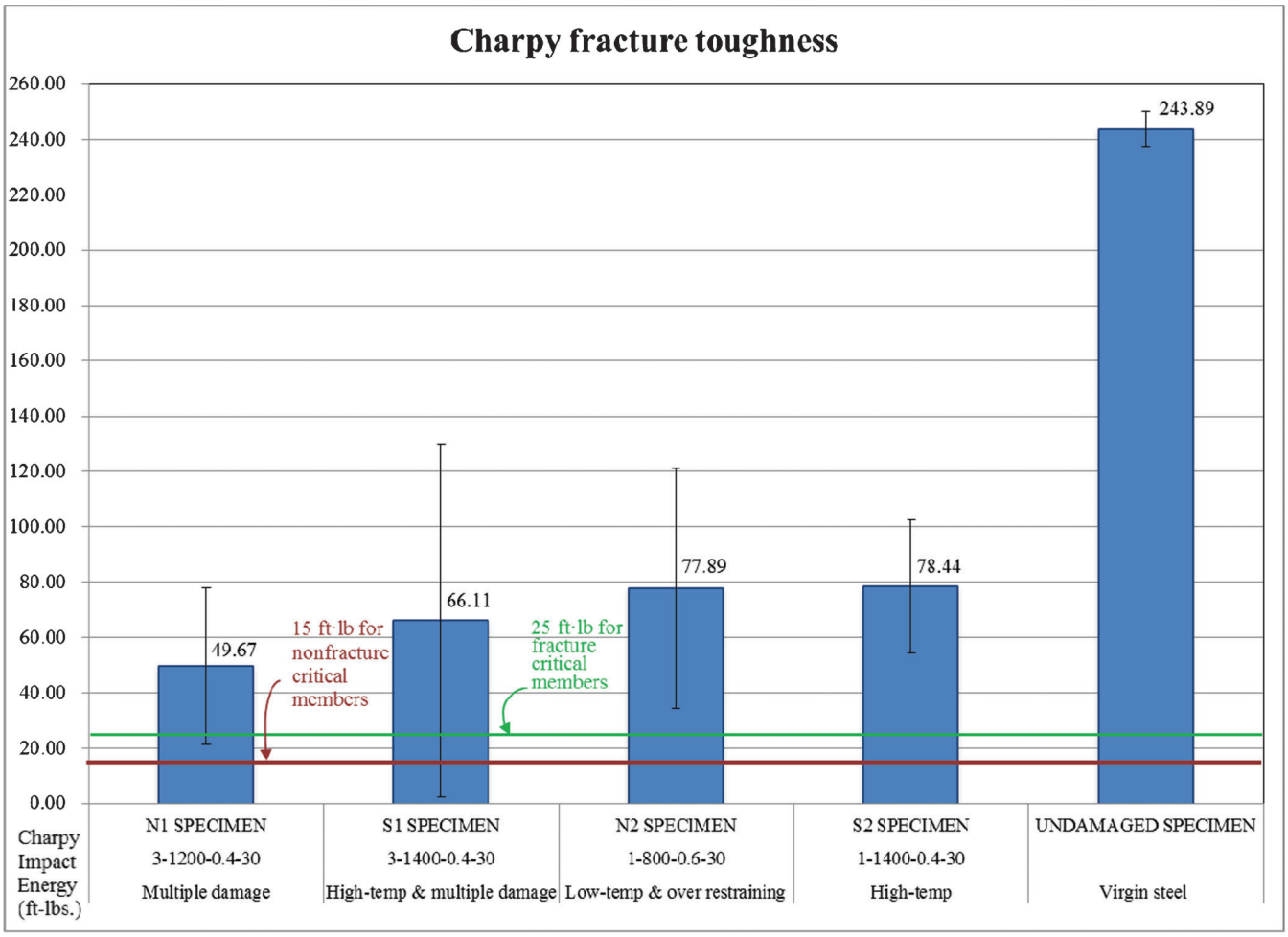

Figure 10.1 Charpy fracture toughness of large scale specimens.

ft·lb @ 40 °F) are also shown in Figure 10.1. Figure 10.2 shows the normalized fracture toughness of the Charpy specimens from the damaged-repaired beams. As seen in the graph, the N1 specimen shows the lowest average Charpy fracture toughness values.

The statistical difference between the fracture toughness values of the undamaged specimen and all the damaged-repaired specimens were evaluated by conducting a student's t test. A student's t test which evaluates the statistical difference between two data groups using their means, standard deviations, and the sizes of samples was performed by using the Excel 2010 data analysis tool. The results from the student's t test contained the t-value and the corresponding probability of the null hypothesis, which implies that the data groups are statistically similar.

Table 10.3 compares the fracture toughness of the undamaged specimen and all other damaged-repaired specimens using the student's t test evaluation. As seen in Table 10.3, all four damaged-repaired specimens show much less than 0.01% probability which means that there is no statistical similarity between the undamaged fracture toughness values and the toughness of all other damaged-repaired specimens.

Table 10.4 shows the fracture toughness comparisons between all damaged-repaired specimens. The probabilities of all comparisons range from 0.03% to 97%. S2 and N2 specimens showed most similar fracture toughness test results (97%). While, S2 and N1 had no similarity between the fracture toughness of those two specimens (0.03%)

The data presented in this section indicates that:

- The overall fracture toughness of the large scale tests was much lower than the undamaged steel toughness (27% of undamaged fracture toughness value)
- Compared with the normal heating specimen (1200 °F), the fracture toughness of the overheated specimen (1400 °F) increased [comparison of S1 with N1].
- The 1-800-0.6-30 specimen (underheating and overstraining) showed almost the same fracture toughness as the 1-1400-0.3-30 specimen [comparison of S2 with N2].
- The fracture toughness of the multiple damage-repair specimen (S1) decreased to 84% of the single damage-repair specimen (S2) toughness [comparison of S1 with S2].
- For all Charpy specimens, the fracture toughness values became smaller closer to the flange-web junction.
- Five individual Charpy coupons showed their fracture toughness values smaller than the fracture critical

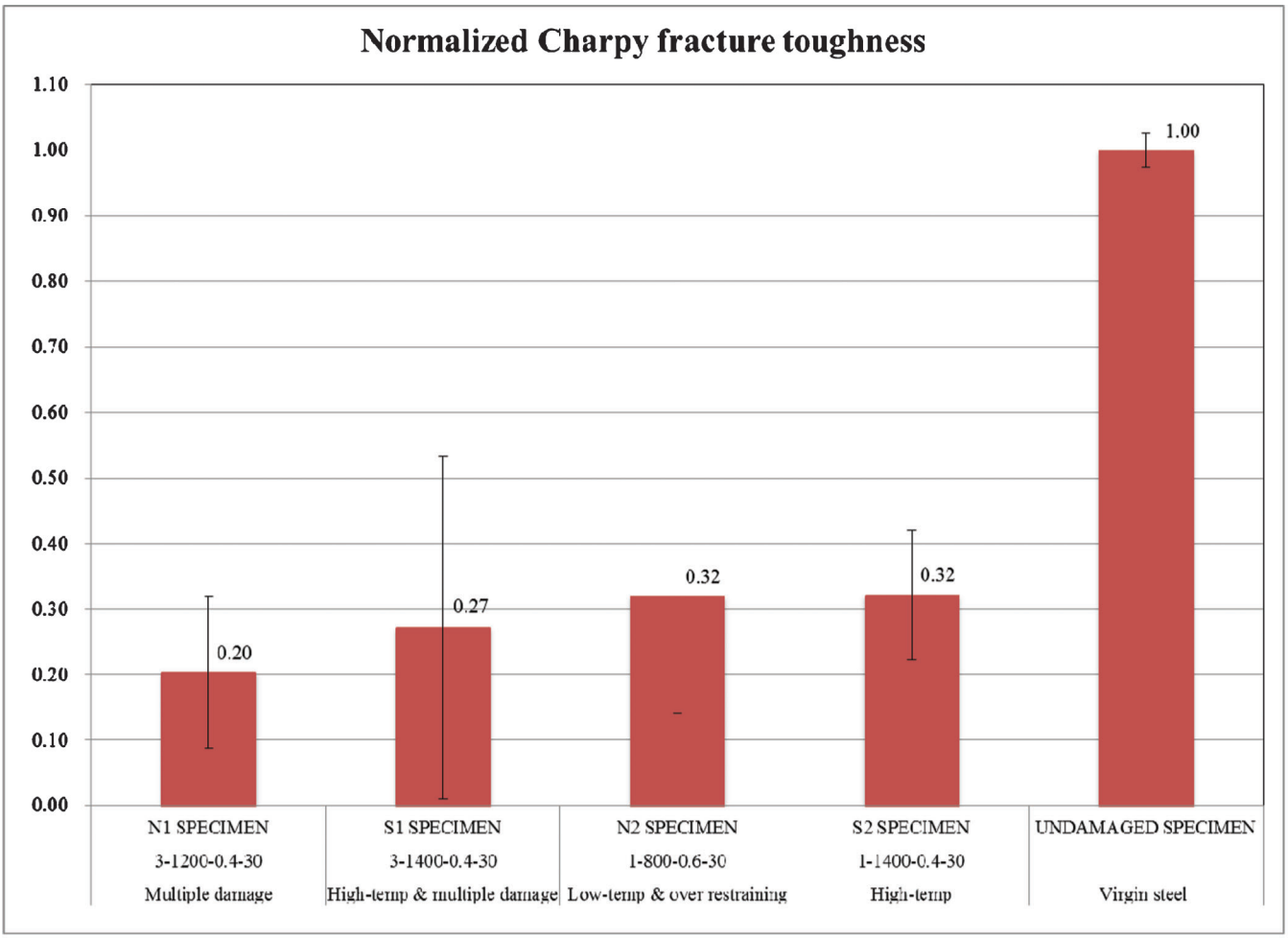

Figure 10.2 Normalized Charpy fracture toughness of large scale specimens.

TABLE 10.3
Statistical values of fracture toughness test results

	Unpaired t-test with Undamaged Specimen and			
Property	**S1**	**S2**	**N1**	**N2**
Degrees of freedom	16	16	16	16
Standard deviation	45.4	17.6	20.5	31.0
t value	8.31	19.94	20.11	11.38
Probability of null hypothesis	< 0.0001 3.35E-07	< 0.0001 1.01E-12	< 0.0001 8.76E-13	< 0.0001 4.44E-09

TABLE 10.4
Statistical values of fracture toughness test results

	Unpaired t-test with					
Property	**S1 & S2**	**S1 & N1**	**S1 & N2**	**S2 & N1**	**S2 & N2**	**N1 & N2**
Degrees of freedom	16	16	16	16	16	16
Standard deviation	48.2	49.4	54.5	26.3	35.0	36.6
t value	0.54	0.71	0.46	2.33	0.03	1.64
Probability of null hypothesis	0.60	0.49	0.65	0.03	0.97	0.12

TABLE 10.5
Uniaxial tension test results

Specimen ID	Specimen Designation	Coupon ID	Yield Stress (ksi)	Ultimate Stress (ksi)	Elongation (%)	Reduction in Area (%)
S1	3-1400-0.4-30	1-XL	46.20	65.00	34.00	63.00
		1-XR	45.90	68.50	33.00	66.00
		avg.	**46.05**	**66.75**	**33.50**	**64.50**
S2	1-1400-0.4-30	2-XL	47.60	64.50	36.00	67.00
		2-XR	50.00	66.00	35.00	64.00
		avg.	**48.80**	**65.25**	**35.50**	**65.50**
N1	3-1200-0.4-30	3-XL	56.00	69.50	31.00	64.00
		3-XR	59.50	73.00	28.00	64.00
		avg.	**57.75**	**71.25**	**29.50**	**64.00**
N2	1-800-0.6-30	4-XL	52.00	66.50	34.00	63.00
		4-XR	56.00	69.50	32.00	63.00
		avg.	**54.00**	**68.00**	**33.00**	**63.00**
UN	Undamaged	5-XL	42.00	61.00	43.00	66.00
		5-XR	39.80	58.50	42.00	69.00
		avg.	**40.90**	**59.75**	**42.50**	**67.50**

member limitation (25 ft·lb) of the AASHTO 2007 bridge specification (*40*). Three of those were slightly smaller than the nonfracture critical member limitation (15 ft·lb).

10.2 Uniaxial Tension Tests

Uniaxial tension tests were conducted according to ASTM E8 (*41*) on tension coupons from each specimen. The detailed coupon dimension is shown in Figure 5.13. The test results are shown in Table 10.5, which includes the yield stress (σ_y), the ultimate stress (σ_t), the percent elongation, and the percent reduction (area). Normalized uniaxial tension results by undamaged specimen results are shown in Table 10.6.

Figures 10.3–10.6 show the normalized steel material properties (σ_y, σ_t, % elongation, and reduction in area) with respect to the corresponding undamaged steel material properties. Standard deviation error bars are also shown in Figures 10.3, 10.4, 10.5, and 10.6.

The tension test data in Tables 10.5 and 10.6 and Figures 10.3–10.6 indicate that:

- The yield stress of all damaged-repaired specimens increased (from 12% to 45%).
- For overheated specimens (S1 & S2), opposite to the small scale tension test results, the yield stress of the multiple damage-repair specimen increased less than the single damage-repair specimen.
- The yield stress and ultimate stress of overheated specimens (S1 & S2) increased less than the normal and under heated specimens (N1 &N2).
- Damage-heat straightening repairs reduced the percent elongation (ductility) of A36 steel. The reduction in ductility ranged approximately from 69% to 84% of the undamaged material. The decrease in the percent elongation of normal and under heated specimens (N1 & N2) was larger than that of overheated specimens (S1 & S2).
- The reduction in area reduced by 3–7% because of the damage-heat straightening repairs. The decrease of the

TABLE 10.6
Normalized uniaxial tension test results

Specimen ID	Specimen Designation	Coupon ID	Yield Stress (ksi)	Ultimate Stress (ksi)	Elongation (%)	Reduction in Area (%)
S1	3-1400-0.4-30	1-XL	1.13	1.09	0.80	0.93
		1-XR	1.12	1.15	0.78	0.98
		avg.	**1.13**	**1.12**	**0.79**	**0.96**
S2	1-1400-0.4-30	2-XL	1.16	1.08	0.85	0.99
		2-XR	1.22	1.10	0.82	0.95
		avg.	**1.19**	**1.09**	**0.84**	**0.97**
N1	3-1200-0.4-30	3-XL	1.37	1.16	0.73	0.95
		3-XR	1.45	1.22	0.66	0.95
		avg.	**1.41**	**1.19**	**0.69**	**0.95**
N2	1-800-0.6-30	4-XL	1.27	1.11	0.80	0.93
		4-XR	1.37	1.16	0.75	0.93
		avg.	**1.32**	**1.14**	**0.78**	**0.93**
UN	Undamaged	5-XL	1.03	1.02	1.01	0.98
		5-XR	0.97	0.98	0.99	1.02
		avg.	**1.00**	**1.00**	**1.00**	**1.00**

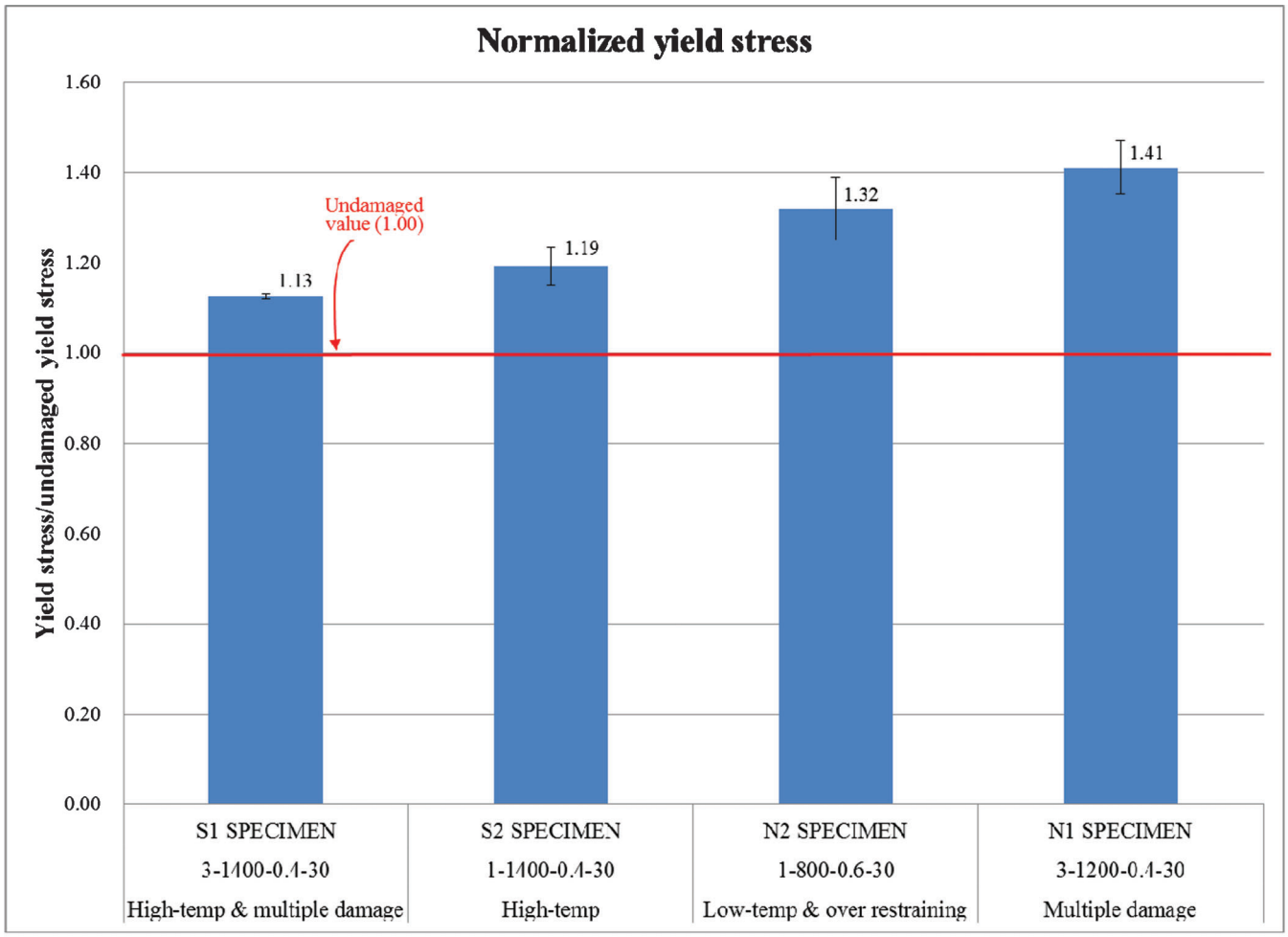

Figure 10.3 Normalized yield stresses of large scale specimens.

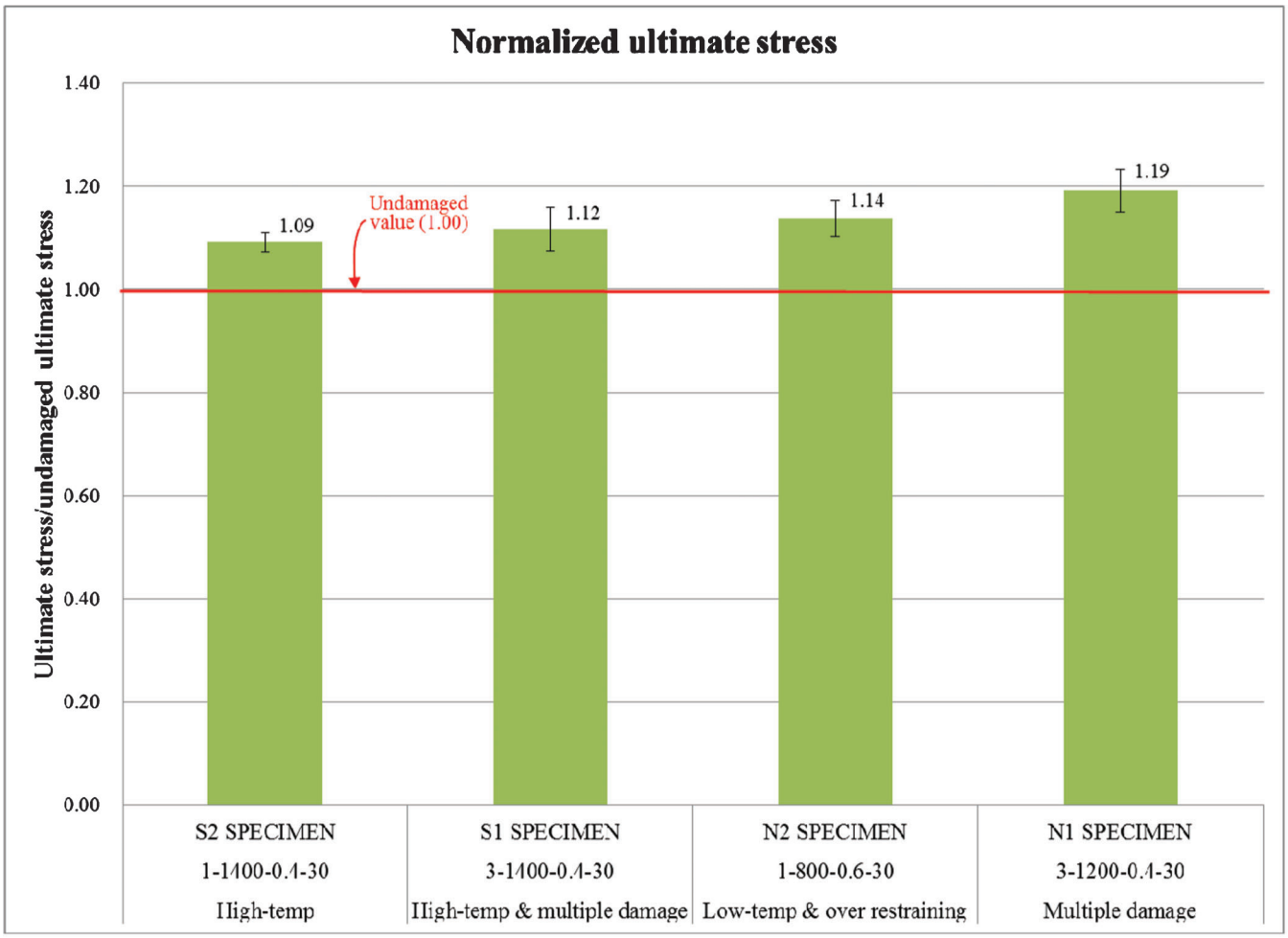

Figure 10.4 Normalized ultimate stresses of large scale specimens.

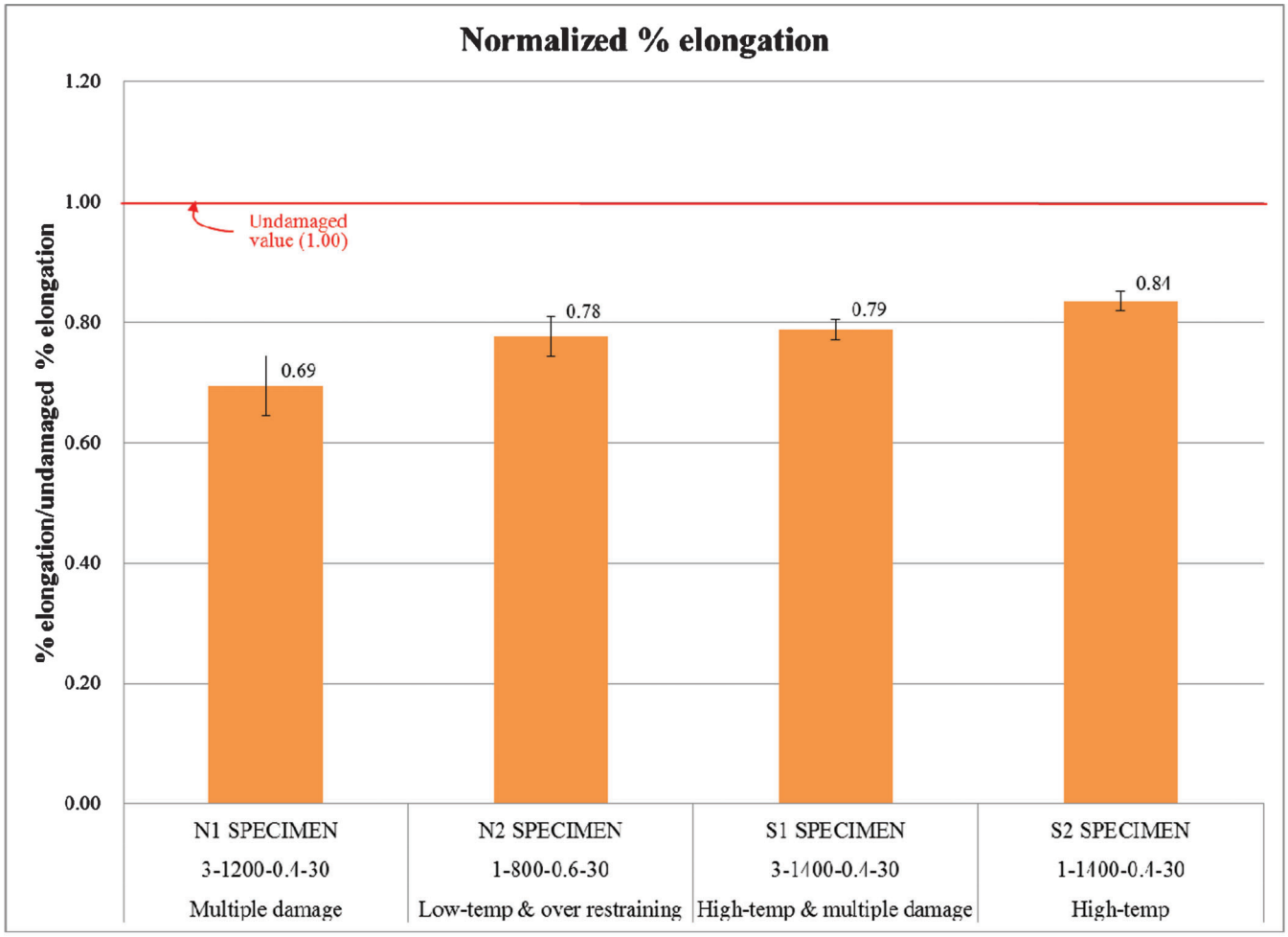

Figure 10.5 Normalized % elongations of large scale specimens.

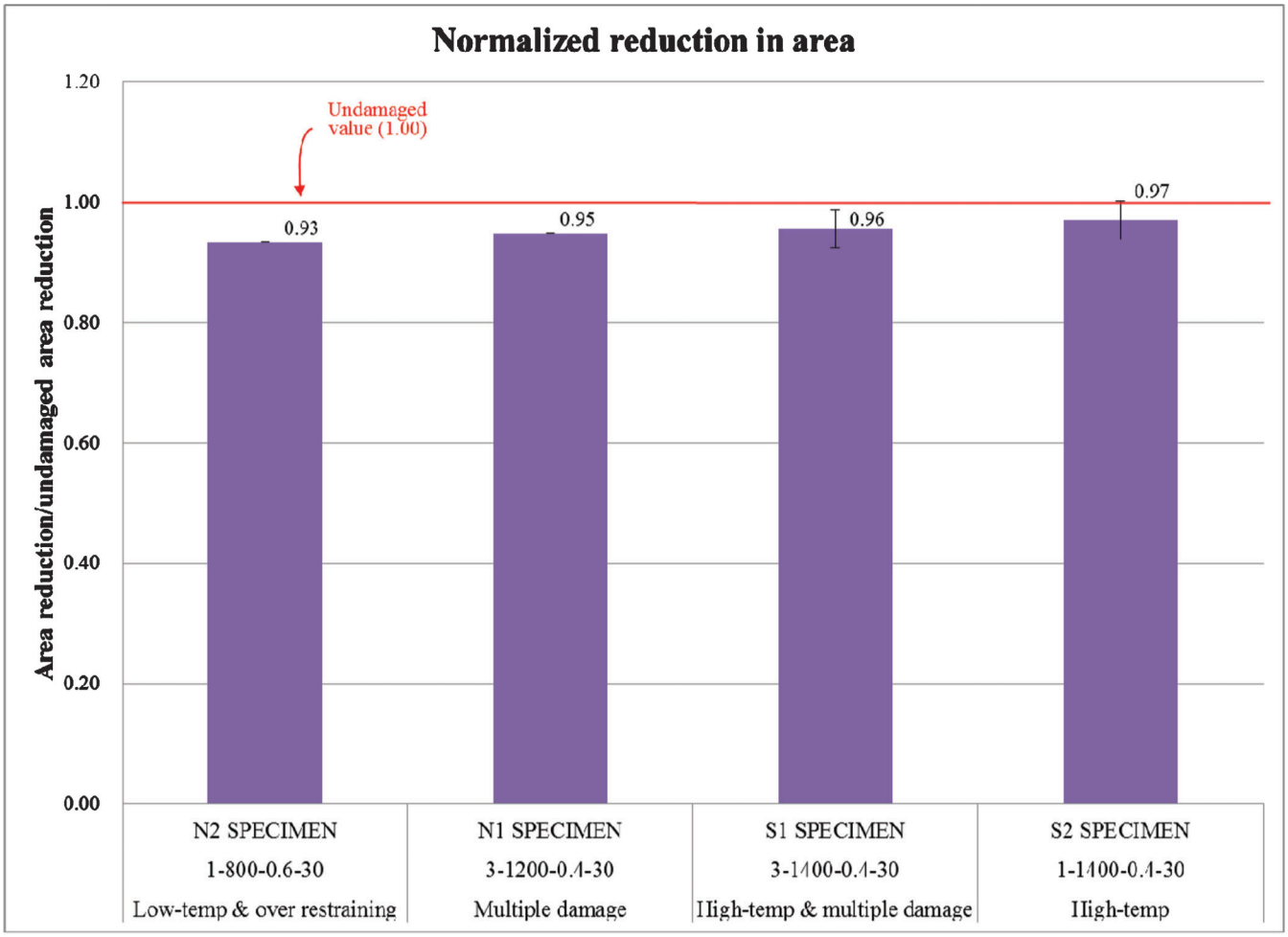

Figure 10.6 Normalized area reductions of large scale specimens.

reduction in the area of normal and underheated specimens (N1 & N2) was larger than that of the overheated specimens (S1 & S2).

10.3 Rockwell Hardness and Microstructure Investigations

Rockwell hardness tests were conducted on Charpy V-notch impact test coupons according to ASTM E18. Four points were taken on every specimen. Figure 7.9 shows the Rockwell hardness points on the Charpy V-notch specimen. Table 10.7 shows the Rockwell hardness test results and normalized values. Figure 10.7 shows the normalized value comparison.

The Charpy specimens used to conduct the Rockwell hardness tests were also used for the microstructure investigations. The Charpy specimen identified as C2 in every large scale specimen was used for the microstructure investigations. The specimens were prepared in accordance to ASTM E3 (*43*).

The etched specimens were placed under a metallurgical microscope with a photo micrographic camera

TABLE 10.7
Rockwell hardness test results

Specimen ID	Specimen Designation	Coupon ID	Rockwell Hardness Point 1	2	3	4	Avg.	Normalized
S1	3-1400-0.3-30	1-C-2	79.5	79.0	78.5	79.0	79.0	1.13
S2	1-1400-0.3-30	2-C-2	75.0	76.0	76.0	76.0	75.8	1.08
N1	3-1200-0.3-30	3-C-2	77.5	79.0	78.0	78.0	78.1	1.12
N2	1-800-0.6-30	4-C-2	76.5	77.0	77.0	76.5	76.8	1.10
UN	Undamaged	5-C-2	70.5	71.0	69.0	69.0	69.9	1.00

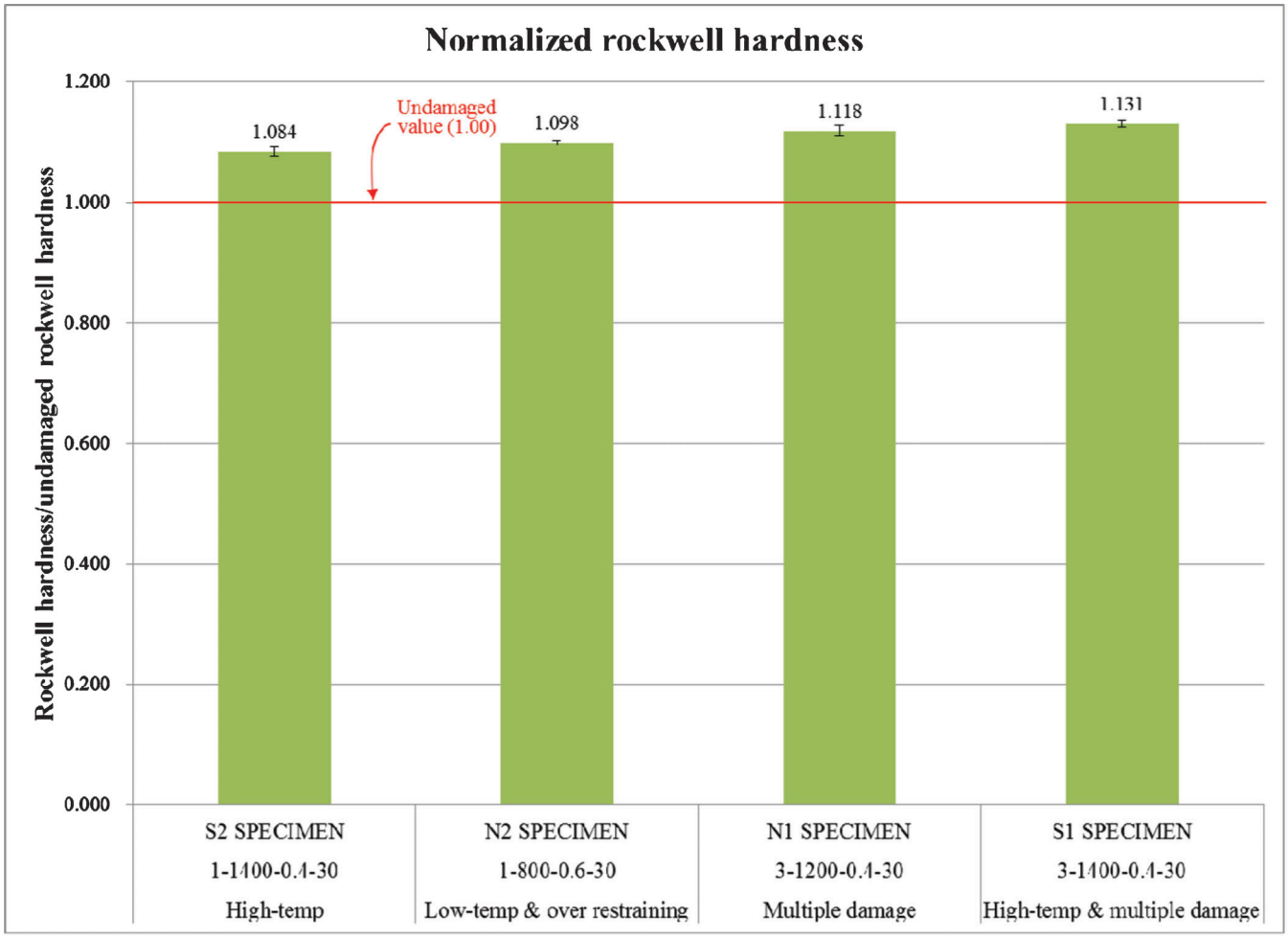

Figure 10.7 Normalized Rockwell hardness results of large scale test.

attached. A magnification of 300x was chosen for determining the grain sizes.

The grain size of each undamaged and damaged-repaired specimen was determined using the general line intercept procedure (Heyn Linear Intercept Procedure) outlined in ASTM E112 (*44*). In this method, a number of random lines are drawn with a known length and the number of grains that intercept each line is counted.

Microstructures of all specimens are shown in Figures 10.8–10.12. Table 10.8 shows the grain size and percent pearlite of each specimen. Normalized values of all specimens compared with the undamaged specimen are also shown in Table 10.8. Normalized values with standard deviation error bars are also compared in Figures 10.13 and 10.14.

The data presented in this section indicate that:

- The Rockwell hardness increased in all damaged-repaired specimens by about 8.4 – 13.1%

Figure 10.10 Microstructure of N1 specimen (3-1200-0.4-30)—300x.

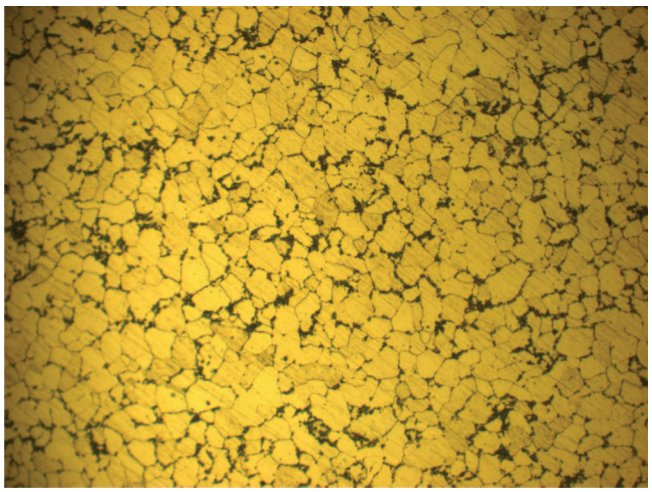

Figure 10.8 Microstructure of S1 specimen (3-1400-0.4-30)—300x.

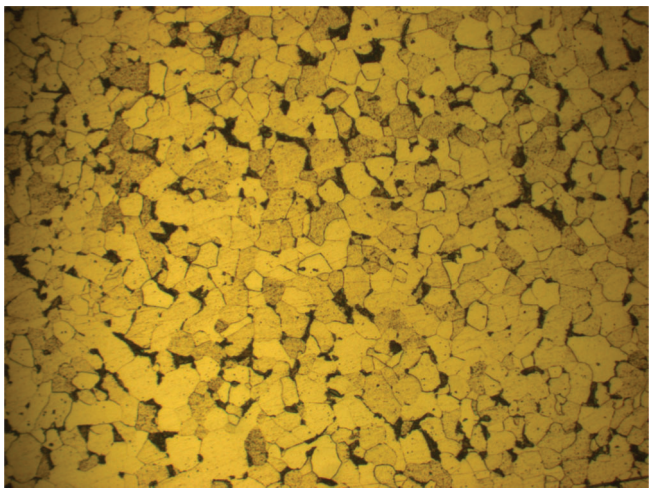

Figure 10.11 Microstructure of N2 specimen (1-800-0.6-30)—300x.

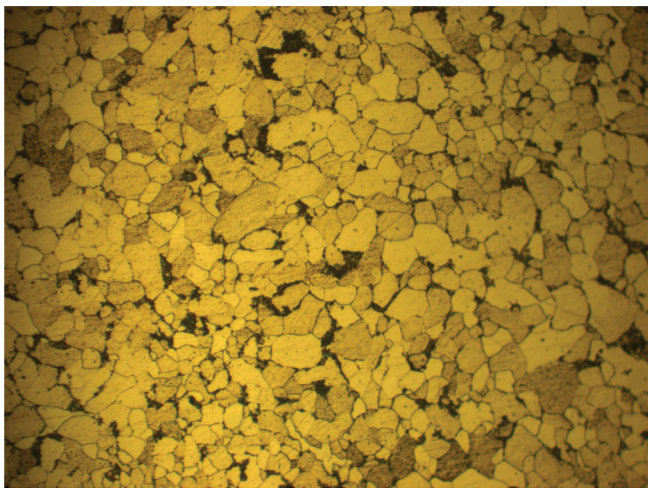

Figure 10.9 Microstructure of S2 specimen (1-1400-0.4-30)—300x.

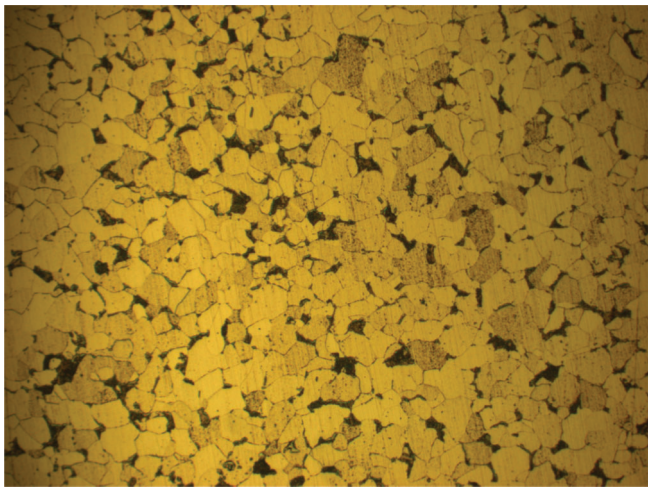

Figure 10.12 Microstructure of undamaged specimen—300x.

TABLE 10.8
Microstructure investigation results of large scale test

Specimen ID	Specimen Designation	Coupon ID	Average Grain Size		% Pearlite	
			Real Value (in.)	Normalized	Real Value (in.)	Normalized
S1	3-1400-0.3-30	1-C-2	0.000766	0.94	16.973	1.01
S2	1-1400-0.3-30	2-C-2	0.000795	0.98	18.657	1.11
N1	3-1200-0.3-30	3-C-2	0.000766	0.94	17.899	1.06
N2	1-800-0.6-30	4-C-2	0.000798	0.98	20.513	1.22
UN	Undamaged	5-C-2	0.000813	1.00	16.873	1.00

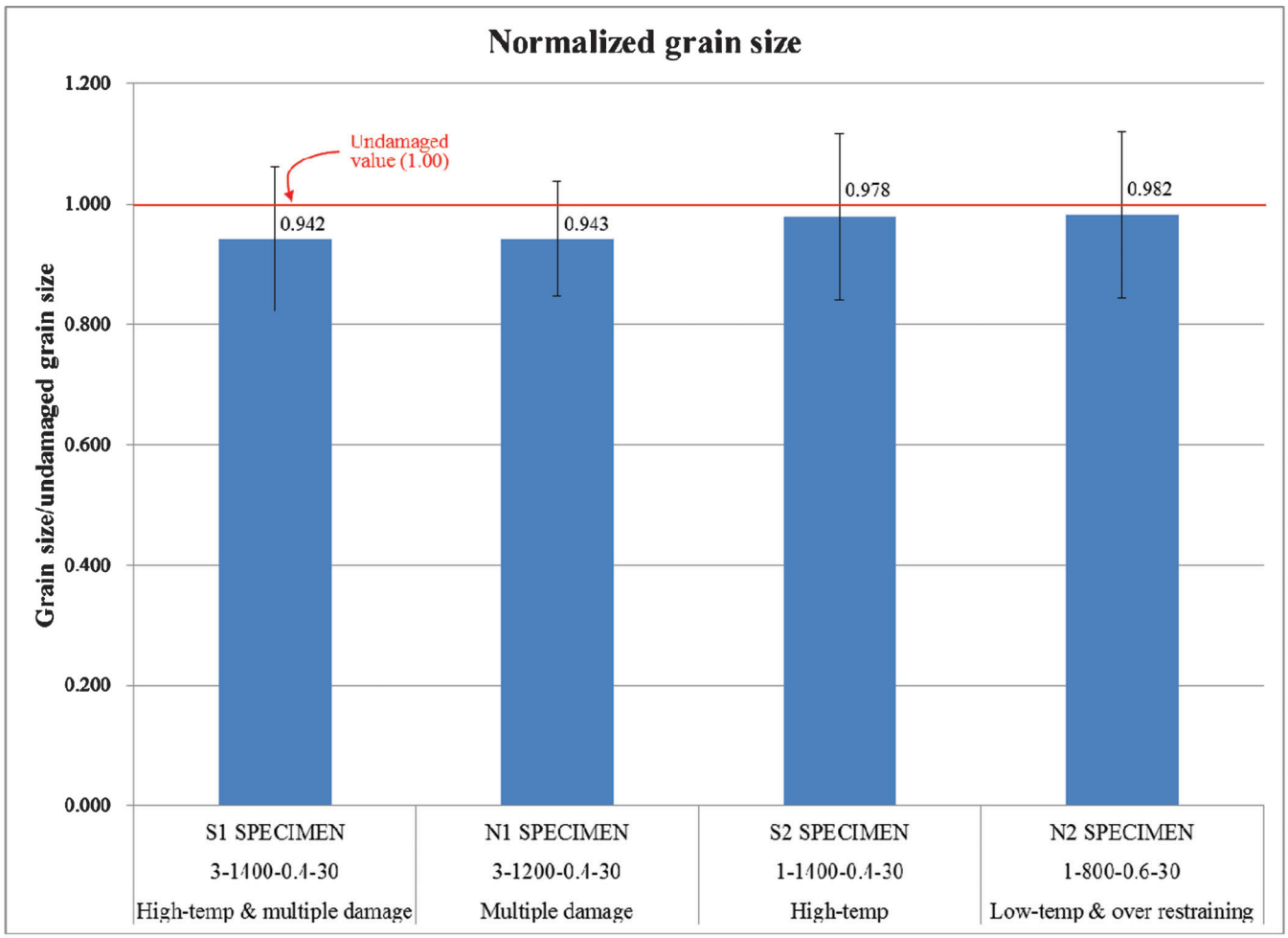

Figure 10.13 Normalized grain size of large scale test.

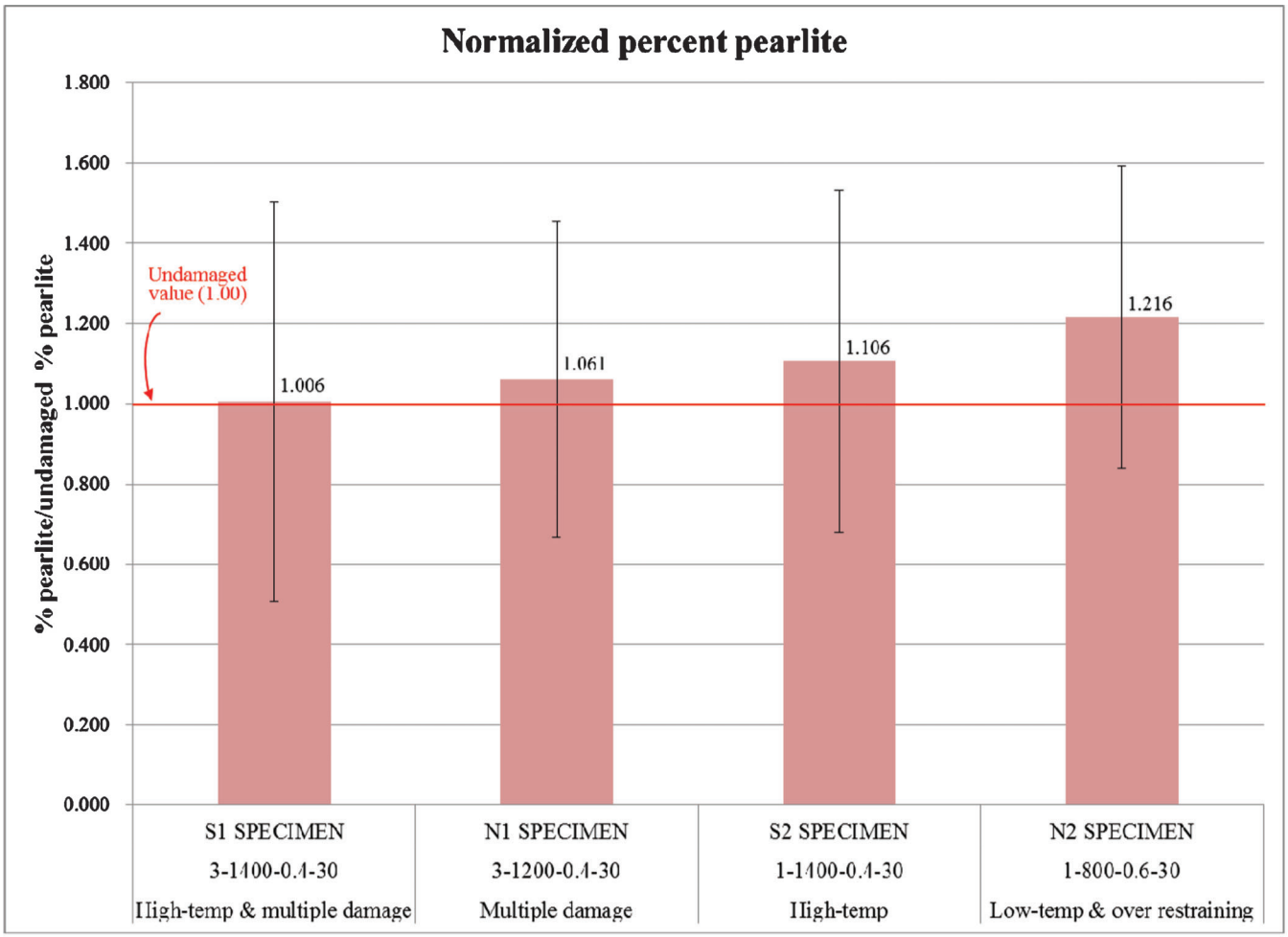

Figure 10.14 Normalized percent pearlite of large scale test.

- Multiple damage-repair specimens (S1 & N1) showed more increase in the Rockwell hardness than single damage-repair specimens (S2 & N2).
- Microstructure investigations indicated that brittle materials like bainite or martensite were not formed during heat straightening or subsequent cooling.
- The grain size of each damaged-repaired specimen decreased from that of the undamaged specimen by about 1.8–3.8%.
- Multiple damage-repair specimens (S1 & N1) showed more decrease in the grain size than single damage-repair specimens (S2 & N2).
- The grain sizes of overheating specimens (S1 & S2) were almost the same.
- The percent pearlite of each damage-repair specimen increased from that of the undamaged specimen by about 0.6–21.6%.
- The percent pearlite increased more in single damage-repair specimens (S2 & N2) than in multiple damage-repair specimens (S1 & N1).

10.4 Chemical Composition Analysis

Chemical composition of A36 steel used for the large scale specimen was determined according to ASTM E415. The chemical composition of undamaged steel was measured three times to determine more accurate results. Table 10.9 presents the chemical composition of the undamaged large scale test specimen. In Table 10.9, the chemical requirements of ASTM A36 steel (same as AASHTO M270 requirements) are also shown. As seen

TABLE 10.9
Chemical composition of large scale test steel

	Large Scale Test			ASTM A36 (AASHTO M270)
	Test 1	Test 2	Test 3	
C	0.180	0.190	0.190	Max 0.25
Cb	0.002	0.002	0.002	
Cr	0.080	0.080	0.080	
Cu	0.210	0.210	0.210	
Mn	0.510	0.510	0.500	
Mo	0.053	0.054	0.054	
Ni	0.100	0.100	0.100	
P	0.010	0.010	0.010	Max 0.04
S	0.010	0.010	0.010	Max 0.05
Si	0.040	0.040	0.040	Max 0.4
V	0.004	0.004	0.004	

TABLE 10.10
A_{c1} & A_{c3} temperatures of large scale test

		Large Scale Test		
		Test 1	**Test 2**	**Test 3**
Krauss (*47*)	**A_{c1} [°F]**	1325.1	1325.1	1325.3
	A_{c3} [°F]	1519.2	1515.0	1515.0
Trzaska & Dobrzan'ski (*48*)	**A_{c1} [°F]**	1337.6	1337.2	1337.3
	A_{c3} [°F]	1541.9	1537.3	1537.6

in the table, all three test results are very similar to each other and also meet the ASTM A36 requirements.

From the chemical composition of the steel, the eutectoid temperature (A_{c1}) and the stable austenite temperature (A_{c3}) were determined by using Equations 7.1–7.4.

The computed Ac_1 and Ac_3 values are presented in Table 10.10. As seen in Table 10.10, empirical equations of A_{c1} & A_{c3} from different researchers showed results similar to each other.

11. EVALUATION OF THE TEST RESULTS

In this chapter, the results of the small and large scale tests are evaluated and compared. The effects of various heat straightening applications on the repair speed of the damaged specimens (i.e., the number of heating cycles to repair the damaged small and large scale specimens) are summarized and compared in Section 11.1. In Section 11.2, the results of material tests on the small and large scale test specimens are also evaluated and compared to evaluate the effects of realistic heat straightening on the material properties of the damaged and repaired steel. Additionally, the serviceability performance of the large scale test bridge is summarized and evaluated in Section 11.3 to determine the effects of heat straightening repair on the serviceability performance of the damaged and repaired bridge.

11.1 The Efficiency of Repair Processes

The experimental behavior of small scale and large scale test specimens in various repair conditions were investigated in this research project. Based on the field visit results and the INDOT heat straightening database analysis, realistic repair conditions were determined. Those repair conditions included the following test variables: (i) the number of multiple damage-repair cycles, (ii) the maximum heating temperature, (iii) the restraining force, and (iv) the damage magnitude.

Table 11.1 presents required numbers of heating cycles to fully straighten each damaged specimen. The test variables of all specimens are also shown in Table 11.1.

To see the effects of the overheating on the number of required heating cycles, Specimens #3 and S1 (heated up to 1400 °F) are compared with Specimens #2 and S1 (heated up to 1200 °F) in Table 11.2. The number of heating cycles are normalized with respect to the number of heating cycles required for the normal-heating specimens (heated up to 1200 °F) and included in Table 11.2.

TABLE 11.1
Test variables and required heating cycles

	Specimen		**Test Variables**				**Heating Cycles**		
			(1)	**(2)**	**(3)**	**(4)**			
	ID	**Designation**	**(Nr)**	**°F**	**$\frac{\%}{100}M_p$**	**x ε_y**	**1st**	**2nd**	**3rd**
Small Scale Test	#1	1-1200-0.4-30	1	1200	0.4	30	102		
	#2	3-1200-0.4-30	3	1200	0.4	30	118	146	211
	#3	3-1400-0.4-30	3	1400	0.4	30	39	69	89
	#4	1-1400-0.4-60	1	1400	0.4	60	276		
	#5	1-1400-0.4-30	1	1400	0.4	30	54		
	#6	1-800-0.6-30	1	800	0.6	30	144		
Large Scale Test	S1	3-1400-0.4-30	3	1400	0.4	30	32	39	58
	S2	1-1400-0.4-30	1	1400	0.4	30	24		
	N1	3-1200-0.4-30	3	1200	0.4	30	42	50	66
	N2	1-800-0.6-30	1	800	0.6	30	410		

(1) = Damage & repair cycles.
(2) = Max. heating temperature.
(3) = Restraining force.
(4) = Max. damage strain (ε_d).

TABLE 11.2
Effect of overheating on the required heating cycles

	Specimen		Heating Cycles			Normalized Heating Cycles (by 1200 °F Values)			
	ID	Designation	1st	2nd	3rd	1st	2nd	3rd	Avg.
Small Scale Test	#2	3-1200-0.4-30	110[1]	146	211	1.00	1.00	1.00	1.00
	#3	3-1400-0.4-30	46.5[2]	69	89	0.42	0.47	0.42	0.44
Large Scale Test	N1	3-1200-0.4-30	42	50	66	1.00	1.00	1.00	1.00
	S1	3-1400-0.4-30	28[3]	39	58	0.67	0.78	0.88	0.78

[1]1st heating cycle is the average value of Specimen #1 & #2.
[2]1st heating cycle is the average value of Specimen #3 & #5.
[3]1st heating cycle is the average value of Specimen S1 & S2.

The overheated specimens required much smaller number of heating cycles to fully straighten the damaged steel beams. In the small scale test, required heating cycles of the overheated specimen was only 44% (average value) of the normal-heating specimens. In the large scale test, the required number of heating cycles reduced to 78% (average value) of the heating cycles of the normal-heating specimens.

Table 11.3 presents the effects of the underheating and overstraining on the required heating cycles of the damaged steel specimen. Specimens #1 and #6 are compared in Table 11.3 to see the difference in the required heating cycles. Specimens #1 and N1 were repaired by 1200 °F of heating temperature and 0.4 M_p of restraining force. While, 800 °F of heating temperature and 0.6 M_p of restraining force were applied on Specimens #6 and N2.

Table 11.3 indicates that Specimens #6 and N2 (underheated and overstrained) required many more heating cycles to fully straighten the damaged steel beams. Specimen #6 needed 31% more heating cycles then Specimen #1, and the N2 specimen needed almost 10 times the heating cycles of the N1 specimen to repair the damage.

Table 11.4 shows the effects of the multiple damage-repair cycles on the required heating cycles. All multiple damaged and repaired specimens of the small and large scale tests are shown in Table 11.4.

As seen in the table, the required number of heating cycles increase with the number of multiple damage-repair cycles. Compared with the first damage-repair cycle, 35% more heating cycles were required in the second damage-repair cycle. In the third damage-repair cycle, 87% more heating cycles were required than that of the first damage-repair cycle to complete the repair processes.

The effects of large damage ($60\varepsilon_y$) on the required heating cycles are shown in Table 11.5. Specimen #4 was applied $60\varepsilon_y$ of the damage magnitude which was twice as large as Specimen #5. As indicated in Table 11.5, the total heating cycles required to straighten the damaged Specimen #4 was six times larger than that of Specimen #5. This result indicated that the required heating cycles to repair the damaged steel specimen were not directly proportional to the damage magnitude.

Important findings in this section are like the following:

- Overheating (1400 °F) reduced the required number of heating cycles to repair the damaged specimen when compared with the normal-heating (1200 °F) specimens.
- Multiple damage-repair cycles increased the required heating cycles when compared with the single damage-repair specimen.
- The underheating case combined with overstraining needed more heating cycles than the normal-heating & restraining case.
- The number of required heating cycles were not directly proportional to the damage magnitude.

11.2 Material Tests

Material tests conducted on the specimens from the small and large scale test included: (i) uniaxial tension tests, (ii) Charpy V-notch tests, (iii) Rockwell hardness tests, and (iv) microstructure investigations. The averaged results of the material tests from the small scale and large scale test specimens are presented, and the relationships with the heat straightening variables are evaluated.

TABLE 11.3
Effect of underheating and overstraining on the required heating cycles

	Specimen		Heating Cycles	Normalized Heating Cycles (by 1200 °F & 0.4M_p Values)
	ID	Designation	1st	1st
Small Scale Test	#1	1-1200-0.4-30	110[1]	1.00
	#6	1-800-0.6-30	144	1.31
Large Scale Test	N1	3-1200-0.4-30	42	1.00
	N2	1-800-0.6-30	410	9.76

[1]1st heating cycle is the average value of Specimen #1 & #2

TABLE 11.4
Effect of multiple damage-repair cycles on the required heating cycles

	Specimen		Heating Cycles			Normalized Heating Cycles (by 1st Heating Cycles)		
	ID	Designation	1st	2nd	3rd	1st	2nd	3rd
Small Scale Test	#2	3-1200-0.4-30	110[1]	146	211	1.00	1.33	1.92
	#3	3-1400-0.4-30	47[2]	69	89	1.00	1.47	1.89
Large Scale Test	N1	3-1200-0.4-30	42	50	66	1.00	1.19	1.57
	S1	3-1400-0.4-30	28[3]	39	58	1.00	1.39	2.07
Average Value						1.00	1.35	1.87

[1] 1st heating cycle is the average value of Specimen #1 & #2.
[2] 1st heating cycle is the average value of Specimen #3 & #5.
[3] 1st heating cycle is the average value of Specimen S1 & S2.

11.2.1 Charpy Impact Fracture Toughness Tests

As mentioned earlier in Chapter 7, two sets of Charpy impact tests were conducted on the specimens from the small scale test at different test temperatures. The first set of Charpy test results conducted at 40 °F showed extremely low Charpy toughness values for all the small scale test specimens. It was later established in Section 7.1 that the reason was that the 40 °F of the test temperature was in transition region of the Charpy impact energy vs. the temperature graph (Figure 7.1). Therefore, additional Charpy tests were performed at 70 °F of the test temperature (room temperature) to see the clear difference between the specimens.

All the Charpy test results are shown in Table 11.6. Normalized values with respect to the Charpy values of corresponding undamaged steel are also presented in Table 11.6. As seen in Table 11.6, the Charpy toughness results of all specimens were reduced by the heat straightening repair process.

Important findings from the Charpy impact toughness tests are:

- The overheating (1400 °F) specimens showed slightly better Charpy impact toughness than the normal-heating (1200 °F) specimens.
- Multiple damage-repair cycles (3 times) decreased the Charpy impact toughness more than single damage-repair cycle
- Large damage decreased the Charpy impact toughness significantly when compared with moderate damage.
- Compared with the undamaged specimen, the Charpy impact toughness values of all specimens were decreased by heat straightening.
- For the small scale test, underheated specimen (800 °F) showed the smallest Charpy impact toughness.

11.2.2 Uniaxial Tension Tests

Uniaxial tension tests were conducted according to ASTM E8 (*41*) on the tension coupons removed from each specimen. As mentioned in previous chapters, four tensile test coupons were fabricated and tested from each small scale test specimen. For the large scale test specimens, two tensile coupons were removed and tested from each specimen.

Table 11.7 presents the test results of uniaxial tension tests, which includes (i) the yield stress (σ_y), (ii) the ultimate stress (σ_t), (iii) the percent elongation, and (iv) the percent reduction (area). Normalized values with respect to the corresponding undamaged steel properties are also presented in the Table 11.7.

As seen in the Table 11.7, the yield stress and the ultimate stress values of all specimens were increased by the heat straightening process. The percent elongation values of all damaged and repaired specimens reduced, which means that the steel became less ductile. The reductions of area of all small scale specimens were increased and those of all large scale specimens were decreased. However the amount of change was very small (1–3% increase in small scale tests and 3–7% decrease in large scale tests). The ASTM A36 steel requirements are also presented in Table 11.7. All the uniaxial tension test results in Table 11.7 meet the ASTM A36 steel requirements.

Important findings from the uniaxial tension tests are:

- The yield stress and the ultimate stress values of all damaged and repaired specimens increased when compared to the undamaged values.
- The percent elongation of all damaged and repaired specimens were decreased when compared to the undamaged values (became less ductile).

TABLE 11.5
Effect of large damage on the required heating cycles

	Specimen		Heating Cycles	Normalized Heating Cycles (by $30\varepsilon_y$ Values)
	ID	Designation	1st	1st
Small Scale Test	#5	1-1400-0.4-30	46.5[1]	1.00
	#4	1-1400-0.4-60	276	5.94

[1] 1st heating cycle is the average value of Specimen #3 & #5.

TABLE 11.6
Results of the Charpy impact fracture toughness tests

	Specimen		Charpy Toughness Results			
	ID	Designation	@ 40°F (ft·lbs)	Normalized	@ 70°F (ft·lbs)	Normalized
Small Scale Test	#1	1-1200-0.4-30	11.8	0.59	27.7	0.58
	#2	3-1200-0.4-30	8.9	0.45	21.4	0.45
	#3	3-1400-0.4-30	12.3	0.62	28.0	0.58
	#4	1-1400-0.4-60	9.3	0.47	21.0	0.44
	#5	1-1400-0.4-30	11.3	0.57	40.1	0.84
	#6	1-800-0.6-30	5.7	0.28	9.6	0.20
	#7	Undamaged	19.9	1.00	47.9	1.00
Large Scale Test	S1	3-1400-0.4-30	66.1	0.27	—	—
	S2	1-1400-0.4-30	78.4	0.32	—	—
	N1	3-1200-0.4-30	49.7	0.20	—	—
	N2	1-800-0.6-30	77.9	0.32	—	—
	UN	Undamaged	243.9	1.00	—	—

- The reduction in area values were changed very little by the heat straightening process.
- The yield stresses of the overheated specimens (heated up to 1400 °F) increased less than those of normally heated specimens (heated up to 1200 °F).

11.2.3 Rockwell Hardness Tests and Microstructure Investigations

Rockwell hardness tests were conducted on Charpy V-notch impact test coupons according to the ASTM E18. The change in surface hardness of each damage-repair specimen was determined by the Rockwell hardness tests. Microstructure investigations were performed on the same Charpy coupons following the ASTM regulations to see the microscopic changes of the damage-repair specimens.

Table 11.8 presents the Rockwell hardness values, average grain size, and the percent pearlite of all test specimens. Normalized values with respect to the corresponding undamaged test results are also shown in Table 11.8.

As seen in Table 11.8, the average grain sizes of all damage-repair specimens were decreased with respect to the undamaged values. The percent pearlite values of the small scale specimens were decreased but the values were increased in the large scale test specimens. The Rockwell hardness values were increased in all damage-repair specimens.

Important findings from the Rockwell hardness tests and microstructure investigations are:

- The average grain sizes of all damage-repair specimens decreased when compared to the undamaged values.

TABLE 11.7
Results of uniaxial tension tests

	Specimen		Material Test Results				Normalized Values			
	ID	Designation	(1) (ksi)	(2) (ksi)	(3) (%)	(4) (%)	(1)	(2)	(3)	(4)
	ASTM A36 Requirements		Min. 36	58–80	Min. 23	—	—	—	—	—
Small Scale Test	#1	1-1200-0.4-30	47.51	69.61	36.76	58.12	1.07	1.07	0.94	1.03
	#2	3-1200-0.4-30	54.78	73.75	29.24	56.25	1.23	1.14	0.75	1.00
	#3	3-1400-0.4-30	53.10	71.61	36.79	58.02	1.19	1.11	0.94	1.03
	#4	1-1400-0.4-60	54.92	71.50	34.69	56.89	1.24	1.10	0.88	1.01
	#5	1-1400-0.4-30	45.48	70.47	31.88	57.19	1.02	1.09	0.81	1.02
	#6	1-800-0.6-30	47.24	71.80	33.80	57.37	1.06	1.11	0.86	1.02
	#7	Undamaged	44.46	64.75	39.20	56.23	1.00	1.00	1.00	1.00
Large Scale Test	S1	3-1400-0.4-30	46.05	66.75	33.50	64.50	1.13	1.12	0.79	0.96
	S2	1-1400-0.4-30	48.80	65.25	35.50	65.50	1.19	1.09	0.84	0.97
	N1	3-1200-0.4-30	57.75	71.25	29.50	64.00	1.41	1.19	0.69	0.95
	N2	1-800-0.6-30	54.00	68.00	33.00	63.00	1.32	1.14	0.78	0.93
	UN	Undamaged	40.90	59.75	42.50	67.50	1.00	1.00	1.00	1.00

(1) = Yield stress.
(2) = Ultimate stress.
(3) = % elongation.
(4) = Reduction in area.

TABLE 11.8
Results of the Rockwell hardness tests and microstructure investigations

	Specimen		Average Grain Size		% Pearlite		Rockwell Hardness	
	ID	Designation	Value (in)	Normalized	Value (%)	Normalized	Value	Normalized
Small Scale Test	#1	1-1200-0.4-30	0.000672	0.86	27.4	0.96	82.6	1.12
	#2	3-1200-0.4-30	0.000771	0.99	22.5	0.79	82.8	1.12
	#3	3-1400-0.4-30	0.000731	0.94	22.2	0.78	80.9	1.10
	#4	1-1400-0.4-60	0.000739	0.95	26.5	0.93	84.6	1.15
	#5	1-1400-0.4-30	0.000692	0.89	21.4	0.75	84.6	1.15
	#6	1-800-0.6-30	0.000763	0.98	27.1	0.95	89.2	1.21
	#7	Undamaged	0.000778	1.00	28.5	1.00	73.8	1.00
Large Scale Test	S1	3-1400-0.4-30	0.000766	0.94	17.0	1.01	79.0	1.13
	S2	1-1400-0.4-30	0.000795	0.98	18.7	1.11	75.8	1.08
	N1	3-1200-0.4-30	0.000766	0.94	17.9	1.06	78.1	1.12
	N2	1-800-0.6-30	0.000798	0.98	20.5	1.22	76.8	1.10
	UN	Undamaged	0.000813	1.00	16.9	1.00	69.9	1.00

- The Rockwell hardness values were increased in all damage-repair specimens when compared to the undamaged values.

11.3 Serviceability Performance

The serviceability performance of the large scale test bridge was determined by subjecting static loads simulating the AASHTO 2007 HL-93 live load which can cause the maximum moment at each midspan (damaged and repaired point).

Vertical deflections at the midspan of all specimens were measured and compared to evaluate the difference of the serviceability performance at each test procedure. The midspan vertical deflections for all specimens are presented in Figure 9.41.

As mentioned in Chapter 9, The AASHTO 2007 bridge specification limits live-load deflections to L/800 for ordinary bridges and L/1000 for bridges in urban areas. Using these limitations with 20 ft. (240 in.) span length, allowable maximum deflection values of the test bridge were 0.3 in. (L/800) and 0.24 in. (L/1000).

Prior to the actual bridge service test, the maximum midspan deflections were predicted by two analysis methods. Hand calculation by using the linear deformation equation and the finite element analysis by using the ABAQUS 6.10 program were performed to predict the bridge midspan deflections with the 56 kips of the midspan static service load.

A two span continuous beam was analyzed by hand calculation using the least work method and conjugate beam method. Using those methods, the maximum midspan deflection caused by two equal midspan concentrated loadings was:

$$\Delta_{\text{midspan}} = \frac{7PL^3}{768\text{EI}} = 0.0118 \text{ in.}$$

Where, P = 55.77 kips
L = 20 ft. =240 in.
$E = E_s$ = 29000 ksi

$I = I_{\text{transformed}} = (I_{\text{con'c}})_{\text{converted to steel}} + I_{\text{steel}} = 20578.93 \text{ in}^4$

The finite element bridge model, which was developed in Chapter 8, was used to predict the bridge midspan deflections caused by the static service load. Figure 11.1 shows the service loading conditions of the FEM bridge model. As seen in Figure 11.1, 56 kips of concentrated service load was evenly distributed at around the midspan region of the solid slab elements.

From this FEM analysis model, the maximum midspan deflections of the test bridge were measured at actual vertical midspan sensor locations (inside edge of the bottom flange). The vertical deflection result of the FEM bridge model is shown in Figure 11.2. The maximum midspan deflection measured in the FEM analysis model was 0.0291 in.

The actual vertical midspan deflections measured in the undamaged large scale test bridge are shown in Table 11.9. The midspan deflections predicted by the two analysis methods are also presented in the table. As seen in Table 11.9, the FEM analysis showed better accuracy than the hand calculation method. The

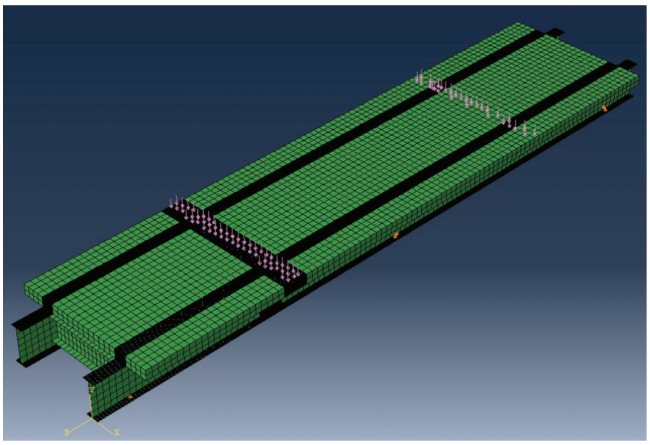

Figure 11.1 Service load conditions of the FEM analysis model.

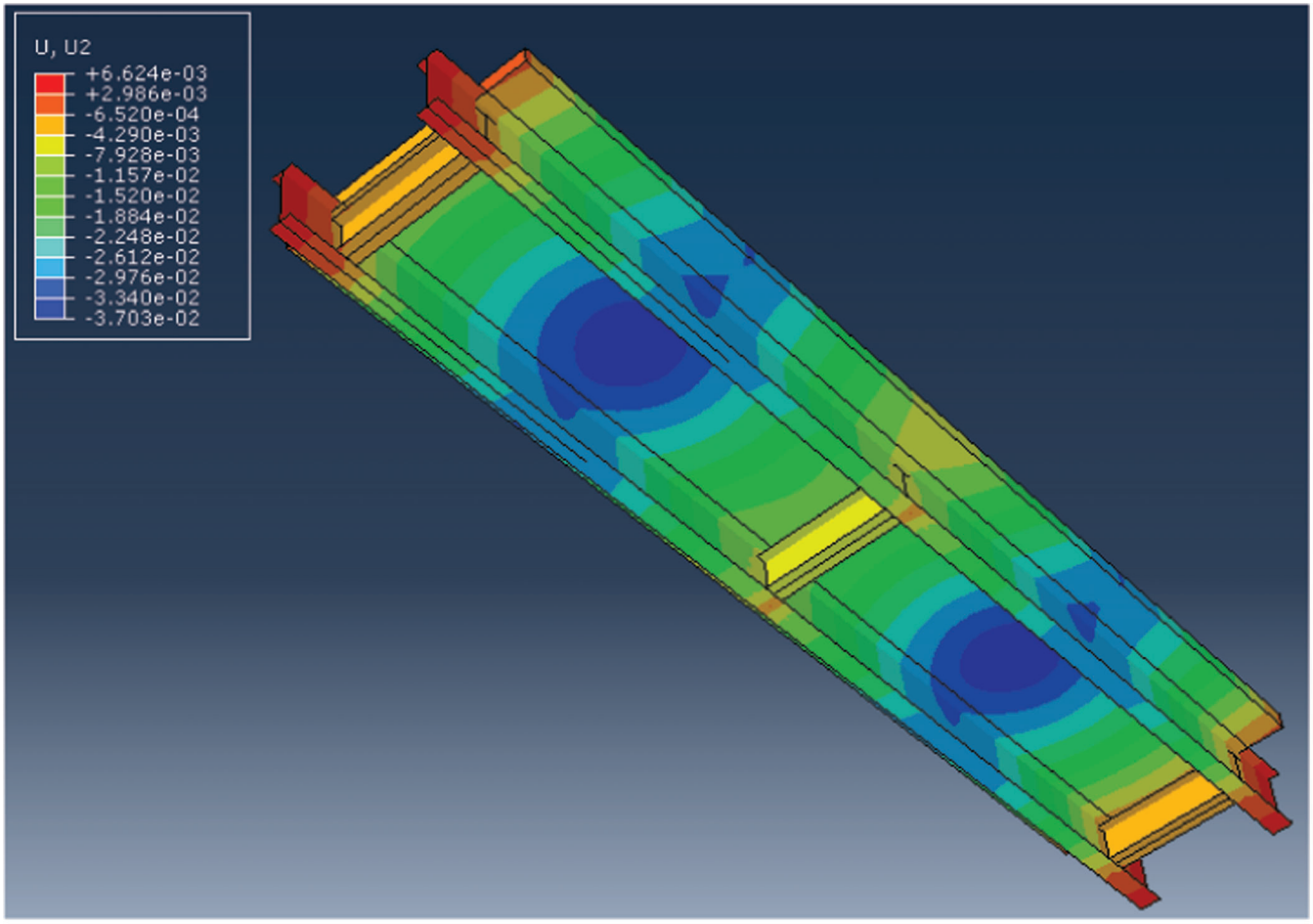

Figure 11.2 Vertical deflection result of the FEM serviceability analysis.

midspan deflection from the FEM analysis was very similar to that measured experimentally.

Figure 11.3 shows all serviceability deflection data and the AASHTO specification deflection limit. All of the midspan deflection data from the test and analysis were much smaller than the AASHTO deflection limit.

Detailed graphs of the midspan deflection during all the stages of testing are shown in Figure 11.4. One notable feature in the graph was the sudden increase of the midspan deflection right after each damage process. As seen in the graph, S1, S2, N1, and N2 midspan deflections were increased about 25, 30, 76 and 43% by the S1, S2, N1, and N2 damages respectively. But all those peak deflections reduced to the undamaged deflections following heat straightening processes.

This implies that the slender bridges, which have relatively lower stiffness and longer spans, may have some serviceability issues by the increased deflections of the damaged girders right after the damage and before repair. However, the serviceability of the damaged bridges can be restored close to their original capacity after the heat straightening repair is conducted. As a result, to avoid serviceability issues, damaged bridges

TABLE 11.9
Vertical deflections of undamaged large scale bridge

	S1	S2	N1	N2	Avg.
Experimental Data	0.0263	0.0310	0.0275	0.0266	0.0279
FEM Analysis Result	0.0291	0.0291	0.0291	0.0291	0.0291
Hand Calculation Result	0.0118	0.0118	0.0118	0.0118	0.0118
AASHTO Limit (Ordinary)	0.300	0.300	0.300	0.300	0.300
AASHTO Limit (Urban)	0.240	0.240	0.240	0.240	0.240

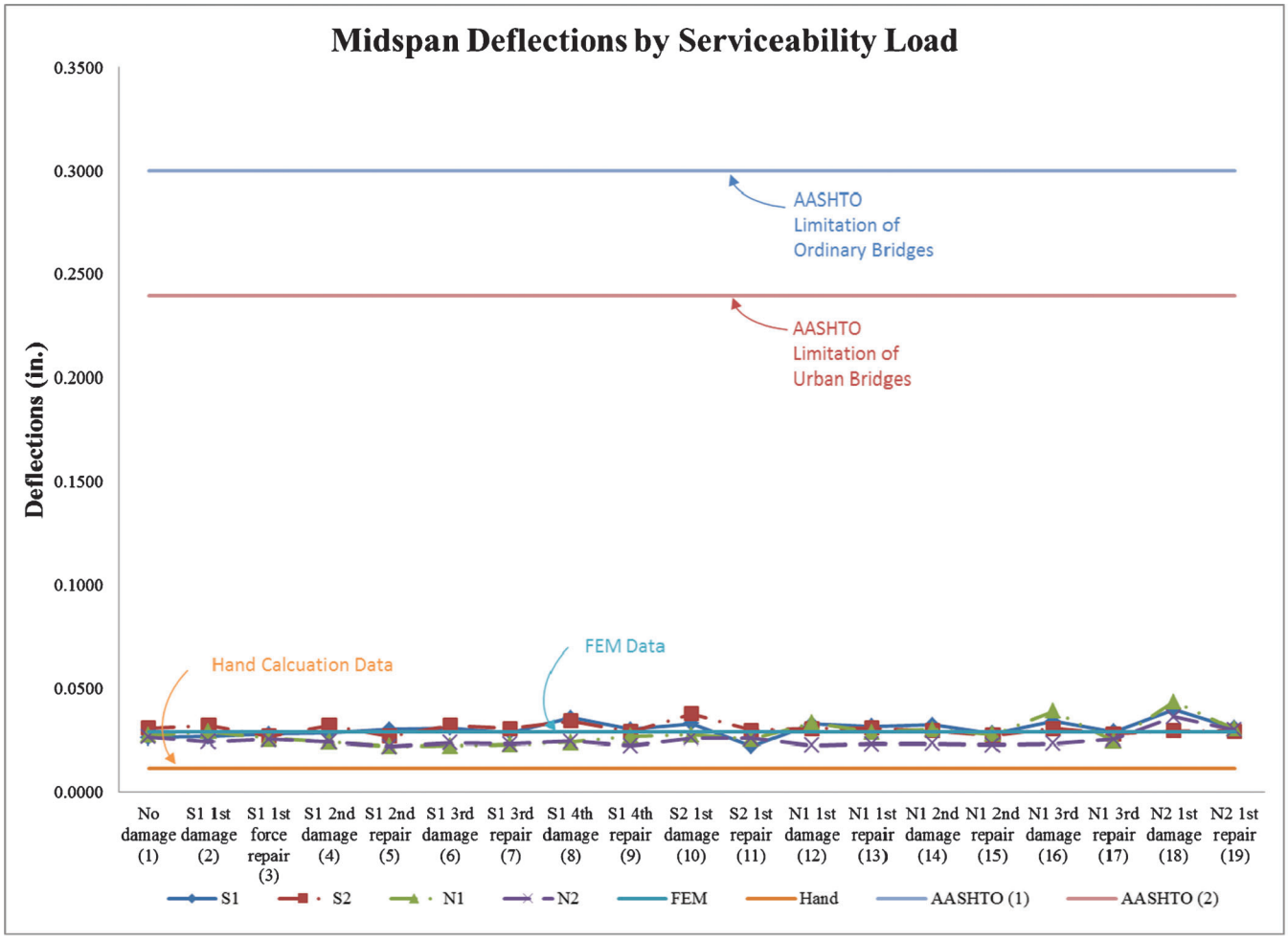

Figure 11.3 Serviceability deflection data and the AASHTO deflection limit.

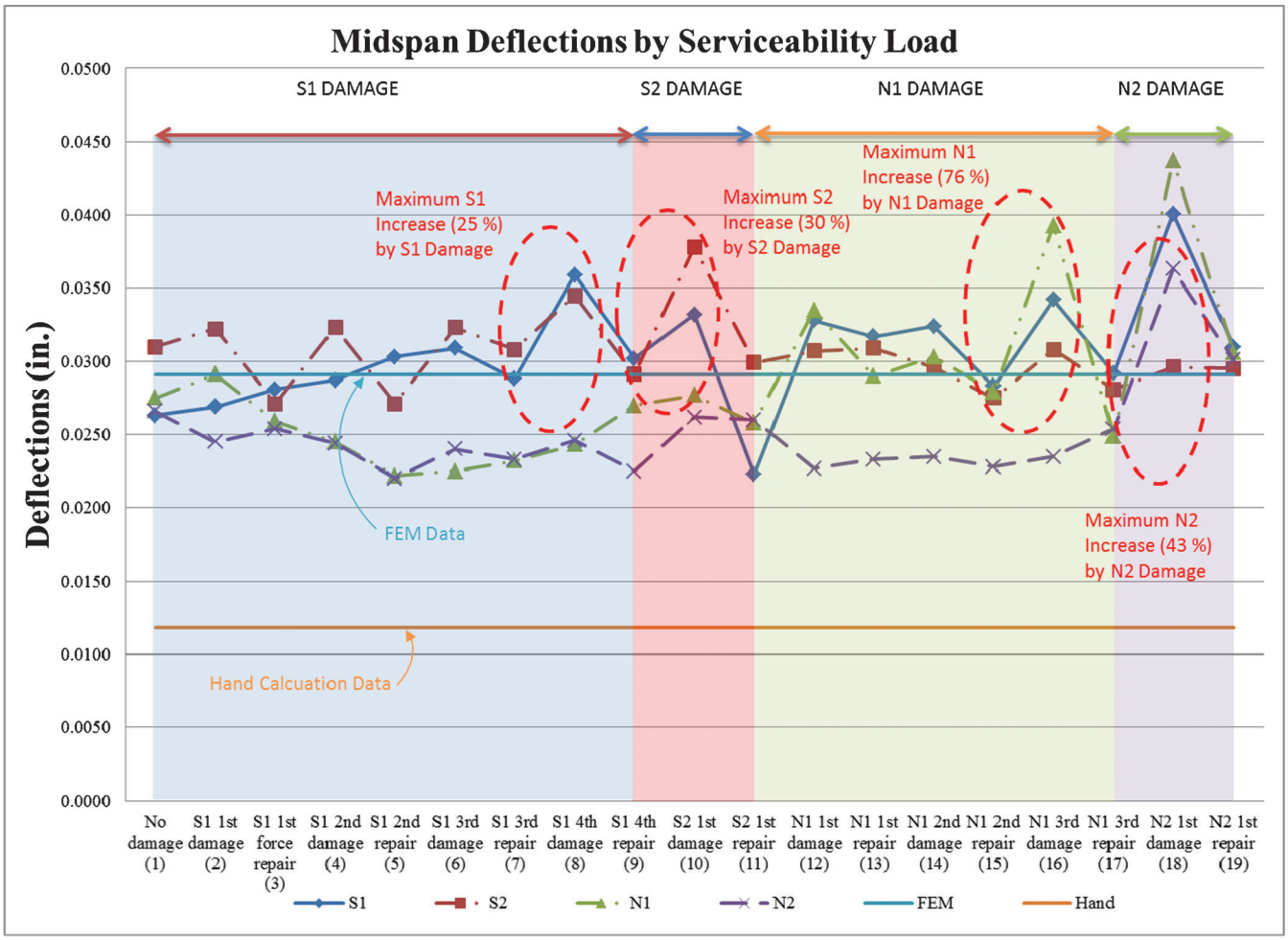

Figure 11.4 Midspan deflections by service load.

should be repaired as soon as possible by the heat straightening repair process.

12. SUMMARY, CONCLUSIONS, AND RECOMMENDATIONS

12.1 Research Objectives

Previous research on heat straightening of damaged steel bridges mainly addressed the following issues: (i) heat straightening repair techniques on damaged steel members, (ii) structural properties of heat straightened steels, and (iii) design guidelines and recommendations for heat straightening. Currently, the heat straightening limits and guidelines have been developed by many agencies based on previous research results. However, these limitations and guidelines are often violated while implementing heat straightening in the field.

These violations include, but are not limited to: (a) underheating below 1200°F, (b) overheating above 1200°F, (c) overstraining above restraining force limit (0.5 M_p), and (d) multiple heat straightening of the same beam more than two times. There is a lack of knowledge of the effects of these imperfections in the heat straightening repair process on the condition and serviceability of the damaged-repaired beams. This knowledge is needed to develop more realistic guidelines for evaluating and approving bridge members subjected to damage followed by imperfect heat straightening repair. The overall goal of this research is to develop recommendations and guidelines for evaluating steel beam bridges subjected to damage followed by heat straightening repair with imperfections (for example, overstraining, overheating, or multiple heat straightening).

12.2 Review of INDOT Heat Straightening Procedures

The INDOT heat straightening guidelines were presented and reviewed in Chapter 4. Most of the guidelines were similar to the FHWA heat straightening guidelines (*1*).

The Indiana heat straightening database analysis was performed to determine the steel bridge types and damage amount that are most relevant to this research. Twenty four heat straightening repair cases of 19 bridges were presented and analyzed. The database

analysis indicated that: (i) A36 was the most frequently damaged and heat straightening repaired steel type, (ii) composite continuous bridge was the most frequently damaged and heat straightening repaired structural type, and (iii) considering elastic rebound of the damaged steel, 30 ε_y was the maximum average damage amount. The steel type, bridge type, and the maximum damage identified in the database analysis were considered in the experimental investigations of this research.

On October 20–21, 2009, the heat straightening project on Allisonville Road, crossing over I465 eastbound near Indianapolis, was visited. Flame On, Inc., conducted heat straightening repair on the east-end girder (eastbound) damaged by an over-height truck.

Several deviations from the INDOT guidelines or the FHWA recommendations (*28*) existed at this specific heat straightening repair site. These included the following:

- Unreliable restraining force on damaged beam (no measurement on the applied force)
- Adjusting restraining force during the heat application
- No temperature measurement during heating
- Overheating (heating temperature over 1200 °F)
- Inaccurate cooling time to cool down below 250 °F (no temperature measurement)

12.3 Small Scale Tests

The small scale tests focused on the damage and realistic heat straightening repair of the bottom flange of steel beam girders. The damage and repair behavior was simulated by taking beam specimens with comparable flanges and subjecting them to weak axis bending. Six built-up specimens were damaged by the weak axis bending at the midspan and repaired by realistic heat straightening with imperfections. Half depth Vee heating was used for the realistic heat straightening.

The damage and repair parameters considered in the small scale test were: (a) the damage magnitude, (b) the restraining force, (c) the maximum heating temperature, and (d) the number of multiple damage-repair cycles. The effects of these parameters on: (i) the structural properties including the yield stress, ultimate stress, and ductility, (ii) the fracture toughness, and (iii) the steel microstructure were evaluated experimentally.

The major findings from the small scale test were as follows:

- Relative to number of damage-repair cycles

1. Overheating (1400 °F) significantly reduced the required number of heating cycles to repair the damaged specimen when compared with the normal-heating (1200 °F) specimens.
2. Multiple damage-repair cycles increased the number of heating cycles required to fully straighten the damaged specimen.

- Relative to fracture toughness

1. The overall fracture toughness of the small scale tests was lower than the undamaged steel toughness.
2. If the fracture toughness of the base steel was low (lower than the AASHTO bridge specification toughness requirements), then the fracture toughness reduction due to heat straightening repair was relatively small.
3. Compared with the control temperature (1200 °F), the fracture toughness of the overheated specimen (1400 °F) was slightly increased.
4. The 1-800-0.6-30 specimen (underheating and over-straining) showed the lowest fracture toughness capacity.
5. Multiple damage-repair cycles further reduced the fracture toughness of A36 steel.
6. For all Charpy specimens, the fracture toughness values became smaller closer to the flange-web junction.

- Relative to uniaxial tension properties

1. All uniaxial tension test results meet the ASTM A36 (AASHTO M270) requirements
2. Damage-repair cycles increased the yield stress of A36 steel (heated to 1200 °F & 1400 °F). Relative to the undamaged specimen, the yield stress of specimens with single damage-repair cycle specimens (Specimens 1 & 5) increased by 2–7%. Similarly for the specimens subjected to the multiple damage-repair cycles (Specimens 2 & 3), the yield stress increased by 19–23%.
3. The ultimate strength of all specimens increased from 8% to 14%. But no specific relationships with test variables were found.
4. Damage-heat straightening repairs reduced the percent elongation (ductility) of A36 steel. The ductility reduced to approximately 75–94% of the undamaged material.

- Relative to Rockwell hardness and microstructure

1. The Rockwell hardness of A36 steel was increased in all damage-repaired specimens by approximately 10–21%.
2. Microstructure investigations indicated that brittle materials like bainite or martensite were not generated during heat straightening.
3. Damage-repair cycles decreased the grain size of A36 steel to 86–99% of the undamaged material.
4. The grain size decreased less when using multiple damage-repair cycles.
5. The percent pearlite of A36 steel decreased to 75–99% of the undamaged steel.

12.4 Large Scale Test

The large scale experimental investigations focused on the effects of realistic heat straightening with imperfections on the condition and serviceability of a steel beam bridge.

A large scale test bridge was constructed considering the findings from the INDOT database analysis in Chapter 4.2. The bridge consisted of: (a) A36 W30x90 steel beams for main girder, (b) full composite continuous bridge,

(c) 20 ft. span length (equivalent to the cross beam distance), (d) 8 in. concrete slab thickness, and (e) 30 ε_y of maximum damage strain (ε_d).

All four spans (specimens) of the large scale test bridge were subjected to damage and realistic heat straightening repair simulating field activities and conditions. The damage and repair parameters considered in the large scale test were: (a) the damage magnitude, (b) the restraining force, (c) the maximum heating temperature, and (d) the number of multiple damage-repair cycles.

After the specimens were subjected to damage and realistic heat straightening repair, the serviceability performance of the repaired bridge was determined by subjecting it to static loads simulating the AASHTO 2007 (*40*) live load.

The material properties including the structural properties, fracture toughness, and microstructure of the damaged and repaired large scale specimens were also determined and evaluated.

The major findings from the large scale test were as follows:

- Relative to number of damage-repair cycles

1. Overheating (1400 °F) significantly reduced the required number of heating cycles to repair the damaged specimen when compared with the normal-heating (1200 °F) specimens.
2. Multiple damage-repair cycles increased the number of heating cycles required to fully straighten the damaged specimen.

- Relative to fracture toughness

1. The overall fracture toughness of the large scale tests was much lower than the undamaged steel toughness (approximately 27% of undamaged fracture toughness value)
2. Compared with the normal heating specimen (1200 °F), the fracture toughness of the overheated specimen (1400 °F) increased [comparison of S1 with N1].
3. The fracture toughness of the multiple damage-repair specimen (S1) decreased to 84% of the single damage-repair specimen (S2) toughness [comparison of S1 with S2].
4. For all Charpy specimens, the fracture toughness values became smaller closer to the flange-web junction.
5. Five individual Charpy coupons showed their fracture toughness values smaller than the fracture critical member limitation (25 ft·lb) of the AASHTO 2007 bridge specification. Three of those were slightly smaller than the nonfracture critical member limitation (15 ft·lb).

- Relative to uniaxial tension properties

1. All uniaxial tension test results meet the ASTM A36 (AASHTO M270) requirements
2. The yield stress of all damaged-repaired specimens increased (from 12% to 45%).
3. For overheated specimens (S1 & S2), opposite to the small scale tension test results, the yield stress of the multiple damage-repair specimen increased less than the single damage-repair specimen.
4. The yield stress and ultimate stress of overheated specimens (S1 & S2) increased less than the normal and under heated specimens (N1 &N2).
5. Damage-heat straightening repairs reduced the percent elongation (ductility) of A36 steel. The reduction in ductility ranged approximately from 69% to 84% of the undamaged material. The decrease in the percent elongation of normal and under heated specimens (N1 & N2) was larger than that of overheated specimens (S1 & S2).
6. The reduction in area reduced by 3–7% because of the damage-heat straightening repairs. The decrease of the reduction in the area of normal and under-heated specimens (N1 & N2) was larger than that of the overheated specimens (S1 & S2)

- Relative to Rockwell hardness and microstructure

1. The Rockwell hardness increased in all damaged-repaired specimens by about 8.4–13.1%.
2. Multiple damage-repair specimens (S1 & N1) showed more increase in the Rockwell hardness than single damage-repair specimens (S2 & N2).
3. Microstructure investigations indicated that brittle materials like bainite or martensite were not formed during heat straightening or subsequent cooling.
4. The grain size of each damaged-repaired specimen decreased from that of the undamaged specimen by about 1.8–3.8%.
5. Multiple damage-repair specimens (S1 & N1) showed more decrease in the grain size than single damage-repair specimens (S2 & N2).
6. The grain sizes of overheating specimens (S1 & S2) were almost equal to each other.
7. The percent pearlite increased more in single damage-repair specimens (S2 & N2) than in multiple damage-repair specimens (S1 & N1).

- Relative to serviceability performance

1. All midspan deflections caused by the static service load were much lower than the AASHTO bridge specification (2007) deflection limit.
2. Service load deflections increased significantly after each damage process. However, the increased deflections reduced to undamaged deflections by the heat straightening repair.

12.5 Recommendations and Guidelines

Based on the findings of this research, the final recommendations are presented in this section. All these recommendations mainly rely on the results of this research. Therefore, to properly apply these recommendations, limitations of this research are presented in Section 12.6 and additional studies required to solidify these recommendations are provided in Section 12.7.

1. A maximum heating temperature of 1400 °F may be an acceptable imperfection. In this research, overheating specimens (heated up to 1400 °F) and normal-heating

specimens (heated up to 1200 °F) showed similar test results. However, additional studies are required to support this recommendation.
2. Three damage-repair cycles might be acceptable. The test results of this research indicated that the difference between three damage-repair specimens and single damage-repair specimens was not that significant. However, additional research will also be needed to validate this recommendation.
3. An excessive restraining force over 0.5 M_p should not be combined with underheating (lower than 1000 °F). To be safer, the restraining force should not be over 0.5 M_p and the heating temperature should be over 1000 °F. The test results of this research showed that the 1-800-0.6-30 specimens of all tests needed the most heating cycles to repair the same damage. Even the 1-800-0.6-30 specimen of the small scale test showed the lowest Charpy impact fracture toughness and the highest Rockwell hardness. As a result, to increase the repair speed and to prevent the brittle material behavior of the bridge specimen, overstraining and underheating should be avoided.
4. Heating temperature must be monitored during the heat application. Temperature-sensitive crayons, pyrometers, or infrared noncontact thermometers can be used to verify temperatures during heating operations (e.g., AWS D1.7/D1.7M 2010) (*49*).
5. The restraining force should not be applied to the damaged bridge without a verified force measurement system.
6. During the heating process, applied restraining force should not be adjusted.
7. To avoid serviceability issues, unless the bridge traffic is closed, damaged girders should be repaired immediately.

12.6 Limitations

1. This study focusses on A36 steel because it was identified as the most frequently damaged and heat straightened steel type in Indiana. The findings, conclusions, and recommendations of this study are limited to A36 steel. They should not be extended to other steel grades like A709, A572, A588 and HPS 70W without additional experimental correlations.
2. Welded details that may be susceptible to fatigue issues were not included in this study. Therefore, these findings, conclusions, recommendations should not be extended to regions near fatigue critical welded details without additional experimental correlations.
3. The experimental investigations in this study were conducted inside the laboratory. The specimens were exposed to conventional air cooling after heating. Other cooling methods like water mist, forced air cooling etc. were not included in this study.
4. The findings, conclusions, and recommendations of this study will not apply if the real bridge is exposed to rapid cooling due to thunderstorms, snow or ice fall etc.
5. Heat straightening of real bridges should be suspended when adverse weather conditions like thunderstorms, snow fall, or hail.

12.7 Recommendations for Future Work

1. Additional heat straightening research with the maximum heating temperature over 1400 °F is needed.
2. The effect of multiple damage-repair cycles on real bridge specimens should be further determined in various test conditions.
3. The fatigue behavior of a heat straightened steel bridge should be determined.
4. Actual wheel loading should be applied on the test bridge to determine the realistic serviceability performance of the test bridge before and after the heat straightening.
5. To determine the detrimental effect of the heat straightening on the serviceability performance of the actual bridge, bridge specimens with a longer span and lower sectional stiffness should be prepared and tested.
6. Additional research should be conducted on the practical tolerances of repaired steel beams. In this research, the repair speed was decreased significantly when the damaged beam was close to being straight. In the real field situation, cost and traffic delays can be reduced by having more relaxed tolerances.

REFERENCES

1. Avent, R. R., and D. J. Mukai. *Heat-Straightening Repairs of Damaged Steel Bridges—A Technical Guide and Manual of Practice*. Publication FHWA-IF-99-004. Federal Highway Administration, U.S. Department of Transportation, 1998.
2. Avent, R. R., and D. J. Mukai. What you should Know about Heat Straightening Repair of Damaged Steel. *Engineering Journal*, Vol. 38, No. 1, 2001, pp. 27–49.
3. Roeder, C. W. Experimental Study of Heat Induced Deformation. *Journal of Structural Engineering*, ASCE, Vol. 112, No. 10, October 1986, pp. 2247–2262.
4. Avent, R. R., D. J. Mukai, and P. F. Robinson. Heat Straightening Rolled Shapes. *Journal of Structural Engineering*, Vol. 126, No. 7, 2000, pp. 755–763.
5. Avent, R. R., D. J. Mukai, and P. F. Robinson. Effect of Heat Straightening on Material Properties of Steel. *Journal of Materials in Civil Engineering*, Vol. 12, No. 3, 2000, pp. 188–195.
6. Avent, R. R., D. J. Mukai, P. F. Robinson, and R. J. Boudreaux. Heat Straightening Damaged Steel Plate Elements. *Journal of Structural Engineering*, Vol. 126, No. 7, 2000, pp. 747–754.
7. Avent, R. R., D. J. Mukai, and P. F. Robinson. Residual Stresses in Heat-Straightened Steel Members. *Journal of Materials in Civil Engineering*, Vol. 13, No. 1, 2001, pp. 18–25.
8. Varma, A. H., and K. J. Kowalkowski. *Effects of Multiple Damage-Heat Straightening Repair on the Fundamental Properties of Bridge Steels*, MDOT Report No. RC-1456, Michigan Department of Transportation, Construction and Technology Division, Lansing, Michigan, pp. 418. 2004.
9. Kowalkowski, K. J. *Effects of Multiple Damage-Heat Straightening Repair Cycles on the Structural Properties and Fracture Toughness of Steel Beam Bridges*, Ph.D. Dissertation, Purdue University, School of Civil Engineering, West Lafayette, Indiana, 2005.
10. Holt, J. E. Flame Straightening: A Friend in Need. *Welding Engineer*, Vol. 40, No. 10, October, pp. 44–46, No. 12, Dec. 1955, pp. 30–31.
11. Ditman, O. *Determination of Thermal Shrinkage in Structural Steel*. MS Thesis, University of Washington, 1961.
12. Chin, W. *Linear Shrinkage of Steel*. MS Thesis, University of Washington, 1962.

13. Holt, R. E. Flame Straightening Basics. *Welding Engineer*, Vol. 50, No. 9, Sept. 1965, pp. 49–53.
14. Holt, R. E. How to Control and Correct Warping. *Welding Design and Fabrication*, June 1977, pp. 98–102.
15. Brockenbrough, R. L., and K. D. Ives. Experimental Stresses and Strains from Heat Curving. *Journal of the Structural Division*, ASCE, Vol. 96, No. ST7, Proc. Paper 7400, July 1970, pp. 1305–1331.
16. Brockenbrough, R. L. Theoretical Stresses and Strains from Heat Curving. *Journal of the Structural Division*, ASCE, Vol. 96, No. ST7, Proc. Paper 7410, July 1970, pp. 1421–1444.
17. Horton, D. L. *Heat Curved Mild Steel Wide Flange Sections: An Experimental and Theoretical Analysis*, MS Thesis, University of Washington, 1973.
18. Weerth, D. E. *Theoretical and Experimental Analysis of Heat Curved Mild* Steel. MS Thesis, University of Washington, 1971.
19. Holt, R. E. Primary Concepts in Flame Bending. *Welding Engineer*, Vol. 56, No. 6, June 1971, pp. 416–424.
20. Moberg, K. L. *Damage Assessment and Contraction Straightening of Steel Structures*. MS Thesis, University of Washington, 1979.
21. Avent, R. R., and G. M. Fadous. Heat straightening Techniques for Repair of Damaged Structural Steel in Bridges, Final Report. *Louisiana Transportation Research Center*Louisiana State University, Baton Rouge, 1988.
22. Roeder, C. W. *Use of Thermal Stress for Seismic Damage Repair*. Final Report on NSF Grant CEE-82-05260, University of Washington, Seattle, Oct. 1985.
23. Avent, R. R., P. F. Robinson, A. Madan, and S. Shenoy. Development of Engineering Design Procedures for Heat straightening Repair of Damaged Structural Steel in Bridges. In *LTRC*, No. 251, Louisiana Transportation Research Center, Baton Rouge, Louisiana, 1992.
24. De Bejar, L. A., P. F. Robinson, and R. R. Avent. Risk Consistent Estimate of Heat-Straightening Applications, I: Plates. *Journal of Structural Engineering*, ASCE. Vol. 118, No. 12, 1992, pp. 3394–3409.
25. De Bejar, L. A., P. F. Robinson, and R. R. Avent. Risk Consistent Estimate of Heat-Straightening Applications. II: Beams. *Journal of Structural Engineering*, ASCE, Vol. 118, No. 12, 1992, pp. 3440–3426.
26. Nichols, J. I., and D. E. Weerth. Investigation of Triangular Heats Applied to Mild Steel Plates. *Engineering Journal*, AISC, Oct. 1972, pp. 137–141.
27. Rothman, R. L. *Flame Straightening Quenched-and-Tempered Steels in Ship Construction*. Report No. 235. U.S. Ship Structure Committee, Washington, D.C., 1973.
28. *Heat straightening Repairs of Damaged Steel Bridges—A Technical Guide and Manual of Practice*. Report NO. FHWA-IF-99-004, Federal Highway Administration, Washington, D.C, 1998.
29. Blodgett, O. W. Distortion… How Metal Properties Affect It. *Welding Engineer*, Feb. 1972, pp. 40–46.
30. Putherickal, J. *Effects of Heat Straightening Structural Steel*. Final Report for MLR-91-3, Iowa Dept. of Transportation, Ames, Iowa, 1992.
31. ASTM E23. *Standard Test Methods for Notched Bar Impact Testing of Metallic Materials*. American Society for Testing and Materials, West Conshohocken, Pennsylvania.
32. Harrison, H. L. Straightening Structural Members in Place. *Welding Journal*, Vol. 31, No. 5, May 1952, Research Supplement, pp. 257s–262s.
33. Pattee, H. E., R. M. Evans, and R. E. Monroe. *Flame Straightening and its Effect on Base Metal Properties*. Summary Report to Ship Structure Committee concerning first phase of Project SR-185, Straightening Distorted Weldments, Battelle Memorial Inst., Columbus, Ohio, 1969.
34. Pattee, H. E., R. M. Evans, and R. E. Monroe. Effect of Flame and Mechanical Straightening on Material Properties of Weldments. *Summary Report on Ship Structure Committee on Project SR-185, Straightening Distorted Weldments*. Battelle Memorial Inst., Columbus, Ohio, 1970.
35. Avent, R. R., and B. L. Brakke. Anatomy of Steel Bridge Heat-Straightening Project. In *Transportation Research Record: Journal of the Transportation Research Board*, No. 1561, Transportation Research Board of the National Research Council, Washington, D.C., 1996, pp. 26–36.
36. Till, R. D. *Effect of Elevated Temperature on Fracture Critical Steel Members*. MDOT Research Report No. R-1344, Materials and Technology Division, Michigan Department of Transportation, 1996, pp. 1–17.
37. Shanafelt, G. O., and W. G. Horn. *Guidelines for Evaluation and Repair of Damaged Steel Bridge Members*. NCHRP Report No. 271, Transportation Research Board, National Research Council, Washington, D.C., June 1984.
38. Totten, G. E., and M. A. Howes. *Steel Heat Treatment Handbook*. Marcel Dekker, Inc., New York, 1997.
39. Connor, R. J., E. J. Kaufmann, and M. J. Urban. Heat-Straightening Repair of Damaged Steel Bridge Girders: Fatigue and Fracture Performance. NCHRP Report No. 604, Transportation Research Board, National Research Council, Washington, D.C., 2008.
40. AASHTO. *AASHTO LRFD Bridge Design Specifications, Fourth Edition*, American Association of State Highway and Transportation Officials, Washington, D.C., 2007.
41. ASTM E8. *Standard Test Methods for Tension Testing of Metallic Materials*, American Society for Testing and Materials, West Conshohocken, Pennsylvania.
42. ASTM E18. *Standard Test Methods for Rockwell Hardness of Metallic Materials*. American Society for Testing and Materials, West Conshohocken, Pennsylvania.
43. ASTM E3. *Standard Guide for Preparation of Metallographic Specimens*. American Society for Testing and Materials, West Conshohocken, Pennsylvania.
44. ASTM E112. *Standard Test Methods for Determining Average Grain Size*. American Society for Testing Materials, West Conshohocken, Pennsylvania.
45. ASTM E415. *Standard Test Method for Atomic Emission Vacuum Spectrometric Analysis of Carbon and Low-Alloy Steel*. American Society for Testing and Materials, West Conshohocken, Pennsylvania.
46. ASTM A36. *Standard Specification for Carbon Structural Steel*. American Society for Testing and Materials, West Conshohocken, Pennsylvania.
47. Krauss, G. *Principals of Heat Treatment of Steel*. American Society for Metals, Metals Park, Ohio, 1980.
48. Trzaska, J., and L. A. Dobrzanski. Modelling of CCT Diagrams for Engineering and Constructional Steels. *Journal of Materials Processing Technology*, Vol. 192–193, October 2007, pp. 504–510.
49. AWS D1.7/D1.7M. *Guide for Strengthening and Repairing Existing Structures*. American Welding Society, Miami, Florida, 2010.

About the Joint Transportation Research Program (JTRP)

On March 11, 1937, the Indiana Legislature passed an act which authorized the Indiana State Highway Commission to cooperate with and assist Purdue University in developing the best methods of improving and maintaining the highways of the state and the respective counties thereof. That collaborative effort was called the Joint Highway Research Project (JHRP). In 1997 the collaborative venture was renamed as the Joint Transportation Research Program (JTRP) to reflect the state and national efforts to integrate the management and operation of various transportation modes.

The first studies of JHRP were concerned with Test Road No. 1—evaluation of the weathering characteristics of stabilized materials. After World War II, the JHRP program grew substantially and was regularly producing technical reports. Over 1,500 technical reports are now available, published as part of the JHRP and subsequently JTRP collaborative venture between Purdue University and what is now the Indiana Department of Transportation.

Free online access to all reports is provided through a unique collaboration between JTRP and Purdue Libraries. These are available at: http://docs.lib.purdue.edu/jtrp

Further information about JTRP and its current research program is available at: http://www.purdue.edu/jtrp

About This Report

An open access version of this publication is available online. This can be most easily located using the Digital Object Identifier (doi) listed below. Pre-2011 publications that include color illustrations are available online in color but are printed only in grayscale.

The recommended citation for this publication is:

Varma, A. H., and Y. Sohn. *Effects of Realistic Heat Straightening Repair on the Properties and Serviceability of Damaged Steel Beam Bridges*. Publication FHWA/IN/JTRP-2013/03. Joint Transportation Research Program, Indiana Department of Transportation and Purdue University, West Lafayette, Indiana, 2013. doi: 10.5703/1288284315184.